

This item was submitted to [Loughborough's Research Repository](#) by the author.
Items in Figshare are protected by copyright, with all rights reserved, unless otherwise indicated.

On the creasing, folding and gluing of corrugated fibreboards

PLEASE CITE THE PUBLISHED VERSION

PUBLISHER

© A.M. Lau

PUBLISHER STATEMENT

This work is made available according to the conditions of the Creative Commons Attribution-NonCommercial-NoDerivatives 2.5 Generic (CC BY-NC-ND 2.5) licence. Full details of this licence are available at:
<http://creativecommons.org/licenses/by-nc-nd/2.5/>

LICENCE

CC BY-NC-ND 2.5

REPOSITORY RECORD

Lau, Andrew M.. 2019. "On the Creasing, Folding and Gluing of Corrugated Fibreboards". figshare.
<https://hdl.handle.net/2134/27793>.

This item was submitted to Loughborough University as a PhD thesis by the author and is made available in the Institutional Repository (<https://dspace.lboro.ac.uk/>) under the following Creative Commons Licence conditions.



For the full text of this licence, please go to:
<http://creativecommons.org/licenses/by-nc-nd/2.5/>

LOUGHBOROUGH
UNIVERSITY OF TECHNOLOGY
LIBRARY

AUTHOR/FILING TITLE

LAU, A.M.

ACCESSION/COPY NO.

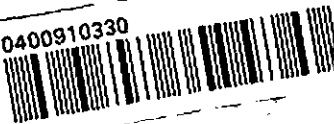
040091033

VOL. NO.

CLASS MARK

LOAN COPY

0400910330



ON THE CREASING, FOLDING AND GLUING OF CORRUGATED FIBREBOARDS

by

A M LAU

MSc, DIC, BEng, ACGI, AMIMechE

A Doctoral Thesis

submitted in partial fulfilment of the requirements

for the award of

Doctor of Philosophy, Ph.D, of the Loughborough University of Technology

31 December 1993

Supervisor: **Mr. T.H.Davies**, MA, CEng, MIMechE, Courtaulds Reader

© by A M Lau 1993

Loughborough University of Technology Library	
Date	June 94
Class	
Acc. No.	040091033

V8911161

To Grandma with loving memory.

SYNOPSIS

A case conversion process has been investigated with a view to understanding and ultimately improving the case quality. In particular, fishtailing, or the squareness of case, has been studied in relation to creasing, folding and gluing. The process has been optimized in terms of fishtailing on the individual panels. Uni-directional fishtailing results have been attributed to the existing method of folding. To this end, the folding mechanism has been studied and two innovations, generic to any continuous folding operations, have been suggested: the coil cam and the twin cam.

The design of the coil cam has been based on the screw theory of three bodies in relative spatial motion; it aims at transferring the folding force from the front edge to a point on or near the centre of the face of the panel. A unique method of computer aided design and manufacture has been proposed whereby a high-level software program is written to produce the cam profile, the results of which are then fed into a proprietary CAD software as macro commands. The twin cam, a more compact design, has been synthesized with the aim of producing rolling contact between the cam and the panel. Perfect rolling, however, cannot be achieved due to computational and manufacturing errors.

The feasibility of a twin roll creaser design, which enables boards of various thicknesses to be processed without the need for roll replacement, has also been examined. A comprehensive literature survey has been conducted on previous research into creasing. Theoretical models for simulating the creasing mechanism have been shown inaccurate by means of an optical technique. As a result, an experimental approach has been adopted, and which has led to the development of special creasing and folding test rigs. Three experiments have been conducted on the twin roll creaser so as to examine the effect of various creaser parameters on the quality of fold. This has led to better understanding of the creasing mechanism and a robust twin roll creaser design. Further research has been recommended in areas which may have generic applications in creasing, folding and paper related processes.

ACKNOWLEDGEMENT

Acknowledgement is given to the Science and Engineering Research Council in respect of the research project grant GR/F 73816.

I would like to thank my supervisor Mr. T.H. Davies for his magnanimous guidance, enthusiasm, constructive criticism and unique sense of humour. Thanks also to Mr. B. Hardisty of the SCM Container Machinery Ltd., and Mr. T. Fountain of the UK Corrugated Ltd. for their excellent technical support. I am also indebted to Mr. P.D. King, the project manager, and my colleagues Miss E. Rushforth and Mr. T.C. West for their active part in the research. Special thanks are due to Mr. J. Petzing for his practical and theoretical proficiency in the optical experimentation, Mr. A. Baggott for his expertise in CNC machining, Miss Heather Jennings for the most efficient inter-library loan service, Mr. K.W. Topley and Mr. V. Scothern for their photographic workmanship and Mr. P. Legood for his sound engineering advice. Suffice it to say that without all the technical assistance provided by the Department of Mechanical Engineering, the three years of research would never have come to fruition.

On a more personal note, I am grateful to Alex and Ada Chung for having literally provided food and shelter, and Adrian Fletcher and Jeff Pitchers for their unswerving friendship. Above all, I wish to express my deepest gratitude to my family for making a dream come true.

CONTENTS

	Page No.
1. INTRODUCTION	1
2. CORRUGATED FIBREBOARD CASES	3
2.1 Corrugated Fibreboards	3
2.1.1 Material and Case Properties	3
2.1.2 Corrugation Structure	8
2.2 Machine Specification	9
2.2.1 Creaser	11
2.2.2 Folder	14
2.2.3 Gluer	16
3. FISHTAILING	18
3.1 Problem synthesis	18
3.2 Experimentation	20
3.2.1 Experimental Requirements	20
3.2.2 Control Settings	21
3.2.3 Procedure	24
3.2.4 Results	25
3.2.5 Discussion	29
3.3 Conclusion	32
4. FOLDING CAM MECHANISMS	33
4.1 Folding Moment	33
4.2 Literature Review	35
4.3 Design Specifications	36
5. COIL CAM	37
5.1 Theory	38
5.2 Design Synthesis	39

5.2.1 Preliminary Study	39
5.2.2 Model Generation	42
5.2.3 Computer Aided Design	48
5.3 Design Optimization	49
5.4 Manufacture of Prototype	53
5.5 Appraisal	54
5.6 Conclusion	55
6. TWIN CAM	57
6.1 Notation	57
6.2 Cam Profile Derivation	58
6.3 Design Optimization	63
6.4 Appraisal	65
6.5 Conclusion	66
7. REVIEW ON CREASING	67
7.1 Crease Theory	67
7.2 Creaser Profile Design	71
7.3 Crease Quality Assessment	73
8. CREASER DEVELOPMENT	78
8.1 Geometrical Analysis	78
8.1.1 Assumptions	79
8.1.2 Single Blade Creaser	80
8.1.3 Twin Roll Creaser	81
8.2 Finite Element Analysis	83
8.2.1 Model design	83
8.2.2 Procedures	85
8.2.3 Results	86
8.2.4 Analysis	94
8.3 Model Verification using ESPI	97
8.3.1 ESPI Theory	97

8.3.2 Objectives	98
8.3.3 Apparatus	99
8.3.4 Procedures	100
8.3.5 Results	102
8.3.6 Discussion	106
8.4 Conclusion	108
9. EXPERIMENTATION	110
9.1 Creasing Rig Design	110
9.2 Folding Rig Design	113
9.3 Principal Experiment	115
9.3.1 Objectives	116
9.3.2 Procedures	116
9.3.3 Experimental Requirements	119
9.3.4 Results	120
9.3.5 Discussion	124
9.3.6 Conclusion	128
9.4 Profile Design Experiment	129
9.4.1 Theory	129
9.4.2 Method	131
9.4.3 Results	132
9.4.4 Discussion	134
9.4.5 Conclusion	134
9.5 Optimization Experiment	135
9.5.1 Methods	136
9.5.2 Results	138
9.5.3 Discussion	140
9.5.4 Conclusion	142
9.6 Experimental Summary	143
10. CONCLUSIONS AND RECOMMENDATIONS	145
10.1 Fishtailing	145

10.2 Folding Mechanism	146
10.2.1 Coil Cam	146
10.2.2 Twin Cam	147
10.3 Twin Roll Creaser	147
10.3.1 Creasing Analysis	147
10.3.2 Experimentation	148
10.4 Remarks	150
10.5 Recommendations	150
 APPENDICES	 152
2a. Tests for corrugated fibreboards and cases	154
3a. Case sample specification	158
3b. Folding rail calibration	159
3c. Glue dispenser calibration	161
3d. Tables of experimental data	163
5a. Determination of the third screw axis	170
5b. Cylindrical coordinate transformation	178
5c. CAD program listing	181
6a. Twin cam design optimization	186
8a. Theoretical model on corrugation	188
8b. Determination of maximum twin roll gap	190
8c. Fourier harmonics for B-flute corrugation	195
8d. ESPI equation derivation	196
9a. Folding rig design specification	202
9b. L_{18} orthogonal array	211
9c. Shear test	212
9d. First experiment results	216
9e. Defective sample results	226
9f. S/N ratio ANOVA tables	227
9g. Optimum settings	233
9h. Confirmation run results	235

9i. Profile design for 2nd experiment 236

9j. Second experiment results 238

9k. Third experiment results 242

REFERENCES 249

LIST OF ILLUSTRATIONS

	Page No.
2.1 Single- and double-wall flute types	4
2.2 Flute types and their relative size range	5
2.3 Flattened case with panel dimensions	6
2.4 Front and plan view of a flexo-folder gluer	10
2.5 Standard creaser profiles	12
2.6 Case in the knock-downed and erected position	15
3.1 Case conversion product-process diagram	18
3.2 Fishtailing measure	19
3.3 Case sample and dimensions	21
3.4 Folding section	21
3.5 Creasing section	22
3.6 Damaged anvil due to wearing	23
3.7 Combined S/N ratio plot	27
3.8 S/N ratio plot for separate panels	27
3.9 Thickness hypothesis for fishtailing	31
3.10 Distribution of fishtailing results	32
4.1 Folding resistance characteristics	34
5.1 Cylindroid of screw axes	38
5.2 Coil cam	40
5.3 Prototype coil cam operation	41
5.4 Screw path followed by a point 'P' on the panel	43
5.5 Cylindroid frame transformation	44
5.6 Frame transformation algorithm	45
5.7 Coil cam profile along its axis	48
5.8 Coil cam with hyperboloidal core	49
5.9 Coil cam with 'pear' cross-sections	50
5.10 Optimized coil cam design	52
5.11 Coil cam operation	53
5.12 Coil cam machined mould	54

6.1	Parabolic motion profile	58
6.2	Cam-panel contact length	59
6.3	Plan and side views of cam	60
6.4	Cam geometry	61
6.5	Twin cam design	64
6.6	Twin cam assembly in operation	65
7.1	B-flute corrugation with creasing locations	69
7.2	Experimental creaser profiles	71
7.3	Edge-wise compression curve	74
7.4	Force-angular displacement plot	75
7.5	Compression ratio definition	76
8.1	Single blade creaser	80
8.2	Worst creasing scenario	80
8.3	Twin roll creaser	81
8.4	Fold with two score marks	81
8.5	Constraint strategy	85
8.6	Creaser profile model	95
8.7	Test jig for optical experiments	99
8.8	Two possible 'C' locations	101
8.9	Test jig setup	101
8.10	Video image of fringes	102
8.11	ESPI calibration plot	103
8.12	Creaser knife at location 'A'	103
8.13	Creaser knife at location 'B'	104
8.14	Creaser knife at location 'C'	104
8.15	Creasing at location 'A' with end constraints	105
8.16	Flute shearing at one clamped end	107
9.1	Creaser roll radius derivation	111
9.2	Experimental creasing rig	112
9.3	Crease roll gap adjustment	112
9.4	Folding test rig assembly	113
9.5	Folding test rig control accessories	114

9.6	Folding resistance plot	114
9.7	Twin roll creaser design	116
9.8	Fletcher's trolley for shear measurement	120
9.9	Defective sample plot	122
9.10	S/N plot on folding resistance	122
9.11	S/N plot on shear deformation	123
9.12	Pre-crusher profile (dimensions in mm)	130
9.13	Twin roll creaser main design parameters	131
9.14	Defective sample plot	132
9.15	S/N plot for folding resistance	133
9.16	S/N plot for shear deformation	133
9.17	Combined profile	136
9.18	S/N defect plot	138
9.19	S/N 1st peak gradient plot	139
9.20	Peak S/N plot	139
9.21	S/N plot for shear resistance	139
9.22	Folding resistance plot with no 1st peak	141

Appendix illustrations:

5a.1	Two rigid bodies in spatial motion	171
5a.2	Three axes screw system	173
5a.3	Angular velocity polygon	173
5a.4	Coil cam prototype	176
5a.5	Coil cam angular velocity polygon	177
5b.1	Coordinate frame	178
5b.2	Cylindrical components in Cartesian frame	178
8a.1	Full penetration of corrugation	188
8b.1	Twin roll design parameters	190
8b.2	Loading at location 'C'	191
8b.3	Twin roll gap at maximum opening	192
8b.4	One-half of twin roll at location 'C'	193
8d.1	Michelson interferometer	198

8d.2	ESPI out-of-plane interferometer	199
8d.3	ESPI in-plane interferometer	200
9a.1	Folding test rig design	204
9c.1	Shear test measure on Fletcher's Trolley	212
9c.2	Calibration plot of shear vs. load	215
9i.1	Twin roll creaser design for 2nd experiment	236

LIST OF TABLES

	Page No.
2.1 Common board types and their properties	5
2.2 Slotted case type classification	7
2.3 Case conversion function-operation diagram	11
3.1 Control variables and settings	24
3.2 L_9 orthogonal array	24
4.1 Case blanks size range	36
5.1 Frame notation	43
5.2 Spreadsheet results at twelve angle increments	47
6.1 Sample data for $r(t)$, $\beta(t)$ and $e(t)$	64
8.1 A summary on the twin roll gap settings and the total creaser width	82
8.2 In-plane displacements for the wide and narrow sections of illumination	105
8.3 ESPI in-plane and out-of-plane displacement results	106
8.4 Finite element model in-plane and out-of-plane displacement	108
9.1 Control factors and their levels of settings	118
9.2 Defective samples count	121
9.3 Optimized settings	123
9.4 Theoretical S/N ratios	124
9.5 Confirmation run results	124
9.6 Design parameters and their settings	131
9.7 Defective sample count	132
9.8 F-ratio summary from the ANOVA tables	133
9.9 Control factors and settings	136
9.10 S/N ratios for pre-crushing defect rate	138
9.11 ANOVA 'F' ratios summary	140
9.12 Experimental and predicted S/N ratio	140

Appendix tables:

3d.1	Experimental results	163
3d.2	S/N values for the various control factors	164
3d.3	Combined S/N ratios at various control operation levels	165
3d.4	ANOVA table for S/N ratio	166
3d.5	Alternative mean and variance analysis	167
3d.6	Confirmation runs	169

CHAPTER 1

INTRODUCTION

Corrugated fibreboards and its conversion into cases by automatic case converters have a history going as far back as some hundred and fifty years ago. As the packaging industry evolves, more attention is paid to the case quality and the added value in the final case products. Not surprisingly, case converters today have reached an unprecedented level of sophistication. Machine operations such as creasing, printing, gluing, folding and palletizing (hence the name "flexo-folder gluers") are carried out at speed in excess of four cases per second.

Creasing, folding and gluing are operations which have a direct influence on the physical strength of a case. The way a board is creased will determine how well it will fold. Once they are folded and glued together, the case panels may end up lying skew to one another. Typically in the trade, the misalignment of bonded case panels is known as fishtailing. Problems with automatic case erection and distorted case appearance are attributed to fishtailing. So what causes fishtailing? How can fishtailing be prevented? What part does the corrugation structure play in the creasing process? Will innovative creaser and folder design be a remedial solution to fishtailing? All these questions have prompted the following investigation.

Under the auspices of the LINK programme, a three-year project was jointly funded by the Department of Trade and Industry and the Science and Engineering Research Council for developing a new generation of case converters. In addition, two industrial collaborators were involved in the project; they were the SCM Container Machinery and the UK Corrugated Ltd. Among the objectives were finding the causes for fishtailing through looking at the creasing, folding and gluing operations, and the study of innovations which will achieve less fishtailing and hence better case quality for a diverse range of boards.

Chapter 2 commences with a description of the corrugated fibreboard cases and the conversion process, in particular, the creasing, folding and gluing operations.

Fishtailing, a major quality characteristic in the case conversion process, is examined in Chapter 3. By means of a Taguchi experiment on an industrial case converter, the relative significance of creasing, folding, gluing and machine speed is put into perspective. Results from the experiment also highlight areas for further investigation.

Chapter 4 looks at the background of folding and reviews past literature on folding mechanisms. Two innovative folding cam mechanisms for folding are proposed. In Chapter 5, a coil cam, which touches the case panel at a single point, is derived by first of all applying the theory of screw motion to the case folding action. This is followed by a design methodology and a discussion on the methods of manufacture. Another non-oscillatory spatial cam mechanism in the form of a twin cam is introduced in Chapter 6. The chapter provides a design methodology for cams that roll on the panel without sliding.

A literature review in Chapter 7 outlines the theory on creasing, past research into the design and optimization of creaser profiles and the ways of assessing crease quality. The twin roll creaser design is studied in the geometrical and finite element analyses in Chapter 8. Optical experiments using the Electronic Speckle Pattern Interferometry, however, show that the finite element model is defective. To compensate for the inaccuracy of a theoretical model, Chapter 9 describes a series of experiments on the twin roll creaser design. Major findings from the experiments have paved way for future work as outlined towards the end of the chapter.

The thesis is concluded with recommendations in Chapter 10.

CHAPTER 2

CORRUGATED FIBREBOARD CASES

Case converters and corrugated fibreboards are essential for the manufacture of corrugated fibreboard cases. This chapter provides some background information on the corrugated fibreboards and the design of a typical case converter.

2.1 CORRUGATED FIBREBOARDS

Corrugated fibreboards are produced by the single facer units on a corrugator. To cater for different board types, there are normally two to three single facers on each corrugator. Within a single facer, the corrugating medium is first of all produced by threading the medium material through a labyrinth between the fluting rolls. On applying adhesive to the flute tips from a glue roll, a single face web is formed by bringing the medium into immediate contact with the liner. This web then travels to the "bridge" which acts as a buffering stage. At the end of the bridge, the single face web is brought down past another glue roll that applies adhesive to the exposed flute tips of the medium. Finally, a double face liner is combined with the single face web to form a typical single-wall board.

Properties of paper matter to the corrugated fibreboards as much as the case conversion process. This section reviews the material and structural properties of the corrugated fibreboards.

2.1.1 Material and Case Properties

In the U.K, corrugated fibreboards are generally manufactured to a "liner grammage" of between 125 and 410 gm² and nominal fluting medium of 113 or 127 gm². Typically a piece of fibreboard with only one layer of corrugation is known as a single-wall board. Double-wall board comprises two fluted layers,

separated by a flat sheet and faced on both sides with a liner (i.e. 5 components in all). For heavy-duty application triple-wall board is also available. Figure 2.1 shows the single- and double-wall flute types.

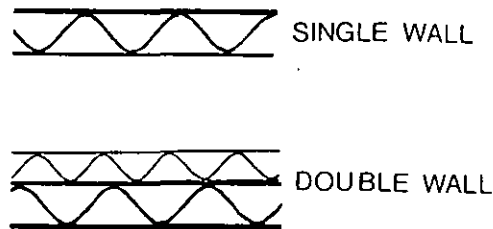


Fig. 2.1 Single- and double-wall flute types.

Historically, butchers' strawpaper was the first material used for the corrugating medium. Today, corrugating medium must be able to fulfil the following criteria:

Combining properties - the characteristics of the sheet must be such as to allow it to pass easily through the corrugator and to accept the flute configuration, then to be adhered to both liners at speeds in excess of 300 m/min.

Conversion properties - after combining into board with the liners, the corrugating medium must possess properties that will allow it to perform satisfactorily in respect of scoring, both at the take-off end of the corrugator and in the printer-slotter. It must also be able to resist the stresses induced during these conversion processes.

Case performance properties - the ability for the end product, ie. the case, to maintain its rigidity despite a high level of nudging often experienced in any form of container transportation.

The fluting itself can be categorized into four size range, as shown in Table 2.1.

Table 2.1: Common board types and their properties.

Flute type	Flutes per metre	Flute height (mm)	Take up factor *	Flat crush (Nm ⁻²)
A	118 +/- 10	4.5 - 4.8	1.53 - 1.57	140
C	138 +/- 10	3.4 - 3.7	1.42 - 1.47	180
B	164 +/- 10	2.4 - 2.6	1.32 - 1.33	165
E	309 +/- 14	1.1 - 1.6	1.23 - 1.30	485

* Take-up factor is the ratio of length of medium divided by the length of single-face linerboard for a given length of combined board.

Figure 2.2 displays the relative size for the various flute types.

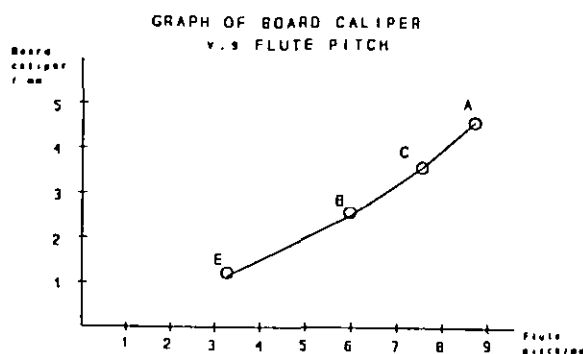


Fig. 2.2 Flute types and their relative size range.

As a rule, corrugated fibreboards with A, B and C flute are widely used in the transit of goods. E-flute boards, however, take on a more decorative role of producing display cases when combined with high quality printed liners. Several types of paper can be used for the corrugating medium, and they are as follows:

Semi-chemical papers made by treating wood chips with chemicals to achieve pulp of the desired properties.

Straw papers made from furnishes of between 25% and 75% straw with various quantities and grades of waste pulp.

Kraft paper used in the UK on some grades of weather-resistant board.

Secondary fibre, chip or waste papers of various grades can be used in their own right after treatment or be added to any of the materials above to give a balance of properties at a moderate cost.

The liners can be divided into three main types: pure Kraft, Jute (test liner that consists of a lower grade of pulp, frequently waste, backed with a pure kraft sheet) and Chip (straw or bogus papers principally used for making fittings).

Recycled fibreboard material is also gaining popularity in the packaging industry. Waste paper can be collected as used cases from retail outlets or from waste generated during the fibreboard production process. The waste is then returned to the paper mills for recycling. 100% recycling however, is impractical due to a substantial reduction in fibre strength.

The single-wall board in A, B, C and E flute construction is a common board type. Double-wall boards are normally available in AB, CB, AA and AC fluting configurations. Triple-wall AAB, CCB and BAE constructions are rarely called for.

The packaging code of BS1133 Section 7 covers a fair selection of fibreboard case styles. Figure 2.3 shows a typical flattened case with the panel dimensions.

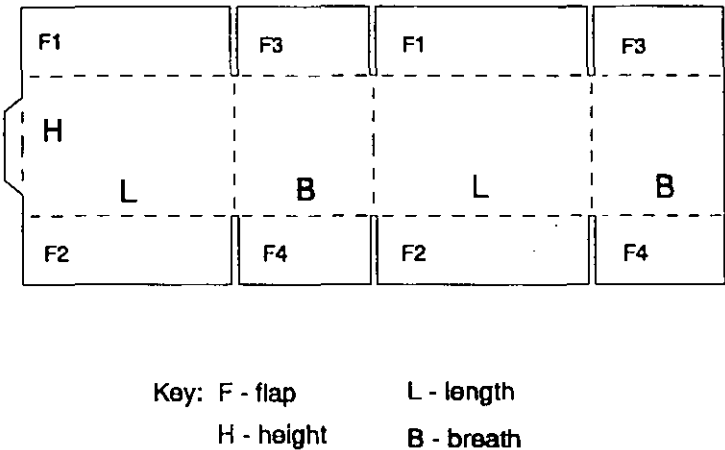


Fig. 2.3 Flattened case with panel dimensions.

The slotted case type is one which can be folded and glued together on an automatic case-maker. A systematic classification of the slotted case style is given in Table 2.2:

Table 2.2: Slotted case type classification.

Code	F1	F2	F3	F4	Feature
0200	0	-	0	-	Container lid
0201	B/2	B/2	B/2	B/2	
0202	-	-	-	-	Unspecified flap dim.
0203	B	B	B	B	
0204	B/2	B/2	L/2	L/2	
0205	L/2	L/2	L/2	L/2	
0206	B	B	L/2	L/2	
2014	B/2	B/2	B/2	B/2	F1 & F3 are inwardly folded.

The slotted case type mainly comes as one piece with a stitched, taped or glued manufacturer's joint, and top and bottom flaps. The cases are shipped flat, ready to use and require closing of the flaps. Fishtailing, or the misalignment of glued panels, is often associated with extremely light or heavy cases, and cases with a narrow body panel (i.e cases with dimension 'H' being much smaller than 'F' as illustrated in Figure 2.3).

As far as storage is concerned, the corrugated boards are normally stored in compartments adjacent to the corrugator. Despite having a steady heat source and humidifier nearby, the storage condition can be affected by seasonal weather fluctuation. For example, the fibreboards tend to lose its water content in dry periods, particularly with paper of lower grades. Unfortunately dry liners are very susceptible to tearing. On the other hand, too much moisture in the paper may produce warp in the board. This is caused by the shrinkage of liners as they lose their water content to the surroundings. As a result, boards which are warped will

suffer during the conversion stage. Fibreboards are therefore recommended to be stored under cover on dry flat board pallets in atmospheric conditions and relative humidity of between 50 and 70 % prior to usage.

Test methods for the corrugated cases and liners can be found in the British Standard and the TAPPI publications from the United States. Some of these tests do however bear limitations in that they may not be sufficiently precise for use in case of dispute. Test methods are becoming increasingly popular as customers demand for higher quality or value added products. Appendix 2a outlines some of the more common test procedures.

2.1.2 Corrugation Structure

The structure of the fluting medium resembles that of a sine wave. For the same amount of paper material, it is mainly the laminated design which gives the fibreboard its enhanced stiffness over its paperboard equivalent. However, the orientation of the corrugations is critical, not only to the bending stiffness, but also the crease performance.

There is often less problem with perpendicular creasing than parallel creasing, as suggested by Vogelpohl [51]. In perpendicular creasing, force is transmitted directly from the creasing tool onto the corrugation. This is less probable in parallel creasing when the position at which the creasing force is applied cannot be pre-determined. The creasing tool may compress the corrugation by means of tensile forces within the creased liner - a situation which encourages tearing of the liner. However, it is debatable whether the resulting board behaviour from creasing is attributable to the corrugation structure or to the paper material itself (see Chapter 8). Analysis on other composite material (e.g textile), as indicated by Kawabata [21], suggests that its mechanical properties must be considered from a structural rather than a continuum standpoint. Corte et al. [6], on the other hand,

have put emphasis on the material by stating that paper ought to be treated as a discontinuous network of fibres.

In the terminology used for tests on corrugated fibreboards, flexural stiffness is defined as the product of the modulus of elasticity 'E' and the moment of inertia 'I'. Methods for calculating the moments of inertia of various corrugated structures can be found in standard text books. There are some examples, however, which deserve mentioning. The moment of inertia for an ellipsoidal corrugation can be estimated from a method developed by Phillips [34]. For a more rigorous analysis, a method as put forward by Smith [44] enables the elastic properties to be calculated for a sheet of corrugated plate. According to Smith, corrugated sheets can be treated as homogeneous and orthotropic flat plates, i.e one having different elastic properties in two mutually perpendicular directions. By homogeneous, it means that the critical shear stress at which elastic buckling occurs can be determined for any shape of repeated corrugations. In addition, Smith describes how warping restraints can inhibit any out-of-plane warping displacements of the corrugation cross-section. Warp is seen as a major obstacle to achieving a satisfactory fold; its effect has been demonstrated to be more damaging than that due to the corrugation structure (see reference [7]).

2.2 MACHINE SPECIFICATION

In the case conversion process, flat blank sheets of corrugated fibreboards are fed into the machine and will emerge as knocked-down cases ready for automatic erection. Figure 2.4 shows the front and plan views of a standard flexo-folder gluer (acknowledgement given to SCM Containers Machinery for the photograph reproduction).

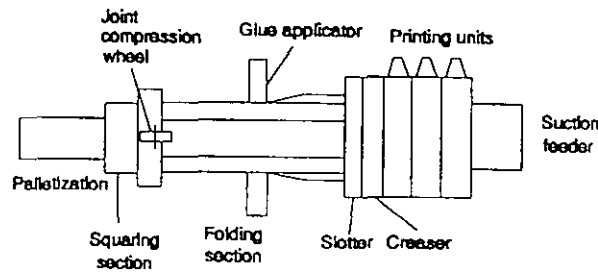
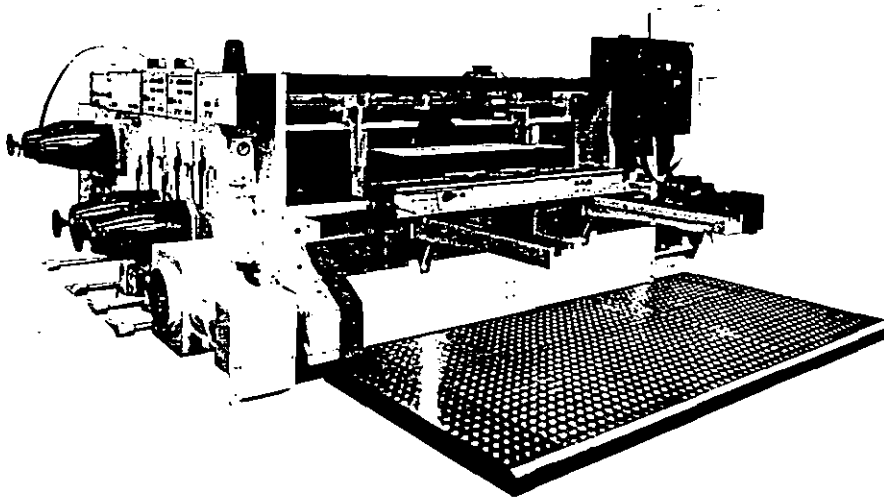


Fig. 2.4 Front and plan view of a flexo-folder gluer.

The physical process in forming a case essentially consists of three sequential stages: creasing, slitting and folding. First, the sheets of corrugated fibreboard or 'blanks' are creased in a direction parallel to the flute orientation. Depending on the case design, the blanks are then cut along the leading and the trailing edges by means of a rotary slotter. These cuts define the edges of the top and bottom flaps of the final cases. The blanks are subsequently folded by a combination of guiding rails and moving belts - the most common existing method of folding, which causes the edge pieces to close together. Misalignment of the glued panels, known as fishtailing, often poses problems at the stage of automatic case erection.

Table 2.3 is an attempt to distinguish the functions from the operations of a standard case converter. Conditions must be met whenever an operation attempts to fulfil the functional requirement(s).

Table 2.3: Case conversion function-operation diagram.

Operations	Conditions	Functions
Storage	Board quality & physical environment.	Preparation for case conversion; buffer stock.
Printing	Colour flexo & ink quality.	Case decoration & identification
Pre-crease crushing	Flat creaser profile.	Preliminary flute weakening.
Creasing	Creaser profile, material, penetration & rotary creaser dimensions.	Flute buckling & fold line definition.
Slotting	Knife configuration.	Case flap preparation.
Gluing	Glue viscosity & curing time.	Glue flap joining.
Folding	Dynamic manipulation of case flaps about a relatively mobile folding hinge.	Joint formation.
Squaring	Mechanical synchronisation.	Squaring the case edges.
Palletizing	In-line shingling.	Counting & stacking cases for shipment.

2.2.1 Creaser

The purpose of creasing is to produce controlled lines of weakness along which folding will preferentially take place. This is brought about by the local crushing or buckling of flutes, hence reducing the section depth and stiffness of the fold region.

In a flexo-folder gluer, creasing takes place after the flexo-printing stage. Creases parallel to the corrugation are produced by four pairs of rotary creasers forming the four edges of an erected case. To ensure a continuous flow of cases, pull rolls are

positioned before and after the crease roll. Roll synchronisation is therefore vitally important in avoiding undue tearing. The use of pre-crush rolls is recommended when creasing boards of thicker caliper.

The creaser itself comprises a rotary creasing head in the form of a circular blade. The creasing head acts against a cylindrical anvil, and the two combine to give the creasing action.

Creaser Components

Broadly speaking, there are four design parameters which give the creaser its functional characteristics: creaser profile, creasing roll gap, material and roll diameter.

The selection of **creaser profile** is entirely subjective as the need varies from one case manufacturer to the next. Figure 2.5 shows a few standard creaser profiles.



Fig. 2.5 Standard creaser profiles.

The blade width also determines the amount of pressure that the liner is likely to receive from the blade. Obviously, too sharp a blade will tend to tear the liner, whereas too blunt a blade will not produce a definite crease line at all. In general, the application of wider profiles is often reserved for thicker boards.

The **crease roll gap** is the separation between the creaser and the anvil. Adjustment of the gap is wholly empirical, and its precision has never been taken seriously. Normal practice is to crease at progressively smaller clearance until cracking becomes perceptible on the outer liner. The crease roll is then backed off

a fraction prior to the actual production run. Typically the amount of backing-off comes from the operators' own experience.

Regarding the **material**, over the years, practical trials have shown that a chrome-plated steel male creaser together with a polyurethane anvil form the best combination. The chrome-plated surface is designed to reduce wear, thereby retaining the shape of the creaser profile. The elasticity of the polyurethane anvil, on the other hand, compensates for the differences in board thickness and any possible damage that would have been caused by a steel anvil on the liner surface.

Pressure exerted on the liner and the corrugation will depend on the **roll diameter** of the creaser blade. From the geometrical viewpoint, a larger roll diameter will extend a longer contact length over the liner. Less pressure is therefore induced in the vicinity of the point of action, and the liner will be less likely to tear as a consequence. Vogelpohl [51] realized the importance of the creaser roll diameter, but did not investigate any further on the basis that any change in the shaft diameter would alter the design of the mechanical coupling. Werner [54], however, regarded the roll diameter as a function of the machine width. Since the roll was supported on both ends, the weight of the roll would cause it to sag in the middle, thereby producing the catenary effect.

Creaser Related Parameters

Other design parameters related to creasing are as follows:

- Dynamic gripping
- Pre-crease crushing
- Speed

Two pairs of pull rolls on either side of the crease rolls provide a gripping action on the fast-moving boards. When dealing with smaller boards, the pull rolls will also act as interstage drives. A situation may occur whereby a small board is

suspended in mid-air on leaving one set of rollers, but not quite reaching the next. Another problem which may lead to roll shearing is when the pull rolls and the crease rolls are not synchronised properly.

Corrugated fibreboards, when more than one-board thick, are usually crushed over a few flutes along the crease before arriving at the creasing stage. This kind of **pre-crease crushing** is to ensure the effectiveness of a crease irrespective of the board's thickness. Pre-crease crushing is also applied to the two edges where the case will be folded by 180°. A crushed section is much preferred on the grounds that, on folding, less resistance will be resulted from the compaction of a larger area of buckled flute.

Most damages occur during the acceleration and deceleration of the case, notably in the feeding section of the case converter. Conventional grip feeding often distorts the board caliper while accelerating the board from a stationary position. Irregular board calipers not only imply uneven colour distribution from the flexo-printers, but may also lead to a deterioration in case strength. For this reason, vacuum suction is increasingly adopted as a better means of feeding.

2.2.2 Folder

Folding is a mechanical process for joining the glue flaps together. Most case converters produce flattened, folded cases with only two 180° edges. It is not until the time of erection that the remaining two edges experience, for the first time, a fold of 90°. Figure 2.6 shows a case sample in its flattened and erected positions.

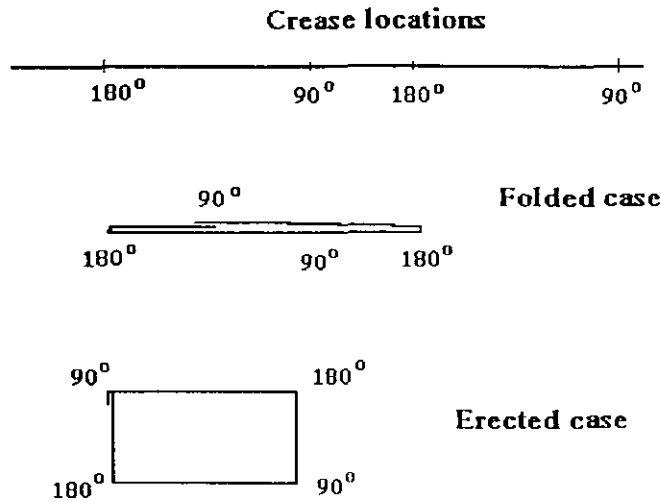


Fig. 2.6 Case in the knocked-down and erected position.

Folding is commonly divided into two operations i.e from 0° to 90° and from 90° to 180° . A standard case converter comprises folding bars and belts which generate the mechanical motion necessary for the folding process. During the first stage of folding, the bars exert a force onto the leading edge of the case, the direction of which runs opposite to the case travel. It is suspected that this force component is ultimately responsible for fishtailing. In the second stage of folding, folding belts help to minimize the relative motion between the folder and the case panels. Hence, a good fold quality will be ensured by the absence of the backward force component and a minimum friction component. It has been known that the two stages of folding can be combined into one by having a single pair of folding belts; however, the required belt length has rendered it impractical.

Seymour and Terle [42] have further improved the concept of relative belt motion by introducing the multi-T belt mechanism for the second stage folding. In essence, T-blocks are attached onto the folding belts which are synchronized with the cases' motion. By directing the folding force normal to the board panels, the backward component of force, which is commonly experienced in the folding rail concept, will be eliminated. As claimed by the manufacturer, the design is capable of keeping fishtailing down to a minimum. Friction, however, is inevitable

between the panels and the lugs because of imperfect synchronisation and relative motion between the two as directed towards or away from the folding hinge.

To complement the folding belts and bars, Rother [39] has introduced air fans at strategic locations along the folding section. It is hoped that the forced air current will produce less mechanical damage to the case panels.

Other novel but less well known folding techniques are the "Rotofold" and the "inclined wheels" which have been documented by Shulman [43]. Rotofold technique conducts the second 90° fold by means of helical rotating rods touching the case blanks at the centre. Inclined wheels, on the other hand, comprise forming rolls with changing roll profiles. As the board progresses through the sequence of rolls, it will be folded stage by stage from 0° to 180°.

All the above techniques, except for the air folding one, have one inherent problem: the smearing of ink. Friction will prevail as long as there is relative motion between the folder and the case blanks while they are in contact. This explains why some of the more dynamic techniques, such as the T-blocks and the "rotofold", are only designed for the second 90° fold, by which time the ink on the case panels will have set. To lessen the effect of ink smearing, one industrial practice is to dilute the ink so that it can be absorbed more readily by the case liners.

2.2.3 Gluer

The basic construction of a piece of corrugated fibreboard consists of a fluted sheet being laminated by two liners. The combined board is held together with adhesive applied to the crests of the fluted sheet. It is this glued sandwich structure which gives the corrugated fibreboard its high stiffness-to-weight ratio.

The glue lapping operation is done by applying a water-based polymer dispersion

such as PVAc and its derivatives. It is important for the applied film of adhesive to have good wet tack property. Two ways of glue application are available, depending on whether it is a down-folding or top-folding machine: they are the glue wheel type and the nozzle extrusion.

In the glue wheel application, a knurled roll deposits a desired band of adhesive to the lap at the same speed as the machine. Adhesive is constantly circulated and fed to the wheel by a small pan feed or 'shoe' arrangement. Extrusion nozzle on the other hand relies on electronic control for the glue flow adjustment. A photocell detects the leading edge of the blanks, thereby monitoring the glue application onto the lap only.

Vyse et al. [53] have found that the cost benefit from a glue extrusion system can be deceptive when compared with the wheel application type. Since, by extruding several thin beads of adhesive and spreading them on compression, the overall film area may be inadequate and lap lifting may occur as a result of the lack of wet tack at high speed. Increasing the bonding area will help, though at the expense of having to apply more glue, thereby off-setting the original cost benefit.

Examples on test standards for adhesives used in the corrugated industry can be found in Appendix 2a.

CHAPTER 3

FISHTAILING

(N.B. This chapter has been presented and published in the 42nd TAPPI Conference, Washington D.C., U.S.A., Oct.1992 under the authorship of A.M.Lau and T.H.Davies [24].)

In the case conversion process, fishtailing is often characterized by the misalignment of case panels once they are joined together. Such distortion may have deleterious effect on the structural integrity and appearance of the cases, not to mention the difficulty in automatic case erection as often experienced by the case users. The causes for fishtailing, however, have never been identified.

Taguchi Methodology [47,48,49], or robust design method [33], is an off-line quality improvement technique designed to optimize the various controllable parameters in a manufacturing process. Optimization, in this context, means the reduction of the process sensitivity to the production noise factors, thereby achieving better and more consistent quality. Process sensitivity can be varied by adjusting the control variables of the process. Through conducting an optimization experiment on a flexo-folder gluer case converter, this chapter investigates the effect of certain machine control parameters on fishtailing.

3.1 PROBLEM SYNTHESIS

Figure 3.1 shows a product-process diagram for the case making process .

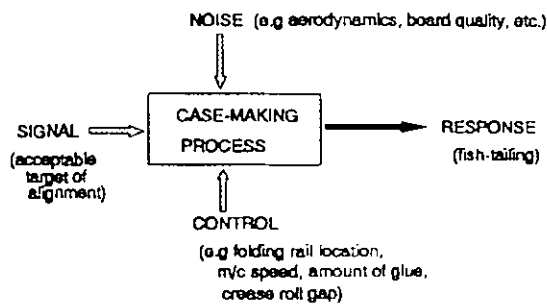


Fig. 3.1 Case conversion product-process diagram.

The diagram, proposed by Phadke [33], is a simplified version of the "cause-and-effect" diagram as developed by Ishikawa [16]; it provides a systematic way of analysing those factors which may influence the quality of the final product. The factors can be defined as follows:

Signal - acceptable criterion for assessing fishtailing, though a standard has yet to be defined.

Noise - parameters such as the board quality or the aerodynamics of the board folding action, both of which cannot be easily controlled.

Control - parameters such as the folding rail location relative to the folding hinge on the case convertor, the machine speed, the amount of glue applied and the gap setting between the crease rollers. These factors are usually related to the settings of the machine, and are best identified through a brainstorming session with the machine operators.

Process response - the fishtailing measure.

Fishtailing, a term often quoted in the corrugated industry, describes the skew edges formed by the case panels during the case conversion. Figure 3.2 shows a typical example of fishtailing.

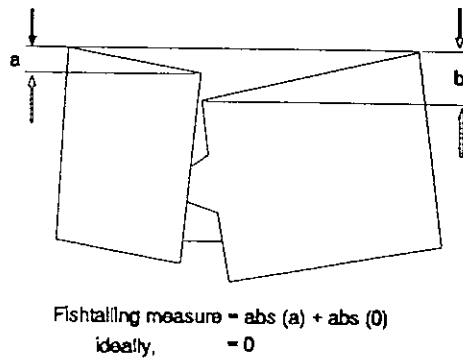


Fig. 3.2 Fishtailing measure.

The extent of fishtailing can be monitored in terms of a geometrical deviation or gap width created by the edges of the two bonded panels and the case edge. This dimensional disparity can be defined by the absolute values of the gap (i.e. dimensions 'a' and 'b') relative to the horizontal edge of the case. One limitation

is that results showing a combined value of zero may imply correct alignment, but not necessarily with the right amount of overlap between the two panels. For the present purpose, however, the measure is thought to be adequate in assessing fishtailing.

3.2 EXPERIMENTATION

Large scale industrial experimentation is often hard to justify economically. A more cost effective approach will be to structure the experiment in such a way that a maximum amount of information can be obtained from a minimum number of trials. Orthogonal arrays are the means whereby experiments can be organized in the most efficient manner.

This section describes an optimization experiment which has been conducted on an industrial flexo-folder gluer case converter.

3.2.1 Experimental Requirements

The experiment was performed on the Simon 470 flexo-folder gluer at UK Corrugated, Weston-Super-Mare, UK.

Apparatus employed in the experiment were as follows:

- Feeler gauges - to measure the crease roll separation.

- Electronic weighing scale - to measure the amount of glue applied (for initial calibration only).

- Metric rule - to adjust the nylon folding rail relative to the folding hinge; to measure fishtailing in terms of values 'a' and 'b'.

- Masking tape - to be attached to the case panels for glue collection.

In accordance with BS3430, a sample size of ten boards was chosen with another ten as spare. The type of board used was the Ginster 300 KY2 which comprised

an outer kraft liner, an inner oyster liner and a B-flute corrugation medium (see Appendix 3a for further details on the case sample). Because of the short case length, it was believed that this particular board type would most likely experience fishtailing. Figure 3.3 shows the overall case dimension.

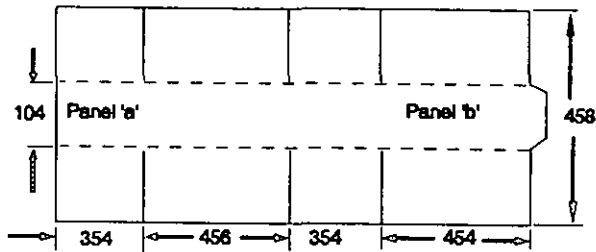


Fig. 3.3 Case sample and dimensions.

3.2.2 Control Settings

Four control parameters were selected for the experiment, and they were: folding rails, creaser roll gap, machine speed and glue dispensation.

a) Folding rails

Nylon rails in the folding section, as shown in Figure 3.4, are responsible for the first 90° fold. The rails can be positioned near to or away from the folding hinge

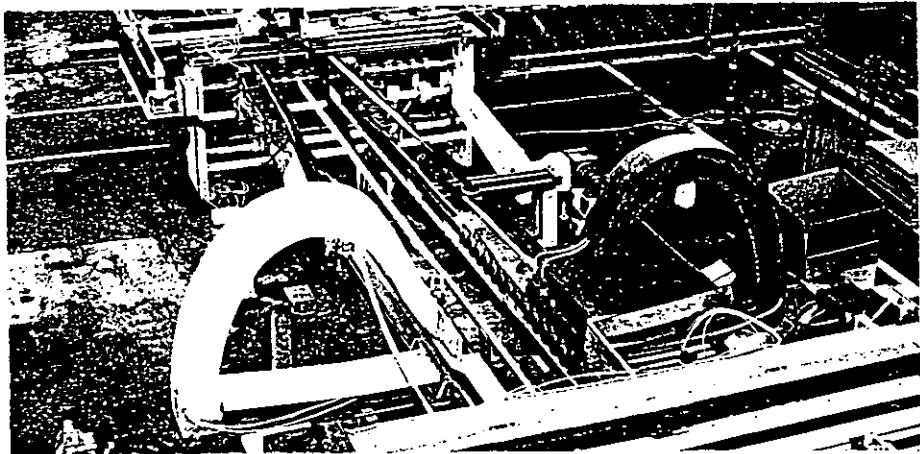


Fig. 3.4 Folding section.

by manually sliding the rail clamps along their support shafts (see Appendix 3b for folding rail calibration).

On previous occasion, distortion of case panels was noticed to have already taken place in the first 90° fold. The amount of distortion could be correlated with the position of the nylon rails relative to the folding hinge. For example, if the rail was positioned nearer to the hinge, then a larger backward force component would be exerted onto the case panel, since the moment arm had shortened and the folding moment should remain the same.

b) Creasing roll gap

Case foldability is believed to be a function of the creaser penetration or the creasing roll gap. Too deep a creaser penetration may tear the inner liner; whereas too shallow may render the crease ineffective. Figure 3.5 shows the creasing section.

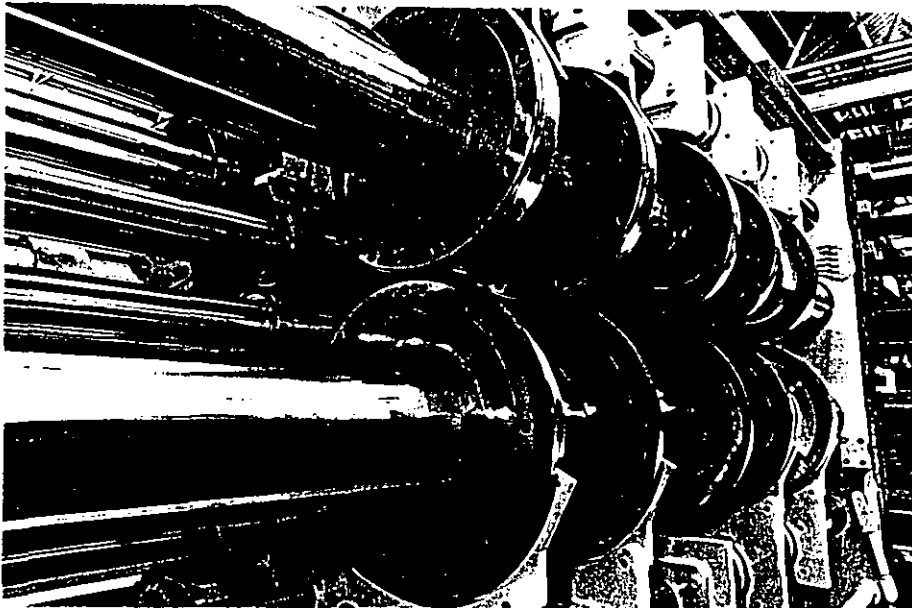


Fig. 3.5 Creasing section.

It was found that the part of the polyurethane anvil immediately below the knife had been worn down over its operation life. For this reason, a meaningful gap

width could be measured only between the creasing knife shoulder and the undamaged part of the polyurethane anvil, as shown in Figure 3.6.

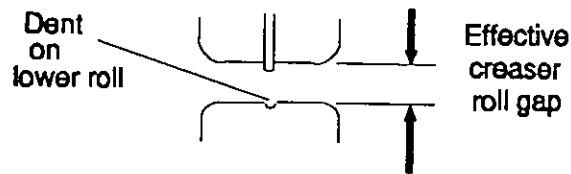


Fig. 3.6 Damaged anvil due to wearing.

c) Machine speed

Running the case converter at maximum speed is, in practice, not recommended on account of factors such as vibration, print consistency and rate of wear. A slow machine throughput is equally undesirable. There is therefore an optimum range of speed settings beyond which it is not advisable to operate.

d) Glue dispensation

Glue is extruded onto the case panels by means of an electrically controlled lap gluing system. The rate of application can reach up to 6 m/s. Speed compensation is performed via a closed loop control system; but the expected linearity between the amount of glue dispensed and the machine speed has not been verified to the author's knowledge. The glue itself is an aqueous emulsion adhesive specially formulated for paper and board bonding operations.

In theory, the glue flow should be controllable via the main control panel. However, a series of glue tests prior to the experiment indicated that the flow adjust had no effect on the amount of glue extruded from the system. Instead, a pressure valve governing the air pressure of the flow line was found to be more effective in controlling the glue quantity.

In summary, a four-factor-three-level (4x3) experiment was decided with the control settings as shown in Table 3.1.

Table 3.1: Control variables and settings.

	1	2	3
A. Rail location from the folding hinge	near	far	middle
B. Glue amount (in gauge pressure, psi)	50	35	20
C. Speed (cases per hour)	6000	9000	3000
D. Crease roll gap (mm)	0.5	0.3	0.7

3.2.3 Procedure

Based on the assumption of an additive model, whereby the joined effect of varying two factors together is the sum of the effects of varying them separately, an L_9 orthogonal array, as shown in Table 3.2, was chosen for the experiment.

Table 3.2: L_9 orthogonal array

Expt. no.	A	B	C	D
1	1	1	1	1
2	1	2	2	2
3	1	3	3	3
4	2	1	2	3
5	2	2	3	1
6	2	3	1	2
7	3	1	3	2
8	3	2	1	3
9	3	3	2	1

While planning the experiment, it was clear that column 'A' should be for settings which were the most time consuming to change. In addition, the first column of

the settings was taken as set on the machine so as to minimize the number of setting changes.

In all, nine experiments were performed with settings corresponding to those of the L_9 orthogonal array. The case samples, twenty in all, were fed into the machine following each setup. Using the smallest-the-best criterion, the signal-to-noise ratios were calculated as follows:

$$S/N_{a,b} = -10 \log_{10} \frac{\sum Y^2}{n}$$

where, Y = abs(a) or abs(b)
 a, b = dimensions defined previously

A model of unit variation, as formulated by Taguchi [47], was adapted for the present purpose. In particular, the absolute function for the dimensions was essential if the above criterion were to remain valid. The smallest-the-best criterion was satisfied by maximizing the signal-to-noise ratio or minimizing the gap difference.

Once the signal-to-noise ratios were collected, they were processed using the Analysis of Variances technique, ANOVA in short. Optimized settings were those with the most positive signal-to-noise ratios. A final test run using the optimized settings should confirm the relative magnitude of the factor effects.

3.2.4 Results

Prior to the experiment, the following procedures were performed:

1. Brief operators.
2. Set up machine for the appropriate job batch.
3. Glue dispenser calibration (see Appendix 3c).
4. Remove print rolls.

5. Test folding rail adjustment.
6. Check board samples and record physical properties.

The four units of flexo graphic printer were taken off line as they were not required during the experiment. Following the stages of creasing, slotting, folding, gluing and slapping, the folded cases were then examined for fishtailing.

Dimensions 'a' and 'b' were measured in mm with an accuracy of ± 0.5 mm. (In Appendix 3d Table 1, the first row represents the 'a' values, while the second row, the 'b' values.) Each of the samples was then checked for foldability by manually erecting and noting the final form of the cases. Cases with relatively high fishtailing values were found distorted and difficult to erect.

Some of the observed defects (with the particular case sample in brackets) were highlighted as follows:

1. Difficult to erect due to flap obstruction (1.16).
2. Required recreasing if it was to be folded, because of crease dislocation (1.17).
3. Severe fishtailing of 10 mm between the folded flaps and body panels (7.1).
4. Excessive glue led to the bonding of body panels of successive cases (7.10, 7.9, 7.6, 7.5, 7.3).
5. Panels not bonded together (9.1, 9.2, 9.7).

The sum of Y and the S/N ratios for the nine experiments (in Appendix 3d Table 2) were added together and grouped in terms of the appropriate control factors (see Appendix 3d Table 3).

The S/N level of effects due to the various control factors at different settings are shown graphically in Figures 3.7 and 3.8. Note that the scales are different for the two plots. The combined mean value, M , for the S/N ratio is -11.6. In terms of the constituent mean values for panel 'a' and 'b', M_a and M_b are -8.5 and -3.2 respectively.

$$\text{Variance ratio, } F = \frac{\text{Mean square}}{\text{Pooled error}}$$

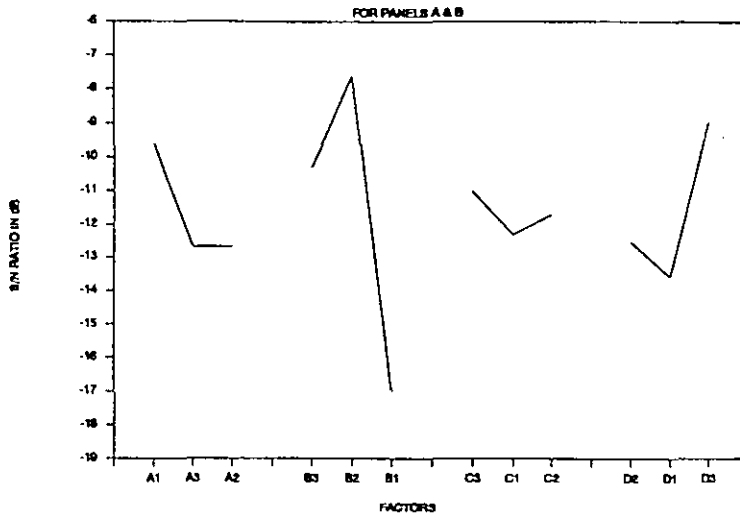


Fig. 3.7 Combined S/N ratio plot.

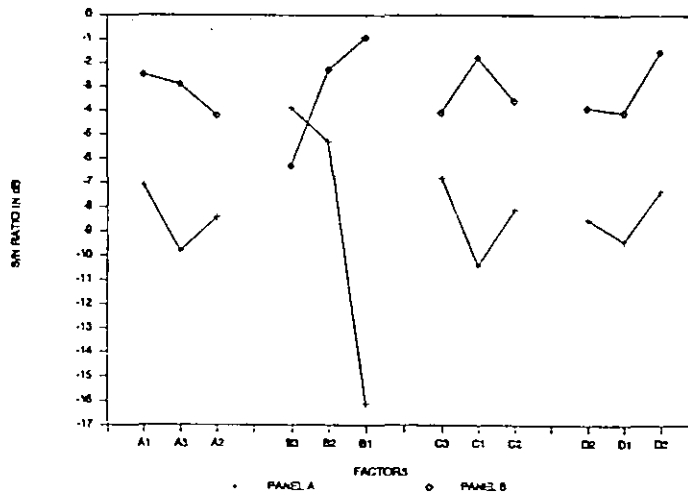


Fig. 3.8 S/N ratio plot for separate panels.

ANOVA, as tabulated in Appendix 3d Table 4, highlighted the overall effect of the control factors. A large F value implied a sizeable contribution to fishtailing due to that particular control factor. Machine speed turned out to be relatively insignificant when compared with the other factors; for this reason, it was used as a pooling factor. Pooling was a computation method which would give an approximate estimate of the error variance. To obtain a better estimate of error variance, a significantly larger number of experiments would be needed, the cost of which would outweigh the added benefit.

By selecting the factors with the lowest S/N ratios in Figure 3.7, the optimum settings for the confirmation run were: **A1 B2 C2 D3**

Under optimum conditions, the S/N ratio was predicted as follows:

$$\begin{aligned} S/N_{pred.} &= M + (S/N_{A,opt} - M) + (S/N_{B,opt} - M) + (S/N_{D,opt} - M) \\ &= -2.8 \end{aligned}$$

With a confidence interval of two standard deviation, the prediction error was calculated as follows:

$$Err_{pred.} = \pm 2 \sqrt{s^2 \left(\frac{1}{n_e} + \frac{1}{n_r} \right)} = \pm 2.9$$

$$\frac{1}{n_e} = \frac{1}{n} + \left(\frac{1}{n_A} - \frac{1}{n} \right) + \left(\frac{1}{n_B} - \frac{1}{n} \right) + \left(\frac{1}{n_D} - \frac{1}{n} \right)$$

where,

n_e	= effective sample size
n	= number of rows of experiments
n_r	= number of verification experiments
s^2	= error mean square in the ANOVA table

Likewise, analysing in terms of individual panel results of 'a' and 'b' would give:

$$S/N_{pred., a} = -2.78 \pm 8.21$$

$$S/N_{pred., b} = -0.08 \pm 5.32$$

A separate analysis on the mean and the variances also proved to be equally valid, with the smallest combined mean values of $\eta(a,b)$ confirming the same optimum settings (see Table 5 of Appendix 3d) .

Finally, two confirmation runs, labelled here as CR1 and CR2, were conducted at the optimum settings (results as tabulated in Appendix 3d Table 6). The reason for having two runs was because for CR1, the squaring section had not been put back together after an earlier jamming incidence. Taking the results from CR2, the combined S/N ratio was calculated to be -6.3.

3.2.5 Discussion

Glue pressure has been identified to be the most critical factor in terms of minimizing fishtailing. This can be seen from the variance ratios F in the ANOVA table. The result tabulation also reveals that, whatever the other control settings, excessive glue pressure at B1 will inevitably give rise to fishtailing.

Regarding the crease roll gap, it was found that a deep crease penetration did not necessarily correlate with a good fishtailing response. Among the three gap width settings used, 0.7mm (roughly a quarter of the board thickness) came out to be the best. One reason could be excessive creasing resulting in the weakening of the corrugation, which would in turn allow lateral movement to take place about the hinge.

During the experiment, a slight asymmetry was noticed between the gap values on the left-hand and the right-hand side of the crease roll in the direction of board travel. This was detected during the crease roll gap setup, when the feeler gauge

was found relatively easier to slide into the gap on the left hand side than the one on the right. However, the pairs of crease rolls, both left and right, were adjusted with gap consistency, as demonstrated by the coherent response on the S/N plots in Figure 3.8.

As far as fishtailing on each individual panel is concerned, optimization has been achieved as shown by S/N_a and S/N_b in both the predicted and confirmation runs. However, a comparison between S/N_{pred} and S/N_{CR2} will show that the latter value has fallen outside the predicted standard deviation. One possible explanation is the inadequacy of the additive model, implying that some other major control factors or interaction may have been overlooked. This proves to be the case when the combined action of gluing and squaring is found to have an important effect on fishtailing. On comparing results from the two confirmation runs CR1 and CR2, the first of which is best described as fortuitous, fishtailing is shown to have been reduced dramatically by the squaring process. Squaring, however, only serves as a corrective measure, when fishtailing must have occurred sometime before the gluing stage. This is demonstrated by the fact that the majority of the 'a' and 'b' values are positive. A likely cause other than the gluing-squaring interaction will be the backward force component as exerted by the folding rail.

The random fashion of fishtailing corresponds to a high degree of unit-to-unit variation, particularly when the glue pressure is at its highest setting. It is not clear why such variation exists, though the possibility that a random noise factor is at work must not be ruled out (e.g glue pressure inconsistency).

Another interesting phenomenon is that the mean values of dimension 'a' consistently exceeds that of dimension 'b', giving rise to an asymmetry between the two case panels. One would expect that dimension 'a', taken from the narrower case panel, would be smaller than dimension 'b', on account of a geometrical amplification and a difference in mass (hence the ease of folding). However, all the worse values associated with high glue pressure are to be found in dimension 'a'. One possible explanation is that the glue may not have set at the

instant when the lowest case is being withdrawn from beneath the stack in the squaring section. Where the shorter panel is glued to the flap of the longer panel, the folded case is three board thick, as can be seen in Figure 3.9. It is in this area that most of the weight of the cases above the lowest case acts on the short panel of the lower case.

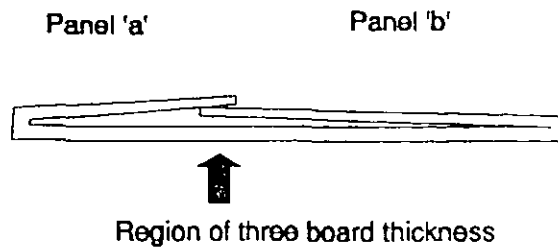


Fig. 3.9 Thickness hypothesis for fishtailing.

While being withdrawn in shingle fashion, the friction force exerted by the case above this part of the lowest case causes the short panel to move backwards relative to the remainder of the case. The resistance to this force, preventing relative displacement and thereby the reappearance of fishtailing, could only come from the glued joint, or if that is not set, the folded hinge. Note however that the cases used in this experiment have hinges which are short by industrial standard, and therefore provide poor resistance to lateral shear - an ideal condition for fishtailing.

Finally, a plot of all the experimental data, as shown in Figure 3.10, gives a normal distribution with the majority of values lying somewhere between -1 and +5 mm. However, such tolerance may not be acceptable for an automatic erection machine.

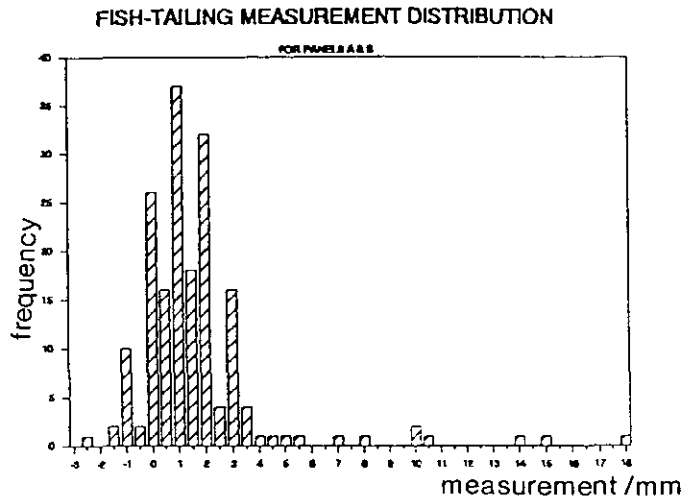


Fig. 3.10 Distribution of fishtailing results.

3.3 CONCLUSION

Fishtailing has been defined geometrically in order to express the case squareness quantitatively. An experiment conducted on a standard flexo-folder gluer case converter has shown that the combined action of gluing and squaring has direct influence on fishtailing. Placing the nylon rails nearest to the folding hinge helps to minimize fishtailing, but the rails have been responsible for the uni-directional fishtailing results. Creaser penetration, when set at the extreme range, can create more fishtailing. On the whole, the effects due to the folding rail location and the crease roll gap have been masked by those of the gluing and squaring. Fishtailing is least dependent on machine speed.

Major research strategies have been adopted as a result of the optimization experiment. One strategy is to investigate ways of eliminating the slapping section, for which E. Rushforth [40], a co-researcher, has developed an in-line squarer for the folding section. The idea behind the in-line squarer is to ensure the correct orientation of cases while they are going through the folding section. Another strategy is to look into ways of improving the present folding method. This will entail the study of some innovative spatial cam mechanisms. The third strategy focuses on the creasing operation. Analysis and experiments will be undertaken in order to study the feasibility of a novel twin roll creaser design.

CHAPTER 4

FOLDING CAM MECHANISMS

Folding devices can be viewed as spatial cam mechanisms, which differ from the planar ones on account of the permitted axial movement of the cam or the follower. Examples such as the globoidal and camoid cams, are typically used for indexing followers that rotate intermittently. Equally uncommon is the concept of a rolling cam mechanism which does not experience rubbing between the cam and the follower. This chapter describes the theoretical background of folding, and provides a literature review on spatial cam mechanisms. A summary on the technical specifications for the spatial folding cam mechanisms is included towards the end of the chapter.

4.1 FOLDING MOMENT

On the theoretical front, little is known about the folding process. Since folding occurs after the creasing process, the quality of fold will go hand-in-hand with the crease quality. Assuming that the fold is as prescribed along the crease, and that there is no false crease in the vicinity of the fold, then the case will be subject to folding resistance as a result of the following factors:

Air resistance - this is most prominent when the case panel approaches the final 180° of fold. When air is expelled from the confined wedge as formed by the closing panel, folding resistance will be experienced the magnitude of which will depend on the rate of air expellation.

Compaction - folding relies on the breaking of the crease on the inner liner and the buckling of the flute structure. As the inner liner and the fluting medium crumple together, folding resistance will increase due to the compaction of material. Suffice it to say that the thicker the board type, the more will compaction contribute to the folding resistance.

Tension - the outer liner in the creased region experiences tension during folding.

Depending on the liner quality, a strong liner will resist folding, whereas a weak one will simply tear away, thus lowering the overall folding resistance. Low folding resistance is preferable, but not at the expense of reducing the case strength and distorting the case appearance as a result of having torn outer liner.

Case inertia - when running an up-folder at constant speed, there is a resistance, first positive and later negative, due to the angular acceleration of the panel.

Compaction and tension are interrelated since the corrugation is structured in such a way that the outer liner will restrict the movement of both the inner liner and the medium as they crumple together. Factors like the air resistance and case inertia are machine speed dependent. In general, the folding resistance characteristics, as construed in Figure 4.1, can be measured separately. There may be difficulties, however, in simulating the high speed motion of the case panels and taking measurements of the folding resistance at the same time.

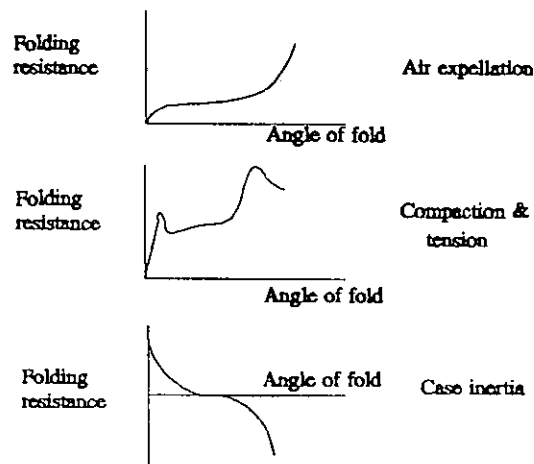


Fig. 4.1 Folding resistance characteristics.

A low folding resistance implies less damage to the case as a consequence of the interaction between the case panels and the folding mechanism. Previous chapters have already discussed how the foldability of a case can be affected by fishtailing. Other machine-related factors may also affect the fold quality. For example, a

study by Edholm [7] has shown that crease quality will only be of secondary importance if the case is not properly constrained during the folding process.

4.2 LITERATURE REVIEW

A typical planar cam mechanism consists of a cam disc and an oscillating follower. The cam and follower axes are parallel to each other and often lie in the same plane. The cam imparts an angular motion to the follower by means of a non-cylindrical curve profile. Spatial cam mechanisms introduce a third dimension which enables the simultaneous relative translation and rotation between the cam and the follower.

Spatial cam mechanisms in the form of camoid and globoidal cams have been mentioned by Rothbart [38] and Chen [5]. Such cams are primarily used for indexing purposes. Fabrication cost however has been a limiting factor for this type of cams.

Chakraborty et al.[4] have applied differential geometry and matrix algebra to designing spatial cam profiles. Essential steps have been suggested by Chakraborty in developing cylindrical, spherical, globoidal, conical and camoid cams. Machining errors have also been considered by specifying the tolerances for each of the cam component in terms of some probability functions. It is interesting to note that Chakraborty has also made use of the screw theory in order to derive the conditions for cam contact.

The concept of rolling cam or direct contact mechanisms has been well established despite its lack of application. As Hain [10] has defined, direct contact mechanisms apply to those with direct contact between two arbitrarily curved bodies shaped in such a way that only pure rolling exists between them. Frictional losses are greatly reduced by thus eliminating any sliding motion between the two cams. Hain [11] has also proposed methods for designing the mating profiles of

rolling cams. Characteristically, rolling is possible only if the motion of the cam mechanism is oscillatory, whether it be translational or rotational.

In summary, there has been no documentation on spatial cam mechanisms whose cams and followers do not oscillate, hence making rolling contact a possible design criterion. The next two chapters will describe two novel spatial cam mechanisms which fall into this category and which will fold corrugated fibreboards at highspeed.

4.3 DESIGN SPECIFICATIONS

The technical specifications for a full size folding cam mechanism are as follows:

- 1) minimum backward force component on the cases.
- 2) rate of folding matching, if not higher than, the existing speed of around 4 m/s.
- 3) capable of processing a range of case blanks as typically shown in Table 4.1.

Table 4.1: Case blanks size range.

	Height/mm	Width/mm
Max. blank size	1206	2832
Min. blank size	318	555

CHAPTER 5

COIL CAM

The uni-directional fishtailing results in Chapter 3 have been attributed to the backward shear force as exerted by the rail onto the front edge of the board panels during folding. A better method of folding will be to direct the folding force normal to the case panel, thereby eliminating any backward force component. The folding mechanism must also be able to roll along the surface of the case panel so as to minimize any ink smearing.

A novel spatial coil cam is introduced as a better method for folding corrugated fibreboards. Three dimensional cams are known to exist but the unusual feature of the coil cam as proposed here is that the follower undergoes screw motion of finite pitch. Even more unusual is the fact that more than one follower can be in contact with the cam at the same time. The coil cam differs from the "Rotofold" design as mentioned in Chapter 2 in that the former aims to confine contact to a single point on the panel and has control over the panel's angular velocity, whereas the latter operates like a helical bar.

This chapter commences with an introduction to the screw theory, or more specifically, the 3-axes theorem of three rigid bodies in spatial motion. The theory has been included on account of its relevance in defining the present design problem; though, as shall be seen later, the theory may not prove to be essential for the design of the spatial coil cam. In the preliminary study, a scaled prototype model, which serves as a visual aid, provides the guess values for the initial design parameters. Based on these estimates, a mathematical model is set up; and following a series of coordinate transformation, the cam profile is generated in a genuinely CAD fashion (since the term 'Computer Aided Design' is often misunderstood to be synonymous with computer drafting). Once the cam is optimized, an attempt is made to produce a prototype using a CAD/CAM system. The chapter is concluded with a design appraisal and problems encountered during the manufacture of the prototype.

5.1 THEORY

The present folding mechanism has a pair of nylon rails that gradually fold the panels to their closed position. Each panel can therefore be regarded as a follower in screw motion about the folding hinge; and the pitch of the screw is defined as the ratio between the translational and angular displacements. The folding rail, in turn, can be seen as a "static" spatial cam, whose folding action relies on the relative motion of the follower. A "dynamic" spatial cam, on the other hand, is one which rotates about an axis skew to that of the followers' screw motion. Depending on the profile geometry, contact between the follower and the cam can be chosen anywhere along the panel, which means that the folding force can be transferred from the leading edge to some other position.

The cam is also in screw motion, though its pitch is zero as there is no translation. The screw axes of the cam and the followers constitute part of a more general ruled surface of motion generators called the cylindroid as shown in Figure 5.1 (with acknowledgement given to Hunt[15] for the reproduction of the figure).

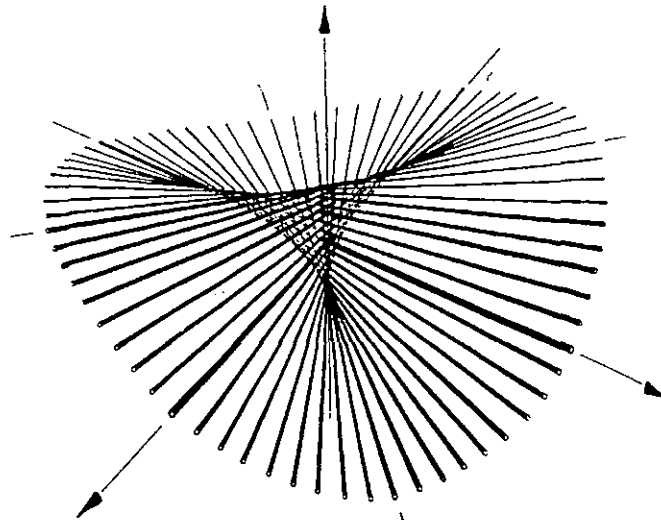


Fig. 5.1 Cylindroid of screw axes.

The cylindroid, first discovered by Plücker (1868-9) [37] and named by Ball (1900) [1], is a twisted, symmetrical ruled surface upon which three screw axes of a three body system reside when in spatial motion. The nodal axis of a cylindroid is a line

in space which intersects and is normal to the three axes. Phillips and Hunt [35] have expounded on the properties of the cylindroid; their work has led to the derivation of the three axes theorem for three bodies in spatial motion. The theorem states that for three rigid bodies in relative spatial motion, their instantaneous screw axes, ISA's, are uniquely defined by the angular velocities, the intersection of the cylindroid and the instantaneous screw pitches 'h'. If the properties about any two ISA's are known, then those of the third ISA can also be established.

5.2 DESIGN SYNTHESIS

Through studying a scaled prototype, the properties of the coil cam are first of all generalized. Major design parameters are then estimated for setting up a mathematical model. After a series of coordinate transformation, the cam profile is generated and is graphically displayed onto a computer. The following section describes in more details the design synthesis of the coil cam.

5.2.1 Preliminary Study

A cam prototype, as shown in Figure 5.2, has been manufactured for the preliminary design study. The coil cam takes the form of a bed spring, the curve of which resembles the intersection of two surfaces: a hyperboloid and a helical conoid. A hyperboloid is essentially a surface generated by rotating a straight line in space about an axis skew to it; its properties have been elaborated at length by Phillips [36]. Except for the variable cross-section of the waist in the middle, the overall shape resembles that of an augur.

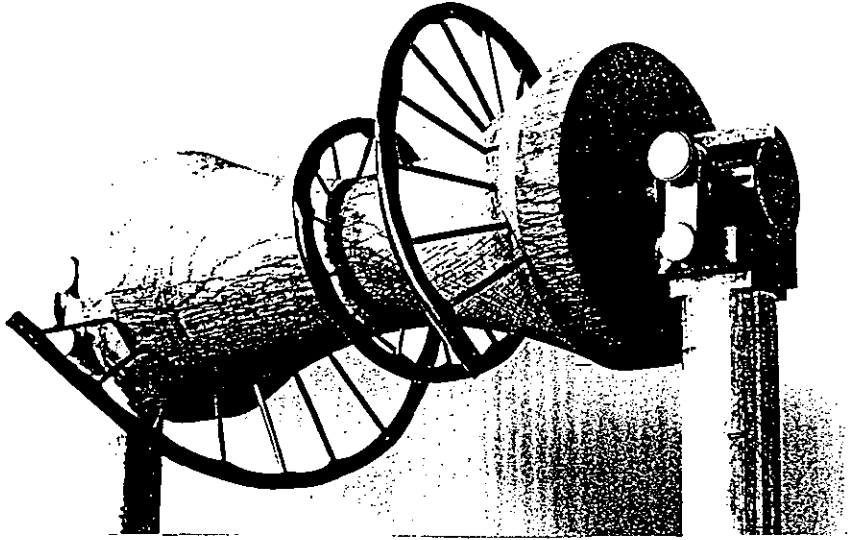


Fig. 5.2 Coil cam prototype.

The operation of the cam is such that for every folding action of 180° , the cam will rotate through one-and-a-half turns (540°), as illustrated in Figure 5.3.

As already mentioned in the previous section, both the case panels and the cam undergo screw motion. The screw axes of the case panels and the cam belong to the same cylindroid instantaneously. This enables the location and properties of the third screw axis to be determined using the three axes theorem. (Parameters for the third screw axis, in terms of dimensions taken from the scaled prototype, have been calculated as documented in Appendix 5a).

Though not a prerequisite, the screw pitches for the cam and the panels are kept constant in order to simplify the instantaneous kinematics of the problem. In practice, however, a constant screw pitch and hence constant angular velocity will be undesirable because of the infinite acceleration and deceleration towards the beginning and end of the motion.

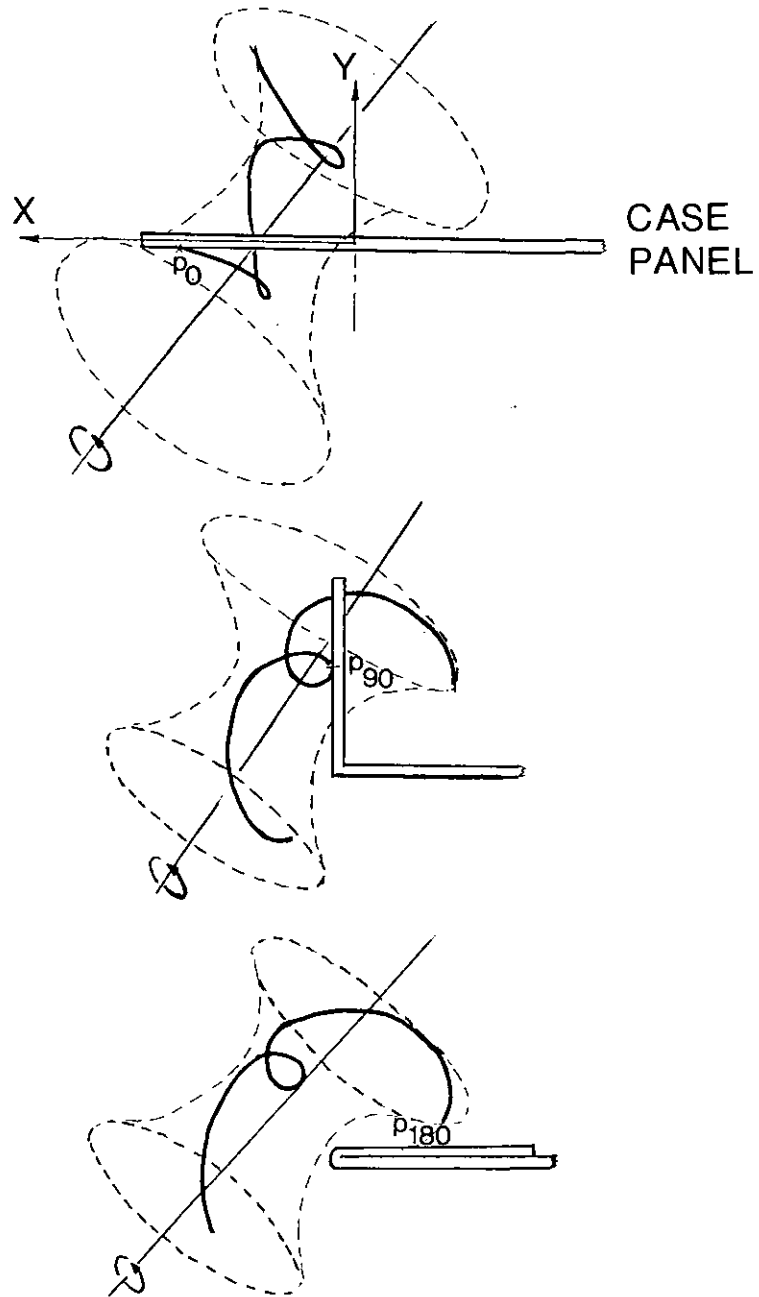


Fig. 5.3 Coil cam operation.

When viewed along the cam axis in the direction whose component is the same as

that of panel translation, then the cam is a right-handed helicoil and rotates counter-clockwise. The velocity of the contact point on the cam is directed away from the folding hinge and backwards. The friction force on the panel, as a result of the shape of the coil, has components in the same directions.

The coil cam is expected to fold cases within a specified size range. For the largest and smallest cases, the point of contact with the coil cam may not be at the centre of the folded panel, but anywhere near the centre will be satisfactory for the present purpose. Having arbitrarily decided that the cam will rotate through 540° while folding a panel over 180° , the number of panels simultaneously in contact with the cam is thus determined. With regards to the axial length of the cam, its lower bound will be limited by the largest panel since there may be a danger of touching the panel in more than one place. From the design specifications in Table 4.1, the height of an average case size is calculated to be 762 mm. Taking a scale of 1:10, the panel height for the prototype cam is therefore 76.2 mm.

5.2.2 Model Generation

With reference to Figures 5.4 and 5.5, the following notation is adopted throughout this section:

a - offset displacement to distinguish cylindroid frame B from frame A.

p - pitch of instantaneous screw axes.

r - instantaneous cam radius.

x,y,z - cylindroid axes with the appropriate subscripts to indicate the cylindroid frame.

θ - pitch angle (r_y with respect to z).

ϕ - roll angle (r_z with respect to x).

ψ - yaw angle (r_x with respect to y).

Table 5.1: Frame notation.

Body	Description
1	static frame of the folding section
2	coil cam
3	case panel being folded

Before defining the dimensions and location of the cam, it is necessary to establish the motion of the case panel. By symmetry of the folding action, only one of the two case panels is considered here. The instantaneous screw axis with respect to the machine frame (1) of the case panel (3), ISA_{13} , is aligned with the folding hinge. Point 'P' is denoted as the mid-point on the panel of an average size case. This is the location where cam contact is anticipated to take place, though it may not be ideal for cases at the extreme size range. As the panel screws about the folding hinge, i.e. ISA_{13} , the mid-point 'P' on the panel will follow a helical path as shown in Figure 5.4. The path is helical only if ω_{13} is constant: an impractical proposition as has been explained previously.

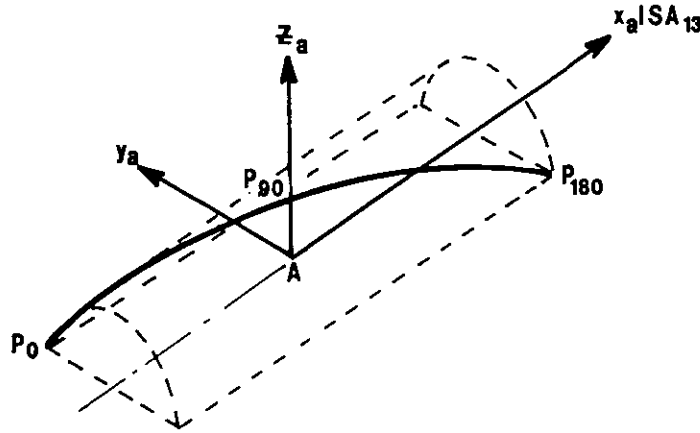


Fig. 5.4 Screw path followed by a point 'P' on the panel.

The location of P at the instants when the panel is in the 0° , 90° and 180° position are labelled P_0 , P_{90} and P_{180} respectively. Only three locations are mentioned here for display purposes; as shall be seen later, more than three locations will be required for the generation of the cam profile.

From the scaled prototype, the path in the x -direction along which the board will traverse and fold is estimated to be 100π mm long. The value is conveniently chosen such that the board panel will undergo a screw motion of π about ISA_{13} with a screw pitch of 100 mm/rad. A fixed reference frame is best located with the origin at the centre point of the crease when the fold is at 90° ; because it is reasonable, as an initial guess, to suppose that the cylindroid nodal line will pass through, or near to, this point. The fixed frame, therefore, is decided with x_a orientated along the crease in the direction of case travel, and z_a vertically upwards. The orientation of y_a is determined by the right-hand convention.

Four quantities are required to specify the location of a ray, i.e a line of indefinite length, in space. This is true of the cam screw axis, ISA_{12} . The first variable is the displacement 'a' from frame A to B along the x_a axis, as shown in Figure 5.5.

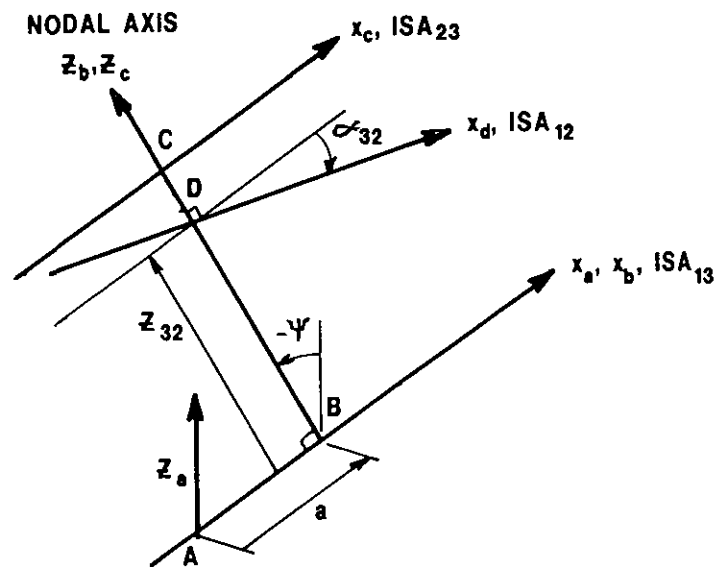


Fig. 5.5 Cylindroid frame transformation.

The next three decisions are concerned with the design variables z_{32} , ψ and α_{32} . z_{32} is the perpendicular distance between ISA_{13} and ISA_{12} (N.B the order of the subscripts signifies the displacement from the screw axis of body 3 to that of body 2). ψ is the angle measured from the z_a axis to the z_b axis about the x_a axis. Estimate from the scaled prototype gives ψ a value of -45° . α_{32} is the angle from the x_a axis (ISA_{13}) to the x_b axis (ISA_{12}) about the z_b axis.

The length of the cam, and hence its angular velocity and pitch, is determined by the number of boards to be folded at any instant. A design decision is that two boards, though it does not have to be an integer, will be folded instantaneously. But there is one moment when three boards will be in contact with the cam - one starting, one at 90° fold and one finishing.

The next stage of cam generation is to transform the locus as followed by the mid-point 'P' from the frame of ISA_{13} to that of ISA_{12} . The transformation is shown graphically in Figure 5.5.

In all, there are three frames in which the coordinates of the point P will be transformed from one to the other. The frames are denoted as 'A', 'B' and 'D' with frame 'A' being the frame of origin, i.e the machine frame. An additional frame 'C' is provisionally included should a need arise to examine the nature of the ISA_{23} . Frames with more than one label indicate axes coincidence. Characteristically, axes z_b , z_c and z_d all coincide with the cylindroid's nodal line z .

Referring to Figure 5.5, frame 'A' is first of all translated along ISA_{13} to position 'B' at an offset displacement 'a'. The frame is then rotated by angle ψ to become frame B. Frame B is translated a distance z_{32} along z_b the nodal line and then rotated by α_{32} to become frame 'D'. Figure 5.6 shows the transformation algorithms.

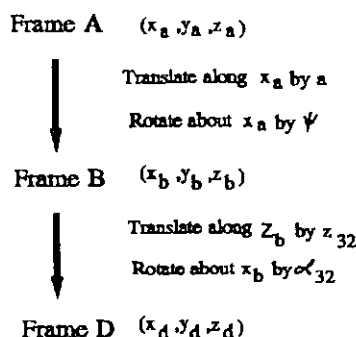


Fig. 5.6 Frame transformation algorithm.

The change of reference frames can be brought about by means of standard

transformation matrices. Since both rotation and translation are involved, it will be reasonable, therefore, to compute the transformation in a mixture of Cartesian and cylindrical coordinates. Equations used for the transformation are as follows:

$$\begin{vmatrix} x \\ \psi \\ r \end{vmatrix}_b = \begin{vmatrix} x \\ \psi \\ r \end{vmatrix}_a + \begin{vmatrix} -a \\ -\psi_{32} \\ 0 \end{vmatrix}$$

$$z_b = r_x \sin \psi_b$$

$$\phi_b = \text{atan2} \left(\frac{r_x \cos \psi_b}{x_b} \right)$$

$$r_{zb} = \sqrt{x_b^2 + r_{xa}^2 \cos^2 \psi_b}$$

$$z_d = z_b - z_{32}$$

$$\phi_d = \phi_b - \alpha_{32}$$

$$x_d = r_z \cos \phi_d$$

$$\psi_d = \text{atan2} \left(\frac{z_d}{r_{zb} \sin \phi_d} \right)$$

$$r_{xd} = \sqrt{z_d^2 + r_{zb}^2 \sin^2 \phi_d}$$

Appendix 5b shows the transformations for the cylindrical coordinates.

The transformation of point P from ISA₁₃ to ISA₁₂, as already stated, requires more than the three locations, namely those at 0°, 90° and 180°. The increment of panel fold angle is represented by δ_{13} .

Like any planar cam design, it is more convenient to regard the cam as fixed and for the follower (3) to rotate about the cam (2). Subsequent positions of the follower stroke can then be set out at fixed intervals of cam rotations. This interval is conveniently labelled as δ_{12} . The size of δ_{12} will depend on the rate at which the cam will rotate in relation to the rate of fold. In fact, the rotation

increments and the angular velocities between the cam and the board panel can be expressed as follows:

$$\frac{\delta_{12}}{\delta_{13}} = \frac{\omega_{12}}{\omega_{13}} = \omega_{ratio}$$

It is not recommended for ω_{13} to be constant as explained previously, except for the purpose of demonstration here. The time function for ω_{13} can of course be tailored to the needs. For example, it may be worthwhile to make ω_{13} small while work done in folding is large. The average ω_{13} , however, determines the length of the cam; whereas ω_{ratio} will determine the average number of boards in instantaneous contact with the cam. For example, a decision to make the cam rotate through 540° for each 180° fold will imply $\omega_{ratio} = 3$. Hence, the average number of boards in instantaneous contact will be ω_{ratio} divided by two, or 1.5.

The first set of spreadsheet results, based on the above transformations at twelve increments of 'P' locations, can be seen in Table 5.2. Figure 5.7 shows a plot of the cam profile as seen along its screw axis.

Table 5.2: Spreadsheet results at twelve angle increments.

Pitch=	100	a=	0						
Rx=	40	α=	-45						
pie	3.1415927								
Angle	x(a)	x(b)	ψ(a)/rad	ψ(b)/rad	z(b)	φ(b)/rad	Rz(b)	ψ(b)	φ(b)
0	-157.0796	-157.0796	0	0.785398163	28.284271	2.9634384	159.6058	45	169.79252
15	-130.8997	-130.8997	0.261799388	1.047197551	34.641016	2.9899764	132.41877	60	171.31303
30	-104.7198	-104.7198	0.523598776	1.308996939	38.637033	3.0430513	105.23026	75	174.35399
45	-78.53982	-78.53982	0.785398163	1.570796327	40	3.1415927	78.539816	90	180
60	-52.35988	-52.35988	1.047197551	1.832595715	38.637033	-2.946387	53.373556	105	-168.8156
75	-26.17994	-26.17994	1.308996939	2.094395102	34.641016	-2.489227	32.945245	120	-142.6222
90	2.132E-14	2.132E-14	1.570796327	2.35619449	28.284271	-1.570796	28.284271	135	-90
105	26.179939	26.179939	1.832595715	2.617993878	20	-0.923626	43.421069	150	-52.91984
120	52.359878	52.359878	2.094395102	2.879793266	10.352762	-0.63572	65.072092	165	-36.4241
135	78.539816	78.539816	2.35619449	3.141592654	4.899E-15	-0.471057	88.13911	180	-26.98955
150	104.71976	104.71976	2.617993878	3.403392041	-10.35276	-0.353462	111.6201	195	-20.25187
165	130.89969	130.89969	2.879793266	3.665191429	-20	-0.258707	135.4058	210	-14.82284
180	157.07963	157.07963	3.141592654	3.926990817	-28.28427	-0.178154	159.6058	225	-10.20748

α32=	50									
α31=	-45									
z(d)	φ(d)/rad	φ(d)	x	ψ(d)/rad	ψ(d)	Rz	ψ(d)'	Y	Z	X
-21.71573	3.7488366	214.79252	-131.0721	-2.907518	-166.5885	93.625293	-166.5885	93.625293	0	-131.0721
-15.35898	3.7753746	216.31303	-106.7022	-2.94818	-168.9183	79.907881	-123.9183	58.75363	54.159767	-106.7022
-11.36297	3.8284494	219.35399	-81.36856	-2.972922	-170.3359	67.688121	-80.33586	4.4238924	67.5434	-81.36856
-10	3.9269908	225	-55.53604	-2.963438	-169.7925	56.429171	-34.79252	-37.60893	42.069222	-55.53604
-11.36297	-2.160989	-123.8156	-29.70352	-2.890747	-165.6276	45.777228	14.372391	-45.77079	-0.767689	-29.70352
-15.35898	-1.703829	-97.62221	-4.369877	-2.701942	-154.8099	36.085894	70.190099	-19.77058	-30.18801	-4.369877
-21.71573	-0.785398	-45	20	-2.315089	-132.6448	29.522413	137.35519	16.484668	-24.4914	20
-30	-0.138227	-7.919845	43.00691	-1.767643	-101.2785	30.590765	213.7215	28.688885	10.61804	43.00691
-39.64724	0.1496777	8.5759026	64.344533	-1.330763	-76.24741	40.817419	283.75259	-0.242997	40.816696	64.344533
-50	0.3143416	18.010446	83.820308	-1.071773	-61.40806	56.944348	343.59194	-49.40468	28.316714	83.820308
-60.35276	0.4319364	24.748134	101.36856	-0.911961	-52.25152	76.327708	397.74848	-69.54503	-31.45485	101.36856
-70	0.5266908	30.177162	117.05496	-0.799411	-45.80289	97.6364	449.19711	-23.97468	-94.64714	117.05496
-78.28427	0.6072439	34.792515	131.07207	-0.710033	-40.68189	120.09392	499.31811	70.430995	-97.27294	131.07207

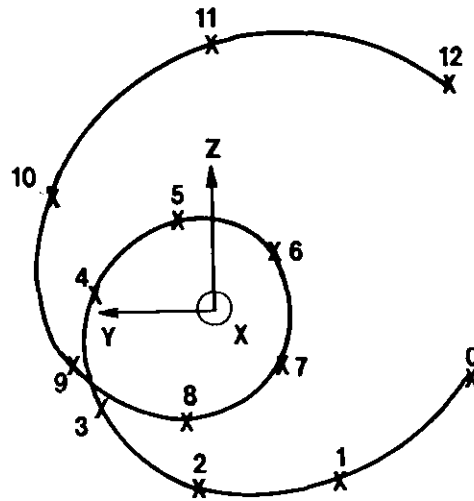


Fig. 5.7 Coil cam profile along its axis.

5.2.3 Computer Aided Design

Problems were encountered on deciding the best way to display the results graphically. At the time, two proprietary software packages were considered; they were AutoCAD and DUCT. One way of displaying the results was to feed the spreadsheet data into AutoCAD through modifying the IGES (Inter Graphics Exchange System) file. An easier alternative was to write a special program which would perform the transformation calculations. Data generated from the program were then formatted into input files which the macro commands in DUCT would accept for automatic graphic display. The program, written in UNIX C, required input for different design parameters such as the velocity ratio, offset displacement, pitch p_{13} , etc. (See Appendix 5c for the program listing.)

The principle of DUCT was based on the definition of a spline and the attachment of transverse sections to the spline points. The sections in turn would be joined up through the B-spline interpolation technique to form a duct surface. Besides being an ideal display package, DUCT was chosen on account of its CAD/CAM capability. In essence, machining codes for the cam could be created on the same

package and downloaded directly onto a CNC milling tool.

5.3 DESIGN OPTIMIZATION

In order to make the cam, it was necessary to specify a transverse section for each of the spline point. A preliminary shape for the sections was chosen to be that of a table-tennis bat. The semi-circular tip of the handle was where contact would take place behind the cam and the panel. Through a series of scaling, rotation and translation, all operated about the spline, the resulting duct, as shown in Figure 5.8, was in the form of an auger with a core resembling the shape of a hyperboloid.

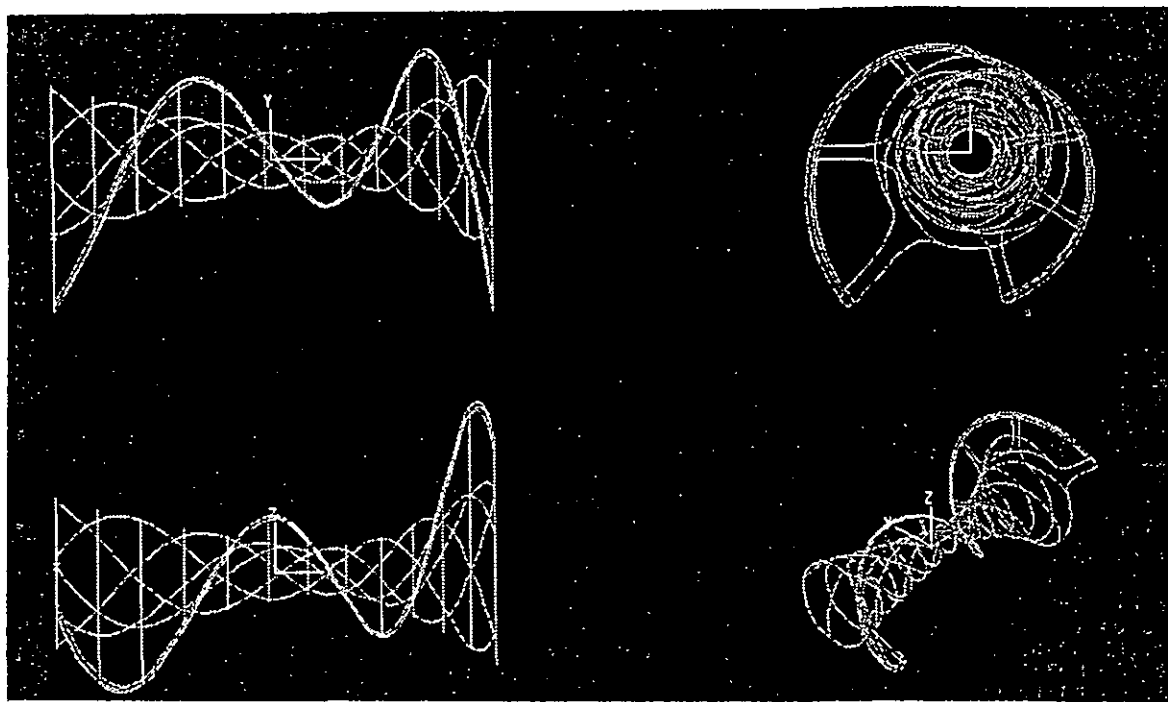


Fig. 5.8 Coil cam with hyperboloidal core.

Interference was suspected between the hyperboloid core and the front edge of the panel when folding large blanks. To verify this suspicion, a function in DUCT called 'oblique duct' was resorted to. Essentially, the function would slice the duct surface with a plane whose normal unit vectors coincided with those of the panel at various points of contact. Any interference would show up graphically. To this

end, a subroutine was added to the source program for working out the normal vectors of the point 'P' on the panel. The highlighted section on the cam, as shown in Plate 1 (overleaf), did indicate interference and its exact location.

The problem of core interference led to the adoption of a coil-like cam in preference to an auger-like one. This time, no scaling of the sections was required. Instead, a small section, in the shape of a pear, was designed such that the sharper tip would touch and fold the panel. A number of pear sections, matching the same number of spline points, were orientated about and radially translated from the spline. Joining the sections would turn the duct surface into a coil cam as shown in Figure 5.9.

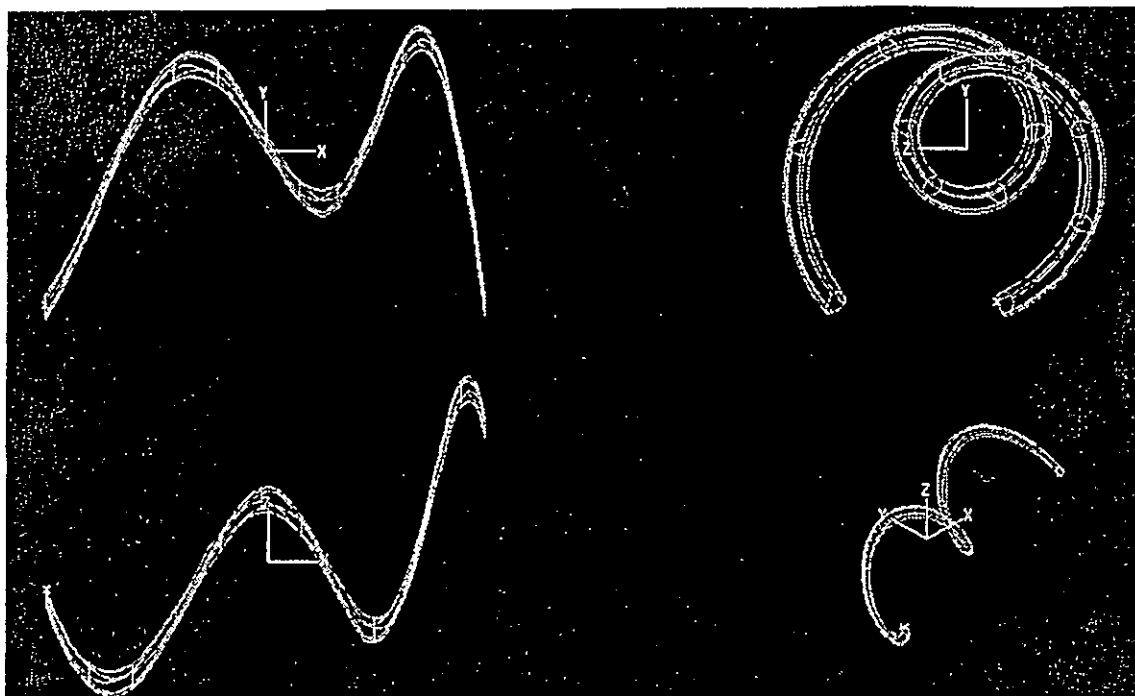
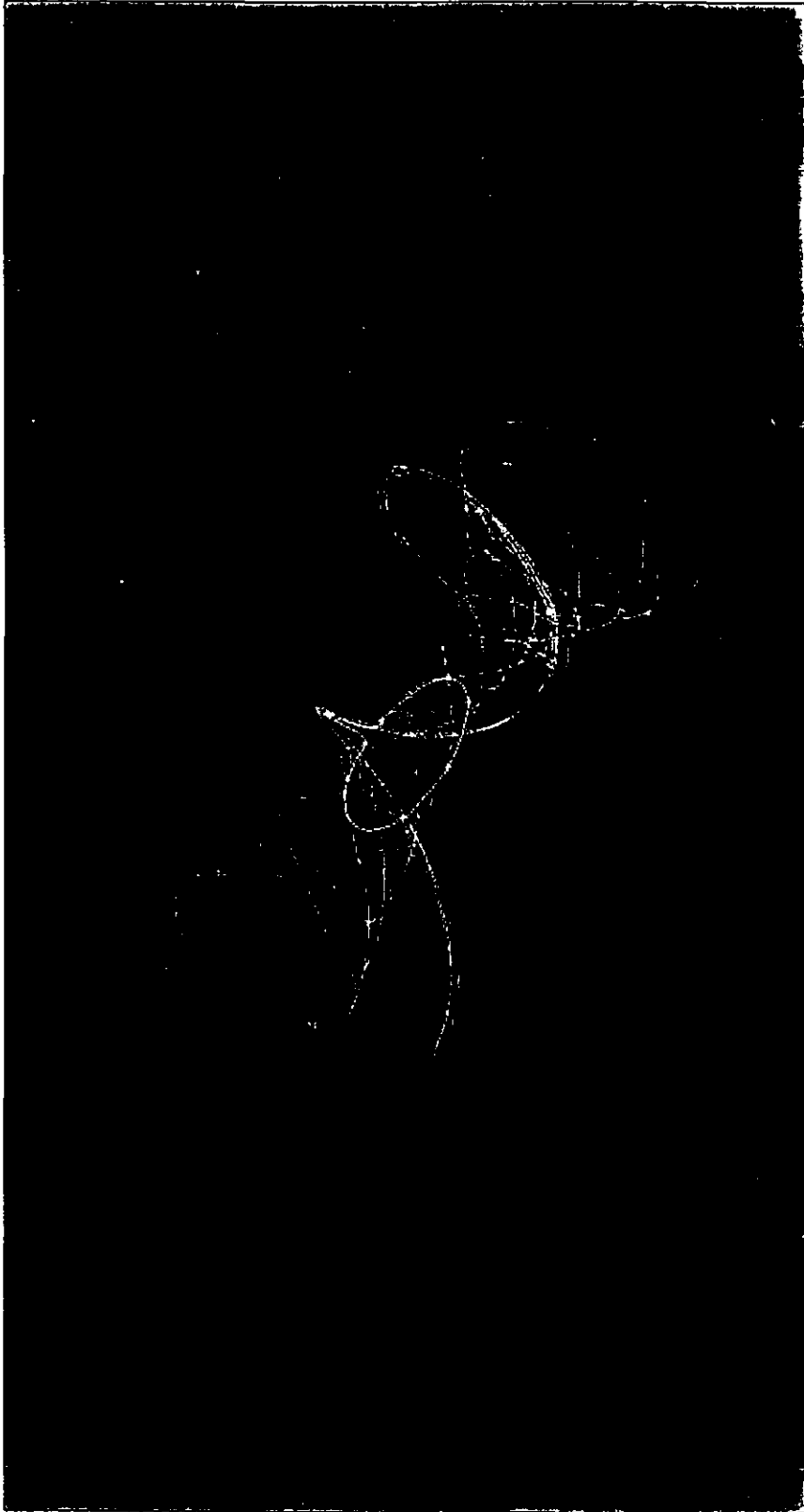


Fig. 5.9 Coil cam with 'pear' cross-sections.

It was noticed that by translating the 'pear' sections radially from a straight spline, part of the cam profile might be 'sheared', leading to a degeneration in the cross-section. The situation was rectified by producing a duct surface with a curved spline that followed the locus of the centrepoint 'P' on the panel. In addition, the 'pear' sections were replaced by circular ones to ensure single-point contact between the cam and the panel.

PLATE 1

DUCT 'slice' function on coil cam design



With regards to the optimization of design parameters, an L_{16} Taguchi experiment was conducted on the following: a , ψ_{32} , α_{32} , z_{32} and r_x of ISA_{13} . The parameters were estimated from the scaled cam prototype, and the response that the experiment was aiming for was the best compromise between a visually balanced cam and one with a minimum overall dimension. Obviously, a cam which required a large work-space would be difficult to mount onto the folding section.

Parameters for the optimized cam were as follows:

$$\omega_{ratio} = 4$$

Offset displacement, $a = 0$

Section radius = 10 mm

Pitch $p_{13} = 100$ mm

Screw radius, $r_x = 40$ mm

$$\psi_{32} = -15^\circ$$

$$z_{32} = 30 \text{ mm}$$

$$\alpha_{32} = -60^\circ$$

Section increment = 12

and the final cam was as shown in Figure 5.10.

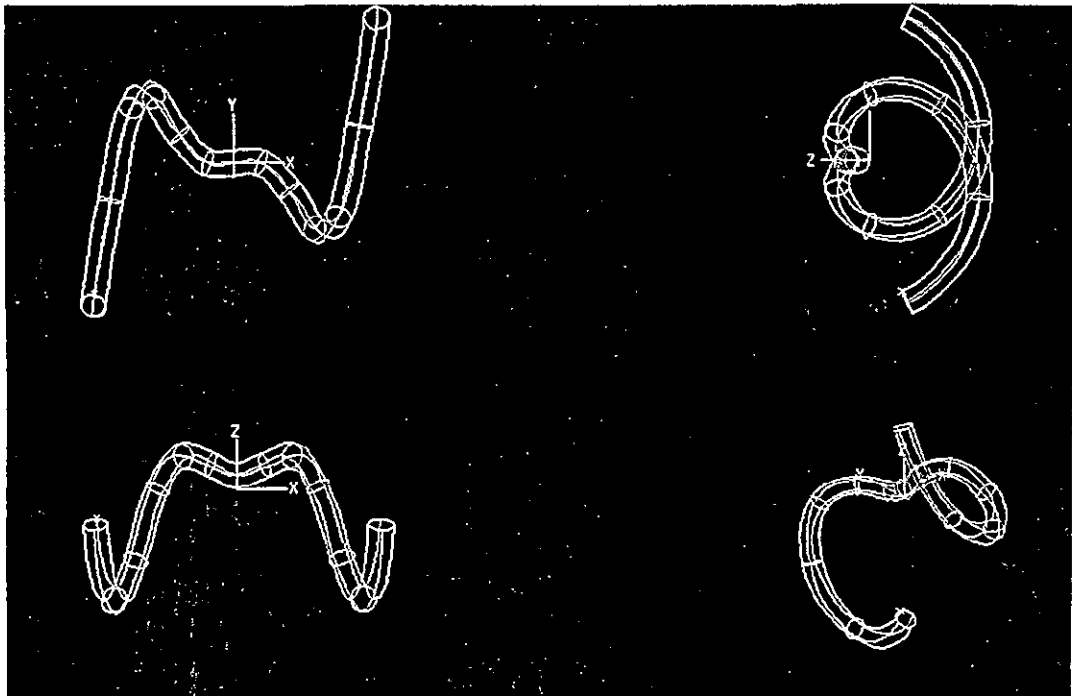


Fig. 5.10 Optimized coil cam design.

The operation of the cam was as shown in Figure 5.11.

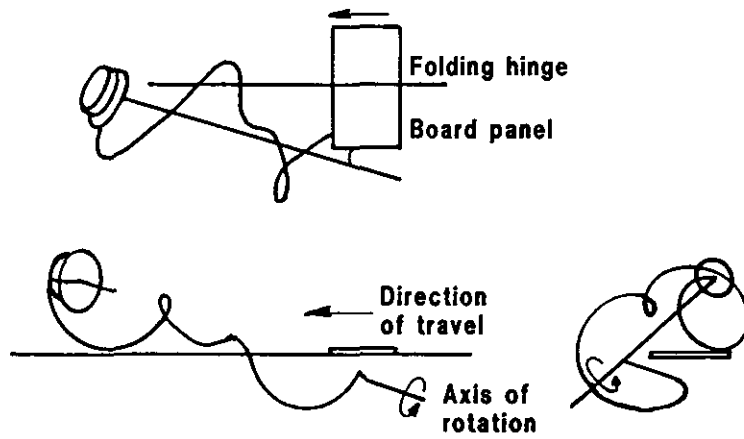


Fig. 5.11 Coil cam operation.

Among some of the design considerations, a cam which allowed more boards to be folded per turn and ran at a slower speed would be more preferable.

Consequently, the 540° cam was replaced by a 720° one with $\omega_{\text{ratio}} = 4$, which meant that on average two panels would be in contact at any instant, except at the start or finish of contact for which there would be three (see Section 5.2.2).

5.4 MANUFACTURE OF PROTOTYPE

DUCT, the surface modelling package, was chosen primarily because of its capability to interface with a CNC machine tool on site. Ideally the cam would be cut by rotating the workpiece with a fourth axis, while the cutter traversing in the x-, y- and z- directions. In practice, however, it would be impossible to manipulate the coil-like cam once the bulk of the material had been removed. As a result, only half of the coil cam was produced as shown in Figure 5.12. Because of the limitation associated with a 3-axis CNC machine and the shape of the coil cam, undercutting was inevitable. Instead, a female mould was reproduced on the same block of material, demonstrating the feasibility of manufacturing the cam by means of casting.

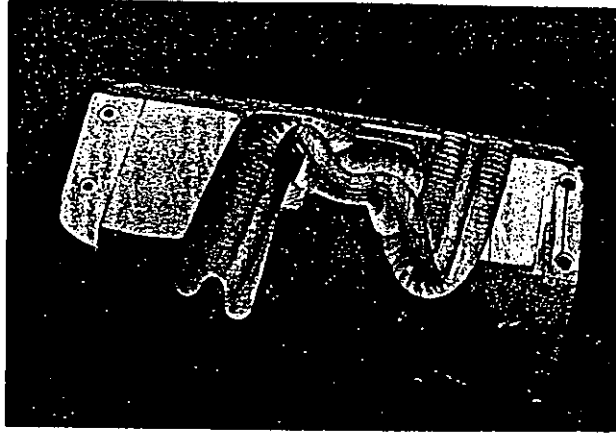


Fig. 5.12 Coil cam machined mould.

Leung [25] has investigated ways of manufacturing the coil cam prototype, e.g direct machining, casting, thermal forming and stereolithography are among the possible options. Casting, as Leung has identified, may produce poor surface texture and the two halves of a die cast may not separate with a consistent split-line. In thermal forming, the difficulty is associated with the control of hot air flow over the malleable material. Stereolithography relies on the hardening of special block modelling resin by means of a laser. As the laser beam is directed into the photosensitive liquid resin, solidification will take place layer by layer. The capability of stereolithographic systems that are currently on the market is limited by the size of the workpiece, and the material used - modelling resin - which may not be suitable for direct engineering application. Short lead time and good surface finish, however, make it an excellent tool for prototyping. Other fast prototyping techniques can be found in a review on rapid prototyping by Sze et al. [46].

5.5 APPRAISAL

In its present form, the cam will fail on account of an initial assumption that the screw pitch for ISA_{12} is constant. What this implies is that the acceleration and deceleration at both ends of the cam are infinite. For a rigid panel, there will be

an impulsive force acting at the beginning of fold, to be followed by a crushing force at the end, both of which are detrimental to the case panel. A gentler motion profile (e.g trapezoidal velocity profile) can be implemented by changing the function of ω_{13} with respect to time. A more sophisticated motion profile will be one which takes into account the folding resistance of a typical board sample.

The design of the coil cam has not been pursued any further because of the following reasons:

- 1) difficult to manufacture
- 2) a similar device, i.e Rotofold, has been patented, though its design is not as refined as the coil cam.
- 3) backward component of friction may still contribute to fishtailing
- 4) cam whirling at high speed
- 5) difficult to balance the cam dynamically
- 6) over-sized cam structure, hence the difficulty in mounting of the coil cam onto the folding section

5.6 CONCLUSION

Based on the screw theory of three bodies in relative spatial motion, the coil cam has been designed with its folding force directed at a single point normal to the case panel. In this way, less ink-smearing and panel distortion will be made possible, when compared with the folding rail design. A methodology which utilizes a high-level software program to run a proprietary CAD software by means

of macro commands has also been demonstrated as a useful design technique. A prototype mould has been manufactured and other means of producing the cam has been reviewed, but the design has not been adopted on account of its practicality.

CHAPTER 6

TWIN CAM

Another innovative design for continuously folding corrugated fibreboards at high speed is the twin cam folding mechanism. Essentially, the folding operation is divided into two stages, with each stage being responsible for a fold of 90° . The cams are to be mounted on the side of the folding section at 45° below and above the horizontal folding level. Each cam is quasi-planar in that the overall shape conforms to a plane but the periphery is curved in the out-of-plane direction, hence enabling rolling contact between the cam and the board. Rolling contact is important because, as soon as the case blanks leave the printing units for the folding section, any wet ink on the panels will be smudged on contact with the folding mechanism (see section 4.2).

This chapter describes the synthesis and the design of the first twin cam folding mechanism which imparts rolling contact onto the follower surface.

6.1 NOTATION

The following notation, as illustrated in Figures 6.1 to 6.4, has been adopted throughout the theoretical synthesis of the twin cam folding mechanism:

$\theta(t)$ - angle between the folded panel and the horizontal; it ranges from 0° to 180° .

ω_0 - maximum angular velocity of board panel during folding.

v - board translational velocity in the machine direction.

l - horizontal displacement on the panel of the instantaneous point of contact with the cam and the first contact point.

c - distance between the first contact point and the folding hinge.

$r(t)$ - instantaneous cam radius.

$e(t)$ - instantaneous eccentricity at periphery of cam for minimizing friction contact (see Figure 6.3).

b - datum line distance as defined between 'B' and 'D' (see Figure 6.4).

x, y - local cartesian coordinates in the plane of the cam.

$\beta(t)$ - cam angle from moment of contact.

$\psi(t)$ - instantaneous angle between y-axis and $r(t=0)$.

$s(t)$ - accumulated peripheral length of cam.

6.2 CAM PROFILE DERIVATION

In the design of cam mechanisms, the first task is to specify the motion of the follower. During the folding operation, the board panel can be seen as the follower which 'screws' along the folding hinge. A preliminary step will therefore be to choose a motion profile for the cam follower, and express it in terms of some known design parameters.

The translation velocity ' v ' of the panel is not subject to choice since it is a design specification. However, the angular displacement $\theta(t)$ can be chosen arbitrarily. A parabolic function has been selected for the angular displacement of the follower; though this would imply infinite acceleration and deceleration at the beginning and end of the motion. Figure 6.1 shows the parabolic motion profile expressed in terms of θ and its higher derivatives.

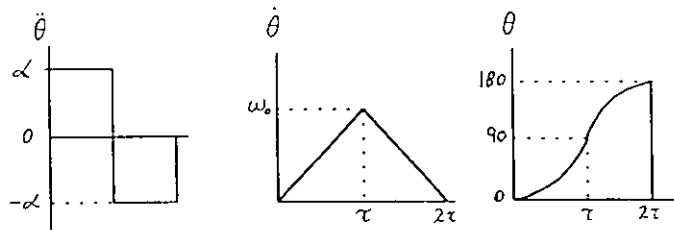


Fig. 6.1 Parabolic motion profile.

For the first 90° fold, the motion equations are as follows:

$$\begin{aligned}\ddot{\theta} &= \alpha \\ \dot{\theta} &= \alpha.t \\ \theta &= \frac{1}{2}\alpha.t^2\end{aligned}$$

and for the second 90° fold, applying the boundary conditions will give:

$$\begin{aligned}\ddot{\theta} &= -\alpha \\ \dot{\theta} &= \omega_o + \alpha(\tau - t) \\ \theta &= \omega_o(t - \tau) + \alpha.\tau.t - \frac{\alpha}{2}(\tau^2 + t^2) + \frac{\pi}{2}\end{aligned}$$

where,

$$\begin{aligned}\alpha &= \frac{\pi}{\tau^2} \\ \omega_o &= \frac{\pi}{\tau} \\ \tau &= \frac{l}{v}\end{aligned}$$

Note that the right-hand side of the basic equations can be adapted for functions other than the parabolic one, e.g. trapezoidal, cycloidal, etc..

If the x-direction is defined as opposite to the board travel, then the design parameter 'l' will correspond to the x-component of the total contact length between the board panel and the rolling cam. The value of 'l' is equal to the height of the shortest case less some tolerance, as shown in Figure 6.2.

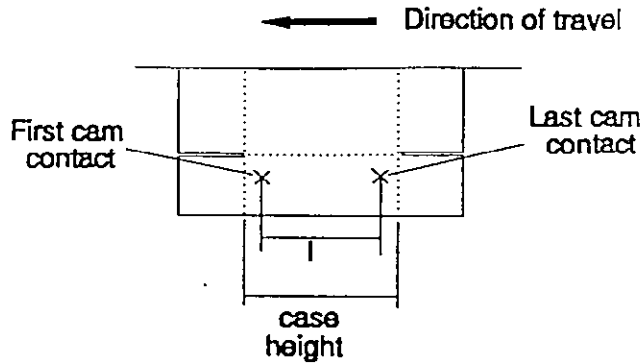


Fig. 6.2 Cam-panel contact length.

The first cam is derived as follows: consider Figure 6.3, which shows the plan and side views of the proposed cam,

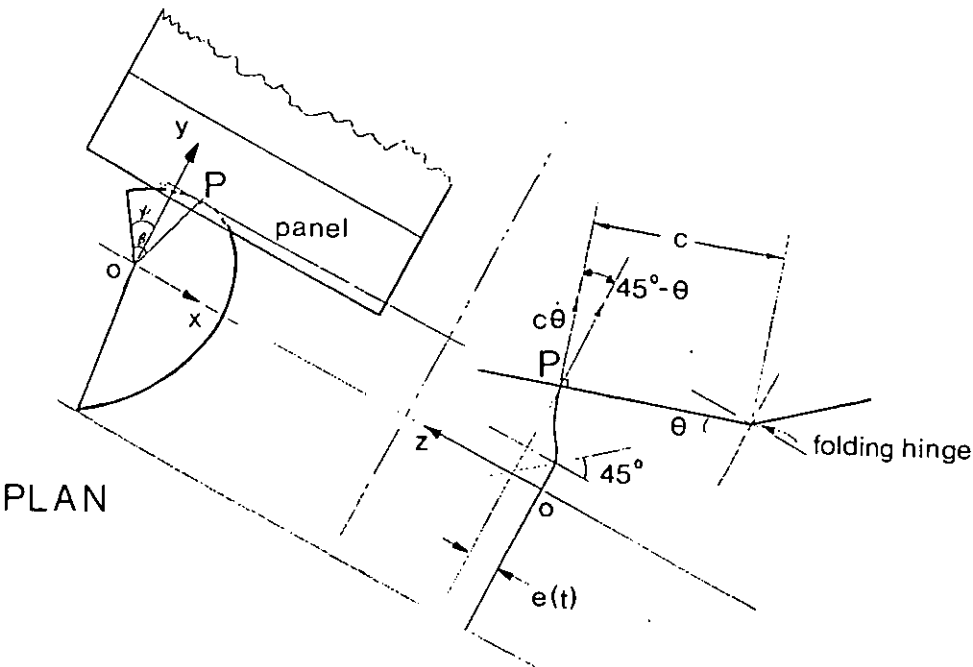


Fig. 6.3 Plan and side views of cam.

the cam is orientated at 45° to the horizontal. Cartesian coordinates on the cam are defined such that the contact point made by the cam and the board panel is enclosed within the x-y plane. In order to avoid rubbing, the plane varies instantaneously along the cam axis, the motion of which will be generated by an offset dimension 'e(t)' in the z-direction (hence the term quasi-planar). Point 'Q' lies along the length 'l' as projected from the point 'P' along the same line, and is defined by the intersection between 'l' and the y-axis. Expressing the kinematics in terms of 'x' and 'y' will give:

$$\begin{aligned} -\dot{x} &= OQ.\dot{\psi}(t) \\ \therefore v &= r(t).\cos[\beta(t) - \psi(t)].\dot{\psi}(t) \dots\dots\dots(1) \end{aligned}$$

$$\begin{aligned} \dot{y} &= PQ.\dot{\psi}(t) \\ \therefore c.\dot{\theta}(t)\cos[45^\circ - \theta(t)] &= r(t).\sin[\beta(t) - \psi(t)].\dot{\psi}(t) \dots\dots\dots(2) \end{aligned}$$

On examining equations (1) and (2), there are 4 unknown quantities, namely,

$$r(t), \beta(t), \dot{\psi}(t), \psi(t)$$

The last two quantities can be established by means of the finite difference method:

$$\psi_{(i+1)} - \psi_{(i)} = \delta t \cdot \dot{\psi}(t) \dots\dots\dots(3)$$

where 'i' represents the i^{th} term in the finite difference table. Finite difference is resorted to instead of analytical methods, since cam variable dependency permits solutions to be derived only by such means.

One more equation is required in order to solve for the four unknown quantities. Referring to the cam geometry as shown in Figure 6.4,

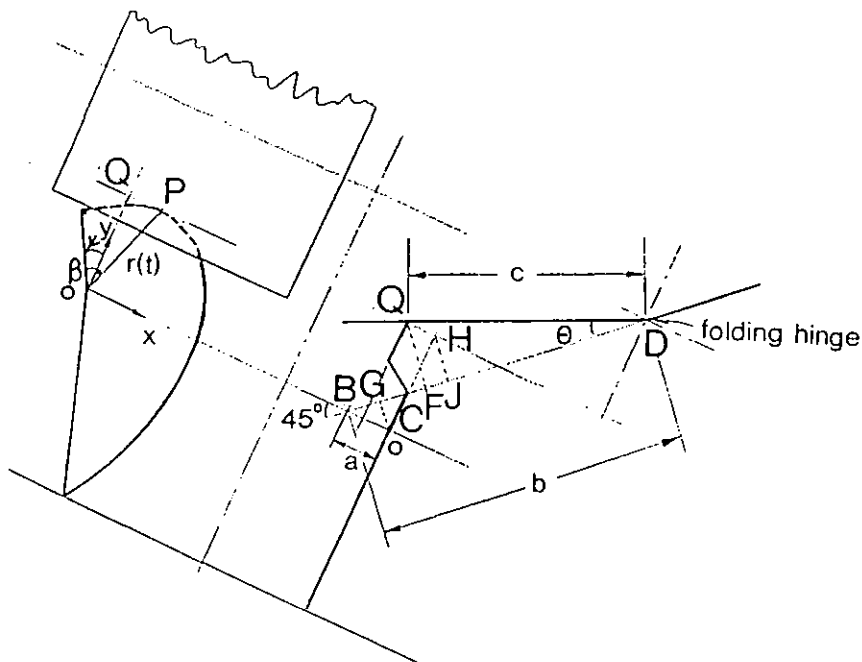


Fig. 6.4 Cam geometry.

the following geometrical expressions can be derived:

$$QF = c \sin \theta$$

$$FD = c \cos \theta$$

$$BG = a \cos 45^\circ$$

$$OH = r(t) \cos[\beta(t) - \psi(t)]$$

$$GJ = r(t) \cos[\beta(t) - \psi(t)] \sin 45^\circ$$

$$QH = e(t)$$

$$FJ = e(t) \cos 45^\circ$$

Now, $BG + GJ - FJ + FD = b$, it follows that:

$$a \cos 45^\circ + r(t) \cos[\beta(t) - \psi(t)] \sin 45^\circ - e(t) \cos 45^\circ + c \cos \theta = b \quad \dots\dots\dots(4)$$

Also,

$$OC = OB = a$$

$$CH = OH - OC$$

$$HJ = CH \sin 45^\circ$$

$$QF = HJ + QH \cos 45^\circ$$

$$\therefore c \sin \theta(t) = [r(t) \cos[\beta(t) - \psi(t)] - a] \sin 45^\circ + e(t) \cos 45^\circ \quad \dots\dots(5)$$

On the condition that the cam axes are orientated at an angle of 45° , hence the terms ' $\sin 45^\circ$ ' and ' $\cos 45^\circ$ ', ' $e(t)$ ' and ' a ' can be eliminated by adding equations (4) and (5):

$$b + c \sin \theta(t) = r(t) \sin 45^\circ \cdot 2 \cos[\beta(t) - \psi(t)] + c \cos \theta(t) \quad \dots\dots(6)$$

which provides the 4th equation with the same unknown $r(t)$, $\beta(t)$ and $\psi(t)$. Since $\beta(t)$ always appears with $\psi(t)$, the term ' $\beta(t) - \psi(t)$ ' can be conveniently replaced by $\phi(t)$.

Dividing equation (2) by (1) will give:

$$\tan \phi(t) = \frac{c \cdot \dot{\theta}(t) \cdot \cos[45^\circ - \theta(t)]}{v}$$

hence $\phi(t)$. Substituting into equation (6) will give $r(t)$, which in turn will determine the camshaft speed i.e. the first derivative of $\psi(t)$ from equation (1).

Incidentally, the camshaft speed must be variable if slipping is to be avoided. $\psi(t)$

itself can be calculated from the finite difference equation (3), and $e(t)$, from equation (4).

6.3 DESIGN OPTIMIZATION

For each of the twin cams, a spreadsheet with 300 time increments was set up to calculate the following parameters:

$$\theta, \dot{\theta}, \ddot{\theta}, \phi(t), r(t), e(t), \psi(t), \dot{\psi}(t), \beta$$

In addition, the peripheral contact length of the cam, ' $s(t)$ ', was determined cumulatively by means of the following equation:

$$s(t)_{acc} = \sqrt{\left[(\beta_{(t)} - \beta_{(t-1)}) \cdot r(t) \cdot \frac{\pi}{180}\right]^2 + [r_{(t)} - r_{(t-1)}]^2} + s_{(t-1)}$$

starting from $t=0$.

Software optimization was conducted using a 3x3 Taguchi experiment (see Appendix 6a). The objective was to select the parameters ' l ', ' c ' and ' a ' which would give the shortest radius $r(t=300)$ at the final time increment. The optimized design parameters, as scaled down by a ratio of 1:4 from an existing flexo-folder gluer design, were as follows:

$$l = 60 \text{ mm}$$

$$v = 1250 \text{ mm/s}$$

$$c = 20 \text{ mm}$$

$$a = 10 \text{ mm}$$

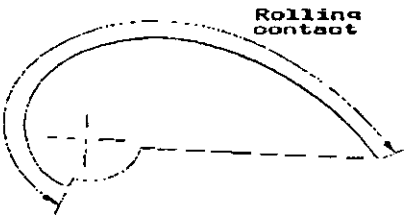
Spreadsheet data for the parameters $r(t)$, $\beta(t)$ and $e(t)$ are as shown in Table 6.1.

Table 6.1: Sample data for $r(t)$, $\beta(t)$ and $e(t)$.

First Cam				Second Cam			
t	r(t)	beta(t)deg	e(t)	t	r(t)	beta(t)deg	e(t)
0	10	0	0	0	12.443116	36.519226	0
20	10.111544	25.694465	0.0983853	20	16.949616	59.331683	2.5548216
40	10.453768	51.05704	0.3893578	40	21.469176	75.730389	4.3220687
60	11.049787	75.763353	0.8600858	60	25.548514	87.779508	5.3761996
80	11.9391	99.523349	1.4882738	80	28.925163	96.761395	5.8226609
100	13.178409	122.08961	2.2409053	100	31.529952	103.52081	5.7817583
120	14.841034	143.25767	3.0727049	120	33.437201	108.66499	5.3761996
140	17.012482	162.86108	3.9245702	140	34.795802	112.67106	4.7223175
160	19.778517	180.76618	4.7223175	160	35.767344	115.93469	3.9245702
180	23.201665	196.87029	5.3761996	180	36.485714	118.78291	3.0727049
200	27.283493	211.10136	5.7817583	200	37.04096	121.46973	2.2409053
220	31.914265	223.41241	5.8226609	220	37.481672	124.17028	1.4882738
240	36.819375	233.76283	5.3761996	240	37.826712	126.98242	0.8600858
260	41.523597	242.08066	4.3220687	260	38.078335	129.9371	0.3893578
280	45.368949	248.1996	2.5548216	280	38.232345	133.01424	0.0983853
300	47.637563	251.76012	0	300	38.284271	136.16039	1.005E-14

Figures 6.5 and 6.6 show the twin cam design and arrangement respectively.

Cam for first
90 fold



Cam for second
90 fold

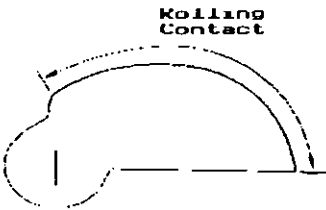


Fig. 6.5 Twin cam design.

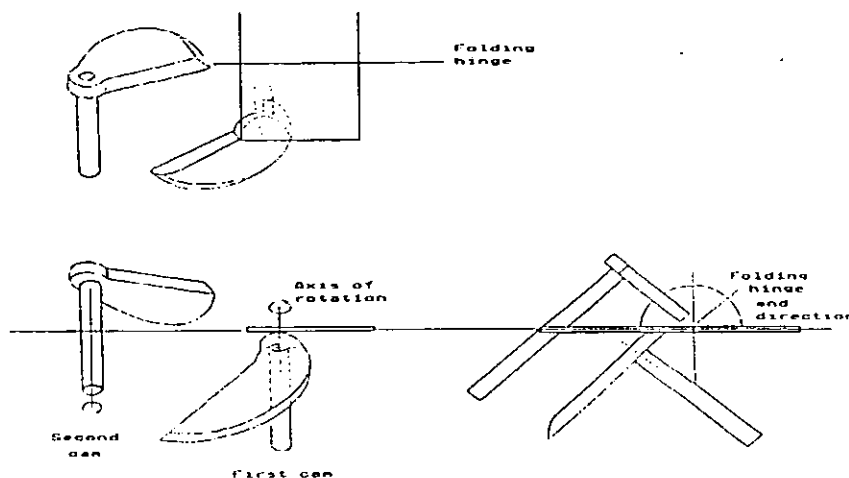


Fig. 6.6 Twin cam assembly in operation.

6.4 APPRAISAL

The twin cam folding mechanism has been demonstrated to be a feasible folding alternative. Further improvements, however, are necessary for a fully operational cam system.

At present, a parabolic motion profile has been adopted for the cam design. Unfortunately, this kind of profile is responsible for sudden acceleration changes and is therefore prone to vibration. When running at high speed, not only the nominal acceleration but also its time derivative will become critical in the overall dynamic integrity of the cam system. The significance of this time derivative, or the 'jerking effect', has been a subject of investigation (refer to Olmstead [31], Hrones [14]), and the subsequent recommendation has been the modification of motion profiles which will minimize this jerking effect (see Chen [5]).

In addition to making provision for the high and impulsive acceleration changes, the cam's motion profile can be correlated with the folding resistance profile (see Figure 7.4 in later section), leading to a more sophisticated motion profile design. The idea is to dampen the buckling effect at the folding peaks (refer to Section 7.3) by means of a gradual cam motion: the result is a more controlled folding action.

The distance between the contact point and the folding hinge, i.e dimension 'c', has been chosen, though arbitrarily, within a reasonable scale range. For a prototype design, the dimension will need to take into consideration the largest possible blank size to be folded. The reason being that for larger case blanks, the centre of gravity in the case panel will be shifted further away from the folding hinge. If the location of the centre of gravity lies beyond some critical point, a short dimension 'c' together with a fast folding action will lead to accidental panel buckling at the point of cam contact. The choice for the length of 'c' will therefore have to be assessed in terms of the size and mass of the largest case blanks.

The cam mechanism can be dynamically balanced by "hollowing out" material from the planar cam structure. Inertia and aerodynamic problems are anticipated as folding by twin cams has to be completed in a much shorter period than by folding rails. In order to keep the cam inertia down to a minimum, material with a high strength-to-weight ratio will be a prerequisite.

Other problems such as ink smearing and mechanical synchronization will be inevitable. Brush fibres can be attached onto the periphery of the cams so as to compensate for the imperfect synchronisation between the cam and the case blanks. Options other than those related to rolling contact between the folding cam and the case panel will need to be investigated in order to avoid ink smearing.

6.5 CONCLUSION

The twin cam, another innovative design, has been examined as a folding alternative. In the twin cam design, the folding operation is divided into two stages, each of which is responsible for a fold of 90°. Rolling contact, an important feature if ink smearing is to be avoided, has also been incorporated into the design.

CHAPTER 7

REVIEW ON CREASING

Creasing is one of the fundamental stages in the case conversion process. How well the case is creased will directly affect the fold quality, and hence the strength of the case and its appearance. Essentially, creases are score marks along which folding will preferentially take place. Part of the creasing mechanism involves the weakening of the corrugation. Sufficient weakening is necessary for the board to fold along a predefined line; but when in excess, the case liners may tear, one consequence of which will be the lowering of the case compressive strength. It is not surprising therefore to find that much interaction exists between the creaser and the corrugated fibreboard.

Sporadic publications since the early 50's (see chronological summary at the end of this chapter) suggest that research into creasing has always been driven by the need to innovate. In particular, new creasing profiles have been developed and tested with increasing sophistication. Optimization is often achieved through experimenting with the appropriate design variables, such as the profile geometry and the depth of penetration. The lack of standard procedures, however, in assessing the crease quality has no doubt downplayed the importance of this one process.

This chapter examines the theory on creasing through looking at the interaction between the creaser and the case. This is followed by a review on previous research into the design and optimization of creaser profiles. The chapter is concluded with a survey on crease quality assessment.

7.1 CREASE THEORY

Creases on the corrugated fibreboards can be orientated perpendicular to or parallel with the corrugation. Perpendicular creases are responsible for the folding of the

top and bottom openings of a case, and are normally produced on the corrugator. Parallel creases, on the other hand, do not appear on the case until the conversion process, where the four vertical edges of a case will be defined by means of a rotary creasing blade. Here, only parallel creases are considered, as they are the ones produced in a case converter.

The mechanism for creasing relies on the compression of the corrugated structure and the definition of a score mark about which the case will subsequently fold. Compression enables the section thickness to be reduced, thereby, resulting in a compaction of the buckled flute medium between the liners. On a case converter or, more specifically, a flexo-folder gluer, this kind of mechanical straining will take place between a pair of creasing rolls. The score mark is in turn produced by the shape of the creaser, the design of which will be discussed in more details in the next section.

The corrugation structure derives its strength from a good stiffness-to-mass ratio. In other words, for an equivalent mass of board material, the corrugated board design will provide a higher bending stiffness than that of a normal sheet. The orientation of the corrugations is critical not only to the bending stiffness of the board, but also the crease performance. In parallel creasing, depending on the position of the crease relative to the flute structure and the creaser profile, different forces can be transmitted from the creasing tool to the corrugation.

Figure 7.1 illustrates an exploded view of a typical corrugation cross-section. The corrugation will be impaired to a different extent depending on where the creasing load acts in relation to locations 'A', 'B' or 'C'. Location 'C' has been arbitrarily chosen to be somewhere between the other two locations, which immediately suggests an asymmetric loading behaviour. During creasing, the inner liner or single-facer liner (as opposed to the outer or double-facer liner) will be subject to the most damage.

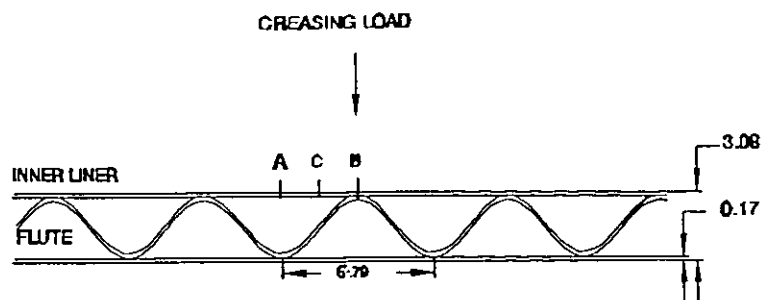


Fig. 7.1 B-flute corrugation with creasing locations.

As Vogelpohl [51] has pointed out, the creasing load, depending on the profile geometry and the point of load application, may compress the corrugation in such a way that sufficient tensile forces will lead to the tearing of the inner liner. On inspection, the ideal position for creasing would be at location 'A' - the mid-point between the two fluting peaks. This permits the creased liner to stretch evenly without undue tearing. Another crease location which bears symmetry is that of 'B', though a greater damage will be imposed onto the flute structure as a consequence of being compressed over a wider area. Location 'C' is considered the worst in that an asymmetric load pattern may lead to an unpredictable buckling behaviour. Both Vogelpohl [51] and Grebe [9] have acknowledged the high tendency to tear when placing the creasing load at location 'C'.

Since creasing and folding are inter-related, a word on the folding mechanism will clarify the role of a crease. Essentially, folding involves the buckling of the corrugation along the crease. As the fold approaches 180° , i.e. when the two case panels come close together, there will be a potential risk of crease wandering. This has been suggested by Grebe [9] who attributes the cause to the cramming of the flute material and the simultaneous stretching of the outer liner. The result will be a redistribution of stress between the inner and the outer liners, leading to a lateral deformation of the case panels.

Creasing mechanism also depends on the physical properties of the liners such as the Young's modulus, flexural stiffness of the board, bending stiffness of the liner component and friction of coefficient. But by far the most important is moisture

content. Vogelpohl [51] has alerted to the fact that a loss of moisture content in the liners will increase the possibility of tearing during the creasing stage. The behaviour of liners which are composed of shorter fibrous material (e.g chip liner) will be more susceptible to the fluctuation in moisture condition than that of liners with longer fibrous material (e.g Kraft liner). Not surprisingly, Vollmer [52] recommends a relative humidity of 60% as the creasing condition for the chip liners, and 55% to 60% for the Kraft liners.

Moisture condition can also affect another property of the liners - coefficient of friction. Runnability is a term for describing the physical behaviour of the flute medium when being passed through a labyrinth in order to be shaped into the corrugation profile. In the investigation into the problems associated with runnability, Thomas [50] has discovered that the coefficient of friction will go up by raising the moisture content in the liners. Whitsitt [55] has emphasized how important the coefficient of friction is to the runnability in a corrugator. More precise still, according to Sprague [45], the coefficient of friction actually decreases with surface contact temperature. Subsequently, Sprague concludes that the total effect of heat and moisture on the medium properties is very complex and has been poorly quantified in the past.

Machine characteristics also play an important role in fulfilling the mechanism of creasing. In addition to the roll profiles, which shall be discussed in the next section, speed is a machine parameter which governs the strain rate during the creasing process.

The high speed nature of the case-making process has been addressed briefly by Vogelpohl [51], who suggests that case liners may tear due to large accelerations and inertial forces. Quoting from other research evidence, a creasing speed of up to 15000 cases per hour (cph) is, according to Vogelpohl, still not high enough to cause tearing of the liners. Experimental evidence collected by McKee and Altmann [26] has shown that the creasing speed has no significant effect on the foldability and the crush resistance of cases. Present research evidence as

described in Chapter 3 also confirms the relative insignificance of the machine speed in the control of fishtailing.

7.2 CREASER PROFILE DESIGN

The choice of creasing profiles is often a subjective matter, and there is no such thing as a single standard profile. Among the various profiles which are commercially available, the single blade creasing profile is by far the most common in the corrugated industry. The blade is normally made of chrome-plated steel, and its female counterpart is moulded from polyurethane. The choice of having two different types of material for the creasing unit is such that, when the creasing blade acts on the corrugation, the polyurethane counterpart will provide compliance for the paper to form into the shape of the blade.

Other profiles have also been developed but their application has not been as widespread. A range of profile examples can be seen in Figure 7.2. The single-V profile is a forerunner of the single blade one, and has been extensively studied by Vogelpohl [51] and Buchanan [3]. Double-V, 3-point and 5-point profiles find their application in the creasing of thicker board types. Asymmetric profiles have also been reported by Vogelpohl [51], though it is not known to what extent the profiles have been successfully adopted in industry.

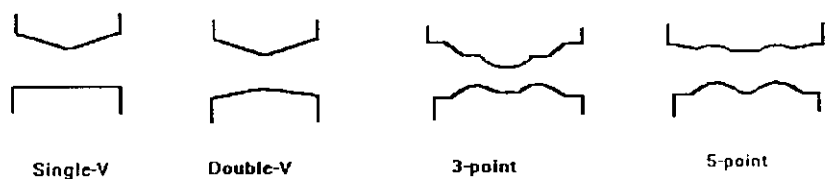


Fig. 7.2 Experimental creaser profiles.

The technique of double creasing is a totally different creasing concept. As documented by Hanlon [12] and Vogelpohl [51], double creasing relies on a pair of creasing tools which have been placed at a distance from each other. The gap

width thus created will be determined as a function of the board caliper. On imparting two score lines, the case will fold with two 90° corners with the tensile stresses in the outer liner being markedly reduced. There are problems, however, related to this type of creasing, e.g dimensional inaccuracy, case strength and appearance. Two sets of creasing shafts, as quoted by Shulman [43], have been used for producing wide creases on case blanks, but further development has been abandoned on account of weakened case corners. Experimental evidence in Chapter 9 will shed some light on this subject matter.

Crushing prior to creasing is another way of creasing cases which are more than one-board thick. Rolls with rounded off edges, or in the form of barrel-like shapes are the preferred norms. From his experiments, Vogelpohl [51] has concluded that a symmetric barrel-shaped crush profile gives the best performance. It is also recommended that crushing must not be too intense, or else subsequent creasing will not produce a sharp fold line. The trade-off with pre-crease crushing, however, is a reduction in the compressive strength of the case. Evidence put forward by Buchanan [3] has highlighted the fact that crushing before creasing with a 3-point profile can reduce the case compressive strength by as much as 25%.

Past research into the development of creasing profiles took the form of experimenting with various shapes and profile combinations. Single- and double-V, 3-point, 5-point, round, asymmetric profiles were among those investigated by McKee [26], Buchanan [3] and Vogelpohl [51]. The profiles were all standard in that they had been accepted by industry and were readily available on the market. Paradoxically the existence of more than one "standard" profile was a controversial matter and could only be resolved by the customers themselves.

In 1980, Grebe [9] broke away from the approach of comparative study on standard creaser profiles. Instead, through a series of factorial experiments, Grebe managed to identify those factors and geometrical dimensions that were critical to the crease performance. Single creaser profiles were tried out with and without

female rubber counterform. Factors such as the slot width on the female counterform, the depth of the slot and the compression ratio were assessed in terms of the accuracy of fold at 90° and 180°, the form and the consistency of the crease. A crease would be considered inaccurate when excessive straying took place between the crease and the line of fold. Crease consistency was expressed in terms of the extent of damage due to tearing. Edge exactness and curvature, collectively known as the form of a crease, were judged by visual inspection. Results showed that the quality of the board liners was equally important in as far as the crease performance was concerned. Only boards with high quality liners were found capable of withstanding the tearing forces induced by the creaser profile.

7.3 CREASE QUALITY ASSESSMENT

As yet, there is no standard method for assessing the crease quality of a case. However, tests on crease quality can be categorized into the following subgroups: strength, damage-related and appearance.

Top-load compressive strength is by far the most frequently quoted in respect of the end-use requirements in the corrugated fibreboard industry. This can be explained by the fact that the predominant mode of case failure is due to compression rather than tension, and this applies equally to the creasing and folding operations. Johnson et al. [19] has reported that on compression, the case reaches its maximum load when the combined board fails at or near the vertical creases of the panel.

The top-load compressive strength, according to Whitsitt [56], is directly related to both the edge-wise compressive strength and the flexural stiffness of the case (flexural stiffness being the product of the moment of inertia and the Young's modulus). Figure 7.3 shows a typical compression curve using the edge-wise compressive strength test. More to the point, McKee et al.[28] have shown that the edge-wise compressive strength is three times more important than the flexural

stiffness, on the basis of comparing the individual contribution to the overall case compressive strength.

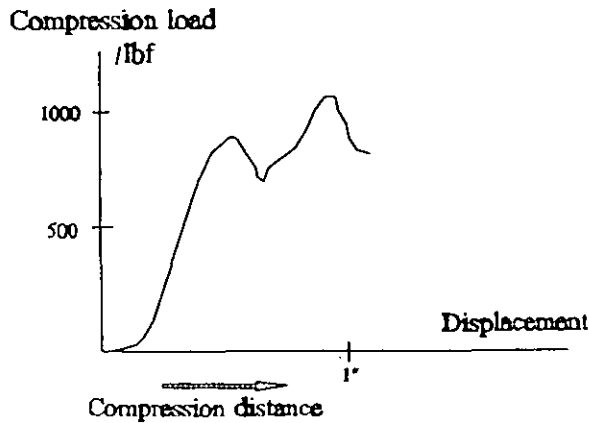


Fig. 7.3 Edge-wise compression curve.

Creaser profile is also believed to play a part in the compressive behaviour of a case. Buchanan [3] has noticed that the compressive strength of a case with glued flaps folded in position can fall to between 80 and 90 % of that of a comparable tube, i.e. one which has no flaps and therefore no horizontal creases. The 10 to 20 % strength reduction may reflect the importance of the horizontal creases, but its significance in relation to vertical creases still needs some clarification. On testing a range of similar creaser profiles, McKee et al. [26] has demonstrated that they have little effect on the case's compressive strength. On a cautionary note, therefore, case compression tests must not be treated as definitive in the assessment of crease quality.

Folding resistance is another strength measure closely associated with creasing. Ruvo et al. [41] has defined creasability of a board as the ability of the creasing operation to reduce the folding resistance. Special folding rigs have been used to measure the folding resistance of the corrugated fibreboards from 0° to the final close position of just under 180° . Vogelpohl [51], Grebe [9] and McKee [26] have all made extensive use of such apparatus and with much success. The result is a force-angular displacement plot as shown in Figure 7.4.

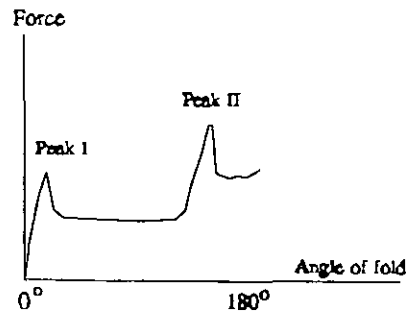


Fig. 7.4 Force-angular displacement plot.

The first peak, normally lies between 8° and 16° , measures the force required to break the crease; its magnitude is a function of the corrugation type and the flatness of the material. Buchanan [3] has been able to show that this peak value increases with liner caliper and decreases with the depth of creaser penetration. The first peak, as discovered by Vogelpohl [51], also provides information on the crease formation, the material type and its dampness. The folding resistance then drops to a constant level before it picks up again at around 135° .

The second peak lies towards the end of the folding process, i.e between 150° and 165° , and its magnitude is much greater than the first one. Vogelpohl suggests that this second peak depends on where the corrugation is attacked by the creaser. An account by McKee et al. [26] has shown that the folding resistance will increase as soon as the board is folded to the point where the inside liners on each panel begin to butt against each other in the creased region. The folding resistance continues to go up until the weaker of the two panels becomes unstable. Consequently, a redistribution of stresses will be accompanied by the deformation of the inner liner and the flute medium. A high second peak is undesirable, as it will encourage the constant reopening of the glued flaps immediately after they have been bonded together.

Quality assessment methods which are damage-related can be grouped into those of liner tearing and false creasing. Creasibility has been defined by Vogelpohl [51] as the minimum gap width at which the inner liner of a certain board caliper will not tear. An alternative measure can be expressed in terms of the compression ratio as

shown in Figure 7.5. Note that the definition will also take into account any gap reduction due to pre-crease crushing. However, negative gap width is inevitable as the male creaser may dig into the female polyurethane rolls.

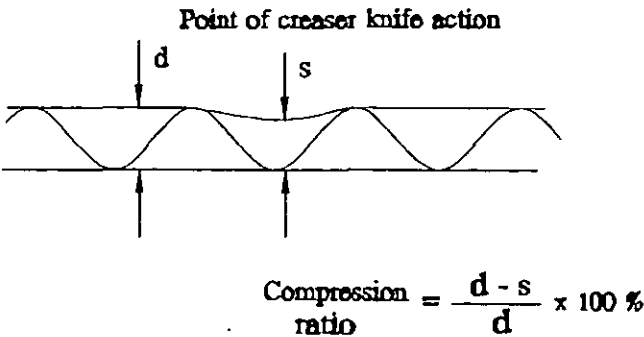


Fig. 7.5 Compression ratio definition.

False creasing, as briefly described by Vogelpohl [51], poses the problems of producing large edge radius, high tensile stress in the outer liner and poor dimensional accuracy once the case is folded.

Case appearance is vital from the aesthetic and the strength point of view. Position of edges, cracking of liners, pressure ridges on narrow folds and crumpled internal rib on wide folds are all examples of case appearance criteria. Apart from the position of edges, which can be assessed using the fishtailing measure as defined in Chapter 3, case appearance can only be treated in a subjective manner.

As a concluding remark, it must be emphasized that the crease quality also depends on other preconditions. For example, Edholm et al. [7] have found that a crease will lose its effectiveness if creasing a piece of warped corrugated fibreboard. Furthermore, there is no point in producing a good crease when the folding mechanism does not match up in terms of quality standard.

Chronological summary of major creasing research to date:

1956 McKee and Altmann [26] compared different creasing wheel contours and their effect on the foldability and compressive characteristics of corrugated boxes. The quality of the creased samples was quantified in terms of the folding resistance.

1963 Buchanan [3] experimented with several types of creaser profiles, fluting medium and liners. The compressive strength and the foldability of cases with both parallel and transverse creases were compared in a series of factorial experiments.

1980 In Munich Fachhochschule, Grebe [9] also resorted to factorial design for his 3-point creaser profile experiment. The properties monitored were the fold accuracy (relative to the crease location), no-tear consistency and the final form. Grebe then quantified the fold quality by means of a special folding rig, which had the capability of measuring the rate of folding, the angular displacement and the folding moment.

1987 Major research into creasing was conducted by Vogelpohl [51] at the Munich Technical University. The research was funded by companies in the packaging industry and the Research Council for Packaging and Food Technology. Vogelpohl investigated the conditions responsible for better creases. Among other design parameters, creasers with different number of knife edges were tried out on B- and C-flute samples. Once creased, the boards were then folded on a pneumatic folding rig. The results were found to be in good agreement with those obtained by Grebe.

CHAPTER 8

CREASER DEVELOPMENT

The development of new creaser profiles has traditionally relied on the empirical and comparative study of profile configurations. Any theoretical analysis without taking into account the complex behaviour of paper will be penalized on the grounds of over-simplification. But to what extent is the creasing effect due to the corrugation and the inner liner individually?

Software simulation is a powerful design tool. Finite element analysis enables creasing conditions like the loading and profile configurations to be modelled in a virtual environment. Most proprietary software, however, is still inadequate in as far as modelling a fibrous composite like paper is concerned.

This chapter commences with a geometrical analysis of the single blade and the twin roll creaser profiles. The analysis proceeds with the hypothesis that the fluting medium is significantly more elastic than the inner liner, hence ensuring the inner liner to be the first to fail as a result of tearing. Design parameters generated from the analysis are then evaluated in the finite element model. Results from the theoretical and the finite element models are subsequently validated using the Electronic Speckle Pattern Interferometry (ESPI). The chapter is concluded with a summary of how well the theoretical analysis and modelling have correlated with the creasing mechanism in reality.

8.1 GEOMETRICAL ANALYSIS

Crease quality depends on the mechanical creasing action and the material properties of both the liners and the fluting medium. Variation in the crease quality may arise as a result of the rheological properties and the fibrous composition of paper. What is predictable, however, is the mechanical interaction

between the creasing profile and the corrugation structure, the latter of which may, under certain circumstances, be treated like a truss.

This section is an attempt to create a geometrical model of creasing. Major assumptions, forming the basis of the model, are first of all stated. The single blade and the twin roll creaser profiles will then be studied from a geometrical perspective. In order to give a fair representation of the market demand, both B- and C-flute boards will be considered in the analysis. Design parameters are then quantified for subsequent analysis and experimentation.

8.1.1 Assumptions

The following assumptions have been made in order to analyse a piece of corrugated board as if it were a truss:

- i) Displacement loading must be chosen within the pre-buckling regime. In other words, only small compression is allowed; for as soon as buckling sets in, paper will behave inelastically. Besides, the finite element analysis in the next section can only handle a linear mode of behaviour.
- ii) Creasing conditions such as temperature and relative humidity are kept constant, which means that any fluctuation in the paper properties due to external factors can be ignored.

Note that the above assumptions do not, in any way, concern the physical properties of paper.¹ What the assumptions try to achieve is to address the creasing mechanism from a structural rather than a material viewpoint. Only an experimental verification, as described in Section 8.3, will prove whether or not this is a justifiable approach.

8.1.2 Single blade creaser

Creaser profiles come in various styles, but the most common is the single blade profile. Figure 8.1 shows the design of the single blade creaser.

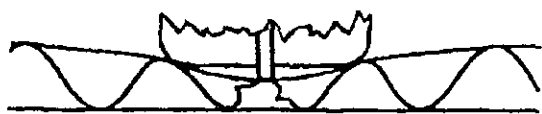


Fig. 8.1 Single blade creaser.

The single blade creaser is extensively used in the creasing of the single- and double-wall boards, and pre-crushing is often a pre-requisite for the latter.

The worst scenario for the single blade design is when it penetrates right down to the trough of the corrugation at location 'A'. As shown in Figure 8.2, if the flute structure remains intact during the creaser penetration, then the inner liner will have split long before it reaches the bottom of the corrugation (see Appendix 8a for a simple theoretical treatment). In practice, however, as the creaser comes down onto the corrugation, the flutes will collapse due to the crushing action of the shoulders, before any tearing can occur in the inner liner. The importance of crushing will be emphasized repeatedly in later sections.

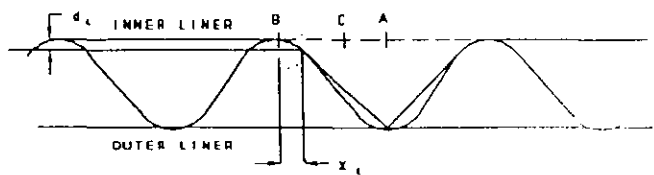


Fig. 8.2 Worst creasing scenario.

8.1.3 Twin roll creaser

The variable gap twin roll creaser, as shown in Figure 8.3, is an inversion of the single blade creaser. Instead of actively creasing the corrugated board by means of a blade, the twin roll creaser relies on the gap between the rolls to perform the creasing operation. As the conical shoulders of the twin roll come down onto the corrugated board, the edges which form the twin roll gap will imprint two score marks onto the board.

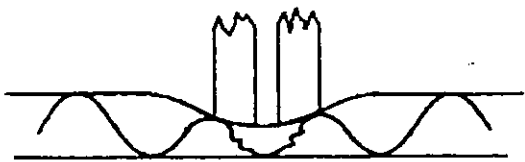


Fig. 8.3 Twin roll creaser.

According to Werner [54], part of the creaser profile must possess at least one acute corner for good crease definition. Sharp creases, however, do not necessarily guarantee a good fold, as uncontrolled flute buckling may arise due to an insufficient crease width. In this case, the crease width is determined by the separation between the two score marks. One immediate question is: how to set the twin roll gap? Should it be based on the board caliper or the flute geometry?

When a piece of board is folded with a crease width, or in this case the score-to-score dimension, equivalent to the board caliper, the case edge will be chamfered as shown in Figure 8.4.

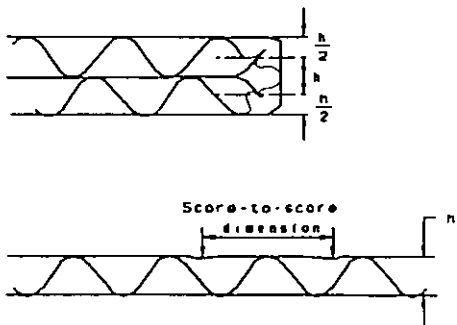


Fig. 8.4 Fold with two score marks.

The ease of fold from having two score marks may, however, be offset by a poor case appearance and extra material cost. If, on the other hand, the score-to-score dimension is a function of the flute geometry, then the interaction between the twin roll creaser profile and the corrugation will be the deciding factor. Assuming rigid support for the corrugation, it can be shown that there is a maximum twin roll gap beyond which tearing of the inner liner will take place (see Appendix 8b). The angle for the conical shoulders on the twin roll is seen to be a function of the liner strain rate and is independent of the flute pitch; its value is found to be approximately 10°. Table 8.1 summarizes the design parameters as derived geometrically for the twin roll creaser. Theoretical values for the creaser gap width with or without slipping are based on the maximum permissible depth of creaser penetration beyond which tearing becomes inevitable.

Table 8.1: A summary on the twin roll gap settings and total creaser width.

Flute type	Gap width without slipping	Gap width with slipping	Creaser width
B-flute	0.59 mm	1.79 mm	17.04 mm
C-flute	0.75 mm	2.26 mm	25.52 mm

There is a strong argument for slippage to occur between the inner liner and the creaser. For if there is no slippage, tension within the inner liner will not be evenly distributed. In this way, the current single blade design will not be able to penetrate to its effective depth without inducing tearing - the effective depth being the protrusion of the blade as measured from the creaser shoulder level. This is true provided that creasing is conducted at ambient temperature and relative humidity. Increasing the moisture content of the inner liner, however, will raise the friction coefficient between the creaser and the liner to the extent that slippage may not take place. The effect of moisture content on friction coefficient can be found in various publications by Thomas [50], Vogelpohl [51] and Vollmer [52] (see Section 7.1).

8.2 FINITE ELEMENT ANALYSIS

Finite element analysis is a computational technique for obtaining approximate solutions to any continuum problem. Section 2.1.2, however, has pointed to the danger of treating paper as a continuum material. If, on the other hand, the creasing mechanism depends mainly on the interaction between the creasing blade and the corrugation structure as a whole, then the individual liners which make up the corrugated board can be regarded as having continuum behaviour with constant elasticity.

This section describes a finite element analysis on the single blade and twin roll creasers using a proprietary software package called Mechanica [29]. The objective is to examine the effect of placing a single blade creaser on each of the three locations 'A', 'B' and 'C' along the corrugation as defined in Section 7.1. Results will then be compared with those from the twin roll creaser.

8.2.1 Model design

The corrugation model was taken from a photograph on a B-flute cross-section. A B-flute sample was first of all cut by a high power laser before it was photographed, magnified and photocopied onto a transparency. By means of a Fourier transform software package, the corrugation structure was traced off from the transparency and reproduced onto a personal computer. Only the first ten harmonics of the sixty Fourier waveforms generated were chosen (see Appendix 8c) for the corrugation model.

Following a series of numerical substitutions and re-scaling, the x- and y-coordinates for the waveform were calculated and re-plotted by means of a CAD package.

Properties for the final model were as follows:

Structure - B-flute corrugation; 9 flutes in all (10 troughs and 9 peaks)

Element type - 2D shells

Average shell size - 0.16954 mm x 0.2 mm

B-flute board caliper - 2.5 mm

Liner & flute thickness - 0.2 mm

Young's modulus E - $1.3 \times 10^9 \text{ Nm}^{-2}$

Liner density - 0.625 kgm^{-3}

Poisson's ratio - 0.3

N.B. The material properties were based on those of the 125 gm^{-2} chip liner.

Locations 'A' and 'B' could easily be identified in the model, since they were both symmetrical in relation to the corrugation. With location 'C', however, a point had to be arbitrarily chosen between 'A' and 'B'. A position some 7 elements (or 1.186 mm) away from the nearest peak 'B' was subsequently defined for location 'C'.

The loading condition was such that a single blade of 0.6 mm wide would be represented by 4 elements, all being subjected to a downward displacement of 0.2 mm. Loading for the twin roll creaser was slightly more sophisticated in that the conical shoulder was represented by a 7-element long 2D shell. One end of the element, being the tip of half a twin roll creaser, was constrained in both the y- and the rotational z-directions. The former provided the required downward displacement, while the latter enabled the angle of the conical shoulder to be modelled at an inclination of 10° . The twin roll was separated with a gap width of 0.59 mm (see Table 8.1), equivalent to approximately 4 element length. Slippage was allowed by freeing the loaded elements in the x-direction.

8.2.2 Procedures

In order to simulate the reaction due to the creasing action, the base of the structure, i.e the outer liner, was restrained in the vertical direction. The present software could only simulate the constraint as if the outer liner was glued to the lower roll. To overcome this limitation, which was essentially a boundary element problem, a constraint strategy was devised as in Figure 8.5:

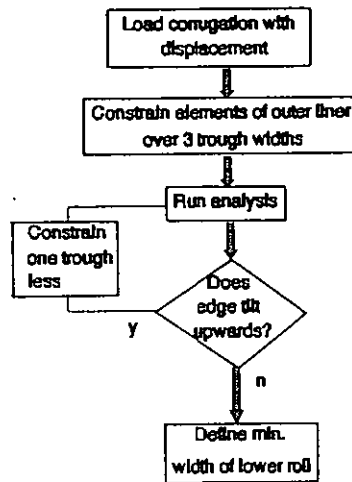


Fig. 8.5 Constraint strategy.

Once the constraint conditions for the outer liner were met, the corrugation was ready for loading. The first analysis modelled a single blade penetrating to a depth of 0.2 mm at locations 'A', 'B' and 'C'. This was followed by another analysis performed under the same conditions but with the twin roll creaser at a gap width of 0.59 mm.

The following graphical displays were obtained for analysis:

1. x-displacement contour graph
2. y-displacement contour graph
3. membrane strain energy fringe plot
4. maximum principal stress fringe plot

From both the displacement graphs, the loading and constraint conditions were checked if they had been applied correctly. Membrane strain energy, representing the work done on the 2D shell elements by the displacement load, would indicate locations where buckling would most likely take place. Due to the nature of loading, bending rather than tensile stress would constitute the main component in the maximum principal stress. Where there was a high level of stress concentration, tearing would be anticipated.

8.2.3 Results

Results, in the form of colour graphical plots, can be found in the following labelled plates:

Single blade creaser:

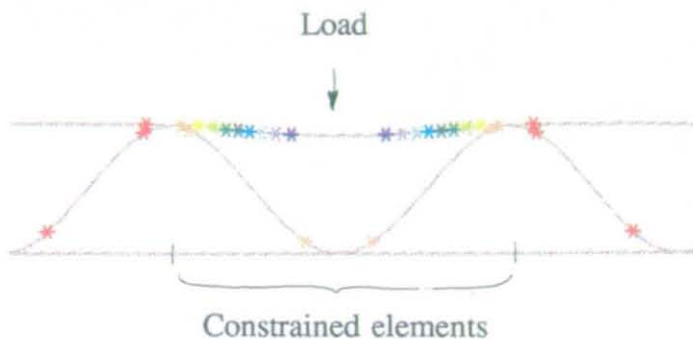
Loading location	Plate no.	Plate label
A	2	load_A
B	3	load_B
C	4, 5	load_C

Twin roll creaser:

Loading location	Plate no.	Plate label
A	6	twin_A
B	7	twin_B
C	8	twin_C

A blown-up y-displacement plot for 'load_C' is also included for showing the end deflections of the corrugation. Scale for the deflections is 1:1. The sign convention on the graphical display complies with the cartesian coordinate system.

Min -2.0000E-04
Deformed Original Model
Max Disp +2.0000E-04
Scale 1.0000E+00



load_A

A +1.709E-05

X -4.679E-06

Y -2.633E-05

Z -4.804E-05

E -6.975E-05

F -9.145E-05

G -1.132E-04

H -1.349E-04

I -1.566E-04

J -1.783E-04

Max +9.674E-06
Min -3.659E-06
Deformed Original Model
Max Disp +2.0000E-04
Scale 1.0000E+00



load_A

A +7.921E-06

X +6.163E-06

Y +4.405E-06

Z +3.649E-06

E +8.886E-07

F -8.695E-07

G -2.627E-06

H -4.386E-06

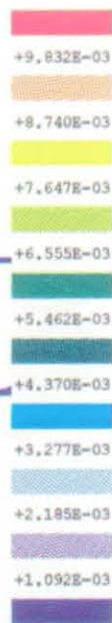
I -6.144E-06

J -7.902E-06

Membrane S.E.
Max +1.0925E-02
Min +0.0000E+00
Deformed Original Model
Max Disp +2.0000E-04
Scale 1.0000E+00



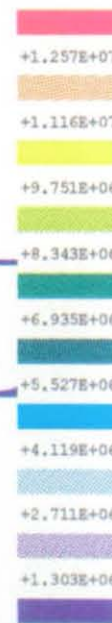
load_A



Stresses Max Print
Max +1.3975E+07
Min -1.0445E+05
Original Model



load_A

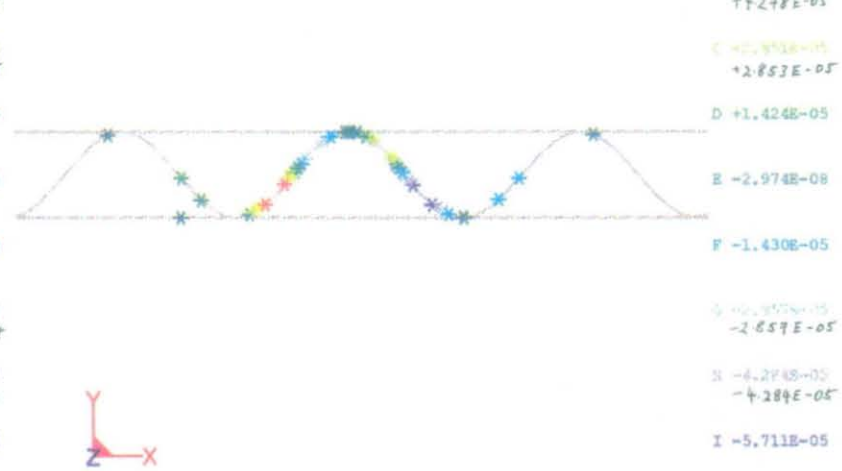
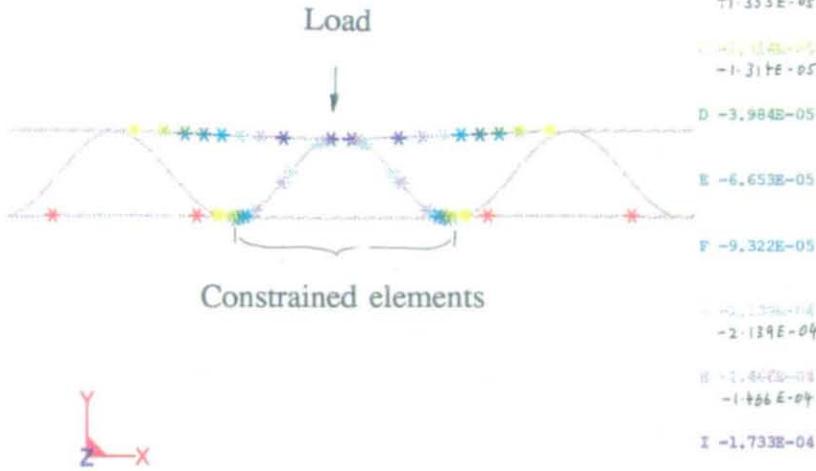


Min -2.0000E-04
Deformed Original Model
Max Disp +2.0000E-04
Scale 1.0000E+00

A +4.025E-05

Min -7.137E-05
Deformed Original Model
Max Disp +2.0000E-04
Scale 1.0000E+00

A +5.705E-05



88

Membrane S.E.
Max +1.419E+01
Min +0.0000E+00
Deformed Original Model
Max Disp +2.0000E-04
Scale 1.0000E+00

+1.278E+01

+1.136E+01

+9.937E+00

+8.518E+00

+7.098E+00

+5.679E+00

+4.259E+00

+2.839E+00

+1.420E+00

Stress Max Prin
Max +5.290E+07
Min -3.848E+06
Deformed Original Model
Max Disp +2.0000E-04
Scale 1.0000E+00

+7.423E+07

+6.555E+07

+5.688E+07

+4.820E+07

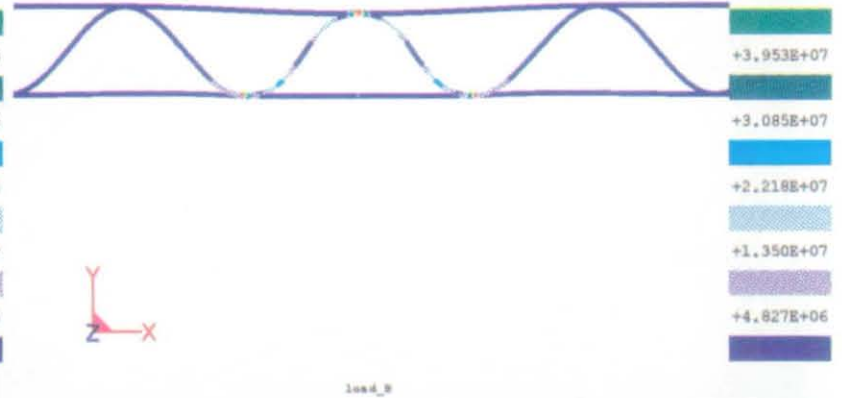
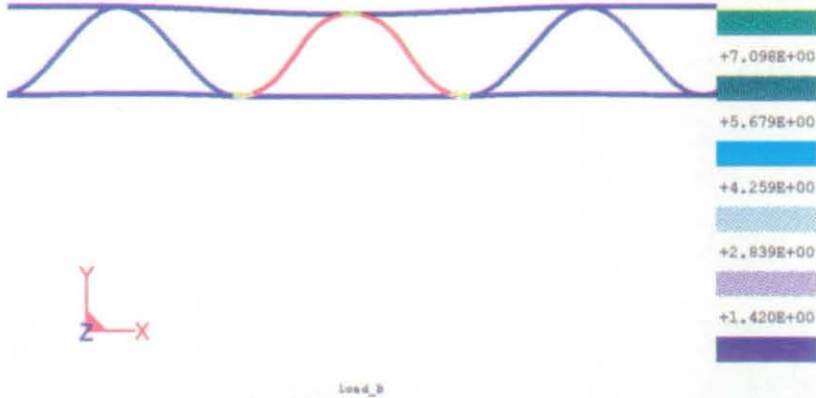
+3.953E+07

+3.085E+07

+2.218E+07

+1.350E+07

+4.827E+06



Max +2.2985E-04
Min -2.0000E-04
Deformed Original Model
Max Disp +2.2985E-04
Scale 1.0000E+00

A +1.869E-04

B +1.879E-04
+1.479E-04

C +2.009E-04
+2.009E-04

D +5.791E-05

E +1.492E-05

F -2.806E-05

G -7.109E-05
-7.109E-05

H -1.210E-04
-1.140E-04

I -1.570E-04

Max +6.153E-05
Min -3.624E-07
Deformed Original Model
Max Disp +2.2985E-04
Scale 1.0000E+00

A +5.528E-05

B +4.903E-05

C +4.278E-05

D +3.653E-05

E +3.028E-05

F +2.403E-05

G +1.779E-05

H +1.154E-05

I +5.286E-06

Load

Constrained elements



load_0



load_0

68

Membrane S.E.
Max +1.7262E+00
Min +0.0000E+00
Deformed Original Model
Max Disp +2.2985E-04
Scale 1.0000E+00

Stress Max Print
Max +7.062E+07
Min -1.4482E+06
Deformed Original Model
Max Disp +2.2985E-04
Scale 1.0000E+00

+1.554E+00

+1.381E+00

+1.208E+00

+1.036E+00

+8.631E-01

+6.905E-01

+5.179E-01

+3.452E-01

+1.726E-01

+7.062E+07

+6.261E+07

+5.460E+07

+4.660E+07

+3.859E+07

+3.058E+07

+2.257E+07

+1.457E+07

+6.559E+06



load_0



load_0

Displacement I
 Max +2.2985E-04
 Min -2.0000E-04
 Deformed Original Model
 Max Disp +2.2985E-04
 Scale 2.0000E+00

A +1.869E-04

B +1.439E-04
 +1.439E-04

C +1.009E-04
 +1.009E-04

D +5.791E-05

E +1.492E-05

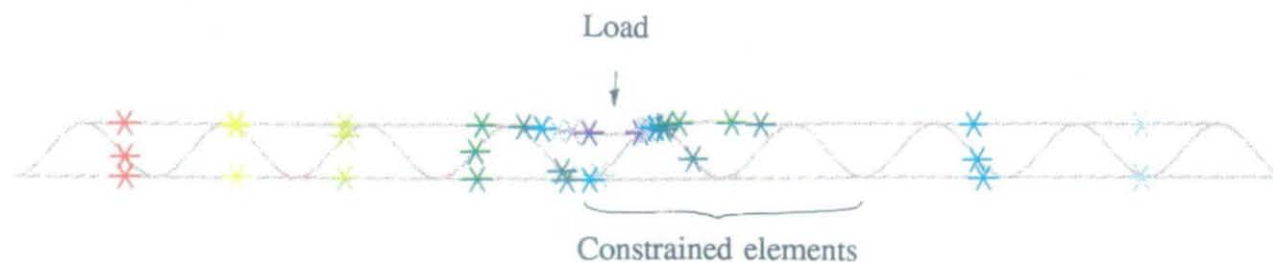
F -2.806E-05

G -7.105E-05
 -7.105E-05

H -1.140E-04

I -1.570E-04

90



load_C

Max +1.3581E-05
Min -2.2959E-04
Deformed Original Model
Max Disp +2.2959E-04
Scale 1.0000E+00

Load



Constrained elements



twi_A

A -8.936E-06

B -2.345E-05

C -5.747E-05

D -8.249E-05

E -1.070E-04

F -1.315E-04

G -1.560E-04

H -1.806E-04

I -2.051E-04

Max +2.7257E-06
Min -2.7316E-06
Deformed Original Model
Max Disp +2.2959E-04
Scale 1.0000E+00



twi_A

A +2.180E-06

B +1.634E-06

C +1.088E-06

D +5.428E-07

E -2.973E-09

F -5.487E-07

G -1.097E-06

H -1.640E-06

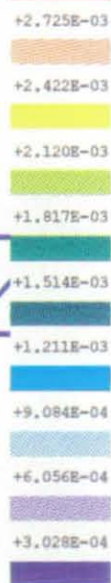
I -2.186E-06

91

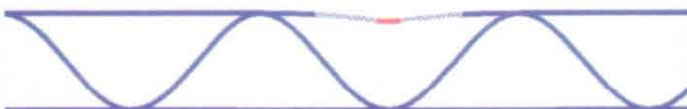
Membrane S.E.
Max +3.0280E-03
Min +0.0000E+00
Deformed Original Model
Max Disp +2.2959E-04
Scale 1.0000E+00



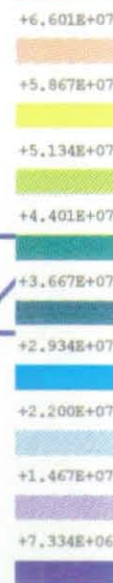
twi_A



Stress Max Princ
Max +7.3342E+07
Min -8.0835E+02
Deformed Original Model
Max Disp +2.2959E-04
Scale 1.0000E+00



twi_A



Max +6.863E-05
Min -2.1547E-04
Deformed Original Model
Max Disp +2.1547E-04
Scale 1.0000E+00

A +4.023E-05

Max +7.6484E-05
Min -7.854E-05
Deformed Original Model
Max Disp +2.1547E-04
Scale 1.0000E+00

A +6.118E-05

Load

+1.182E-05

+4.588E-05

-1.66E-05

+3.058E-05

D -4.501E-05

D +1.527E-05

E -7.342E-05

E -3.078E-05

F -1.018E-04

F -1.533E-05

Constrained elements

-1.302E-04

-3.064E-05

-1.586E-04

-4.594E-05

I -1.871E-04

I -6.124E-05



twin_B

twin_B

92

Membrane S.E.
Max +1.621E+01
Min +0.0000E+00
Deformed Original Model
Max Disp +2.1547E-04
Scale 1.0000E+00

Stress Max Prin
Max +1.2609E+08
Min -4.1413E+06
Deformed Original Model
Max Disp +2.1547E-04
Scale 1.0000E+00

+1.459E+01

+1.131E+08

+1.297E+01

+1.000E+08

+1.135E+01

+8.702E+07

+9.730E+00

+7.400E+07

+8.108E+00

+6.097E+07

+6.487E+00

+4.795E+07

+4.865E+00

+3.493E+07

+3.243E+00

+2.191E+07

+1.622E+00

+8.882E+06



twin_B

twin_B

Max +2.1172E-04
Min -2.2959E-04
Deformed Original Model
Max Disp +2.3042E-04
Scale 1.0000E+00

A +1.676E-04

Max +5.3692E-05
Min -9.4164E-07
Deformed Original Model
Max Disp +2.3042E-04
Scale 1.0000E+00

A +4.823E-05

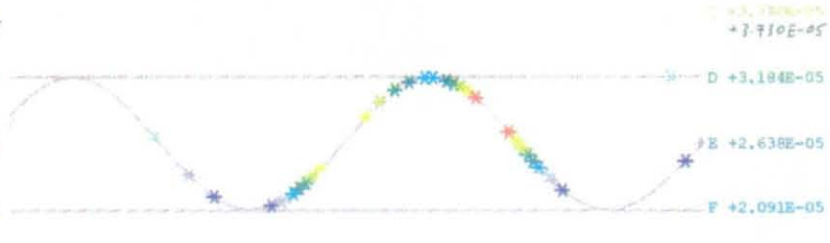
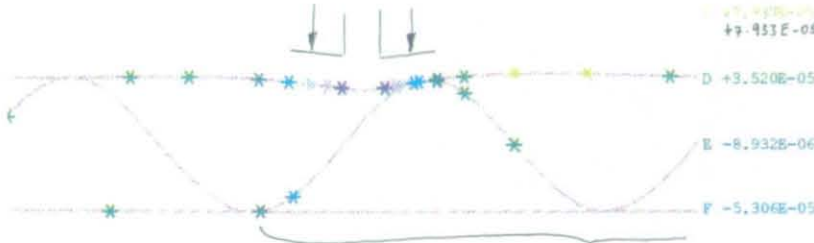
Load

B +1.215E-04

C +7.933E-05

B +4.297E-05

C +3.130E-05



Constrained elements

D +3.520E-05

E -8.932E-06

F -5.306E-05

D +3.184E-05

E +2.638E-05

F +2.091E-05



twin_c

twin_c

93

Membrane S.E.
Max +8.151E-01
Min +0.0000E+00
Deformed Original Model
Max Disp +2.3042E-04
Scale 1.0000E+00

+7.336E-01

+6.521E-01

+5.706E-01

+4.891E-01

+4.076E-01

+3.261E-01

+2.445E-01

+1.630E-01

+8.151E-02

Stress Max Print
Max +7.3410E+07
Min -9.9248E+05
Deformed Original Model
Max Disp +2.3042E-04
Scale 1.0000E+00

+6.597E+07

+5.853E+07

+5.109E+07

+4.365E+07

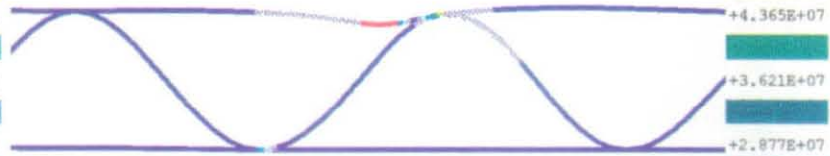
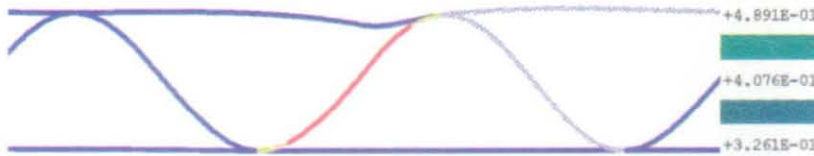
+3.621E+07

+2.877E+07

+2.133E+07

+1.389E+07

+6.448E+06



twin_c

twin_c

8.2.4 Analysis

Before interpreting the results, the finite element model can be verified by means of simple checks. For example, the y-displacement at the point of load application should be the same as the blade penetration. In cases where the load had been symmetrically applied relative to the flute, the x- and y-deflections should also exhibit symmetry.

a) Single blade creaser

Referring to plot 'load_A', it can be seen that a mid-span load will lift the sides of the corrugation off from the lower roll as a result of bending moments about the two flute peaks. The flanks of the flute will be compressed downwards and pushed away from each other. Compression at location 'B', as shown in plot 'load_B', enables the two troughs to act as pivots, as the two neighbouring peaks are being pulled towards each other. Again, two sides of the corrugation will leave the lower roll, as indicated by the displacement contours at the base of the corrugation. But compared with 'load_A', the flanks of the loaded flute will deform more, as the S-shape becomes more prominent.

Plot 'load_C', on the other hand, provides some insight into the asymmetric loading behaviour of the corrugation. From the enlarged y-displacement plot, one side of the corrugation is found to tilt upwards, while the other side curves downwards, despite the support as provided by the lower roll. Except for the base elements, the x-displacements are all positive, implying a uni-directional shear along the whole corrugation. One possible explanation is as follows: as a bending moment is applied about the flute peak which is nearer to the point of load application, that part of the flute above the line O-O will be given an anti-clockwise twist. On superposing with the depression due to the downward load, the net result will be a lateral shift in the positive x-direction.

The highest membrane strain energy is recorded in 'load_B', whereas 'load_A' shows a distribution of strain energy over a much wider area. Both 'load_A' and 'load_B' exhibit even distribution of strain energy, which suggests symmetrical buckling behaviour, as compared to an uneven buckling failure in 'load_C'.

When loading at location 'B' and 'C', the maximum principal stresses are of similar order of magnitude. High stress concentrations can be found at the tip of the single blade creaser. Lower maximum principal stress in 'load_A' may be due to the ability for more elements to bend freely.

b) Twin roll gap creaser

In the case of 'twin_A', the sides of the corrugation show no sign of an upward tilt. Instead, the flanks can be seen to have been pushed symmetrically away from location 'A' in the x-direction as in 'load_A'. The magnitude in the x-displacement, however, is less than that of the single blade creaser. This may be due to the way the inner liner deflects when being loaded with a single blade, and can be explained as follows: consider the deflection of the inner liner due to a single blade load, as shown in Figure 8.6.

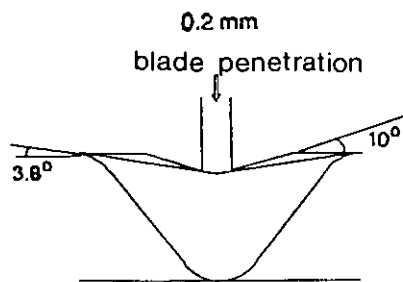


Fig. 8.6 Creaser profile model.

For a B-flute configuration at a creaser penetration of 0.2 mm, the angle of deflection of the elements in contact with the adjacent flute peaks is calculated to be 3.8° . But with a twin roll creaser, the profile angle of 10° is simulated by

orientating a long element about the tip of the creaser. Consequently, the bending moments responsible for pushing the flanks apart as in 'load_A', will be counteracted by the pulling in of the neighbouring flute peaks. The net result is a smaller x-displacement compared with that of the single blade.

The same line of reasoning can be used for explaining the significant difference in the maximum principal stresses. In the twin roll arrangement, the elements within the gap are subject to higher bending stresses because of the larger profile transition (10° conical profile compared with 3.8° for the single blade). Much lower membrane strain energy is experienced by the inner liner and the flute in the case of the twin roll creaser. Intuitively, the inner liner within the twin roll creaser gap will tend to tear, whereas the preferred mode of failure is flute buckling when a single blade is applied at location 'A'.

On loading at location 'B', evidence from the plot 'twin_B' suggests that more upward deflection and higher maximum principal stress are experienced than in the case of the single blade loading. Again, this can be due to the large profile angle transition of 10° as explained previously. The x-displacement plot reveals a more distorted S-shaped flank, but the magnitude for the membrane strain energy is similar to that of the single blade load.

The x- and y-displacements for the loading condition in 'twin_C' bear resemblance to those of the single blade loading. It is interesting to note that, when creasing at location 'C', the maximum principal stress for the single blade is, for the first time, higher than that for the twin roll creaser. One possible reason is due to the short section of liner between the position 'C' and the peak, giving a sharper profile transition. Elements at the tip of the creaser will, in the case of load_A, be forced to wrap over a larger angle and constrained by a higher bending stress.

To summarize, the twin roll creaser is considered better than the single blade creaser in terms of producing lower membrane strain energy in the corrugation structure. A lower maximum principal stress, the main component of which is due

to bending, is also expected from the twin roll creaser when creasing at location 'C'. However, when it comes to creasing at locations 'A' and 'B', a higher maximum principal stress can be found in the section of the liner between the twin roll gap than in the case of the single blade. Where there is a high stress concentration, the liner will be more susceptible to tearing.

8.3 MODEL VERIFICATION USING ESPI

Important questions have been raised from the theoretical analysis and computer simulation of the corrugation structure. For example, how localized is the straining effect on the inner liner of the corrugation? Does sliding take place under the creasing blade? Certain assumptions adopted in the finite element model, such as the elasticity of paper, may also need to be scrutinized. This section describes the use of the Electronic Speckle Pattern Interferometry in the study of the planar displacement behaviour of corrugated fibreboards when subjected to a creasing load.

8.3.1 ESPI Theory

Speckle interferometry is an optical method designed to measure the displacement and shape of surfaces at sensitivities in the order of the wavelength of light. The method relies on the speckle effect which is a random interference pattern observed when coherent light is scattered from a rough surface. High coherence and intensity are required for the light source, hence the use of laser illumination.

Electronic speckle pattern interferometry, ESPI, is one speckle technique which utilizes a TV system for the detection, measurement and processing of speckle patterns in real time. The principle behind ESPI has been widely understood and documented in the field of applied optics (see Wykes [57] and Jones et al.[20]). By recording the speckle patterns before and after a displacement, and subtracting

the images electronically using the frame store facility on a video system, fringes will thus be correlated and ready for analysis.

A fringe order number 'n', which is directly related to the displacement, is obtained by counting the number of live fringes (i.e. those with zero intensity) passing a fixed point as the load is applied. Substituting 'n' into the following equations will give the out-of-plane and in-plane displacements respectively:

$$d_1 = \frac{1}{2}n\lambda$$

$$d_2 = \frac{n\lambda}{2\sin\theta}$$

where λ corresponds to the wavelength of the laser, and θ is the angle of incidence between the laser illumination and the surface normal. (For further details on the theoretical derivation, refer to Appendix 8d).

8.3.2 Objectives

The experiment was set out with the following objectives:

- i) To calibrate the interferometer with respect to the test rig.
- ii) To examine the strain behaviour of the inner liner when under the creasing action.
- iii) To verify the results from the finite element model.

Displacements obtained through ESPI must be checked against the actual micrometer displacements as an initial calibration. The second objective would focus on the localization effect of strain on the inner liner due to the structural composition, i.e, a sandwiched corrugation structure. More important was the verification of the finite element model: to see if it would correlate with the actual physical behaviour of a B-flute corrugated board.

8.3.3 Apparatus

The experimental jig, as shown in Figure 8.7, comprises two loading mechanisms: one for pulling the sample laterally and the other one for simulating the creasing action.

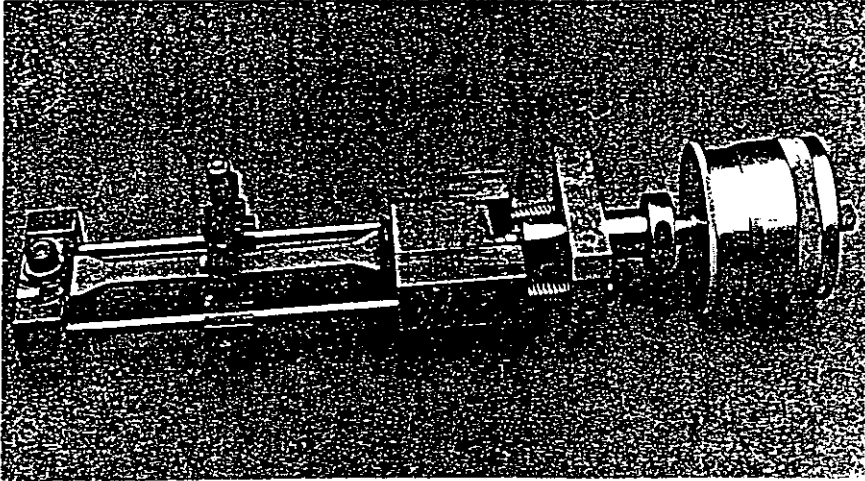


Fig. 8.7 Test jig for optical experiments.

The micrometer which controls the lateral strain has a resolution of ± 0.0002 mm and the range of travel is set to 10 mm, well above the experimental requirement. Resolution on the smaller micrometer, which is responsible for the vertical adjustment of the creasing blade, is limited to ± 0.01 mm on account of its available size range. Because of the limitation as imposed by the optical arrangement (essentially, clearance for the laser illumination), the smallest micrometer was chosen for the jig design.

B-flute board samples of grade 400 KT were cut into spatula shape by means of a 500 W CO₂ laser. Liners towards the ends of the samples were detached from the flute to allow for attachment. Normally, a more uniform surface reflectivity could be obtained by spraying the sample matt white; but in the case of paper samples, such action might significantly alter their mechanical properties.

Two lasers were employed in the experiment: a 10 mW HeNe laser ($\lambda = 632.8$ nm)

and a 200-500 mW Argon ion laser ($\lambda = 514 \text{ nm}$) for the out-of-plane and in-plane displacement sensitive interferometers respectively. (Arrangements for the two interferometers can be found in Appendix 8d).

8.3.4 Procedures

A preliminary step was to establish whether fringes could be produced from the surface of a corrugated board sample. To this end, an in-plane displacement sensitive interferometer was set up with a board sample loaded in the lateral direction only. The mirror together with the blade assembly were positioned near to the clamped end of the inner liner, where displacement was most likely to be found.

The in-plane interferometer was calibrated with respect to the test jig by loading a piece of liner sample. The spatula sample, with an effective length of 100 mm, was cut from a piece of Kraft linerboard (210/300 g). Once the sample was clamped and loaded under tension, it was stretched incrementally. Readings from the micrometer were then compared with the in-plane displacements as calculated from the number of fringes.

The second objective proceeded by obtaining fringe counts for the in-plane displacements of a datum point some 10 mm away from the locations 'A', 'B' and 'C'. The sample itself was held by friction under the creasing blade and its ends were left unconstrained. In-plane displacements were derived from counting the fringes across the illuminated section, and substituting the value into the appropriate equation (see Section 8.3.1). The test was then repeated but with the datum restricted to within one flute span. Position 'B' obviously could not be used as it would sit right at the end of the flute span. The only possible loading locations would be 'A' and 'C'. Two arbitrary locations, however, became available as the blade could be situated away from or near to a particular peak; these locations, defined as ' C_a ' and ' C_n ', are as shown in Figure 8.8.

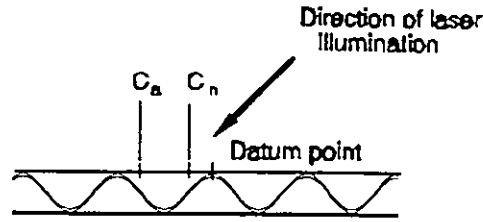


Fig. 8.8 Two possible 'C' locations.

The finite element model could be verified by comparing its in-plane and out-of-plane displacements with those of the optical experiment. Both the in-plane and out-of-plane interferometers were operated such that the fringes could be captured simultaneously under identical conditions.

A sample was held by friction under the creasing blade at location 'A'. Since the jig was lying on its side, as shown in Figure 8.9, care must be taken to ensure that sufficient friction would prevent the sample from falling.

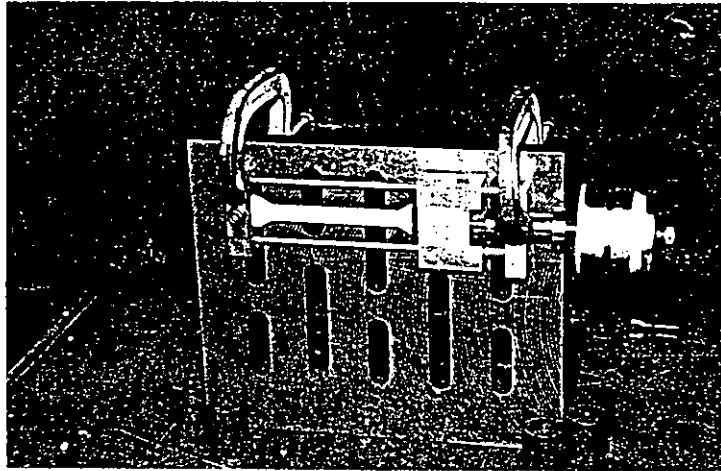


Fig. 8.9 Test jig setup.

Displacing the blade by 0.2 mm all at once would overwhelm the sensitivity of the interferometers. For this reason, the load was applied incrementally. Fringes were then recorded after each load increment. The fringe count for the in-plane displacement was taken from the illuminated section between the blade and a point some 11.5 mm away from the blade. As for the out-of-plane displacement, two sections, and hence two sets of readings, were considered for extrapolation

purposes. The sections were bounded by the blade and two points 11.5 mm and 43.5 mm away from the blade. The total number of fringes would represent the displacement of the datum point from the blade reference.

8.3.5 Results

Figure 8.10 shows a typical video image of fringes within the illuminated section.

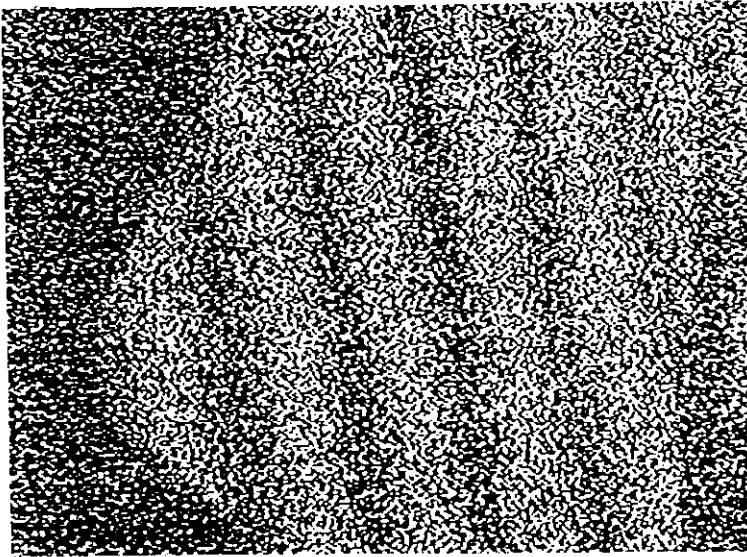


Fig. 8.10 Video image of fringes.

The calibration plot, as shown in Figure 8.11, compares the strain measurements as obtained from the micrometer readings with the ESPI in-plane displacement results.

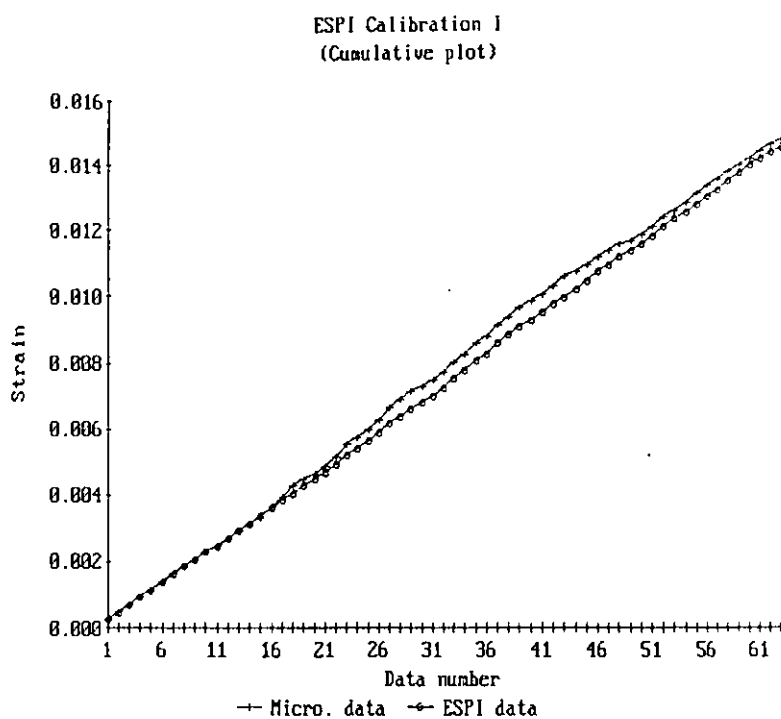


Fig. 8.11 ESPI calibration plot.

Loading conditions at locations 'A', 'B' and 'C' are shown in Figures 8.12, 8.13 and 8.14 respectively.

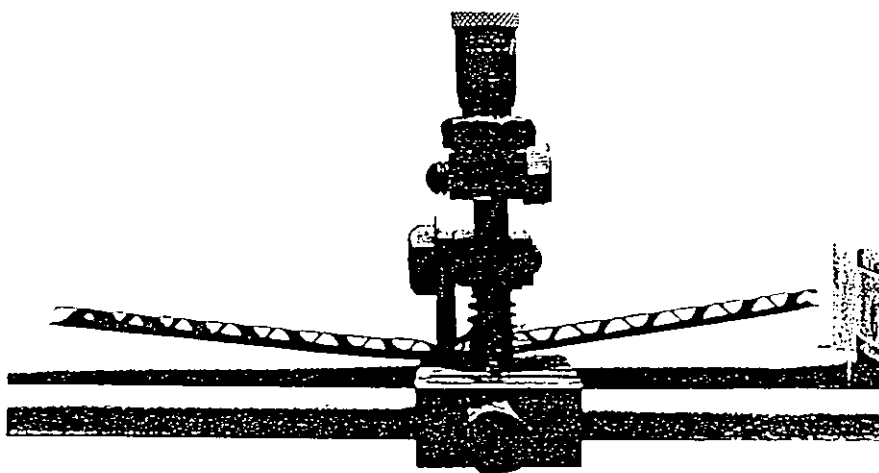


Fig. 8.12 Creaser knife at location 'A'.

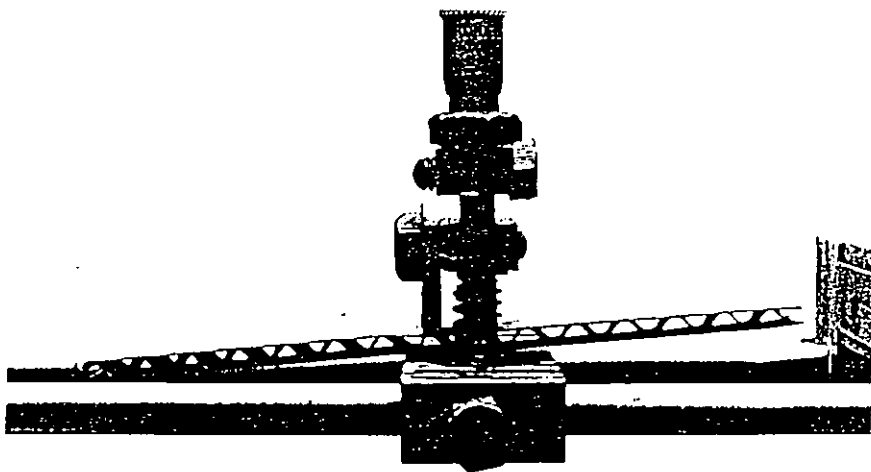


Fig. 8.13 Creaser knife at location 'B'.

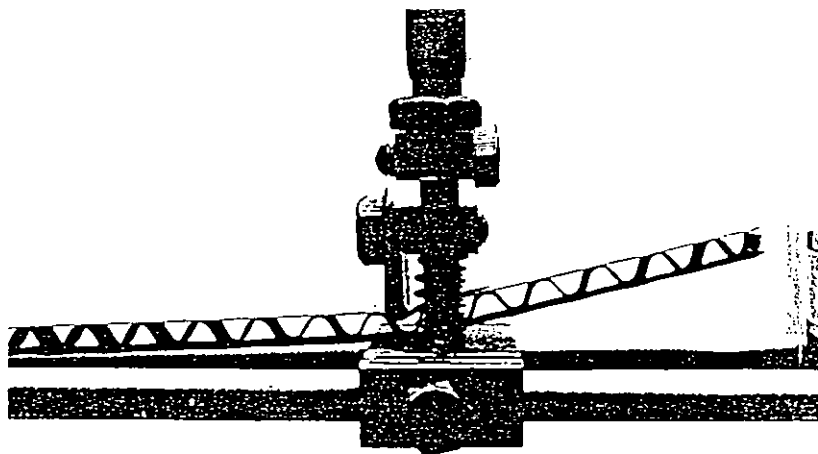


Fig. 8.14 Creaser knife at location 'C'.

Figure 8.15 shows creasing at location 'A' with the sample being constrained at both ends.

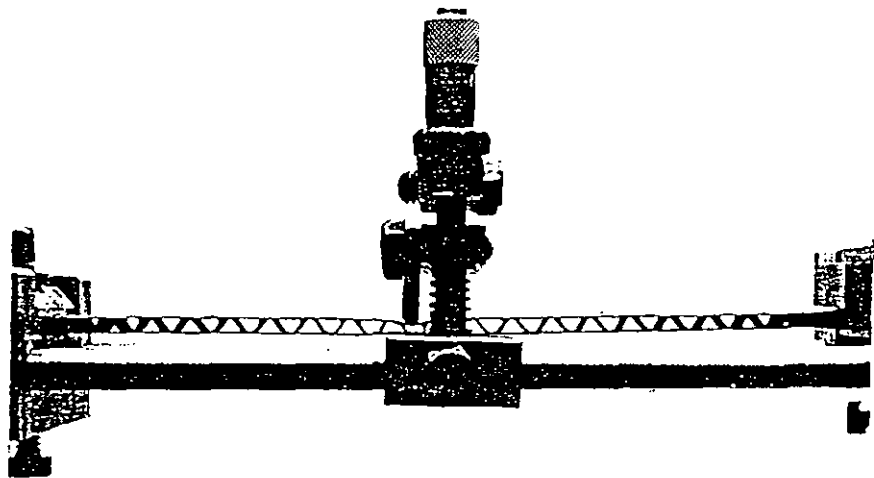


Fig. 8.15 Creasing at location 'A' with end constraints.

With reference to the first objective, as described previously, Table 8.2 gives the in-plane displacements and fringe counts at various loading positions for the wide and narrow sections of illumination. The wide section is 10 mm long whereas the narrow one is composed of just one flute span.

Table 8.2: In-plane displacements for the wide and narrow sections of illumination.

Section of illumination	Location	Number of fringes	In-plane displacement / m
Wide	A	235	1.20×10^{-4}
Wide	B	517	2.65×10^{-4}
Wide	C	356	1.82×10^{-4}
Narrow	A	73	3.41×10^{-5}
Narrow	C _a	80	3.74×10^{-5}
Narrow	C _n	47	2.20×10^{-5}

The in-plane and out-of-plane displacements as derived from ESPI for the verification of the finite element model are as shown in Table 8.3.

Table 8.3: ESPI in-plane and out-of-plane displacement results.

Mode	Illuminated length / mm	Number of fringes	Displacement / m
In-plane	11.5	1107	5.68×10^{-4}
Out-of-plane	11.5	1128	3.56×10^{-4}
Out-of-plane	43.5	3022	9.56×10^{-4}

8.3.6 Discussion

Photographic evidence from the experimental arrangement demonstrates that the symmetrical behaviour as expected from creasing at location 'A' and 'B' is impossible in reality. Loading at location 'A', in the finite element model, implies the balancing of the whole structure at a fulcrum point, which happens to coincide with the trough immediately below the load. But any offset in loading, no matter how small, will lead to dynamic instability, thereby twisting the corrugated structure over to one side. Equally unstable is the location 'B', the flute below which will shear to one side instead of depressing symmetrically. The reason lies in the inhomogeneity of paper when one of the two flanks may give way preferentially. The shearing effect from loading at location 'B' can be seen in Figure 8.13.

In the preliminary test, it was noticed that by loading the creasing blade at location 'C', fringes would move closer to each other in increasing number, and the overall movement was towards the blade. This behaviour, known as the "hollowing effect", represented the downward displacement of the inner liner. On adding a

lateral load, i.e. pulling the inner and outer liners in opposite directions, it was found that the fringes would propagate in the same manner. But the spacing between fringes would widen for a few seconds after the load had been applied. Under normal room temperature and humidity, it would be inappropriate to explain the fringe separation over such a time period in terms of the relaxation behaviour of the liner material. Slipping would be a more plausible reason.

Figure 8.11 shows the consistency between the strain readings as obtained from the micrometer and the ESPI in-plane displacement results.

The localized strain effect of the liners is more apparent in the photographic evidence than the optical experiment. Figure 8.16 shows a board sample subject to a lateral load. The end where the inner liner is clamped displays shearing action of the flute.

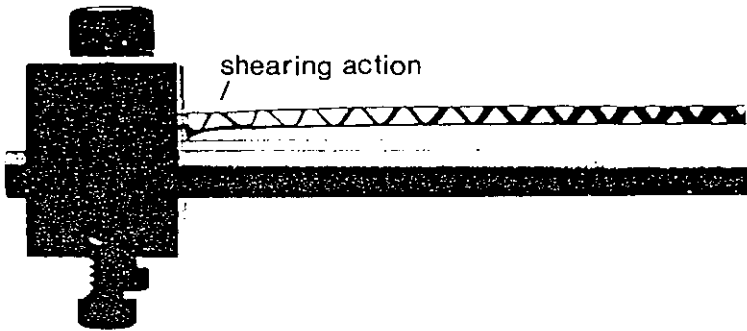


Fig. 8.16 Flute shearing at one clamped end.

In-plane displacement results in Table 8.2 exhibit a decreasing trend for locations 'C_s', 'A' and 'C_n'; which indicate that the longer the liner span, the more effectively it will pull.

After allowing for a load offset due to the blade thickness, the finite element model has been recalculated for creasing at location 'A'. At a point 11.5 mm away from the blade, the displacement results are as shown in Table 8.4.

Table 8.4: Finite element model in-plane and out-of-plane displacement.

Mode	Displacement / m
In-plane, x	6.6×10^{-6}
Out-of-plane, y	4.5×10^{-5}

On comparing the displacement results of those between the optical experiment and the finite element model, there is discrepancy in orders of magnitude. The significant difference cannot be accounted for geometrically (as the confounding effect of one displacement direction due to the other can be shown to be negligible); nor can it be explained by the sliding phenomenon. At present, no explanation is available for the result discrepancy, other than that which attributes to the material property, namely, the fibrous nature and compliance of paper.

8.4 CONCLUSION

The starting position of this chapter has been prompted by one question: "how much of the creasing effect is due to the corrugation structure and how much is due to the inner liner?" A hypothesis, wrong as it may seem, is then made on the assumption that the creasing of a corrugated board can be compared to the loading of a homogeneous and isotropic truss structure. Major assumptions such as small loading displacement and constant creasing conditions have been made in order to substantiate this claim. Based on this hypothesis, design parameters have been derived through the finite element analyses on the single-blade and the twin roll creaser profiles.

In the finite element analysis, only the pre-buckling mode of load application has been considered. This is where paper can still be assumed to behave elastically. On increasing the load, however, paper will behave inelastically up to the point of buckling. Any theoretical treatment beyond this point will be rendered invalid due to the stochastic buckling behaviour. In addition, the proprietary software is found

incapable of modelling the boundary interaction between the corrugation and the creasing blade. Instead, the creasing boundary conditions have to be simulated by directly displacing the liner elements. Nonetheless, the model has provided better understanding in the way the strain mechanism works for a piece of homogeneous and isotropic corrugation.

ESPI has been effective in analysing the displacement behaviour of the corrugated board samples when subject to the creasing action. Sliding of the inner liner under the creasing blade has been demonstrated by the moving fringes. The localized strain effect is more apparent from photographs on the experimental set up than through interpreting the ESPI results. Results from ESPI, however, have shown displacements of orders of magnitude higher than those derived in the finite element model. The only explanation available relates to the fibrous, and hence discontinuous, nature of paper - a property which has not been accounted for in the geometrical and the finite element analyses. An experimental approach, as described in the next chapter, is therefore needed in the assessment of the twin roll creaser.

CHAPTER 9

EXPERIMENTATION

The geometrical and finite element analyses in the previous chapter have been based on the model that paper behaves within the elastic regime. But as soon as inelasticity appears, there will be an element of unpredictability with regards to the mode of failure. Paper failure is difficult to model, as it involves the random distribution and bonding of pulp fibres on a microscopic level. The true performance of the twin roll creaser will therefore need to be evaluated experimentally.

This chapter commences with the design of the creasing and folding test rigs. The first experiment investigates the effect of various control and noise factors on the overall crease performance. This will be followed by a study on the geometry of the creaser profile. Twin roll creasing with pre-crushing will be covered in the final experiment. The chapter is concluded with major findings from the experiments, which will help towards designing a feasible twin roll creaser.

9.1 CREASING RIG DESIGN

An experimental creasing rig must be able to simulate the creasing conditions while assessing the various creaser profiles. Scaling, therefore, becomes a major issue, as the diameter of the creasing wheels will ultimately govern the size of the test rig. Figure 9.1 shows the theoretical relationship between the induced strain in the inner liner and the radius of the creaser roll. From the plot, a radius of 50 mm, which is well below the strain limit of paper (1.3%), is chosen; and the value corresponds to a scale of 1:4.

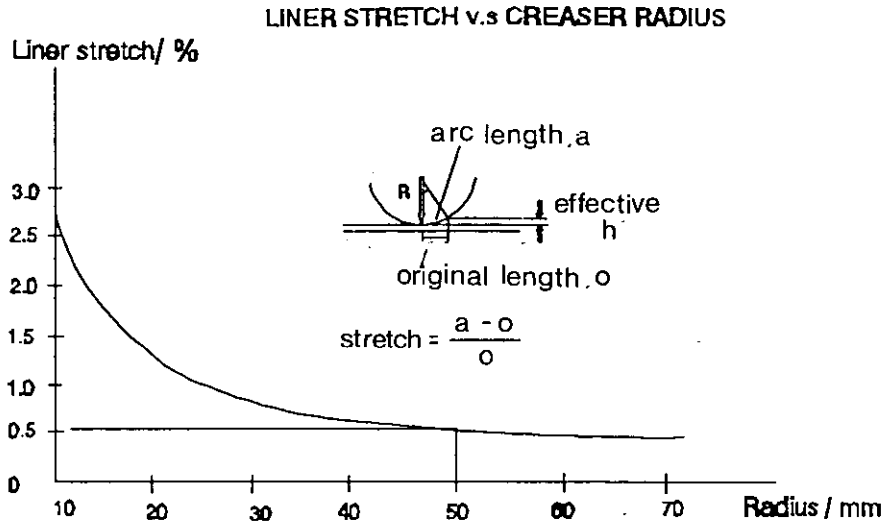


Fig. 9.1 Creaser roll radius derivation.

The creaser roll gap is accurate to within ± 0.05 mm. The inability to position the creaser accurately in relation to the flute, as Vogelpohl [51] has realized, implies a high level of sampling in order to select the few which will satisfy the position requirements - namely, locations 'A', 'B' and 'C' (as already described in Section 7.1). Fine flute positioning and flute alignment are therefore vital features in the experimental rig.

A photograph of the experimental creasing rig is shown in Figure 9.2. A micrometer, hidden from view, is located behind the guide bar which fulfils both the functions of fine flute positioning and crease alignment. A sample size of 400 mm x 200 mm is chosen, the shorter dimension of which runs parallel with the flute.

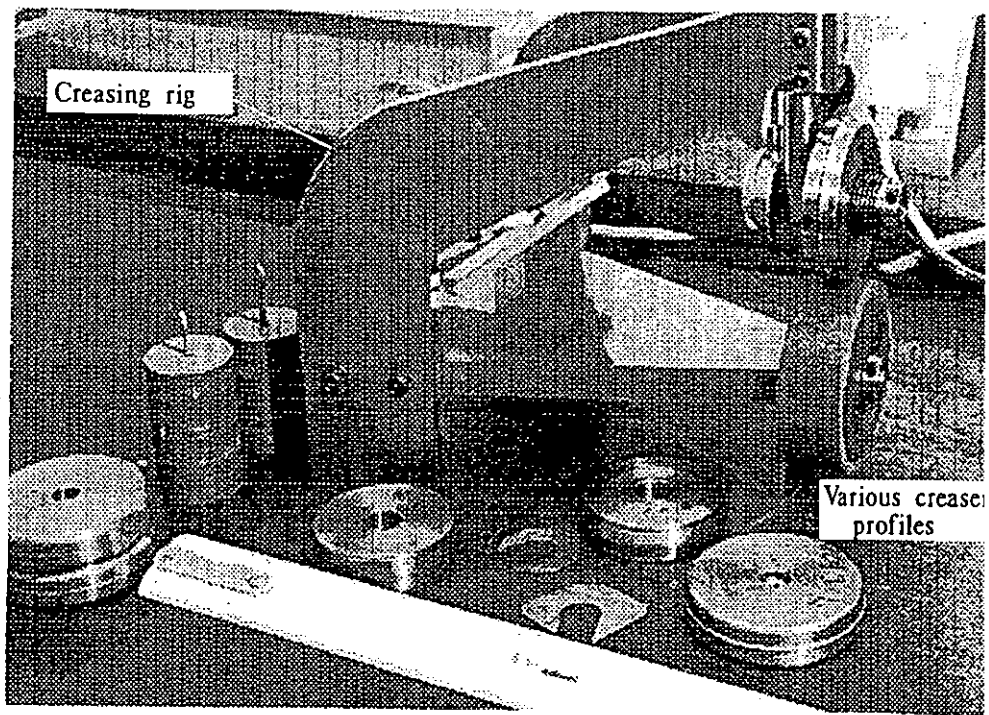


Fig. 9.2 Experimental creasing rig.

A close up photograph in Figure 9.3 shows the creaser unit and the dial gauge attachment. As the creaser moves vertically, the dial gauge, acting against a fixed datum at the top, will provide a direct measurement for the creaser roll gap.

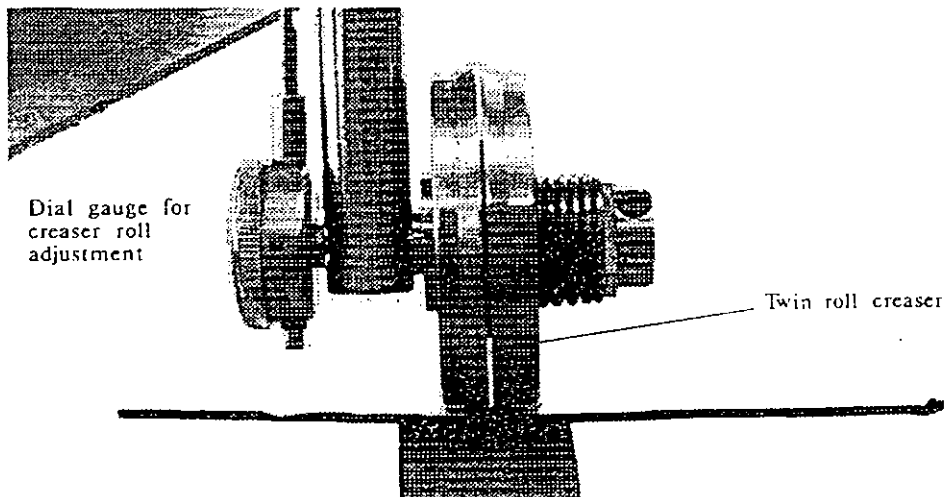
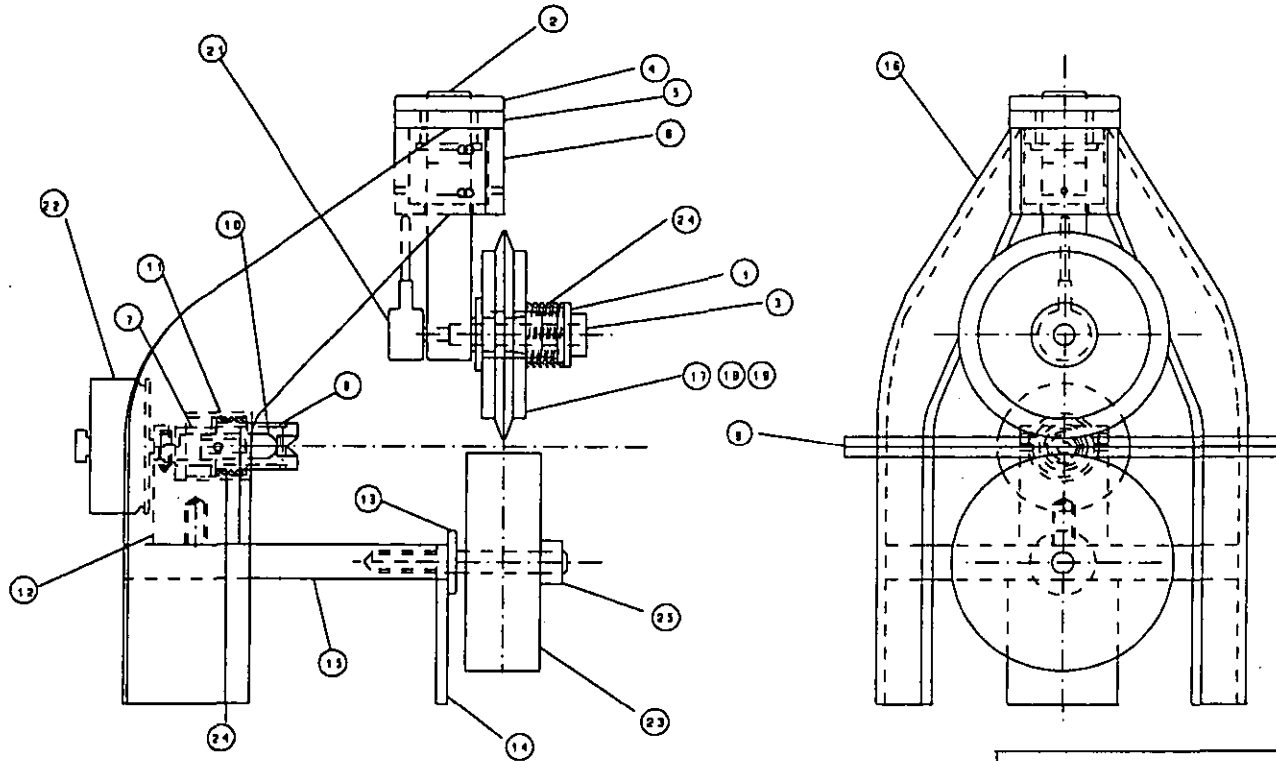
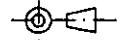


Fig. 9.3 Crease roll gap adjustment.

ENG. NO. CR0

THIRD ANGLE PROJECTION



PART LIST

1. Wedge assembly
2. Cresser shaft
3. Brass shaft
4. Handle knob
5. Split ring assembly
6. Casing
7. Split tube
8. Brass barrel
9. Sample guide
10. Brass cap
11. Gauge cover
12. Gauge block assembly
13. Female cresser pin & nut
14. Base plate support
15. Platform
16. Side plate
- 17, 18, 19. Cresser
20. Cresser spacer
21. Dial clock
22. Micrometer gauge
23. Female cresser
24. Springs (low spring rate approx. 50 N/mm)
25. Collar clamp

Note:
CR15 & CR16 contain parametric variables, i.e. some dimensions need to be adjusted depending on the size of the board sample used.

LOUGHBOROUGH UNIVERSITY OF TECHNOLOGY DEPARTMENT OF MECHANICAL ENGINEERING

DESIGNATION AND NO.	THIS AND PREVIOUS EDITIONS TO BE KEPT	APPROVED	DATE	
DESIGNED	DRAWN	DATE	8/3/93	
CHECKED (DATE)	DATE	SIGNED		
REVIEW	DATE	SIGNED		
NOT TO SCALE	SURFACE TREATMENT	APPROVED		ENG. NO. CR0

9.2 FOLDING RIG DESIGN

Creases can be categorized quantitatively in terms of their folding stiffness by means of a folding test rig. Figures 9.4 shows the folding test rig assembly.

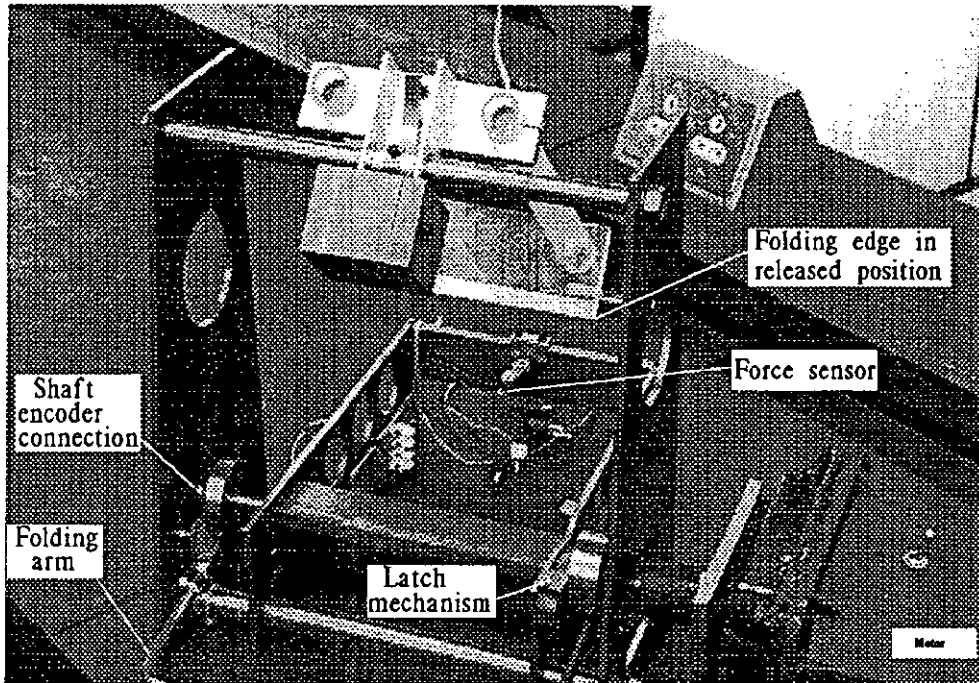


Fig. 9.4 Folding test rig assembly.

The basic mechanical features comprise a counter-balanced folding leg the end of which is fitted with a folding edge. With the board sample placed on top of the principal support bar and one end of it sitting on the edge of the cantilever, the folding leg is now ready to be latched into position. To ensure correct folding, the crease on the sample must align with the folding edge. Strain gauges on the cantilever enable it to act as a force sensor. As soon as the d.c motor is switched on, and the board panel is folded to slightly over 90° , the folding leg will be unlatched automatically. The whole folding leg assembly is then allowed to swing to its balanced position, thereby clearing way for the board sample. The d.c motor will be deactivated once the board is folded through 180° . Signals from the force sensor and the shaft encoder are sampled continuously at a rate of half a degree for every strain sample reading. In this way, the test results are made independent of the rate of folding. Figure 9.5 shows the control accessories for the folding test

rig. Detailed specifications for the rig can be found in Appendix 9a.

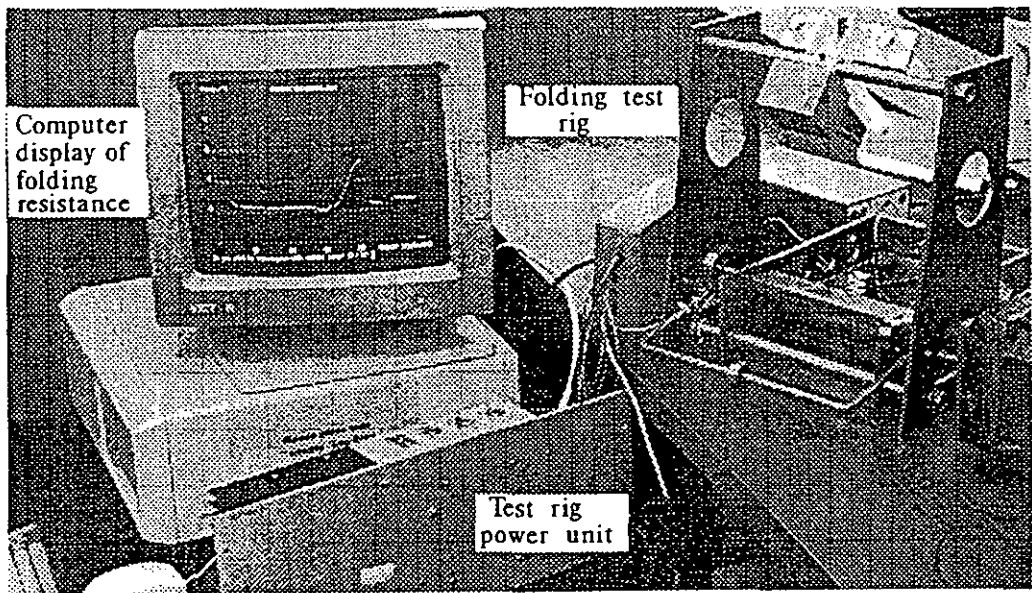


Fig. 9.5 Folding test rig control accessories.

As a board sample is folded from 0° to a closed position of 180°, the folding torque can be measured in relation to the angular displacement. The result is a torque-displacement or force-displacement (if the moment arm about the folding hinge is constant) diagram which provides a continuous history of folding. Figure 9.6 illustrates a typical plot of the folding test.

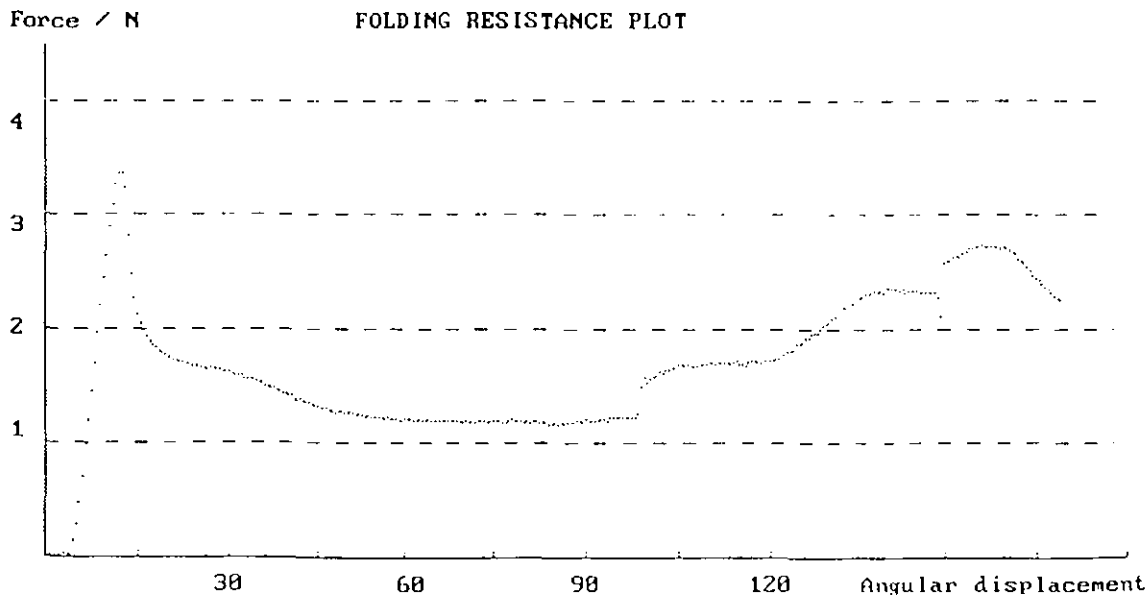
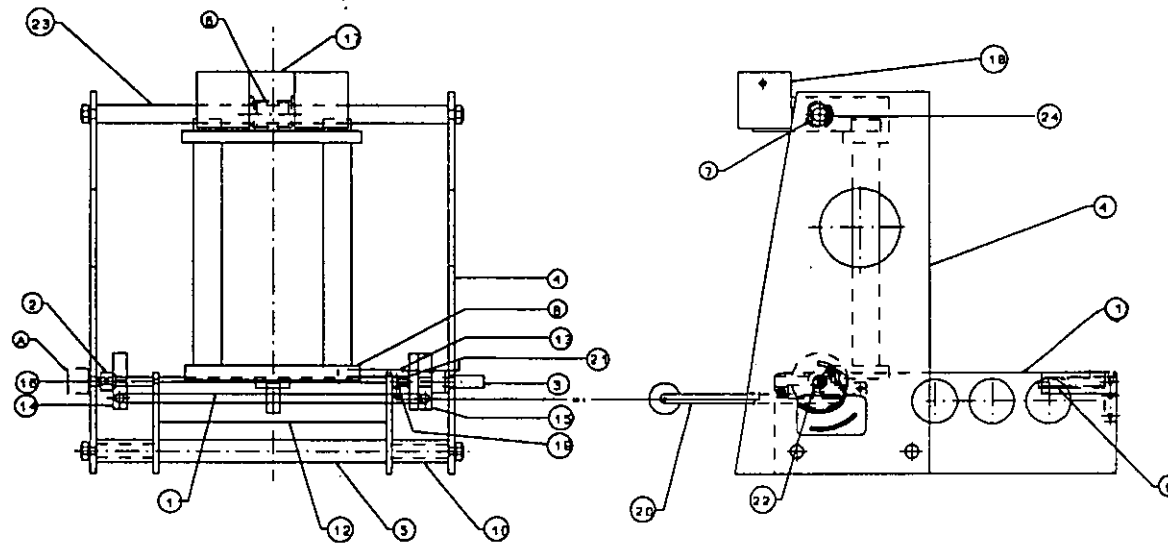
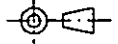


Fig. 9.6 Folding resistance plot.

DWG NO. FTD

THIRD ANGLE PROJECTION



N.B. A - location for shaft encoder

PART LIST

1. Inner side plate
2. Drive shaft (encod.)
3. Drive shaft ass'ly
4. Body plate
5. Tie bar
6. Locking ring
7. Brass bearing
8. Folding edge
9. Stress cantilever
10. Tube spacer
11. Support bar I
12. Support bar II
13. Latching pin
14. Latch disc
15. Shoulder disc
16. Shaft connector
17. Balance weight I
18. Balance weight II
19. Stepper
20. Folding arm ass'ly
21. Latch ass'ly
22. Brass bush
23. Cross bar

LOUGHBOROUGH UNIVERSITY OF TECHNOLOGY
DEPARTMENT OF MECHANICAL ENGINEERING

ALL DIMENSIONS IN MM	THIS CAD DRAWING CONFORMS TO BS2838	SIGNATURE	DATE	
TOLERANCE +/- 0.05 (UNLESS STATED)	MATERIAL	DRAWN A M LAU	17/1/82	TITLE FOLDING TEST RIG ASSEMBLY DWG
SCALE NOT TO SCALE	FINISH	CHECKED <i>[Signature]</i>		
	SURFACE TEXTURE	APPROVED		DWG NO. FTD

The 1st and 2nd peaks, the gradient of the 1st peak and the total work done in folding the board sample can all be identified from the plot; their magnitudes are calculated and displayed with the plot.

The 1st peak folding resistance represents the force required to break the crease on the inner liner (see Section 7.3). The rate at which the crease is broken can be evaluated from the gradient of the curve between the origin and the 1st peak. This gradient will give a fair indication to how well a crease has been defined.

However, the gradient must be interpreted in the light of the 1st peak folding resistance, since the absence of a crease may also produce a steep gradient. The 2nd peak (or peaks) of the folding resistance provides information on the closing of the board panels. Essentially the inner liners on either side of the crease are brought into contact, leading to further flute buckling in the process. The type of board tested can be categorized in terms of the total folding work done.

9.3 PRINCIPAL EXPERIMENT

Design parameters such as the creaser profiles at different shoulder angles, the twin roll gap and the creaser roll gap, as shown in Figure 9.7, were derived geometrically in the previous chapter. Optimization in this context would imply the consistency of crease quality irrespective of any noise effect. The noise factors inherent in the case conversion process could be simulated as control factors during the design stage. Examples of noise factors were the crease location and alignment relative to the flute structure, the moisture content in the fibreboards and the time lapse between conditioning and creasing. Creasing with hot rolls was also included in the investigation, as the liner was suspected to become more resilient to mechanical scoring at elevated temperature.

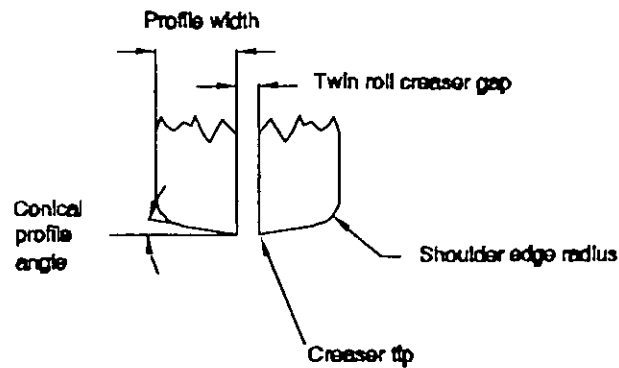


Fig. 9.7 Twin roll creaser design.

9.3.1 Objectives

The objectives of the experiment were primarily:

1. To determine the optimum creaser design parameters.
2. To investigate the effect of noise factors on creasability.
3. To study creasing at elevated temperature.

9.3.2 Procedures

In all, eight factors were thought to affect the creaser performance. Four factors were parameters at the designers' disposal; they were the **creaser profile**, **creaser temperature**, **twin roll creaser gap** and **creaser roll gap**.

The creaser profile was defined in terms of the angle of attack and hence the sharpness of the profile. Three cone angles of 10° , 15° and 30° were chosen in order of increasing sharpness (see Figure 9.7). Creaser temperatures ranging from room temperature of 25°C to 55°C were chosen as preliminary settings. Values for the twin roll gap were based on those as derived previously in Section 8.1.3. The range for the twin roll gap settings was adjusted upwards at fixed increments of 0.5 mm. Settings for the creaser roll gap must take into account the liner

grades, as boards with weaker inner liners were found to be more vulnerable to tearing.

The remaining four factors were noise factors which would normally be subject to random variation; here, they were simulated as control parameters. The factors were the **time delay**, **relative humidity** for sample conditioning, **crease alignment** and **crease location** relative to the flute.

The time delay was taken from the end of the conditioning period to the beginning of the test. Immediate creasing took place soon after the samples were taken out of the environmental cabinet; whereas samples which had been left under laboratory condition for more than three hours after conditioning would be considered as relaxed. The samples were conditioned over 24 hours in the environmental cabinet to relative humidity levels of 30 %, 50 % and 70 %. To simulate the condition of creaser misalignment, the guiding rail was set to an arbitrary angle of 1.5°. Crease location was defined in terms of the trough (A), peak (B) and the in-between (C) positions (see Section 7.1). It must be emphasized that the noise factors were included here purely for investigation purposes, as distinct from design optimization.

Table 9.1 summarizes the settings for the control factors.

Table 9.1 Control factors and their levels of settings.

Factors \ Levels	1	2	3
A. Time delay	Immediate	Relaxed	-----
B. Relative humidity %	30	50	70
C. Creaser profile	10°	20°	30°
D. Creaser temp.°C	25	40	55
E. Crease alignment	Parallel	Parallel	Skew
F. Twin roll gap	0.5 mm	1.0 mm	1.5 mm
G. Creaser roll gap*	0.5 / 1.75	1.0 / 2.0	1.5 / 2.25
H. Crease location	Trough	Peak	Between

* Two levels were set for the single- and double-walled boards.

An L_{18} ($2^1 \times 3^7$) orthogonal array (see Appendix 9b) was chosen for the experiment. Apart from the first column, which was a 2-level one, all the factors had three levels of variation, which would allow for the detection of any monotonicity within the preset range.

Three responses were measured during the experiment; they were the percentage of defective folded samples, the minimum force required to break the crease (i.e the first peak on the folding resistance plot) and the resistance to shear.

One precondition for fishtailing was the presence of shear forces acting on the case panel while it was being folded. In order to simulate this effect, shear was deliberately introduced by applying a constant moment about the hinge of the creased and folded panels. The subsequent shear deformation would be recorded in terms of the distance between the corner of the overlapping panel and the edge of the base panel (see Appendix 9c for more detail on the shear test).

A good creaser would therefore be expected to produce a minimum number of defective samples with low first peak folding resistance (hence the high likelihood to break the crease) and low shear deformation.

The signal-to-noise or S/N ratios for both the folding resistance and the shear

deformation were based on the same criterion of "smallest-the-best", and could be calculated as follows:

$$S/N = -10\log_{10}\frac{\sum Y^2}{n}$$

Converting the percentage of defects to S/N ratios would be unnecessary; since there might not be any defective samples and the logarithmic operation on a zero term ($Y=0$) would be meaningless.

Both the percentage of defective samples and the S/N ratios were then plotted against the control factors at their individual settings. Only the S/N ratios for samples which had not failed were included in the plots, as the defects criterion would take precedence over all the other quality characteristics. Optimized settings were those with the most positive S/N ratios and the lowest percentage of defective samples.

The S/N ratios were then examined using ANOVA. From the ANOVA tables, the relative importance of each control factor could be identified. Finally, the optimized settings for the design parameters were verified in the confirmation runs.

9.3.3 Experimental Requirements

In order to test the robustness of the new creaser, a representative range of board samples was chosen for the experiment. The types of board were as follows:

- 230 CC(B) - low liner strength
- 250 TH(B) - medium liner strength
- 400 KT(B) - high liner strength
- 400 KT(Gemini) - C-flute caliper with double flute lamina
- 250 TCH(B/C) - double wall heavy-duty

For each type, a batch of five was used in each of the eighteen experiments. The board samples were conditioned according to BS3431. Permission was kindly granted by the Institute of Polymer Technology and Material Engineering for conditioning the samples in their environmental cabinet.

The main equipment featured in the experiment was the creasing and folding test rigs. A Fletcher's trolley, as shown in Figure 9.8, was also converted into a test platform for measuring the shear deformation. Other accessories such as micrometer, steel rule, bunsen burner and gas supply, 50 g weights, hygrometer and psychrometric chart, and digital pyrometer were also used in the experiment.

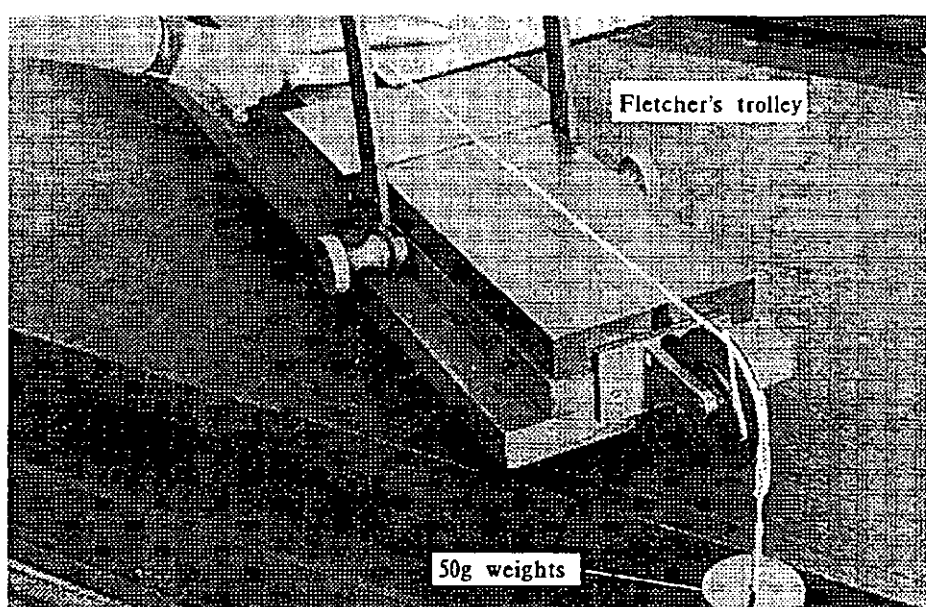


Fig. 9.8 Fletcher's trolley for shear measurement.

9.3.4 Results

The experiments took a total of three days to complete. During this period, the relative humidity in the laboratory fluctuated at around 50 % ($\pm 5\%$) and the room temperature, between 25°C and 27°C. (All test data can be found in Appendix 9d.)

Two modes of failure, as a result of creasing and folding, were observed in the test samples, and which could effectively alter the case property. Principally, the two

modes were tearing of the inner liners and secondary flute buckling (or more generally known as false creasing). Tearing was noticed to have been caused by the tip of the creaser profile and its shoulder edge.

The percentage of defective samples was calculated in terms of the number of unacceptable creased samples which failed due to tearing and buckling. In all, a test batch should contain a total of 90 samples for each type of boards. Samples which were discarded as a consequence of human errors were excluded from the subsequent analysis.

Results on the defective samples can be found in Appendix 9e. A summary of the number and types of failures, and the number of missing samples is shown in the Table 9.2.

Table 9.2 Defective samples count.

Board Types	Cracked liners	Secondary flute buckling	Missing samples
230 CC (B)	3	57	1
250 TH (B)	1	30	1
400 KT (B)	-	1	3
400 KK (GEMINI)	14	2	1
250 TCH (B/C)	59	4	1

Figure 9.9 shows the percentage of defective samples plotted against the control factors at their various settings.

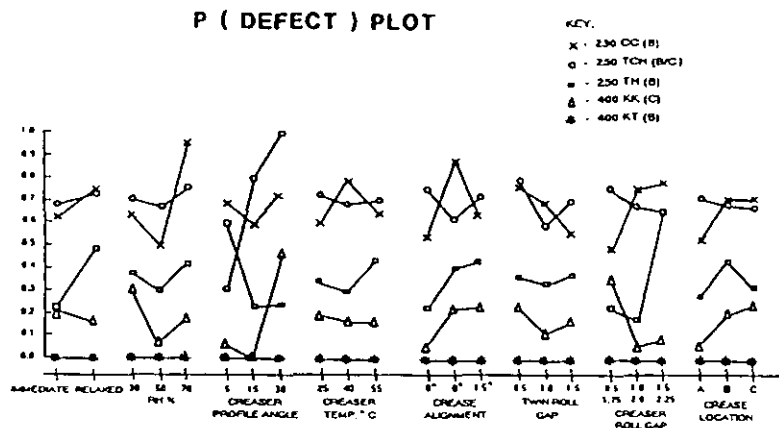


Fig. 9.9 Defective sample plot.

Likewise, the S/N ratios for both the folding resistance and the shear deformation are as plotted in Figure 9.10 and Figure 9.11 respectively.

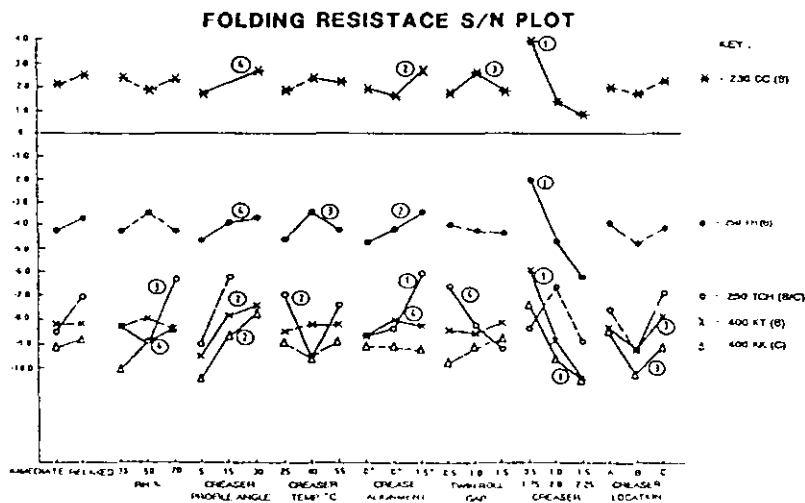


Fig. 9.10 S/N plot on folding resistance.

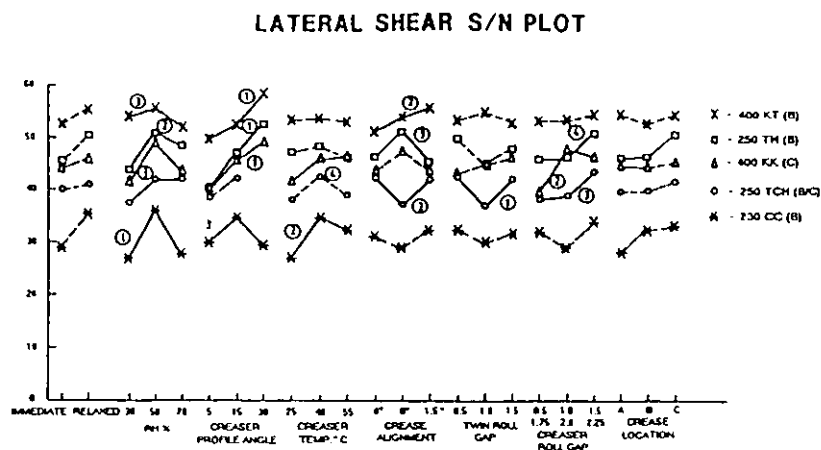


Fig. 9.11 S/N plot on shear deformation.

ANOVA tables for the folding resistance and the shear deformation S/N ratios can be found in Appendix 9f.

Factors 'C', 'D', 'F' and 'G' were optimized as they were the only design parameters in the experiment. Optimum settings were those whose S/N ratios were the most positive on the scale (based on the 'smallest-the-best' criterion). Apart from the percentage of defective samples, which were not subject to the S/N ratio criterion, factors from both the folding resistance and the shear deformation could be ranked in order of significance. The best compromised set among the three responses was then selected as the optimum (see Appendix 9g). Optimized settings, as shown in Table 9.3, were then tested in the confirmation runs.

Table 9.3 Optimized settings.

230 CC (B)	G1	D2	C2	F2
250 TH (B)	G2	C3	D2	F2
400 KT (B)	G1	C3	-	-
400 KK (C)	C2	G2	D3	F2
250 TCH (B/C)	F2	G3	C1	D1

The theoretical S/N ratios in Table 9.4 were calculated using the equation:

$$S/N_{opt} = M + (S/N_A - M) + (S/N_B - M) + (S/N_C - M) +$$

excluding those pooling factors in the ANOVA.

Table 9.4 Theoretical S/N ratios

Board type	Folding resistance S/N	Lateral shear S/N
250 TH (B)	-3.46	50
250 TCH (B/C)	-8.49	36.4

Only two sets of confirmation runs were performed with the above optimum settings. The board samples chosen were the 250 TH and the 250 TCH, and the results (see Appendix 9h) were summarized in Table 9.5.

Table 9.5 Confirmation run results.

Board type	Folding resistance S/N	Lateral shear S/N
250 TH (B)	-4.44	55.2
250 TCH (B/C)	-10.73	41.06

9.3.5 Discussion

The confirmation runs showed that the shear resistance had been improved, albeit at the expense of raising the folding resistance or lowering its S/N ratio. No conclusion could be drawn on the rate of defects since only five samples were used in each of the confirmation runs.

Several areas of interest have been highlighted as a result of the experiment, and they are as follows:

a) Modes of failure

In general, samples failed because of torn liners or secondary flute buckling.

Tearing must not be allowed to happen, since the sandwiched structure relied solely on the liners to bind the corrugation into position. Any damage to the liners might lead to crack propagation and jeopardize the integrity of the corrugation structure.

Tearing could occur any time while the creaser was in contact with the sample. The middle of the panel was just as likely to tear as the leading edge where the creaser would first come into contact with the board sample. Causes for tearing failures could be due to a combination of factors such as a small creaser roll diameter (as compared to a full-size one), a sharp creasing profile (at both the tips and the edges) and an incorrect creaser roll gap. The suggestion that the twin roll was the main cause for tearing must not be ruled out, when the creaser shoulders could stretch the part of the liner which was within the twin roll gap. Stress induced in this part of the inner liner could be lessened by having a wider twin roll gap. However, setting the twin roll gap too far apart might encourage the two halves of the creaser to behave independently as if they were two single blades.

Secondary flute buckling, or false creasing, was characterized by the buckling of flute(s) other than that along the crease. (In the present context, primary buckling was used for describing the intentional buckling and folding of the corrugated board about its crease.) This kind of failure could be caused by an insufficient creaser penetration or a localized weakness already present in the board. Short pulp fibres and impurities in the recycled liners, especially in chip liners, were examples of the sources of weakness.

b) General trends

Referring to the previous plots on defective samples and S/N ratios, the distinct levels of results on all three plots clearly reflected the importance of board grades on the crease quality.

Some of the noise factors had hardly made an impact on the folding and shear resistance. An example was the instant of fold which served as a pooling factor in every analysis of variances. The crease location, however, showed direct correlation with the folding resistance. From the folding resistance plot, position 'B' or the flute peak (referring to Figure 7.1) could be seen to be the least favourable, i.e it was the position where the highest resistance to folding was experienced. One interpretation could be that extra effort was required to buckle not just the inner liner, but also the flute situated immediately below position 'B'. By comparison, less resistance to folding was experienced at positions 'A' and 'C', when only the inner liner was buckled to form the fold. It was not until the folded panels came to a close, however, that boards with creases at positions 'A' and 'C' would experience flute buckling for the first time. For boards which were creased at location 'B', flute compaction would have been well underway upon closing of the panels. The folding resistance plots would therefore be expected to show a higher first peak (as demonstrated by the S/N plot on the folding resistance) and a lower second peak for creases at position 'B' than those at position 'A' and 'C'. Moisture content in the board samples, a noise factor by nature, also exhibited some form of correlation with shear as shown on the shear deformation plot.

Definite trends were also found among some of the design parameters. An example was the correlation between the folding resistance and the crease roll gap. By having a small roll gap, and hence a deep creaser penetration, the folding resistance would decrease substantially. This applied to all the single-wall boards, whereas for the double-wall boards, the roll gap effect was marred by other factors. Optimized settings in Table 9.3 would suggest that sharper creasing profiles were more suitable for single-wall B-flute boards with strong inner liners. But as soon as a weaker liner or a thicker board is creased, a gentler creasing profile would be more appropriate. Sharper creasers too could lower the folding resistance and the shear deformation, though the risk of tearing would increase with board calipers. Shear resistance for the 230 CC samples, however, proved to be an exception, as their behaviour was more sensitive to the moisture condition than the creaser sharpness.

Similar trends for individual factors such as the twin roll gap setting could be observed between the 250 TCH and 250 TH samples. It was noticed that both types of boards shared the same inner and outer liners, namely the T- and H-liners. It would be presumptuous to conclude that the similar trends in all three responses were entirely due to the same liner constituents. But the importance of the liner in relation to the creasing, folding and shearing responses could not be overlooked.

c) Extreme board grades

In general, both the 230 CC and the 250 TCH, being the light and the heavy ends of the case range, appeared to be the most problematic. The two types of boards were shown to be sensitive to crease alignment, and the 230 CC boards exhibited more shear deformation than any other B-flute types in the experiment.

When creasing the double-wall boards, the optimum profile, being the shallowest of all, was behaving more or less like a pre-crease crusher. This reinforced the idea that the thickness of the creased region must be reduced to such an extent that the subsequent creasing force could be transferred directly onto the liners. With regards to the shear resistance, the twin roll gap setting for the double-wall boards was identified to be the most significant factor, more so than in the single-wall boards.

The physical behaviour of the 230 CC board samples was extremely sensitive to the moisture condition. The ideal creasing condition was when the samples had been prepared at a relative humidity of 50%. Any deviation from the median value by 20% would drastically alter the performance of this type of boards. Equally important, the creaser must penetrate deep enough or else the board might fail due to secondary flute buckling.

d) Result inconsistency

One major problem still to be resolved was the inconsistency in the crease alignment result. The settings were chosen such that the first two levels were the same, i.e both were set with the crease parallel to the flute. In theory, the same

two levels should yield identical results. The three plots, however, revealed inconsistency at the two levels, suggesting that either the rig design was fallible or some kind of interaction had not been accounted for.

Another curious phenomenon was observed from heating the creaser roll to the mid-range temperature of 40° C. Under this condition, the first peak of the folding resistance reached its highest level for the double-wall boards, whereas the least shear deformation was experienced in the 230 CC. This was surprising because one would anticipate a monotonic trend for the temperature effect.

On the whole, it must be emphasized that any results in this experiment must be interpreted in the light of a small sample size together with a high defect rate.

9.3.6 Conclusion

An optimization experiment was conducted on the novel twin roll creaser. The objectives were to identify the optimum design parameters for the creaser and investigate the relative effect on creasability due to a range of noise factors.

Three quality characteristics were measured during the experiment; they were the percentage of defective folded samples, the first peak folding resistance and the shear deformation under a constant load. Results showed that boards would fail on account of liner tearing and secondary flute buckling. Tearing was mainly due to the tip of the creaser and the conical profile edge. Board grades were seen to have a significant effect on the creasing and folding performance. Both the 230 CC and the 250 TCH, belonging to the light- and the heavy-duty categories respectively, were identified to have caused the most problems. Trends from the result plots had revealed correlations between the various factors (both design and noise) and the responses. Shear resistance for the selected samples was improved in the confirmation runs, though their folding resistance had not reached the desirable level.

The experiment has prompted further investigation into the geometrical properties of the twin roll creaser: in particular, the creaser shoulder edge responsible for the majority of tearing failures and the pre-crushing function when creasing double-wall boards. From the theoretical as well as practical viewpoints, any future experimentation will have to aim at minimizing the number of defects. Other measures such as the second peak of folding resistance and the gradient of the first peak are to be included in the analysis. Second peak folding resistance will indicate the ease of panel closure, while the first peak gradient will show how well the crease has been defined. On reflection, the ranges for the relative humidity and temperature have been set too close for them to produce any observable difference in the results. But since the present prerogative is to optimize the twin roll creaser design, any investigation into the temperature and moisture effect on liners will have to be left as future work.

9.4 PROFILE DESIGN EXPERIMENT

The first experiment has revealed that different creaser profiles are needed for different board thicknesses in order to avoid tearing. For example, a shallow profile is more suitable for the double-wall boards; whereas for single thickness boards, except when the inner liners are weak, a steep profile will be more appropriate. Experimental evidence, however, suggests that the majority of tearing has been due to the sharp edges on the creaser. Hence, the objective of the second experiment is to study the creaser shoulder effect and the tip radii on the twin roll creaser.

9.4.1 Theory

At present, creasing of double-wall boards is preceded by pre-crushing. Typically, a B/C-flute board of 6.1 mm in thickness is pre-crushed to 4 mm, representing a

34 % reduction in caliper. In doing so, the creasing force can be transferred more effectively into the already compressed region.

The current design of the pre-crusher is as shown in Figure 9.12.

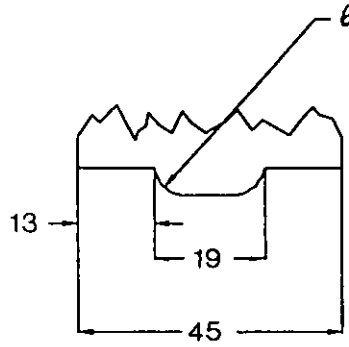


Fig. 9.12 Pre-crusher profile (dimensions in mm).

One hypothesis is that if the total width of the creaser amounts to more than the width of the pre-crusher, then, for the same depth of creaser penetration, damage may spread over a much wider section leading to higher shear deformation. This hypothesis, at present only a speculation, will be validated in the following experiment. The width of the twin roll creaser, however, is designed to within that of the pre-crusher, such that depending on the twin roll gap width, the overall creaser width can be adjusted to within or beyond the pre-crusher width.

Radial shoulders and creasing tip edges, as shown in Figure 9.13, are the main design parameters in this experiment. Both 'R' and 'w' have been chosen to be within the pre-crusher width constraint (see Appendix 9i). Gap values 'g' wider than those used in the first experiment are tested in order to study how the separation between two score lines is related to the board calipers (see Section 8.1).

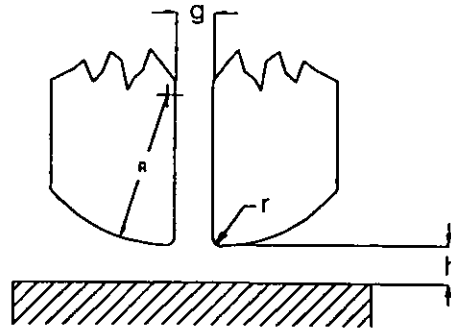


Fig. 9.13 Twin roll creaser main design parameters.

9.4.2 Method

The control factors and settings were as shown in Table 9.6, and an L_9 orthogonal array was adopted.

Table 9.6 Design parameters and their settings.

Factors\ Levels	1	2	3
Radius, r / mm	1.5	2	2.5
Radius, R / mm	15.57	20.31	25.78
*Gap, g / mm	0 / 2	1 / 5	2 / 8
*Roll gap, h / mm	0.5 / 1.5	1.0 / 2.0	1.5 / 2.5

* 2 sets of values correspond to the single- and double-wall boards.

In all, nine pairs of creasing rolls were manufactured to represent the nine possible combinations of ' r ' and ' R ' (see Figure 9.13).

The samples 230 CC (B) and 250 TCH (B/C) were chosen because they had been found to have caused the most problems in the previous experiment. The number of defective samples, the first peak of the folding resistance and the shear deformation were responses measured during the experiment.

9.4.3 Results

The laboratory conditions at the time were 22.5 °C and 50 % relative humidity. No samples were discarded as a result of human error during the experiment.

Table 9.7 shows the number of defects recorded in the experiment. Note that a total of 45 samples was tested for each type of boards.

Table 9.7 Defective sample count.

Sample types	Cracked liners	2nd flute buckling
230 CC (B)	1	21
250 TCH (B/C)	43	-

A high rate of tearing had meant that neither the folding resistance nor the shear deformation responses could be evaluated for the double-wall boards.

Tabulated results for the 230 CC (B) samples can be found in Appendix 9j. A result summary on the rate of defects and the S/N ratios can be seen in Figures 9.14, 9.15 and 9.16.

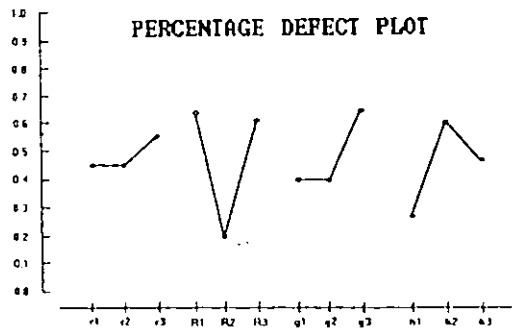


Fig. 9.14 Defective sample plot.

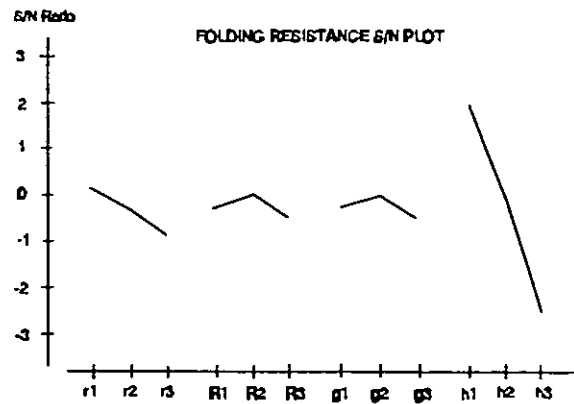


Fig. 9.15 S/N plot for folding resistance.

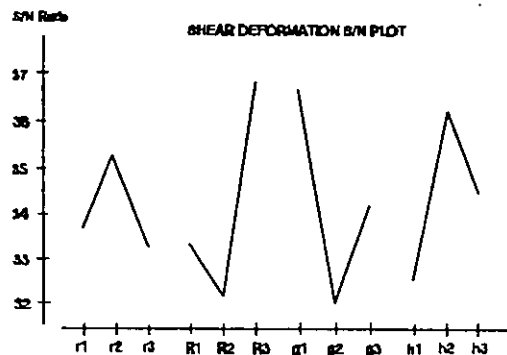


Fig. 9.16 S/N plot for shear deformation.

ANOVA tables for both the folding resistance and the shear deformation can be found in Appendix 9j. Table 9.8 summarizes F ratios for the four control factors.

Table 9.8 F ratio summary from the ANOVA tables.

Control factors	F(folding)	F(shear)
Radius, r	3.7	---
Radius, R	---	4.5
Gap, g	---	4.4
Roll gap, h	27.8	2.8

No confirmation runs were performed because of the investigative nature of the experiment.

9.4.4 Discussion

As in the first experiment, the mode of failure for the 230 CC (B) was predominated by secondary flute buckling; and for the 250 TCH (B/C), tearing of the inner liners. A majority of 43 out of a total of 45 failed among the double-wall samples. Failures could not be prevented even with a creaser roll gap as large as 2.5 mm (or a 59 % reduction in board thickness). This clearly demonstrated the discrepancy in the initial design criterion, namely that of a wide rounded-off profile as a replacement for the pre-crushing and creasing functions.

With regards to the 230 CC (B) samples, the creaser roll gap 'h' appeared to have the most significant effect on the folding resistance. Again, as in the first experiment, the trend for the roll gap was monotonic and the narrowest gap was found to be the most desirable. In terms of shear deformation, a large shoulder radius and a small twin roll gap were the most preferred combination. A small twin roll gap had the effect of producing a clearly defined crease. The advantage for having a large shoulder radius, however, was not immediately obvious.

Increasing the shoulder radius will gradually flatten out the curved profile, hence enabling the latter to act like a shallow conic profile. As described in Section 8.1.2, a 10° conic profile is recommended on the basis that tension within the inner liner will be relieved by the time the profile starts to depress the neighbouring flute peaks. The shear deformation results for the 230 CC boards in the first experiment have also confirmed that a 10° profile angle will give the least shear.

9.4.5 Conclusion

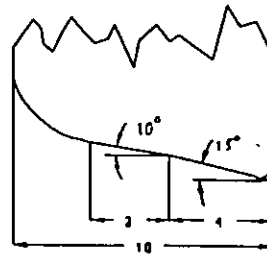
In an attempt to develop a single stage creaser for both the single- and double-wall boards, the shoulder and the tip radius effect of the twin roll creaser were investigated. An unacceptable number of defects, however, suggested that pre-crushing for the double-wall boards was indispensable with the current twin roll

creaser design. For a twin roll creaser whose width was limited to that of the pre-crusher, it was found that a large shoulder radius would give low shear deformation. More important was the width of the crease which would be governed by the twin roll creaser gap. The twin roll creaser would succeed in crushing and creasing the double-wall boards only if its width was extended to beyond that of the pre-crusher. Although the objective of a single stage creaser and crusher could be achieved with low folding resistance and shear deformation, a reduction in the section thickness over a much wider area would imply lower structural stiffness and hence the case compressive strength.

9.5 OPTIMIZATION EXPERIMENT

Previous experiments have shown that a single stage twin roll creaser will cater for the double-wall boards only if the crushing profile is wide enough for a sufficient creaser penetration. However, the width of the creaser must not be wider than the present pre-crusher, or else a larger area of flutes will be crushed and the case strength substantially reduced. A compromise will, therefore, be to check if the twin roll creaser, with a total width less than that of the pre-crusher, will operate in conjunction with a pre-crusher on double-wall boards.

Experimental evidence has so far suggested that a shallow creaser profile is suitable for the double-wall boards. Essentially, a shallow profile fulfils both the crushing and creasing functions simultaneously. Single-wall boards, on the other hand, prefer a sharper creaser profile. For this reason, a combined profile, as shown in Figure 9.17, will also be assessed in this experiment. Note that the two profile angles are designed to cater for the single- and double-wall boards, and that sharp edges on the creaser have all been rounded off so as to prevent tearing.



All dimensions in mm.
Not to scale

Fig. 9.17 Combined profile.

The objectives for this experiment are as follows:

1. To study pre-crushing and creasing of double-wall boards.
2. To assess the performance of a combined twin roll creaser profile.

9.5.1 Methods

An L_9 orthogonal array was adopted for the experiment, and the control factors and settings were as shown in Table 9.9:

Table 9.9 Control factors and settings.

Control Factors \ Levels	1	2	3
A. Pre-crusher roll gap /mm	2.6	3.0	3.5
B. Twin roll gap /mm	0.5	2.5	4.5
C. Creaser roll gap /mm	1.0	1.5	2.0
D. Creaser profile	10°	20°	CP*

CP* - compromised profile (see Figure 9.17)

The 10° and 20° profiles were the same as those in the first experiment. The type of board chosen was the double-wall 250 TCH, and a sample size of ten was assigned to each of the nine experiments. All the board samples were conditioned to 50 % RH and 23 °C prior to the experiment.

Below were the responses measured in the experiment, and which would be

maximized in the subsequent analysis. For notation purposes, ' η ' was used to represent the S/N ratio.

1.) Fraction of defective samples

S/N ratio :

$$\eta = -10\log_{10}\frac{p}{1-p}$$

where p = proportion of defective samples.

2.) Folding resistance

S/N ratios for the two peaks 'A' & 'B' (see figure 7.4) using the 'smaller-the-better' criterion:

$$\eta_{A,B} = -10\log_{10}\frac{\sum_{i=1}^n y_i^2}{n}$$

S/N ratio for the gradient of the first peak, 'D', using the 'larger-the-better' criterion:

$$\eta_D = -10\log_{10}\frac{1}{n}\sum_{i=1}^n \frac{1}{y_i^2}$$

3.) Shear

The definition for shear deformation was same as before. The load used on the Fletcher's trolley weighed 1813.8g. S/N ratio for shear deformation using the 'smaller-the-better' criterion:

$$\eta = -10\log_{10}\frac{\sum_{i=1}^n y_i^2}{n}$$

9.5.2 Results

The experiment was conducted at a room temperature of 26° and a relative humidity of 55%. Due to a limited period of access, the boards were conditioned for only seven hours; but the ambient conditions were not far off.

All test results have been tabulated and can be found in Appendix 9k. S/N ratios for the defect rate due to pre-crushing is as shown in Table 9.10.

Table 9.10 S/N ratios for pre-crushing defect rate.

Factor Levels	S/N ratios
A1	3.59
A2	8.36
A3	9.54

S/N plots for the defect rate as a result of creasing, first peak and its gradient and second peak of the folding resistance, and the shear deformation are as shown in Figures 9.18 to 9.21.

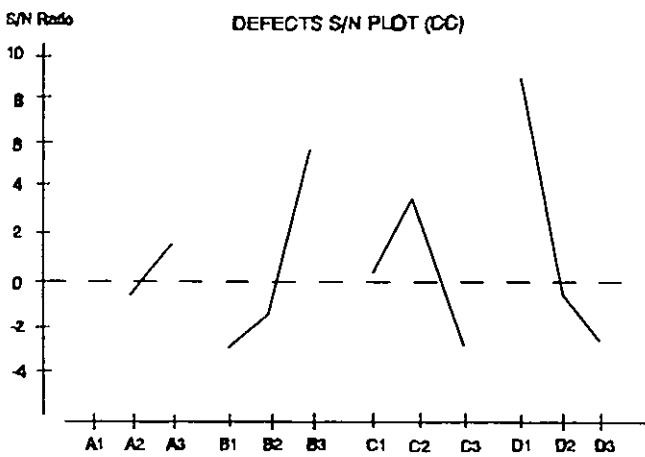


Fig. 9.18 S/N defect plot.

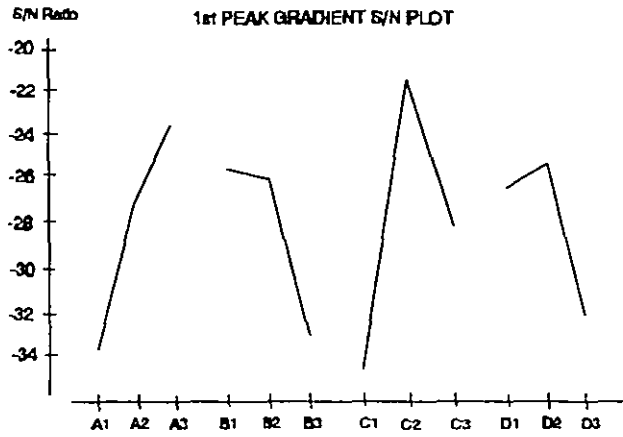


Fig. 9.19 S/N 1st peak gradient plot.

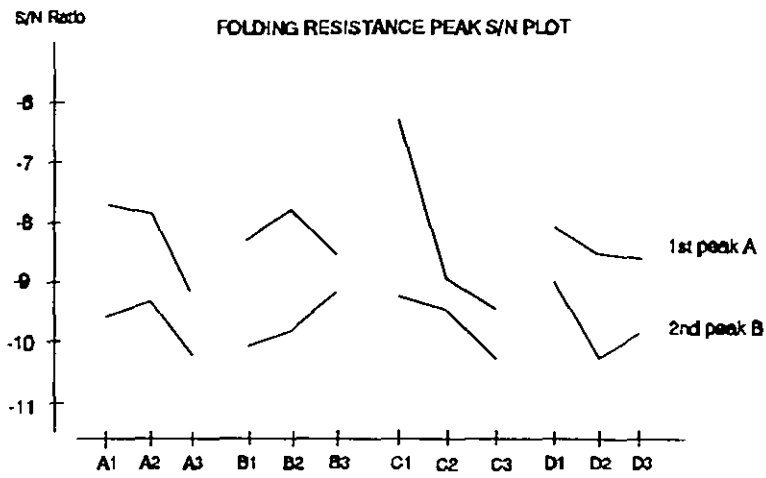


Fig. 9.20 Peak S/N plot.

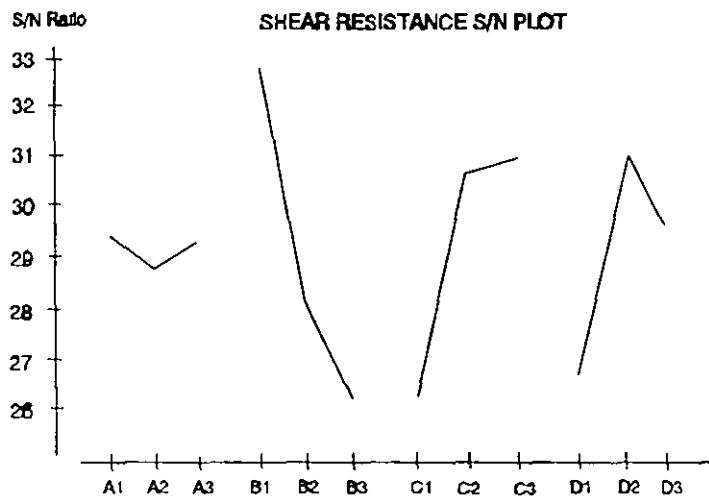


Fig. 9.21 S/N plot for shear resistance.

From the results, the optimized levels for each response and control factors were obtained and ranked in order of significance (through comparing the F ratios). A summary of the ANOVA 'F' ratios is as shown in Table 9.11.

Table 9.11 ANOVA 'F' ratios summary.

Control Factors \ F	Defects (CC)	η_A	η_B	η_D	η_{shear}
Pre-crusher roll gap	----	5.56	----	2.02	----
Twin roll gap	18.7	----	----	----	80.95
Creaser roll gap	8.27	29.7	1.57	3.33	51.91
Creaser profile	33.76	----	2.4	----	33.48

The settings for the confirmation run were as follows: D1, B2, C2, A2. Table 9.12 shows the S/N ratios predicted for these settings together with the acceptable standard deviations and those which were derived from the confirmation run.

Table 9.12 Experimental and predicted S/N ratio.

Responses	$S/N_{\text{expt.}}$	$S/N_{\text{pred.}}$	$\pm 2\sigma_{\text{pred.}}$
Defect rate (CC)	9.03	8.78	3.57
Shear deformation	24.95	27.2	0.96
Folding 1st peak gradient	-20.79	-21	1.33
Folding 1st peak 'A'	-9.18	-7.9	11.59
Folding 2nd peak 'B'	-9.12	-8.8	1.18

9.5.3 Discussion

The 1st peak folding resistance was found to have been ignored by the software for some of the test samples (see tabulated results in Appendix 9k). A sharp yield point which would normally be associated with the initial stage of folding had, instead, become a point of inflexion as illustrated in one test sample in Figure 9.22.

This phenomenon, according to Nordman et al. [30], could be explained by the material flow within the board samples.

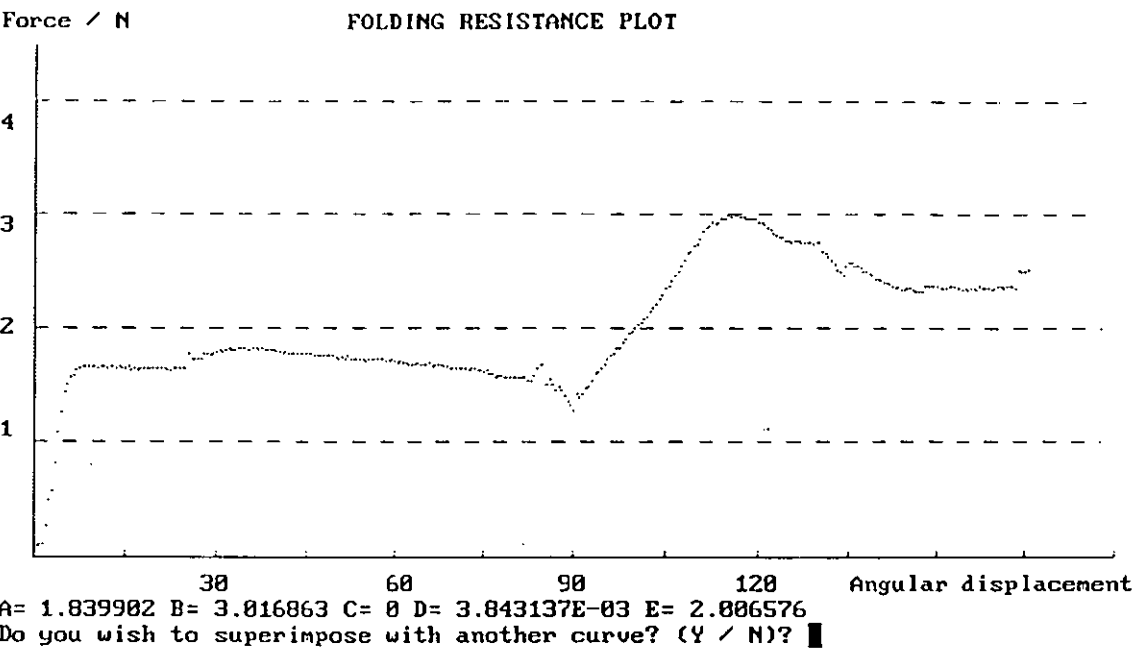


Fig. 9.22 Folding resistance plot with no 1st peak.

On comparing the predicted and the experimental S/N ratios in Table 9.12, an improvement has been achieved in the defect rate and the gradient of the 1st peak folding resistance. Shear deformation is found to lie just outside the acceptable tolerance. In fact, it is difficult to optimize both the defect rate and shear deformation, as shall be discussed later in this section. The rest of the experimental S/N ratios are not far from the predicted ones. The fact that the ratios fall within the tolerance band suggests the adequacy of an additive model. Present rate of defect however is still too high for the creaser design to be of any practical value.

Pre-crushing was proved vital in the creasing of double-wall boards. A high defect rate during the pre-crushing stage might imply a fault in the experimental design, or more to the point, an incorrect range roll gap settings for the pre-crusher. Enquiries with a machine user, one of the industrial collaborators, revealed that the roll gap should normally be set to between 3.5 mm and 4 mm. The magnitude and

gradient of the 1st peak folding resistance were also found to be correlated with pre-crushing. Less pre-crushing would result in a steeper gradient, or a more definite crease, and a higher 1st peak of folding resistance.

Among the various control parameters, twin roll gap setting was identified to be the most effective in controlling shear deformation. For minimum shear, the lowest gap value would be the most appropriate. However, there was a conflict of interest as the least defect due to creasing would correspond to the highest twin roll gap value. Evidence from the finite element model in the previous chapter also suggested that the highest principal stress could be found in that part of the inner liner which was within the twin roll gap. Lengthening this section of the liner, hence widening the twin roll gap, would diffuse the principal stress over a much larger area and therefore minimize the chance of tearing.

The creaser roll gap had a significant effect on the gradient and the magnitude of the 1st peak folding resistance. As in the previous experiments, monotonicity was expected between the peak resistance and the roll gap. As for the gradient, there was no immediate explanation for the mid-range gap value being the most preferred one.

The creaser profile was also found to be crucial in determining the rate of creasing defects, the 2nd peak of folding resistance and, to a less extent, the shear deformation. The 10° profile, being the shallowest of all, was demonstrated to be the most robust, though a sharp profile would minimize shear deformation and therefore fishtailing.

9.5.4 Conclusion

The third Taguchi experiment has been conducted with the aim of optimizing the twin roll gap creaser for the double-wall boards. A 10° profile was found to be the best among the three choices. Creaser roll gap, be it the pre-crusher's or the

creaser's, has a significant impact on the gradient and the magnitude of the 1st peak folding resistance. Reducing the roll gap will lower the 1st peak folding resistance, but the relationship between the roll gap and the 1st peak gradient does not appear to be monotonic. One possible explanation may be due to the property of a double-wall board. Apart from the discrepancy of setting the pre-crush roll gap closer than required, results achieved with the optimized factor levels are still less than satisfactory. Defect rate can be reduced by widening the twin roll gap, hence allowing more liner to be stretched under the same stress level. But the disadvantage for having a wide twin roll gap is an increase in shear deformation.

9.6 EXPERIMENTAL SUMMARY

The creasing and folding test rigs have both been proven indispensable in the experimental study of creaser profiles.

In the first experiment, it was found that the crease location had direct correlation with the folding resistance. Sharp creaser profiles too were shown to have the effect of lowering the folding resistance and the shear deformation. Unfortunately, the risk of tearing due to sharp profiles would increase dramatically with board calipers. Furthermore, boards were found to have failed on account of liner tearing and secondary flute buckling (or false creasing). From observation, tearing seemed to have initiated from the tip and the shoulder edge of the creaser profiles.

Board grades were shown to have a significant effect on the creasing and folding performance. The 230 CC and the 250 TCH, being the light- and the heavy-duty cases respectively, were identified to have caused the most problems. In an attempt to develop a single stage creaser for both types of boards, the shoulder and the tip radius effect of the twin roll creaser were studied in the second experiment. An unacceptable number of defects, however, suggested that pre-crushing for the double-wall boards was a prerequisite in as far as the twin roll creaser design was concerned. The twin roll creaser would succeed in crushing and creasing the

double-wall boards only if its width was extended to beyond that of the pre-crusher. But the benefit from combining the creaser and crusher into a single stage would be outweighed by the reduction in section thickness over a much wider area. The net effect would be a lower structural stiffness for the final case.

The third experiment demonstrated that a 10° profile for the twin roll creaser was the best of the range. Creaser roll gap, whether it was the pre-crusher's or the creaser's, would determine the gradient and the magnitude of the 1st peak folding resistance. Tearing could be reduced by widening the twin roll gap, though at the expense of increasing the shear deformation.

CHAPTER 10

CONCLUSIONS & RECOMMENDATIONS

Research has been conducted on improving the performance of the case conversion process. In particular, the study has investigated the effect of creasing, folding and gluing on fishtailing - a quality characteristic which describes the squareness of a case. Through performing an industrial experiment on a standard "flexo-folder gluer" case converter, important factors have been identified and which have led to new innovations for the correction and reduction of fishtailing. Design methodologies for the folding innovations have been described in depth.

The feasibility of a twin roll creaser design, which processes boards of different thicknesses without the need for roll replacement, has also been examined. Analytical and experimental studies have resulted in better understanding of the mechanism of creasing, and a functional twin roll creaser design.

The following subheaded conclusions refer to the set objectives aimed for in this study.

10.1 FISHTAILING

Fishtailing, or the lack of case squareness, was measured in the industrial experiment in terms of the geometrical deviation formed by the folded case panels relative to the edge of the case body. The case conversion process was optimized with minimum fishtailing on individual case panels. The amount of glue applied and the subsequent application of pressure on the glued joints were shown to have direct influence on fishtailing. Interaction was discovered between gluing and the slapping section. Machine speed, on the other hand, was found to have played a minor role in causing fishtailing. Uni-directional fishtailing results were attributed to the present method of folding. The mechanism of folding was studied, and two folding innovations were developed as a consequence.

10.2 FOLDING MECHANISM

The present method of folding takes the form of a stationary and twisted rail which guides the case panel through the first 90° of fold. Inevitably, a backward force component is introduced onto the leading edge of the case panels, thereby causing fishtailing. This is consistent with the uni-directional fishtailing results obtained in the industrial experiment.

Folding mechanism, in essence, can be viewed as cam mechanisms. An unusual feature which distinguishes the folding mechanism from other spatial cams is that the cam follower, i.e. the case panel, twists in kinematic screw motion about an axis relative to the machine frame. The screw axis, in this case, lies coincident with the line of fold. A kinematic system can thus be constructed whereby three pairs of bodies, namely the case panel, the cam and the machine frame, are in instantaneous screw motions; with the rotation of the cam relative to the machine frame having a screw motion of zero pitch.

Based on the principle of three bodies in spatial screw motion and the aim to eliminate the backward force component in folding, two folding innovations were investigated; they were the coil cam and the twin cam.

10.2.1 Coil Cam

The coil cam was designed with the principal objective of transferring the folding force from the leading edge to a point on or near the centre of the face of the case panels. Minimization of ink smearing and panel distortion due to a single point contact was inherent in the design.

The design methodology involved the derivation of kinematic equations for the cam profile. Using the screw theory, the kinematic properties of the cam system in spatial motion were established. A high-level software program was written to

perform the transformation calculations. Results were formatted into macro commands and fed into a proprietary CAD software for the generation and automatic display of the cam profile. Computer Aided Manufacture of a prototype was proved feasible on downloading the design data into a CNC machine.

10.2.2 Twin Cam

A design more compact than the coil cam was synthesized in the form of a twin cam. The cam was unique in that it divided the folding operation into two stages, each of which was responsible for a 90° fold. Rolling contact was designed into the cam with the intention to prevent ink smearing. It was realized, however, that computational and manufacturing errors would make perfect rolling impossible to achieve.

10.3 TWIN ROLL CREASER

The requirement for shorter batch runs without increasing the downtime through replacing creasing rolls for various board thicknesses has prompted an investigation into a separable twin roll creaser design. A comprehensive literature survey has been conducted on previous research into creasing. In particular, the mechanism of creasing in relation to the physical properties of the corrugated fibreboards, the approaches adopted in designing creaser profiles, and the methods for crease assessment have been reviewed. From this, a creasing analysis and experimentation have been performed on the twin roll creaser.

10.3.1 Creasing Analysis

Geometrical and finite element models were set up in an attempt to simulate the creasing mechanism for the standard single blade and the twin roll creasers. The

models were shown inaccurate by means of an optical technique (Electronic Speckle Pattern Interferometry). Sliding phenomenon was also demonstrated between the creasing blade and the inner liner of the board samples. Inability to model the fibrous and compliant nature of paper thereby gave way to an experimental approach.

10.3.2 Experimentation

Special creasing and folding test rigs were designed for studying the twin roll creaser. The creasing rig was capable of providing a roll gap accuracy to within ± 0.05 mm, and fine flute positioning and board alignment relative to the flute. Some features of the folding rig were the continuous force sensing over 180° fold and the instant display and characterization of the folding resistance. In all, three major experiments were conducted on the twin roll creaser.

a) Principal Experiment

Three sets of twin roll creasers were studied at various control and noise parameter settings. Results showed that board failures were primarily due to tearing of the inner liner and false creasing. Tearing was further identified to have been originated from the shoulder edge and the tip of the creaser; whereas insufficient crease definition was ultimately responsible for false creasing.

Crease location was found to have a direct influence on the folding resistance, with location 'B' (i.e. the peak of the corrugation) producing the most resistance. Reducing the creaser roll gap or creasing with a sharper profile would, in general, lower the folding resistance for the single-wall boards. Sharp creaser profiles also had the effect of increasing the board's resistance to shear, so long as the inner liner could withstand tearing.

The extreme board grades, namely the 250 TCH double-wall and the 230 CC single-wall boards, were identified as the most problematic. The double-wall

board, as demonstrated in the experiment, needed to have its thickness reduced substantially prior to creasing; its crease performance was most sensitive to the twin roll gap setting. On the other hand, 230 CC boards, fabricated mostly from recycled material, was shown to be more sensitive to moisture conditions.

The twin roll creaser was optimized to produce minimum shear in the board samples. Further work, however, was required to investigate the geometrical parameters of the creaser design and the rheological properties of paper in relation to temperature and humidity.

b) Profile Design Experiment

The shoulder edge and the tip radii were the main areas of investigation. Board samples studied were those which had been identified as causing the most problem. Results showed that the twin roll creaser with rounded-off profiles would still tear the double-wall boards while creasing at the nominal roll gap settings; and that pre-crushing would be indispensable. Profile with the largest shoulder radius, hence resembling a 10° conic profile, was found to have caused the least shear.

c) Optimization Experiment

The objectives in the final experiment were to verify the operations of the twin roll creaser in conjunction with the pre-crusher, and to investigate a combined profile for creasing single- and double-wall boards. Only the 250 TCH double-wall boards were considered.

Optimization was achieved for the rate of defects and the 1st peak folding resistance. The 10° creaser profile was demonstrated as the most robust in minimizing shear deformation and therefore fishtailing. Smallest twin roll gap was also shown to give the least shear, but the largest gap setting would correspond to the least number of defects. This was consistent with the result from the finite element model, which indicated that the highest principal stress would appear in that part of the inner liner lying within the twin gap. A full scale experiment would be required so as to verify the true performance of the optimized creaser.

10.4 REMARKS

Some unique engineering techniques have been adopted in the research. For example, in addition to optimizing the case conversion process, Taguchi method was proved useful as an investigative tool. In the design of the coil cam, the method of running a high-level software program in order to drive a proprietary software by means of macro commands was demonstrated as a powerful technique for iterative design. ESPI, a non-contact optical method for measuring displacements was successfully applied on corrugated fibreboards.

10.5 RECOMMENDATIONS

Further research is recommended in the following areas:

- i) Other means of folding which avoids any ink smearing and backward force component as found in the folding rail arrangement. Any mechanical action on the case panel will inevitably impart physical damage onto the case, be it undesirable force component or print quality. The objective therefore will be to minimize contact between the case and the conversion machine.
- ii) Rheological properties of paper in relation to temperature and humidity, as the experimental results have shown that paper is a hygroscopic material. Other research has shown that paper will become more resilient at elevated temperature. Investigations into the effect of controlled heat and moisture on creasing may lead to understanding not only in the behaviour of paper, but also other fibrous material.
- iii) Optimized twin roll creaser design.
The original intention of reducing the double wall boards from 6.1 mm to 2 mm all in one stage has been shown unsatisfactory. Hence, the twin roll creaser must operate in conjunction with the pre-crush rolls for multi-

layered boards. A full scale experiment is proposed on the grounds that it will verify the relative case strength with creases produced from the single blade and the twin roll creasers, and any dynamic response on creasing at high speed will be available for examination.

APPENDICES

Appendix	Description	Page No.
2a	Tests for corrugated fibreboards and cases.	154
3a	Case sample specification.	158
3b	Folding rail calibration.	159
3c	Glue dispenser calibration.	161
3d	Tables of experimental data.	163
5a	Determination of the third screw axis.	170
5b	Cylindrical coordinate transformation.	178
5c	CAD program listing.	181
6a	Twin cam design optimization	186
8a	Theoretical model on corrugation.	188
8b	Determination of maximum twin roll gap.	190
8c	Fourier harmonics for B-flute corrugation.	195
8d	ESPI equation derivation.	196
9a	Folding rig design specification.	202
9b	L_{18} orthogonal array.	211
9c	Shear test.	212
9d	First experiment results.	216
9e	Defective sample results.	226
9f	S/N ratio ANOVA tables.	227
9g	Optimum settings.	233
9h	Confirmation run results.	235
9i	Profile design for 2nd experiment.	236
9j	Second experiment results.	238
9k	Third experiment results.	242

Appendix 2a

Tests for corrugated fibreboards and cases

Structural property tests:

BS4817 Caliper test to determine the thickness of the liner or corrugated board.

BS4686 Test procedure to determine the flat crush resistance of corrugated fibreboards used in the manufacture of packing cases. The test applies to single faced and single wall (double faced) corrugated fibreboard, but not double wall (double-double faced) corrugated fibreboard. When applied to printed boards, the test may reveal any damage done to the flutes by the printing rolls.

BS2644 More generally known as the Cobb method, this is to determine the water absorbancy of paper and board in a given time. The capacity of water absorption is a function of the various characteristics of paper or board, such as sizing, porosity, etc.

BS3137 Or known as the Mullen burst test, the method determines the bursting strengths of paper and board. The test sample, placed in contact with a circular elastic diaphragm, is rigidly clamped at the periphery but is free to bulge with the diaphragm. Hydraulic fluid is pumped at a constant rate, bulging the diaphragm until the test piece ruptures. The maximum value of the applied hydraulic pressure will be the bursting strength of the test sample. Usually, corrugated boards with kraft liners have higher bursting strength than those with recycled material; this is because of the longer fibres, and hence the higher fibre strength, found in the kraft liners.

BS4816 The determination of the puncture resistance of board is outlined in this method; it applies to all types of heavy boards (as distinct from the test on bursting strength). Test pieces from a representative sample of board are

subjected to puncture by a triangular pyramid puncture head attached to a pendulum. The energy required to force the puncture head completely through the test piece, i.e. to make the initial puncture and to tear and bend open the board, is measured as the puncture resistance.

BS4826:VII Case compression test designed to measure the maximum force sustainable by an erected case. The test differs slightly from the ISO3037 [17].

ISO3037: Determination of edgewise crush resistance. This forms the standard for determining the edge-wise compressive strength of a case. A new method for measuring the edge-wise compressive strength has also been proposed by Jackson et al. [18], through which the load and deformation characteristics can be recorded simultaneously.

Edge-wise compressive strength depends on the compressive properties of the board components as well as its dimensions. Johnson et al. [19] have defined a slenderness ratio λ in terms of the length, thickness and width of a board sample:

$$\lambda = 2\sqrt{3} \frac{l}{h}$$

where l = length of column

h = thickness of column

The slenderness ratio can then serve as a criterion for deciding what mode of compressive failure will incur on the board sample of a specific size. For example, a short column sample with a slenderness ratio of less than 30 will provide the true compressive strength. A medium column of slenderness ratio between 30 and 100 will fail as a result of inelastic buckling. When the slenderness ratio is higher than 100, then long column elastic buckling will take place, giving rise to excessive out-of-plane deformation.

Flexural stiffness is a strength property which refers to the combined board rather than its individual component. Various methods such as the 3-point and 4-point beam tests have been explored by McKee et al. [27] and Hohmann [13], who have subsequently called for the standardization of such tests. Kellicutt [22] has progressed further by examining the constituents of flexural stiffness, which comprise the modulus of elasticity and the moment of inertia. Modulus of elasticity is an inherent property that results from the fibre type. Moment of inertia, however, varies with the dimensions and the arrangement of the individual board components. Both properties can be affected by the type, thickness and weight of the liners and the corrugating medium, the adhesive bond and the manufacturing process.

Glue tests:

TIS 0304-05 "Quality assurance of a corrugating adhesive: starch gelatinization temperature", TAPPI, 1992.

TIS 0304-10 "Troubleshooting a glue lap problem", TAPPI, 1992.

BS1133 "Guidance on adhesives used for conversion of packaging materials and the assembly, sealing and labelling of packages", section 16, 1987.

Other tests:

BS4818 This is a recommendation for determining the creasing quality of carton board as measured by the Packaging Industry Research Association (PIRA) carton board creaser. The test provides a numerical assessment of the creasing qualities of carton board in terms of the depth of crease and the width of groove. However, subjective judgement is made on the foldability of boards once creased.

ISO R 287 A method for determining the moisture content of paper boards. The moisture content is expressed in terms of the mass of water originally present in the board.

Appendix 3a

Case Sample Specification

Customer description: RC1 3028 Lynher Mis-shapes

Colour: black

Style	Description	Case	Regular	Glued
Manuf	Seq 101	1	512	1
	Corrugation	Case-maker		

Board: 300YT, flute B
Quantity: 5000
SQM 753
KGS 362
No off 1 (one-off for experimental purposes)

OALL DIM 458 1646
INT DIM 453 331 98

RIB SCORE
177 104 177

CUMUL RIB SCORE
137 339 476

PANEL SCORE
28 273 499 273 497

(N.B. All dimensions in mm.)

Property test on one of the case samples selected from CR2:

Cobb - outer liner 83 gsm, inner liner 74 gsm

Flat Crush - 408 kNm²

Caliper - 2.9 mm

Mullen - 1075 kPa

Puncture - 4.3 joules

Case compression - 2.6 kN

Pin adhesion - 140 (in-house test)

Appendix 3b

Folding rail calibration

The objective is to adjust the position of the first set of folding rails (i.e folding from 0° to 90°).

The folding section is divided into the left-hand side (LHS) and the right-hand side (RHS) in the direction of board travel. Each folding rail progresses from a horizontal to a vertical position, and is held rigidly at three points. The first point of contact, being a horizontal one, allows the rail clamp to slide into or out of the folding section. The third point of contact enables the clamp to be raised or lowered in the vertical direction. The middle point of contact can be varied in both the vertical and horizontal directions.

Before conducting the experiment, the position of the rail was noted down in terms of the displacement measured between the clamps and the end of the supporting rods. It so happened that the rails were set close to the folding hinge. This was subsequently used as the first rail setting. Afterwards, the rails were adjusted to the other extreme positions (i.e away from the folding hinge) for the next set of experiments. Finally, the third set of rail settings was chosen to be somewhere between the previous two positions.

The actual experimental settings in mm taking the clamp position as origin were as follows:

		Point of contact			
	Setting	First	Second		Third
			x	y	
LHS:	A1	166	168	90	173
	A2	96	98	65	103
	A3	124	124	101	243
RHS:	A1	220	170	133	248
	A2	150	100	90	108
	A3	185	100	95	178

N.B With regard to A2 and A3, the second positions of the folding rails were set in their natural position when the rails were suspended from the horizontal and vertical end-points. During the confirmation run, it was impossible to return the second position of A1 to its original setting; for this reason, the rails were clamped in their natural positions as in the case of A2 and A3.

Appendix 3c

Glue Dispenser Calibration

Two calibration tests were performed in order to establish gluing as a controllable process factor.

The first calibration test was performed on the glue flow adjust situated at the front panel of the VC-352 unit. Strips of masking tapes were weighed prior to being attached onto the glue flaps of the trial boards. The glue flow adjust was then set at a maximum value. The trial boards were subsequently run through the machine at a constant speed. The machine was stopped before the flaps were closed and bonded together. At this stage, the masking tapes, which were carrying the glue, would be carefully detached from the case's glue flaps and reweighed. The change in mass would represent approximately the amount of glue applied at that particular setting. The whole procedure was repeated, but with the glue flow adjust being set at a minimum.

The results for the first calibration were as follows:

	Mass before / g	Mass after / g	Difference / g
Maximum	0.67	1.00	0.33
	0.66	0.95	0.29
	0.64	0.95	0.31
Minimum	0.72	1.00	0.28
	0.75	1.06	0.31
	0.63	0.91	0.28

The results conclusively showed that the glue flow adjust would not be suitable for providing three levels of glue amount settings. Incidentally, 0.01g of board fibre was recorded on the adhesive side of the masking tape after being removed from the glue panel.

The second glue calibration test was performed using the gauge pressure valve inside the EPC unit. The pressure line supplied air which would in turn eject the glue onto the glue flaps. Three levels of pressure settings were chosen and the same glue weighing technique was employed. The results were as follows:

Gauge pressure	Mass before / g	Mass after / g	Difference / g
20 Psi	0.71	----	----
	0.67	0.75	0.08
	0.69	0.77	0.08
35 Psi	0.68	0.90	0.22
	0.67	0.90	0.23
	0.67	0.90	0.23
50 Psi	0.68	0.92	0.24
	0.63	0.90	0.23
	0.61	0.93	0.32
	0.64	0.95	0.31
	0.65	0.96	0.31

The results from the second test showed that the pressure flow regulator would be a better glue controller.

Appendix 3d

Tables of experimental data

1. Experimental Results

No	1	2	3	4	5	6	7	8	9	10
1	1	0.5	3	15	14	1	10.5	1	1	7
	1	1	0	-1	-1	1	0.5	1	1	1.5
2	1	-0.5	0	0	0	0	0	1.5	4	2
	0	-1	0	-1	-1	0	-1	0.5	3.5	1.5
3	0	2	2	1	0.5	0	0	0	0.5	0.5
	3	1.5	2	1	1.5	1	0.5	2.5	2	1
4	5.5	1	3	1.5	3	10	2	5	3	10
	-2.5	0	0	0	-0.5	0	-1	-1	-1.5	-1
5	3	1.5	2	1	0.5	1	1.5	1.5	2	2
	3	1	2	1	1	2	1.5	1.5	2	2
6	1.5	2	3	2.5	3	1.5	2	1	1	1
	3	3	0	3.5	3	2	1.5	0	1	1
7	18	0.5	0	8	0	0	1	2	1	1.5
	-1.5	0.5	0	2	1.5	1	2	1	0	1.5
8	2.5	4.5	1	3	0.5	3	1	0.5	0.5	3
	1	0.5	1.5	-1	0.5	1	1	0	0.5	1
9	2	2	2	3	2	2	2	1	2	1
	2	2	2	3.5	3.5	2	0	5	2.5	2

2. S/N values for the various control factors.

Expt. no.	Samples	Ortho. array	Y_{tot}	S/N
1	20-11a	1111	54	-17.7
	20-11b		9	0.2
2	7-16a	1222	9	-3.7
	7-16b		9.5	-2.7
3	1-10a	1333	6.5	0.1
	1-10b		16	-4.9
4	1-10a	2123	44	-14.6
	1-10b		7.5	-0.7
5	1-10a	2231	16	-4.8
	1-10b		17	-5.1
6	1-10a	2312	18.5	-6.0
	1-10b		18	-6.8
7	1-10a	3132	32	-16.0
	1-10b		11	-2.3
8	1-10a	3213	19.5	-7.5
	1-10b		8	1.0
9	3-12a	3321	19	-5.9
	3-12b		21.5	-7.4

3. Combined S/N ratios at various control operation levels.

Factor	Y _{tot}	No.	Y _{mean}	S/N	No.	S/N _{ave}	S/N _{tot}
A1	69.5	30	2.3	-21.3	3	-7.1	
	34.5	30	1.1	-7.4	3	-2.5	-9.6
A2	78.5	30	2.6	-25.4	3	-8.5	
	42.5	30	1.4	-12.6	3	-4.2	-12.7
A3	70.5	30	2.4	-29.4	3	-9.8	
	40.5	30	1.4	-8.7	3	-2.9	-12.7
B1	130	30	4.3	-48.3	3	-16.1	
	27.5	30	0.9	-2.8	3	-0.9	-17.0
B2	44.5	30	1.5	-16.0	3	-5.3	
	34.5	30	1.1	-6.9	3	-2.3	-7.6
B3	44	30	1.5	-11.8	3	-3.9	
	55.5	30	1.9	-19.1	3	-6.4	-10.3
C1	92	30	3.1	-31.2	3	-10.4	
	35	30	1.2	-5.6	3	-1.9	-12.3
C2	72	30	2.4	-24.2	3	-8.1	
	38.5	30	1.3	-10.8	3	-3.6	-11.7
C3	54.5	30	1.8	-20.6	3	-6.9	
	44	30	1.5	-12.3	3	-4.1	-11.0
D1	89	30	3.0	-28.4	3	-9.5	
	47.5	30	1.6	-12.3	3	-4.1	-13.6
D2	59.5	30	2.0	-25.7	3	-8.6	
	38.5	30	1.3	-11.8	3	-3.9	-12.5
D3	70	30	2.3	-22.0	3	-7.3	
	31.5	30	1.1	-4.6	3	-1.5	-8.9

4. ANOVA table for S/N ratio

Combined Response

Factor	DoF	Sum of sq.	Mean square	F
A - Rail	2	19.2	9.6	7.8
B - Glue	2	14.1	70.7	57.9
C- Speed	2	2.4	1.2	-----
D - Crease	2	36.1	18.1	14.8
Total	8	199.1		
(Error)	(2)	(2.4)	(1.2)= s^2	

Panel 'a' Response

Factor	DoF	Sum of sq.	Mean square	F
A - Rail	2	10.9	5.4	0.6
B - Glue	2	267.4	133.7	14.1
C- Speed	2	18.9	9.4	-----
D - Crease	2	7.3	3.6	0.4
Total	8	304.7		
(Error)	(2)	(18.9)	(9.5)= s^2	

Panel 'b' Response

Factor	DoF	Sum of sq.	Mean square	F
A - Rail	2	4.7	2.3	0.6
B - Glue	2	49.0	24.5	6.1
C- Speed	2	7.9	3.9	-----
D - Crease	2	12.5	6.2	1.6
Total	8	74.3		
(Error)	(2)	(7.9)	(3.9)= s^2	

5. Alternative mean and variance analysis.

Expt. no	Mean (μ)	Variance (σ^2)
1	5.4	33.5
	0.5	0.8
2	0.8	1.9
	0.1	2.1
3	0.7	0.6
	1.6	0.6
4	4.4	10.7
	-0.8	0.7
5	1.6	0.5
	1.7	0.4
6	1.9	0.6
	1.8	1.7
7	3.2	32.7
	0.8	1.2
8	1.9	2.0
	0.6	0.5
9	1.9	0.3
	2.1	0.9

cont./..

	nu_{tot}	no.	nu_{ave}	nu_{a,b}	Var	no.	Var_{ave}	Var_{a,b}
A1	6.9	3	2.3		36.1	3	12.0	
	2.3	3	0.8	3.0	3.4	3	1.1	13.2
A2	7.8	3	2.6		11.8	3	3.9	
	2.8	3	0.9	3.5	2.8	3	0.9	4.8
A3	7.1	3	2.4		35.0	3	11.7	
	3.5	3	1.2	3.5	2.6	3	0.9	12.5
B1	13.0	3	4.3		76.9	3	25.6	
	0.6	3	0.2	4.5	2.6	3	0.9	26.5
B2	4.4	3	1.5		4.4	3	1.5	
	2.4	3	0.8	2.3	2.9	3	1.0	2.5
B3	4.4	3	1.5		1.6	3	0.5	
	5.6	3	1.9	3.3	3.2	3	1.1	1.6
C1	9.2	3	3.1		36.2	3	12.1	
	2.9	3	1.0	4.0	2.9	3	1.0	13.0
C2	7.1	3	2.4		12.9	3	4.3	
	1.5	3	0.5	2.9	3.7	3	1.2	5.5
C3	5.5	3	1.8		33.8	3	11.3	
	4.1	3	1.4	3.2	2.2	3	0.7	12.0
D1	8.9	3	3.0		34.4	3	11.5	
	4.3	3	1.4	4.4	2.1	3	0.7	12.2
D2	5.9	3	2.0		35.2	3	11.7	
	2.8	3	0.9	2.9	4.9	3	1.6	13.4
D3	7.0	3	2.3		13.3	3	4.4	
	1.5	3	0.5	2.8	1.8	3	0.6	5.0

6. Confirmation Runs

CR1 1-10a 3.5 3.0 2.0 3.5 2.0 3.0 3.5 5.0 3.0 5.5 $Y_{tot}=34.0$
S/N = -5.3

1-10b 3.0 2.0 0.5 2.0 4.5 1.0 5.0 2.5 3.5 4.0 $Y_{tot}=28.0$
S/N=-4.5

CR2 1-10a 4.0 1.0 2.0 0.5 0.5 0.0 2.0 1.0 0.5 1.5 $Y_{tot}=13.0$
S/N=-4.6

1-10b 2.5 1.0 1.0 0.0 0.0 0.0 2.5 0.5 0.0 0.0 $Y_{tot}=7.50$
S/N=-1.7

Combined S/N ratio for CR2 = -6.3

Appendix 5a

Determination of the Third Screw Axis

Referring to publications by Hunt [15] and Phillips [36], the following section provides a summary on the three axes theorem and the derivation of the relevant equations. Scaled parameters from the prototype model are then substituted into the appropriate equations in order to determine the characteristics of the third screw axis, ISA₃₂, between the coil cam and the case panel.

Notation:

- ω = angular velocity of a body in the right hand screw convention (ω_{12} = angular velocity of body 2 with respect to body 1).
- h = pitch of screw (+ve if right-handed).
- τ = linear velocity along an instantaneous screw axis, ISA.
- v = instantaneous linear velocity of a rigid body.
- z = displacement along the cylindroid axis with respect to its origin.
- ψ = angles as measured clockwise from a specified line to the relevant ω vector that radiates outward from the z-axis.

Three Axes Theorem

At an instant during the relative spatial motion of two rigid bodies 1 and 2, an instantaneous screw axis ISA₁₂ can be uniquely defined, about or along which the body 2 is said to be screwing with respect to body 1. All points I₂ in the body 2 instantaneously resident in ISA₁₂ have equal linear velocities τ_{12} relative to 1 along the ISA, while all other points in the body 2 have velocities other than this. The linear velocity with respect to 1 of body 2, τ_{12} , can be calculated as follows:

$$\tau_{12} = h_{12}\omega_{12}(1)$$

where, ω_{12} = angular velocity with respect to 1 of body 2
 h_{12} = instantaneous screw pitch

In general, for finite motion, the location in space and the h-value of an ISA changes continuously.

Rigid body motion can be generalized further such that the instantaneous linear velocity with respect to body 1 of any point R_2 in body 2 is given by:

$$v_{1R_2} = (\omega_{12} \times r) + \tau_{12} \dots\dots\dots(2)$$

where, r = position vector of R_2 originating at a point O chosen anywhere on ISA_{12}

Figure 5a.1 (with acknowledgement given to Hunt [15] for the reproduction of the figure) shows two rigid bodies in relative spatial motion. ω_{12} is a free vector, therefore it may be drawn anywhere with significance; v_{1R_2} and τ_{12} however are bound vectors such that they must be drawn from the points in body 2 to which they specifically refer.

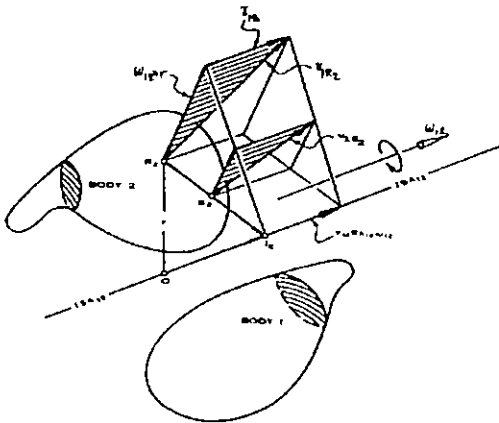


Fig. 5a.1 Two rigid bodies in spatial motion.

When three bodies are in relative spatial motion, the vector polygon of the three angular velocities will close; hence:

$$\omega_{12} + \omega_{23} + \omega_{31} = 0 \dots\dots\dots(3)$$

This vector polygon is in the form of a planar triangle, which means that the three ISA's reside respectively in three planes all parallel to one another. Phillips and

Hunt [35] have also shown that the three ISA’s have the same line as common perpendicular. By taking the directed distance along the common perpendicular from ISA₁₂ to ISA₂₃ to be z_{12,23}, it can be shown graphically that:

$$\begin{aligned} \omega_{21} \times z_{21,13} + \omega_{32} \times z_{32,13} + \Sigma \tau &= 0 \\ \omega_{13} \times z_{13,32} + \omega_{21} \times z_{21,32} + \Sigma \tau &= 0 \\ \omega_{32} \times z_{32,21} + \omega_{13} \times z_{13,21} + \Sigma \tau &= 0 \dots\dots\dots(4) \end{aligned}$$

where, $\Sigma \tau = \tau_{12} + \tau_{23} + \tau_{31}$
 $= h_{12}\omega_{12} + h_{23}\omega_{23} + h_{31}\omega_{31}$

Hence, the three axes theorem states that, for three rigid bodies in spatial motion, their instantaneous screw axes must reside in parallel planes and share a common perpendicular. Kennedy-Aronhold’s theorem [23] is a special case whereby all the ISA’s are orientated parallel to each other.

The three axes theorem is useful from the practical point of view. For example, if properties about two ISA’s are known, then those of the third ISA can also be identified. It is interesting to note that while the unique solution for ‘ω’ depends upon the actual values assigned to the other two ‘ω’, the corresponding values of the directed distance, pitch and axis orientation for the third ISA will depend solely upon the ω-ratio of the two known ISA’s.

Derivation of the third ISA and its properties

If the three bodies are represented as follows:

Body	Description
1	static frame of the folding section
2	coil cam
3	case panel being folded

a cylindroid system can be drawn with the corresponding ISA’s as shown in Figure 5a.2.

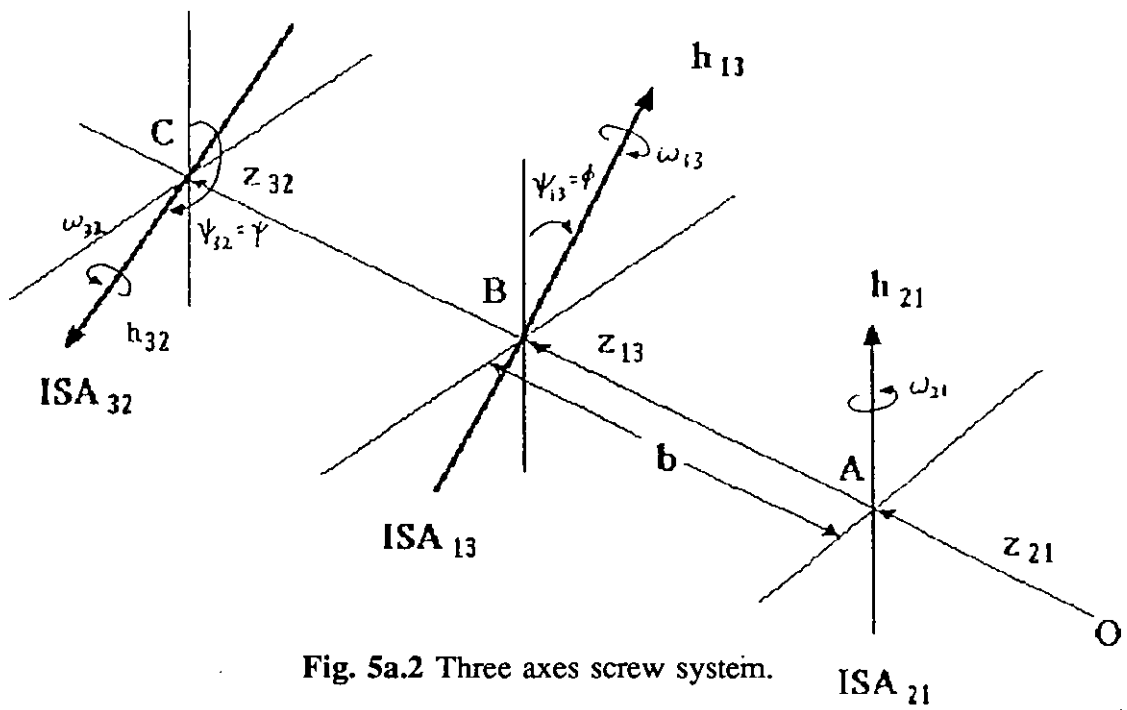


Fig. 5a.2 Three axes screw system.

The known distance AB between the specified axes is:

$$|z_{13} - z_{21}| = b$$

and the known angle between them is:

$$\psi_{21,13} = \psi_{13} - \psi_{21} = \phi$$

Figure 5a.3 shows the velocity polygon for the three angular velocities:

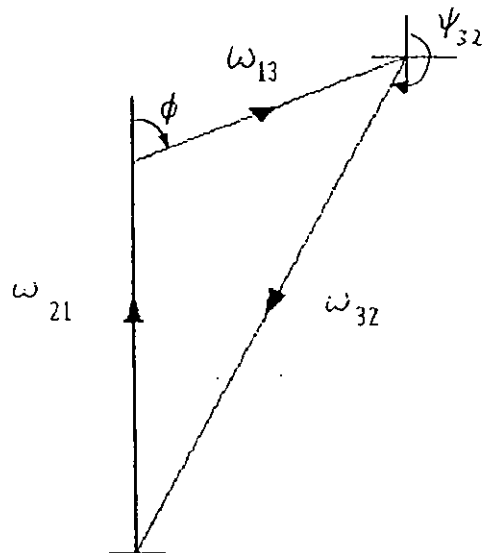


Fig. 5a.3 Angular velocity polygon.

From the three axes theorem, the sum of the angular velocities can be expressed in terms of equation (3). Also, from Figure 5a.3, the following expressions can be derived geometrically:

$$\tan \psi_{32} = \frac{\omega_{13} \sin \phi}{\omega_{21} + \omega_{13} \cos \phi}$$

hence,

$$\frac{\omega_{21}}{\omega_{13}} = \frac{\sin \phi}{\tan \psi_{32}} - \cos \phi \dots\dots\dots(5)$$

From the Sine Rule,

$$-\frac{\omega_{32}}{\omega_{13}} = \frac{\sin \phi}{\sin \psi_{32}} \dots\dots\dots(6)$$

Expressing $|\omega_{13} \times z_{13,32}|$ in equation (4) as $\omega_{13}(z_{32} - z_{21} - b)$, and resolving perpendicularly to ISA₃₂ will give:

$$-h_{32}\omega_{32}\sin\psi_{32} + \omega_{21}(z_{32}-z_{21}) + \omega_{13}(z_{32}-z_{21})\cos\phi - \omega_{13}b.\cos\phi-h_{13}\omega_{13}\sin\phi = 0 \dots\dots\dots(7)$$

similarly, resolving along ISA₃₁ will give:

$$-h_{32}\omega_{32}\cos\psi_{32} - h_{21}\omega_{21} - \omega_{13}(z_{32}-z_{21}).\sin\phi + \omega_{13}b.\sin\phi - h_{13}\omega_{13}\cos\phi = 0 \dots\dots\dots(8)$$

Solving equations (5), (6), (7) and (8) simultaneously for z_{23} , h_{23} , ψ_{23} and ω_{23} , a unique solution will be derived in terms of ω_{31} and ω_{12} for ISA₂₃. Dividing equations (7) and (8) by ω_{12} and then substituting (5) and (6) will result in the following equations:

$$z_{32} - z_{21} = [b.\cot\phi + (h_{13} - h_{32})]\tan\psi_{32} \dots\dots\dots(9)$$

$$h_{32} - h_{21} = [(z_{32} - z_{21}) - (h_{21} - h_{13})\cot\phi - b]\tan\psi_{32} \dots\dots\dots(10)$$

which can be explicitly expressed as:

$$z - z_{21} = [b \cot \phi - (h_{21} - h_{13}) \sin \psi \cos \psi + [b + (h_{21} - h_{13}) \cot \phi] \sin^2 \psi] \dots (11)$$

$$h - h_{21} = [b \cot \phi - (h_{21} - h_{13}) \sin^2 \psi - [b + (h_{21} - h_{13}) \cot \phi] \sin \psi \cos \psi] \dots (12)$$

The constants in equations (11) and (12) can be represented by:

$$[b + (h_{21} - h_{13}) \cot \phi] = 2P \sin \alpha \dots (13)$$

$$[b \cot \phi - (h_{21} - h_{13})] = 2P \cos \alpha \dots (14)$$

where, $2P$ = length of the cylindroid.

From equations (13) and (14), P and α can be calculated as follows:

$$P = \frac{\sqrt{b^2 + (h_{31} - h_{12})^2}}{2 |\sin \phi|} \dots (15)$$

$$\alpha = \tan^{-1} \left[\frac{b + (h_{31} - h_{12}) \cot \phi}{b \cot \phi - (h_{31} - h_{12})} \right] + n\pi \dots (16)$$

where 'n' is even if numerator in bracket term is positive, and odd, if it is negative.

Also, substituting equations (13) and (14) back into equations (11) and (12) will finally give:

$$z = z_{21} + P[\sin \alpha + \sin(2\psi - \alpha)] \dots (17)$$

$$h = h_{21} + P[\cos \alpha - \cos(2\psi - \alpha)] \dots (18)$$

Third axis properties from scaled prototype

During the initial design stage, a coil cam prototype, as shown in Figure 5a.4, has been constructed in order to estimate some of the scaled design parameters.

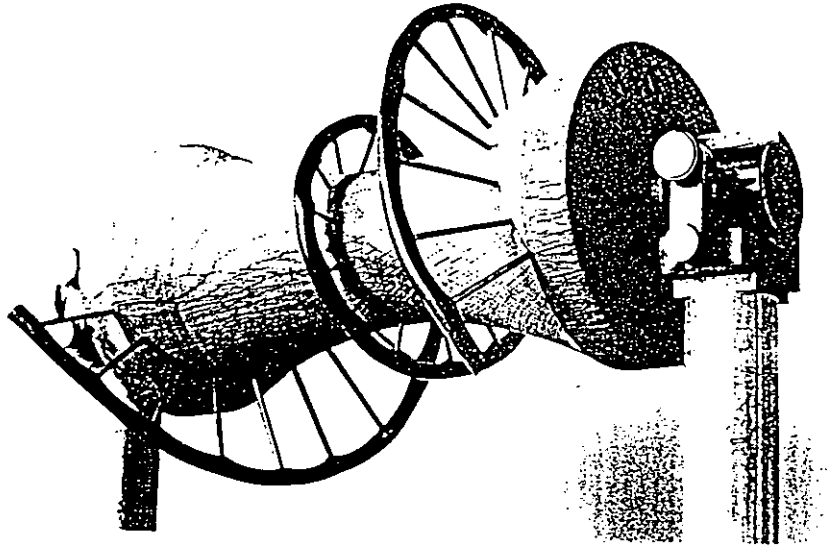


Fig. 5a.4 Coil cam prototype.

Based on the scaled prototype, the following design parameters have been arbitrarily chosen:

$$\omega_{13} = 1 \text{ rad / s}$$

$$\omega_{21} = 3 \times \omega_{31} = 3 \text{ rad / s}$$

$$h_{13} = 100 \text{ mm / rad}$$

$$h_{12} = 0$$

$$b = 50 \text{ mm}$$

$$\phi = 45^\circ$$

Substituting the above values into equations (15), (4), (6) and (2) will yield the following results:

$$P = 79.06 \text{ mm}$$

$$\psi_{32} = 10.8^\circ$$

$$\omega_{32} = -3.77 \text{ rad / s}$$

$$h_{32} = -29.36 \text{ mm}$$

The velocity polygon is shown in Figure 5a.5:

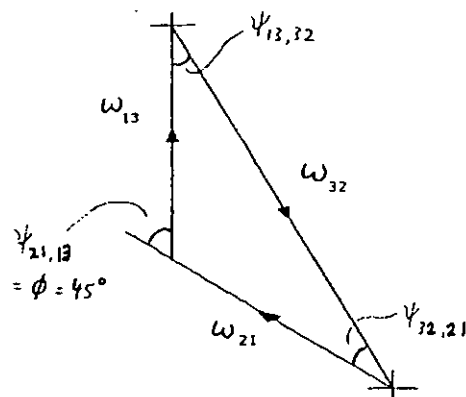


Fig. 5a.5 Coil cam angular velocity polygon.

Finally, from Sine Rule, the angle $\psi_{32,21}$ can be derived as follows:

$$\begin{aligned} \psi_{32,21} = \alpha_{31} &= \sin^{-1}\left[\frac{\omega_{13}}{\omega_{32}} \sin(135)\right] \\ &= 10.81^\circ \end{aligned}$$

The same results can be arrived at using screw coordinates.

Appendix 5b

Cylindrical Coordinate Transformation

The three angles (ϕ, θ, ψ) shown in Figures 5b.1 and 5b.2 are those of roll, pitch and yaw (refer to Paul [32]).

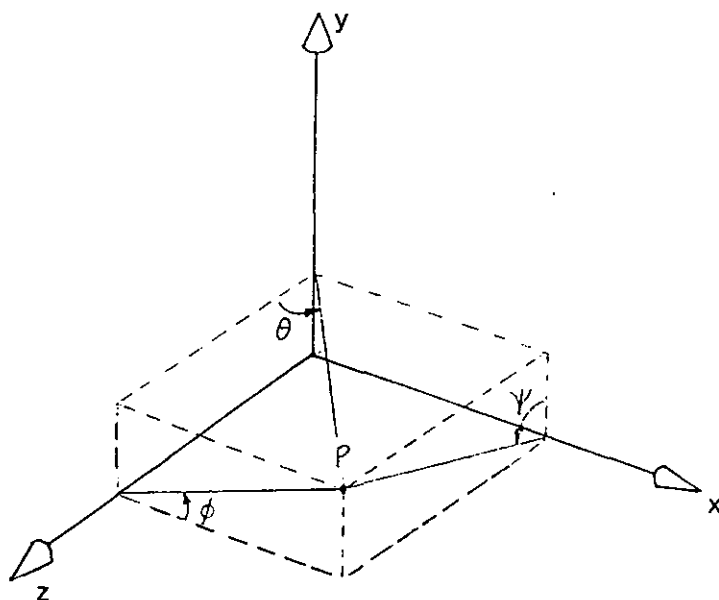


Fig. 5b.1 Coordinate frame.

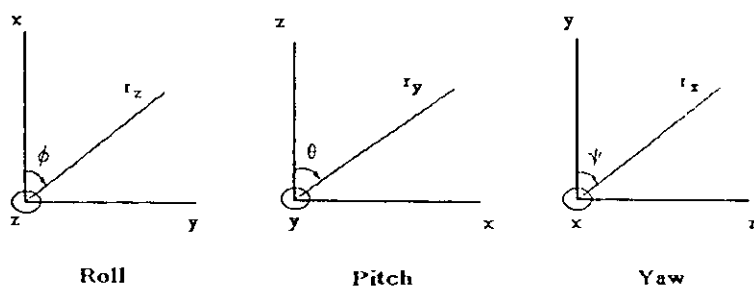


Fig. 5b.2 Cylindrical components in Cartesian frame.

Transforming the coordinates (x, ψ, r_x) from a cylindrical frame about the x-axis to one about the z-axis will require the following equations:

$$\begin{aligned} z &= r_x \sin \psi \\ \phi &= \text{atan2}\left(\frac{r_x \cos \psi}{x}\right) \\ r_z &= \sqrt{x^2 + r_x^2 \cos^2 \psi} \end{aligned}$$

the inverse of these are as follows:

$$\begin{aligned} x &= r_z \cos \phi \\ \psi &= \text{atan2}\left(\frac{z}{r_z \sin \phi}\right) \\ r_x &= \sqrt{z^2 + r_z^2 \sin^2 \phi} \end{aligned}$$

Other transformations are as follows:

i) x-axis to y-axis

$$\begin{aligned} y &= r_x \sin \psi \\ \theta &= \text{atan2}\left(\frac{r_x \cos \psi}{x}\right) \\ r_y &= \sqrt{x^2 + r_x^2 \cos^2 \psi} \end{aligned}$$

ii) y-axis to x-axis

$$\begin{aligned} x &= r_y \cos \theta \\ \psi &= \text{atan2}\left(\frac{y}{r_y \sin \theta}\right) \\ r_x &= \sqrt{y^2 + r_y^2 \sin^2 \theta} \end{aligned}$$

iii) y-axis to z-axis

$$\begin{aligned} z &= r_y \sin \theta \\ \phi &= \text{atan2}\left(\frac{r_y \cos \theta}{y}\right) \\ r_z &= \sqrt{y^2 + r_y^2 \cos^2 \theta} \end{aligned}$$

iv) z-axis to y-axis

$$y = r_z \cos \theta$$

$$\theta = \operatorname{atan2}\left(\frac{z}{r_z \sin \phi}\right)$$

$$r_y = \sqrt{z^2 + r_z^2 \sin^2 \phi}$$

Appendix 5c

CAD Program Listing

1. Cam profile optimization program in Unix-C.
2. Input lists generated the optimization program.
3. DUCT Macro commands for importing input lists in order to generate coil cam profile.

```

#include <math.h>
#include <stdio.h>
#include <assert.h>
#define FALSE 0
#define TRUE 1

double x[250],y[250],z[250],r_fac[250],psi_dinc[250]; /* 1.4 degree accuracy */
double xp[250],yp[250],zp[250],xq[250],yq[250],zq[250];
double pi,a,p,rx_a,psi_ab,z32,alpha32,poq,w_ratio;
int delta,count;

void data_input(); void transform(); void data_output(); void data_pq();

main(){
    pi=4*atan(1);
    poq=0;
    data_input();
    transform();
    data_output();
    poq=(-atan(3.0/4.0))*180/pi;
    rx_a=sqrt(pow(rx_a,2)+900);
    transform();
    data_pq();
}

void data_input(){
    printf("\n3D CAM PROFILE OPTIMIZATION \n\n");
    printf("Enter values for the following:\n");
    printf("Angular vel. ratio = ");
    scanf("%lf",&w_ratio);
    printf("Offset distance, a = ");
    scanf("%lf",&a);
    printf("Pitch of ISA 1, p = ");
    scanf("%lf",&p);
    printf("Radial distance of panel, rx = ");
    scanf("%lf",&rx_a);
    printf("Angle psi(ab) = ");
    scanf("%lf",&psi_ab);
    printf("Cylindroid axis distance, z32 = ");
    scanf("%lf",&z32);
    printf("Twist angle alpha32 = ");
    scanf("%lf",&alpha32);
    do {
        printf("Number of angular increments = ");
        scanf("%ld",&delta);
    }
    while (((delta > 2) && (delta < 252)) == FALSE);
}

void transform(){
    double xa[250],xb[250],psia[250],psib[250],zb[250],rx_tmp;
    double phi_b[250],rz_b[250],zd[250],phi_d[250],psi_d[250],rx_d[250];
    int count = 1;

    for (count=1; count<=delta+1; count++){
        if (poq==0) {xq[count]=0; yq[count]=0; zq[count]=0;}
        if (count==1) xa[count]=(-p*pi/2);
        else xa[count]=xa[count-1]+100*pi/delta;

        /* Axis x(a) to axis x(b) */
        xb[count]=xa[count]-a;
        psia[count]=(count-1)*180/delta+poq;
        psib[count]=(psia[count]-psi_ab)*pi/180;

        /* Axis x(b) to axis z(b) */
        zb[count]=rx_a*sin(psib[count]);

```

```

phi_b[count]=atan2(rx_a*cos(psi_b[count]),xb[count]);
rz_b[count]=sqrt(pow(xb[count],2)+pow(rx_a,2)*pow(cos(psi_b[count]),2));

/* Axis z(b) to axis z(d) */
zd[count]=zb[count]-z32;
phi_d[count]=phi_b[count]-alpha32*pi/180;

/* Axis z(d) to axis x(d) */
/* x,y,z = P coordinates in 1st loop */
/* = PQ direction vector in 2nd loop */
x[count]=rz_b[count]*cos(phi_d[count]);
psi_d[count]=180*atan2(zd[count],rz_b[count]*sin(phi_d[count]))/pi
+(count-1)*180*w_ratio/delta;
rx_d[count]=sqrt(pow(zd[count],2)+pow(rz_b[count]*sin(phi_d[count]),2));
y[count]=rx_d[count]*cos(psi_d[count]*pi/180);
z[count]=rx_d[count]*sin(psi_d[count]*pi/180);
if (pq==0) {xp[count]=x[count]; yp[count]=y[count]; zp[count]=z[count];}
else {xq[count]=x[count]; yq[count]=y[count]; zq[count]=z[count];}

/* Rotation and scaling factors for DUCT */
r_fac[count]=rx_d[count];
if (count==1) psi_dinc[1]=psi_d[count];
else psi_dinc[count]=psi_d[count]-psi_d[count-1];

} /* End of FOR loop */

}

void data_output(){
FILE *data1,*data2,*data3;
data1=fopen("data1.com","w+");
fprintf(data1,"INPUT LIST @D1 %d \n", (delta+1)*4);
for (count=1; count<=delta+1; count++){
if (count == 1) {fprintf(data1,"APPEND LIST @D1 %f %f %f %d \n",y[count],
z[count],-(psi_dinc[count]-90),count);}
else {if (count != delta+1) fprintf(data1,"APPEND LIST @D1 %f %f %f %d \n",
y[count],z[count],-psi_dinc[count],count);
else fprintf(data1,"APPEND LIST @D1 %f %f %f %d",y[count],z[count],
-psi_dinc[count],count);
}
}
fclose(data1);

data2=fopen("data2.com","w+");
fprintf(data2,"INPUT LIST @D2 %d \n", (delta+1)*2);
for (count=1; count<=delta+1; count++){
if (count != delta+1)
fprintf(data2,"APPEND LIST @D2 %d %f \n",count,x[count]);
else fprintf(data2,"APPEND LIST @D2 %d %f",count,x[count]);
}
fclose(data2);

}

void data_pq(){
FILE *data3;
data3=fopen("data3.com","w+");
fprintf(data3,"INPUT LIST @D3 %d \n", (delta+1)*6);
for (count=1; count<=delta+1; count++){
if (count != delta+1)
fprintf(data3,"APPEND LIST @D3 %f %f %f %f %f %f \n",xp[count],
yp[count],zp[count],xq[count]-xp[count],yq[count]-yp[count],
zq[count]-zp[count]);
else fprintf(data3,"APPEND LIST @D3 %f %f %f %f %f %f",xp[count],yp[count],
zp[count],xq[count]-xp[count],yq[count]-yp[count],zq[count]-zp[count])
fclose(data3);
}
}

```

cont./..

2. Input lists generated the optimization program.

```
INPUT LIST @D1 60
APPEND LIST @D1 -7.711547 -6.687407 229.068370 1
APPEND LIST @D1 -3.334692 -9.647238 -30.000000 2
APPEND LIST @D1 -0.362589 -0.209341 40.931630 3
APPEND LIST @D1 -7.065869 4.330099 -298.499241 4
APPEND LIST @D1 -14.641016 -1.009084 -35.443446 5
APPEND LIST @D1 -14.364277 -12.394408 -36.847017 6
APPEND LIST @D1 -4.131927 -20.708441 -37.926333 7
APPEND LIST @D1 10.000000 -18.637033 -39.500461 8
APPEND LIST @D1 18.182761 -6.408167 -42.369469 9
APPEND LIST @D1 14.058777 7.781973 -48.379933 10
APPEND LIST @D1 0.000000 13.133052 298.965901 11
APPEND LIST @D1 -13.463274 4.024598 -73.356933 12
APPEND LIST @D1 -14.120288 -14.941658 -63.261972 13
APPEND LIST @D1 3.334692 -30.352762 -49.650726 14
APPEND LIST @D1 18.064309 -24.618917 -30.000000 15
```

```
INPUT LIST @D2 30
APPEND LIST @D2 1 40.000000
APPEND LIST @D2 2 50.000000
APPEND LIST @D2 3 76.322124
APPEND LIST @D2 4 103.255250
APPEND LIST @D2 5 130.687256
APPEND LIST @D2 6 158.472024
APPEND LIST @D2 7 186.439395
APPEND LIST @D2 8 214.406766
APPEND LIST @D2 9 242.191534
APPEND LIST @D2 10 269.623540
APPEND LIST @D2 11 296.556666
APPEND LIST @D2 12 322.878790
APPEND LIST @D2 13 348.519431
APPEND LIST @D2 14 373.454548
APPEND LIST @D2 15 383.454548
```

```
INPUT LIST @D3 52 13
APPEND LIST @D3 1 -162.397147 -0.834692 -19.306496
APPEND LIST @D3 2 -136.699245 8.150120 -5.294526
APPEND LIST @D3 3 -110.302151 2.472919 6.709628
APPEND LIST @D3 4 -83.281457 -9.641016 7.356079
APPEND LIST @D3 5 -55.755250 -16.787902 -3.020186
APPEND LIST @D3 6 -27.876069 -12.497090 -15.878812
APPEND LIST @D3 7 0.179492 0.669873 -21.225224
APPEND LIST @D3 8 28.222821 13.438318 -14.920876
APPEND LIST @D3 9 56.066139 16.767437 -1.668624
APPEND LIST @D3 10 83.535296 8.660254 8.303423
APPEND LIST @D3 11 110.481643 -3.848111 6.689164
APPEND LIST @D3 12 136.792157 -9.120288 -6.281404
APPEND LIST @D3 13 162.397147 0.834692 -20.693504
```

cont./..

3. DUCT Macro commands for importing input lists in order to generate coil cam profile.

```
$$ DUCT VERSION 4.4 COMMAND FILE DD5 22 Sep. 1992 15.34.51
$$ Command file to display cam duct
RUN COMFILE DATA3
EDIT INTB (ITEM @D3 1)
EDIT INTC (ITEM @D3 2)
EDIT INTA 3
LOOP LIST @D3
INPUT SPINE ITEM @D3 (INTA) X ITEM @D3 (INTA+1) Y ITEM @D3 (INTA+2) $
Z ITEM @D3 (INTA+3)
EDIT INTA (INTA+4)
IF (INTA>INTB) GOTO 20
NEXT
$20 ABANDON LIST
RUN COMFILE CIRCLE
EDIT INTD 1
LOOP LIST (1 TO INTC)
KEEP SECTION (INTD)
EDIT INTD (INTD+1)
NEXT
RUN COMFILE ISOM
EDIT DUCT COLOUR 1
DRAW DUCT
DRAW SPINE
INPUT REGISTER @DIREC 1 0 0
ROTATE TRANSFORM
ERASE
DRAW DUCT
DRAW TRANSFORM
```

Appendix 6a

Twin cam design optimization

A 3-factors by 3-levels Taguchi experiment was performed using an L₉ orthogonal array. The factors and their levels were as follows:

Factors \ Levels	1	2	3
A. Contact length, 'l' /mm	40	50	60
B. Hinge length, 'c' /mm	20	30	40
C. Cam initial radius, a /mm	10	15	20

Since there were four factors in an L₉ orthogonal array, and only three were needed to be optimized, one factor column was therefore left empty as dummy.

Two criteria, designed to minimize the final cam radius and the cam velocity ratio, were studied in the optimization process. The signal-to-noise ratios were as follows:

$$\begin{aligned}
 S/N_{(r=300)} &= -10\log_{10}r^2 \\
 S/N_{(\psi)} &= -10\log_{10}(\frac{\psi_0}{\psi_{300}})^2
 \end{aligned}$$

Results from the spreadsheet program were as follows:

Expt	A	B	C	Γ_{300}	S/N_r	Ψ_{ratio}	S/N_Ψ
1	1	1	1	57.21	-35.15	3.82	-11.66
2	1	2	2	111.58	-40.95	3.82	-11.66
3	1	3	3	186.53	-45.41	3.82	-11.66
4	2	1	2	57.9	-35.25	2.88	-9.2
5	2	2	3	104.02	-40.34	3.12	-9.88
6	2	3	1	135.74	-42.65	6.65	-16.46
7	3	1	3	60.08	-35.57	2.41	-7.65
8	3	2	1	78.35	-37.88	5.24	-14.39
9	3	3	2	127.89	-42.13	4.77	-13.57

The S/N ratios due to various factors were tabulated as below:

Factor	S/N_r	$S/N_{\Psi_{ratio}}$
A1	-40.5	-11.66
A2	-39.41	-11.84
A3	-38.52	-11.87
B1	-35.32	-9.5
B2	-39.72	-11.97
B3	-43.39	-13.89
C1	-38.56	-14.17
C2	-39.44	-11.47
C3	-40.44	-9.73

Optimized settings were: A3, B1, C1 (min. r) & A1, B1, C3 (min. Ψ ratio)

Appendix 8a

Theoretical Model on Corrugation

Figure 8a.1 shows a point load acting at location 'A' as it penetrates deep into the corrugation.

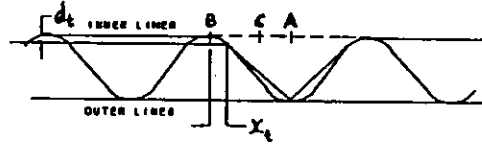


Fig. 8a.1 Full penetration of corrugation.

The flute can be modelled as a simple sinusoidal structure whose function is:

$$y = y_{\max} \cos \frac{2\pi x}{p} \quad (1)$$

As the inner liner curves over the flute, it will tangent off at some distance x_t and a depth d_t such that:

$$d_t = y_{\max} \left(1 - \cos \frac{2\pi x_t}{p} \right)$$

Hence the line equation for the inner liner becomes,

$$y - (y_{\max} - d_t) = \frac{2y_{\max} - d_t}{x_t - \frac{p}{2}} (x - x_t) \quad (2)$$

Differentiating eq(1) and equating with the line tangent from eq(2) will give:

$$-y_{\max} \left(\frac{2\pi}{p} \right) \sin \left(\frac{2\pi x}{p} \right) = \frac{2y_{\max} - d_t}{x_t - \frac{p}{2}}$$

substituting d_i into the above expression and converting it into an iterative function:

$$x_i = \frac{p}{2\pi} \sin^{-1} \left[\frac{p}{2\pi} * \frac{1 + \cos \frac{2\pi x_i}{p}}{\frac{p}{2} - x_i} \right] \quad (3)$$

x_i can be determined by iteration with a seed value of x equal to $p/4$ (see Figure 8a.1 for approximation), putting each successive x_i into the right-hand side of the equation.

The next step is to consider the total length of the inner liner which has been stretched between the two peaks of the corrugation (i.e one flute pitch). The length 's' for a curve with function $f(x)$ can be expressed as follows:

$$s = \int \sqrt{1 + (f'(x))^2} dx$$

The total extension of the inner liner will therefore be:

$$\delta p = 2 \int_{x=0}^{x=x_i} \sqrt{1 + B \left(\sin \frac{2\pi x}{p} \right)^2} dx + 2 \sqrt{\left(\frac{p}{2} - x_i \right)^2 + [y_{\max} \left(\cos \frac{2\pi x_i}{p} + 1 \right)]^2} - p$$

$$\text{where} \quad B = \left(y_{\max} \frac{2\pi}{p} \right)^2$$

Taking a B-flute configuration, $p=1000/164$ mm and $y_{\max}=2.5/2$ mm, x_i will converge to 0.786526 after 5 iterations and hence, $\delta p = 1.878111$. This corresponds to a net strain of 31 %, which far exceeds the empirical value of 1.5 % (see Section 2.2.1 on the tensile properties of paper or refer to test results by Benson [2]). Hence, the inner liner will have torn long before it reaches the bottom of a B-flute board.

Appendix 8b

Determination of Maximum Twin Roll Gap

The idea for adopting a variable gap twin roll design is to avoid a roll change when it comes to creasing boards of different calipers. Currently there are three major design variables that need to be established; they are the twin roll gap, the cone angle ' θ ' and the creaser width, as shown in Figure 8b.1. This appendix aims to estimate the three parameters which will serve as seed values for the finite element model and experimentation.

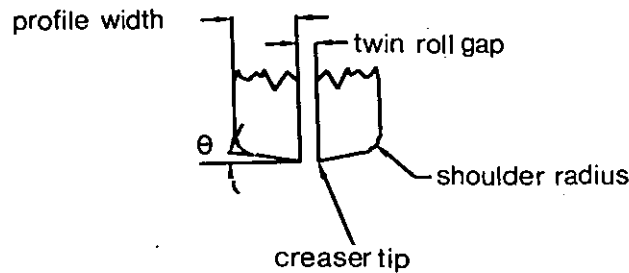


Fig. 8b.1 Twin roll design parameters.

Theoretical derivation

At present, there are two propositions for setting the twin roll gap. One way is by relating the gap width to the thickness of the board; but this may result in a crease width larger than required and therefore poor appearance at the case corners.

Another way is to correlate the twin roll gap setting with the flute geometry. To be more precise, a twin roll gap is chosen in such a way that the least damage is imparted to that part of the corrugated board which will be most susceptible to tearing, i.e the inner liner.

Figure 8b.2 models a flute structure subject to a point load at location 'C' - somewhere between the peak and the trough of the flute.

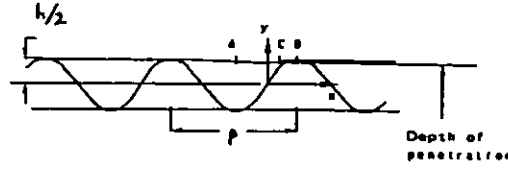


Fig. 8b.2 Loading at location 'C'.

Placing a point load at location 'C' will depress the liner by δ . Assuming no slippage between the creaser and the inner liner, the part of liner most likely to tear will be that between the points 'C' and 'B'. If the liner has a maximum permissible strain rate of ϵ , then the condition for no tearing will be:

$$\sqrt{\left(\frac{p}{4}-x\right)^2+\delta^2}-\left(\frac{p}{4}-x\right) \leq \epsilon\left(\frac{p}{4}-x\right)$$

from which,

$$\delta \leq \left(\frac{p}{4}-x\right) \sqrt{2\epsilon+\epsilon^2} \quad (1)$$

Expressing δ in terms of $y(x)$ will give:

$$y(x) \geq \frac{h}{2}-\left(\frac{p}{4}-x\right) \sqrt{2\epsilon+\epsilon^2} \quad (2)$$

By moving the point 'C' from $x=0$, the point on the liner will eventually meet the flank of the flute, after which the original load will be supported by the flute rather than the liner. For the present purpose, this point 'x' beyond which the liner is off-loaded will be called x_{crit} . Using the harmonic components for a typical B-flute corrugation (see Appendix 8c), $y(x)$ in equation (5) can be expressed in terms of the corrugation curve. From experimental data on load elongation, as quoted by Thomas [50], most liners in the moisture range of dry to 10 % RH can stretch by 1.5 % to 2.5 % without breaking. Hence, by assuming a liner strain rate of 1.5%,

x_{crit} can be derived from equation (5) and the corrugation curve, and is shown in the following table:

Flute type	Pitch / mm	x_{crit}
B-flute	5.97	1.194
C-flute	7.547	1.509

If the twin roll creaser lands on the corrugation such that the twin rolls staddle over a peak, then the tips of the creaser will behave like two point loads. The maximum gap width for the twin roll, as shown in Figure 8b.3, can therefore be determined from the previous x_{crit} values.

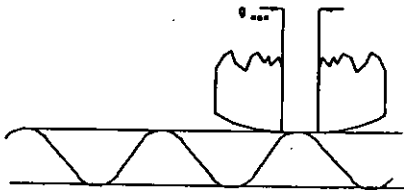


Fig. 8b.3 Twin roll gap at maximum opening.

Furthermore, if the liner is allowed to slip, which is most likely in a dynamic situation, then the creaser may penetrate deeper without tearing. In other words, the twin roll gap can be spaced further apart within the tearing constraint. The new gap setting with slipping taken into consideration can be worked out by deriving the maximum possible depression which the inner liner can tolerate. This condition is satisfied by loading at location 'A' in Figure 8b.2. Being the mid-point of the section, it can be shown mathematically that the greatest liner extension takes place at location 'A'. With the new value ' δ ', the x_{crit} can be calculated accordingly.

A summary on the twin roll gap settings is as follows:

Flute type	No slipping	Slipping
B-flute	0.59 mm	1.79 mm
C-flute	0.75 mm	2.26 mm

What happens if the twin roll gap lands at or in the vicinity of location 'A'? This is where the twin roll shoulder effect comes into play. Figure 8b.4 shows one half of the twin roll creaser, where the coordinate origin has been shifted along the corrugation centreline to location 'A', such that the y-axis is now coincident with the centreline of the twin roll.

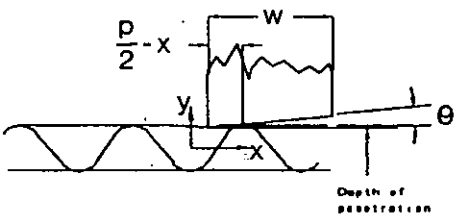


Fig. 8b.4 One-half of twin roll at location 'C'.

The creaser profile gradient can be determined by examining the strain imposed on the liner when the creaser begins to penetrate into the corrugation. It follows that:

$$\theta = \tan^{-1} \frac{\delta}{\frac{p}{2} - x} \tag{3}$$

where,

$$\delta = \left(\frac{p}{2} - x\right) \sqrt{2\epsilon + \epsilon^2}$$

In fact, θ is independent of the flute pitch; its value is calculated to be 9.86° for a liner strain rate of 1.5 %. Using this value as our creaser shoulder angle, the twin roll creaser width can be derived in terms of the minimum number of flutes affected by the crushing action. For example, if the board is reduced to 'k' times its original thickness, then the creaser shoulder angle will affect a certain width of the flute. Referring to Figure 8b.4, half the creaser width can be determined by:

$$w = \frac{(1-k)h - \delta}{\tan \theta} \tag{4}$$

When the middle of the twin roll gap falls in line with location 'A' (i.e $x=0$), creasing of single-wall boards to a penetration of 'k' equal 20 % will imply 'w' values of 8.52 mm and 12.76 mm for the B- and C-flute respectively. Doubling these values will give the total twin roll creaser width.

With double wall boards, since the top layer is essentially a C-flute board, it may seem logical to adopt a twin roll creaser whose width is designed for crushing C-flute boards. However, interaction between the two layers prevents the board from being treated like two sheets of independent lamina. Hence, it is not feasible to derive a twin roll creaser width for the double-wall boards.

Finally, the assumption that there is no slipping between the creaser roll and the inner liner is invalid (unless the friction coefficient between the two media is very high - a situation made possible by increasing the moisture content of the liner). Since the maximum permissible depression for a single-wall board is found to be 0.051 mm using equation (5). However, the present single blade design has an effective blade penetration of 0.762 mm with no sign of liner tearing. If slipping is accounted for, a value of 0.518 mm will be arrived at after a similar calculation. Further penetration will have to be due to the compliance of the corrugation structure.

Appendix 8c

Fourier Harmonics for B-flute Corrugation

The following table provides the first ten Fourier components of the B-flute corrugation waveform. Each harmonic component is represented by the sum of a sine wave and a cosine wave. In the table below, the 'real' number is the amplitude of the cosine wave, and the 'imaginary' number is that of the sine wave. The magnitude of each component is the square root of the sum of the squares of the real and imaginary values. The phase value is the number of degrees that the harmonic component is shifted from a pure cosine wave. Harmonic 0 is the d.c component.

Harmonic	Real	Imaginary	Magnitude	Phase
0	0.0048	0.0000	0.0048	0.0
1	-0.0042	-0.0031	0.0052	-143.9
2	-0.0060	0.0029	0.0067	154.0
3	-0.0096	0.0108	0.0145	131.4
4	-0.0162	0.0186	0.0247	131.0
5	-0.02	0.0930	0.0951	102.1
6	0.0089	-0.0636	0.0642	-82.1
7	0.0062	-0.0271	0.0278	-77.1
8	0.0011	-0.0133	0.0133	-85.4
9	0.0002	-0.0105	0.0105	-88.8
10	-0.0007	-0.0096	0.0096	-93.9

Appendix 8d

ESPI Equation Derivation

When an optically rough surface is illuminated by coherent light and imaged by a lens, the intensity of the image varies randomly across the surface. If the surface is displaced or deformed, the phase of an individual component of light will be changed as it scatters from the resolution area to a given point in the image plane. The phase change of all the scattered components may be considered approximately equal if the displacement is not too large. The intensity of the speckle pattern therefore remains unchanged in the image plane. By superimposing a second light beam (a reference beam) onto the speckle pattern in the image plane, the complex amplitude at a point $P(\mathbf{r})$ of the object beam before displacement, U_o , and of the reference beam, U_r , can be described as follows:

$$U_o = u_o e^{i\phi_o} \dots\dots\dots(1)$$

$$U_r = u_r e^{i\phi_r} \dots\dots\dots(2)$$

where, u_o and ϕ_o vary randomly across the image,
 u_r and ϕ_r may or may not be random depending on the reference beam.

Intensity at point $P(\mathbf{r})$ is therefore given by:

$$I_1 = u_o^2 + u_r^2 + 2u_o u_r \cos(\phi_o - \phi_r) \dots\dots\dots(3)$$

When the surface is displaced, the phase of all the scattered components changes by the same amount $\Delta\phi(\mathbf{r})$ such that the complex amplitudes of the object beam at $P(\mathbf{r})$ is now:

$$U_o = u_o e^{i[\phi_o + \Delta\phi(\mathbf{r})]}$$

and the intensity is given by:

$$I_2 = u_O^2 + u_R^2 + 2u_O u_R \cos[\phi_O - \phi_R + \Delta\phi(r)] \dots\dots\dots(4)$$

Comparing the equations for I_1 and I_2 , the intensities will be the same when $\Delta\phi(r) = 2n\pi$. This is also the case when the intensities of two sets of randomly distributed speckle pattern are correlated using the correlation coefficient:

$$\rho = \frac{E[XY] - E[X]E[Y]}{\sqrt{E[(X-E[X])^2]E[(Y-E[Y])^2]}}$$

Expressing intensities in terms of the two random variables 'X' and 'Y' will give:

$$\rho(\Delta\phi) = \frac{1}{2}[1 + \cos(\Delta\phi)]$$

see references [57] and [8].

Hence for maximum correlation, $\rho(\Delta\phi) = 1$, and

$$\Delta\phi = 2n\pi\dots\dots\dots(5)$$

where $n = 1,2,3,\dots$

On comparing the two speckle patterns, fringes formed by lines of equal intensities will provide information about the relative displacements of different parts of the surface. In ESPI, the comparison of speckle patterns is achieved by means of a TV system. In order to compensate for the low spatial resolution of a video system, a small aperture viewing lens is needed for resolving the speckles (see Wykes [57]).

The image plane is first of all positioned to coincide with the face plate of a TV camera. In its undisplaced state, the object image is recorded on a video store. The object is then displaced and the live image is subtracted electronically from the stored picture, hence the term 'electronic' in ESPI. Areas of zero intensity will be those where $\Delta\phi = 2n\pi$. Conversely, the speckle pattern will have a maximum contrast and mean intensity when $\Delta\phi = (2n+1)\pi$. It is the variation of mean

contrast and mean intensity when $\Delta\phi = (2n+1)\pi$. It is the variation of mean intensity and the contrast of the speckle pattern across the subtracted speckled images that constitute the fringe pattern. The fringes represent the correlation between the two images and are therefore referred to as correlation fringes (which must not be confused with interference fringes).

In an orthogonal coordinate system, if an object lies in the x_2, x_3 plane and viewing is in the x_1 direction, then fringes can be obtained which represent contours of constant out-of-plane displacement (d_1) and in-plane displacement in a specific direction d_2 or d_3 .

i) **Out-of-plane** displacement sensitive interferometer

The Michelson arrangement of out-of-plane displacement sensitive speckle pattern correlation interferometer is as shown in Figure 8d.1.

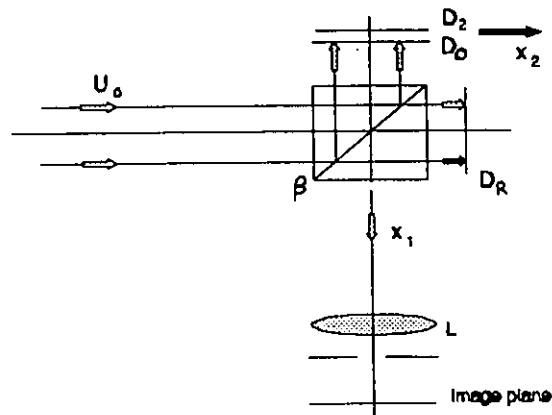


Fig. 8d.1 Michelson interferometer.

Two optically rough surfaces D_0 and D_R are illuminated by a plane wavefront U_0 which is split into two components of equal intensity by the beam splitter B. On scattering from D_0 and D_R , the wavefronts interfere and recombine at B, and are subsequently recorded in the image plane of the lens-aperture combination L. The intensity distribution in that plane will consist of the interference pattern formed

between the image plane speckle pattern of D_o and the 'dashed' position D_R . For a given point in the image plane, the intensity I_1 is given by equation (3).

Now, when D_o is displaced a distance d_o parallel to the surface-normal, the resultant phase change is as follows:

$$\Delta\phi(d_1) = \frac{4\pi d_1}{\lambda} \dots\dots\dots(6)$$

which changes the intensity at the point to I_2 as shown in equation (4). Combining equations (5) and (6) will give the maximum correlation between I_1 and I_2 . Hence,

$$d_1 = \frac{1}{2}n\lambda \dots\dots\dots(7)$$

The optical arrangement used in ESPI is as shown in Figure 8d.2.

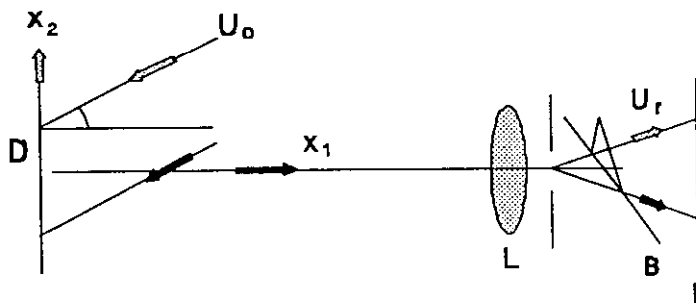


Fig. 8d.2 ESPI out-of-plane interferometer.

For a general form of $\Delta\phi$ such that either or both the viewing and illumination directions are not parallel to the surface-normal,

$$\Delta\phi = \frac{2\pi}{\lambda}(n_o - n_s).d \dots\dots\dots(8)$$

where n_o = illumination direction
 n_s = viewing direction

The situation arises when divergent illumination is used or the object is non-planar. But for any deviation of less than 15° from the normal, the following will be true to a good approximation:

$$\Delta\phi = \frac{2\pi(\cos\theta_1 + \cos\theta_2)d_1}{\lambda}$$

where, θ_1 = angle of object illumination to surface-normal

θ_2 = angle of viewing direction to surface-normal

Setting θ_1 and θ_2 to near 0° will reproduce equation (6).

ii) In-plane displacement sensitive interferometer

Figure 8d.3 shows the optical arrangement for an in-plane displacement sensitive speckle pattern correlation interferometer.

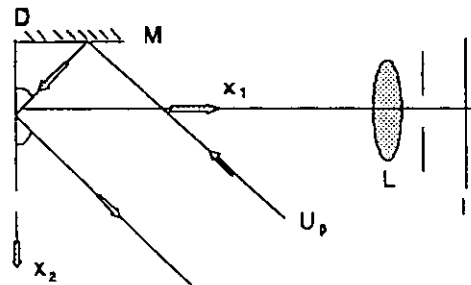


Fig. 8d.3 ESPI in-plane interferometer.

Wavefronts U_o' and U_o'' are obtained by allowing half the incident plane wavefront U_o to illuminate the object D directly, while the other half is reflected onto the surface by the mirror M. In this way, U_o' and U_o'' will be inclined at equal and

opposite angles to the x_1 -axis surface-normal. Displacing the object D by a distance $\mathbf{d}(d_1,d_2,d_3)$ will give:

$$\Delta \phi = \frac{4\pi}{\lambda} d_2 \sin \theta \dots\dots\dots(9)$$

as derived from equation (8).

Since the relative phase of U_o' and U_o'' is constant over planes lying parallel to the x_1x_3 -plane, the displacement components d_1 and d_3 in the plane will not introduce a relative phase change. From equation (5) and (9), the in-plane displacement can be calculated as follows:

$$d_2 = \frac{n\lambda}{2\sin \theta} \dots\dots\dots(10)$$

Refer to Wykes [57] and Jones et al. [20] for further information on ESPI.

Appendix 9a

Folding Rig Design Specification

BACKGROUND

Special folding rigs are known to have been used in paper research. The main purpose of the rigs is to obtain the crease stiffness or the folding resistance of corrugated fibreboards from its initial position of 0° to the final folded position of slightly less than 180° . Though there is no detailed publication on the rig design, Vogelpohl [51], Grebe [9] and McKee [26] have all reported substantial findings from such apparatus.

The folding test rig used by Vogelpohl is unique in design, in that it consists of a platform which is symmetrically divided along a folding hinge. One half of the platform performs the folding action, while the other half remains static. Vacuum pads on the platform enable the board samples to be held down, though it is not clear how the force sensor is allowed to operate at the same time. Force sensing is performed by means of strain gauges, and a rotational transducer measures the angular displacement simultaneously. The signals, once digitized, can be displayed and analysed on a dual channel plotter.

Other folding test rig design reported by Buchanan [3] and Grebe [9] are capable of recording the force required to fold a 127 mm wide strip of creased sample. The angle of fold at any instant can be displayed on an oscilloscope over a range of folding speeds.

DESIGN SPECIFICATIONS

The repetitive nature of experimentation highlights the importance of having a minimal set-up time. Quick fit mechanisms and open access are therefore two

factors which must be built into the rig. The test rig must be robust enough to process a range of board samples. Graphical representation of the folding resistance is particularly informative, when different board samples can be compared at a glance. The overall rig, including instrumentation and software, must be economically viable and fit for the present purpose.

To summarize, the folding test rig design is expected to fulfil the following criteria:

1. To measure the folding resistance relative to the angular displacement when a board sample is subject to the folding action.
2. To give a graphical representation for instant interpretation.
3. Design must be robust enough to cater for corrugated fibreboards of various thicknesses and liner grades.
4. Inexpensive to build.

FOLDING RIG DESIGN

Figure 9a.1 shows the folding test rig design. The basic mechanical features of the folding rig consist of a counter-balanced folding leg the end of which is fitted with a knife edge. A board sample is placed onto the principal support bar, whilst one edge of the board is sitting on the tip of the cantilever. By latching the folding leg, and hence the knife edge into position, the crease will lie immediately under the knife edge. When the d.c motor is switched on, the centre roller on the folding arm will act against the board panel. At this instant, the centre roller and the tip of the cantilever act as though they were two point contacts, imposing a folding couple on the board about the knife edge.

Once the board is folded to slightly over 90°, the folding leg will be unlatched automatically. This enables the folding leg to swing to its balanced position, thereby clearing way for the board sample. The d.c motor is deactivated by means of two limit switches at both the forward and the reverse strokes.

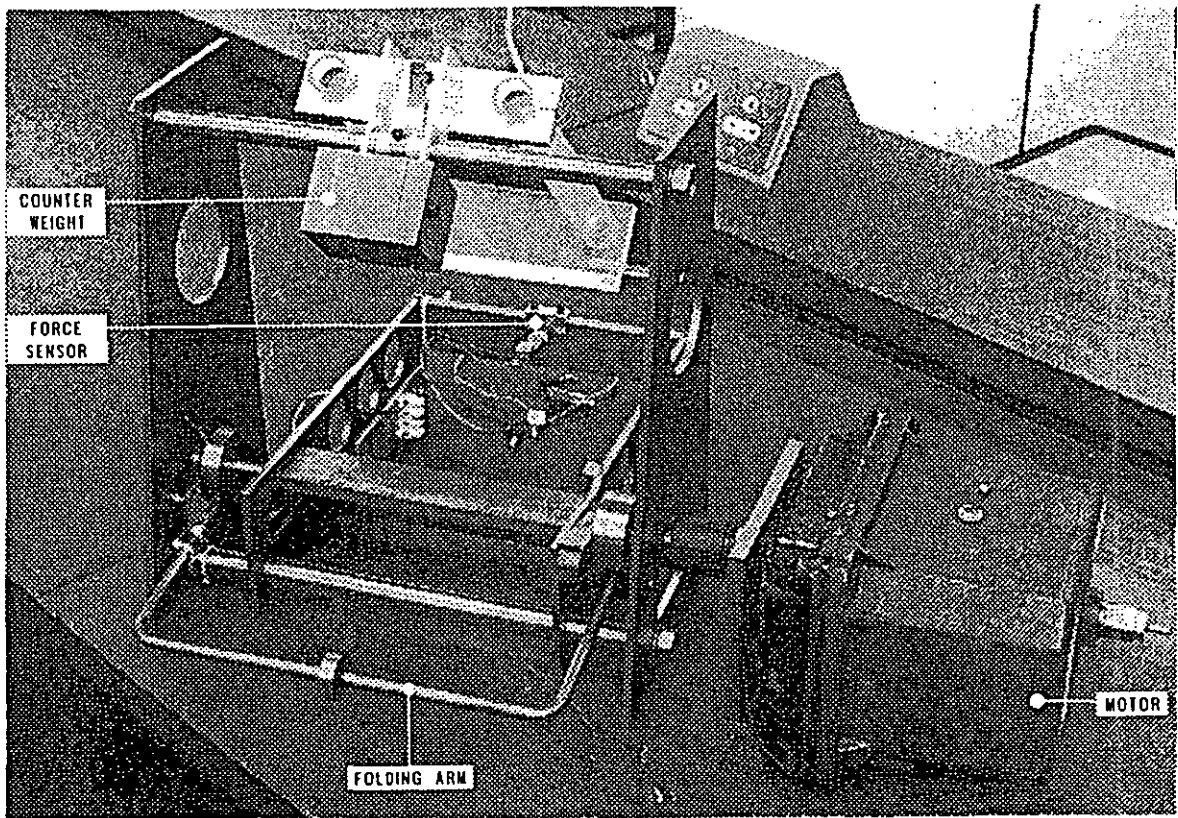


Fig. 9a.1 Folding test rig design.

During the folding action, the strain and the encoder signals are sampled continuously. The sampling rate corresponds to half a degree for every strain sample reading.

The test results, represented by a plot of folding resistance versus angular displacements, are independent of the rate of folding. The area under the plot indicates the total work done in folding a board sample about a particular crease.

Several minor problems were highlighted during the calibration of the folding test rig. One problem occurred when the board sample momentarily left the support edge as soon as the folding leg was unlatched. Together with the high sensitivity of the strain gauges on the cantilever, the net effect was a sudden transition in folding resistance as indicated by the kink in the middle of the folding resistance

curve. Side shims were therefore added to prevent the board from leaving the support bar. In addition, a piece of spring steel was fitted onto the locking ring at the top of the folding leg so as to dampen the swinging motion.

Technical specifications for the folding test rig are as follows:

Force range - 4 N max.

Fold rate - 0° to 180° in 10 secs

Force sensing - temperature compensated strain gauges on spring steel cantilever

Angular displacement - 2 channel quadrature output optical encoder running at 720 pulses/rev

Analogue output - $\pm 5V$

Motor voltage setting - 8V

Motor running speed - 2 rpm

Automatic latching mechanism

ADC data acquisition at 100 Hz and 16 bit resolution

Sample size - 200 mm (along flute) x 400 mm

Strain gauge amplifier - $\pm 15 V$ supply voltage

The rig was calibrated by adjusting the gain in the electronic strain gauge amplifier for a known weight at the tip of the cantilever. A calibration factor was subsequently included in the operation program FOLD3.BAS, a listing of which is included in this appendix.

To operate the test rig, the board sample is first of all loaded with the folding leg properly latched in position. After initializing the program 'foldrig2.exe', folding is commenced by pressing the key '5' and switching on the motor simultaneously. Upon saving the test data, the results can be displayed at a later stage by retrieving the datafile via the display program 'fold3.exe'.

cont./..

PROGRAM LISTING: FOLD3.BAS

```

'*****
' *      Folding Test Rig Data Analysis Program      *
' *      (Adapted from D. Holman's program for flute height measurement) *
' *
' *      By A M Lau 10/8/93
' *
' *      Department of Mechanical Engineering, Loughborough University *
'*****

DEFINT A-N
DEFSNG O-Z
'$DYNAMIC      'Allocate storage space for arrays only when the program is
                'running and not during compilation

DECLARE SUB Main ()
DECLARE SUB Extract (Curve())
DECLARE SUB DrawProfile ()
DECLARE SUB Startup ()
DECLARE FUNCTION GetFileName$ ()

COMMON SHARED Mincount, Maxcount
COMMON SHARED filesize, XStep, FileName$, YMax, XMax, FoldE!

CONST Limit = 680                ' Only 340 data are sampled
CONST FALSE = 0, TRUE = NOT FALSE
CONST CalFac = 2.1213            ' Calibration factor for graphics
CONST SConFac = .49 / 102        ' Conversion factor for force unit
                                   ' (re: TE2.ALF)
CONST TotalX = 360               ' Intervals along the x-axis
CONST entrylimit = 100           ' Limit for first peak detection

DIM SHARED profile(0 TO Limit) AS INTEGER 'UPPER BOUND OF PROFILE & FILTER

CLS
SCREEN 9
CALL Startup                    ' Screen & graphics start up.
CALL Main
END

DEFINT A-N
SUB DrawProfile
' *****
' Procedure for plotting points in array "profile" onto screen
' *****
SHARED profile() AS INTEGER
count = 1
FOR X = 0 TO XMax STEP 1
    PSET (X, profile(X))
NEXT X
END SUB

DEFINT A-N
SUB Extract (Curve())
' *****
' Algorithms for extracting the curve characteristics.
' *****
YAmaz = 0
YBmax = 0
ScanWidth = 5                  ' Proportion of 1st peak curve to be sampled
                                   ' for determining the gradient of curve.
FOR X = 0 TO (XMax / 2) STEP 1
    IF Curve(X) > YAmaz THEN
        YAmaz = Curve(X)
        MkA = X                ' 1st peak marker.
    
```

```

        END IF
        IF Curve(XMax / 2 + X) > YBmax THEN
            YBmax = Curve(XMax / 2 + X)
            MkB = XMax + X ' 2nd peak marker.
        END IF
    NEXT X

    YC = YAmax
    FOR X = (MkA + 1) TO MkB STEP 1
        IF Curve(X) < YC THEN YC = Curve(X)
    NEXT X

    GradD! = (Curve(MkA) - Curve(MkA - ScanWidth)) * SConFac / ScanWidth

    PRINT "A="; YAmax * SConFac; "B="; YBmax * SConFac; "C="; YC * SConFac;
    PRINT "D="; GradD!; "E="; FoldE! * SConFac
    END SUB

DEFINT A-N
' *****
' Returns a file name from user input
' *****
FUNCTION GetFileName$ STATIC
    INPUT "Enter data file to load (press ENTER to quit): ", FTemp$
    GetFileName$ = FTemp$
END FUNCTION

DEFINT A-N
SUB Main
' *****
' Main Program
' *****

DIM P!(0 TO 20)

TopValue = Limit
DO ' Program main DO loop.
    OPEN "OUT.DTA" FOR OUTPUT AS #2
    FileName$ = GetFileName$ ' Input file data.
    IF FileName$ = "" THEN ' End if <ENTER> pressed.
        END
    ELSE OPEN FileName$ FOR BINARY AS #1
    END IF

    GET #1, 1, filesize
    IF filesize > TopValue THEN
        filesize = TopValue ' Keep filesize within limits
    END IF

    '***** Detect first peak of folding resistance plot *****

    entry = 3 ' Data file counter.
    count = 1 ' General loop counter.
    slope = FALSE ' Set slope condition.
    WHILE (count < 6) AND (entry < entrylimit)
        GET #1, entry, number ' Read in data from #(*.alf) files
        P(count) = number / CalFac
        GET #1, entry + 2, number ' Read in data from #(*.alf) files
        P(count + 1) = number / CalFac
        IF (P(count) > P(count + 1)) OR (P(count) <= 0) THEN
            count = 0
        ELSE

```

```

                                count = count + 1
                                END IF
                                IF count = 6 THEN slope = TRUE
                                entry = entry + 2
WEND

IF (slope = TRUE) THEN
    entry = entry - 12          ' Reset entry to read first non-zero data
    ELSE
    entry = 3                  ' Reset entry to read first data
    PRINT "Data not filtered!"
END IF

count = 1
FoldE! = 0
DO WHILE entry <= filesize
    GET #1, entry, number
    Value = number / CalFac
    WRITE #2, Value
    profile(count) = CINT(Value)
    FoldE! = FoldE! + Value
    entry = entry + 2
    count = count + 1
LOOP

IF count <> 1 THEN
    XMax = count - 1
    FoldE! = FoldE! / XMax          ' Calculate average energy.
END IF

IF (slope = TRUE) THEN
    CALL Extract(profile())
END IF

CALL DrawProfile
CLOSE #1, #2
CLOSE                                ' OUT.DTA

INPUT "Do you wish to superimpose with another curve? (Y / N)"; Q$
LOOP UNTIL Q$ = "N" OR Q$ = "n"

END SUB

DEFINT A-N
SUB Startup
' *****
' Set up graphics and screen for curve display.
' *****
' ***** Draw markers on plot. *****
LOCATE 1, 1
PRINT "Force / N"
LOCATE 1, 25
PRINT "FOLDING RESISTANCE PLOT"
LOCATE 23, 60
PRINT "Angular displacement"
LOCATE 17, 1
PRINT "1"
LOCATE 13, 1
PRINT "2"
LOCATE 9, 1
PRINT "3"
LOCATE 5, 1
PRINT "4"

```

```

LOCATE 23, 15
PRINT "30"
LOCATE 23, 28
PRINT "60"
LOCATE 23, 40
PRINT "90"
LOCATE 23, 52
PRINT "120"

' ***** Draw frame of plot *****
Style% = &HFF00
Factor = 1
YBottom = 0
YTop = 1000
Begin = 0
Endpoint = 0
Xend = (TotalX - Endpoint) / Factor
LINE (20, 300)-(620, 300), 2
LINE (20, 20)-(20, 300), 2
VIEW (20, 2)-(620, 300)
WINDOW (Begin, YBottom)-(Xend, YTop)
LINE (0, 210)-(355, 210), 3, , Style%
LINE (0, 420)-(355, 420), 3, , Style%
LINE (0, 630)-(355, 630), 3, , Style%
LINE (0, 840)-(355, 840), 3, , Style%
LINE (30, 0)-(30, 10), 3
LINE (60, 0)-(60, 10), 3
LINE (90, 0)-(90, 10), 3
LINE (120, 0)-(120, 10), 3
LINE (150, 0)-(150, 10), 3
LINE (180, 0)-(180, 10), 3
LINE (210, 0)-(210, 10), 3
LINE (240, 0)-(240, 10), 3
LINE (270, 0)-(270, 10), 3
LINE (300, 0)-(300, 10), 3
LINE (330, 0)-(330, 10), 3
LINE (360, 0)-(360, 10), 3

VIEW PRINT 24 TO 25
END SUB

```

' x-margin
' y-margin
' Confine graphics viewport.
' Horizontal grid lines.
' Confine print viewport to rows 24 & 25

Appendix 9b
L₁₈ Orthogonal Array

Expt.	Control Factors							
	A	B	C	D	E	F	G	H
1	1	1	1	1	1	1	1	1
2	1	1	2	2	2	2	2	2
3	1	1	3	3	3	3	3	3
4	1	2	1	1	2	2	3	3
5	1	2	2	2	3	3	1	1
6	1	2	3	3	1	1	2	2
7	1	3	1	2	1	3	2	3
8	1	3	2	3	2	1	3	1
9	1	3	3	1	3	2	1	2
10	2	1	1	3	3	2	2	1
11	2	1	2	1	1	3	3	2
12	2	1	3	2	2	1	1	3
13	2	2	1	2	3	1	3	2
14	2	2	2	3	1	2	1	3
15	2	2	3	1	2	3	2	1
16	2	3	1	3	2	3	1	2
17	2	3	2	1	3	1	2	3
18	2	3	3	2	1	2	3	1

Appendix 9c

Shear Test

Procedures

The objective of the shear test is to provide a measure for fishtailing. The shear test arrangement is as shown in Figure 9c.1.

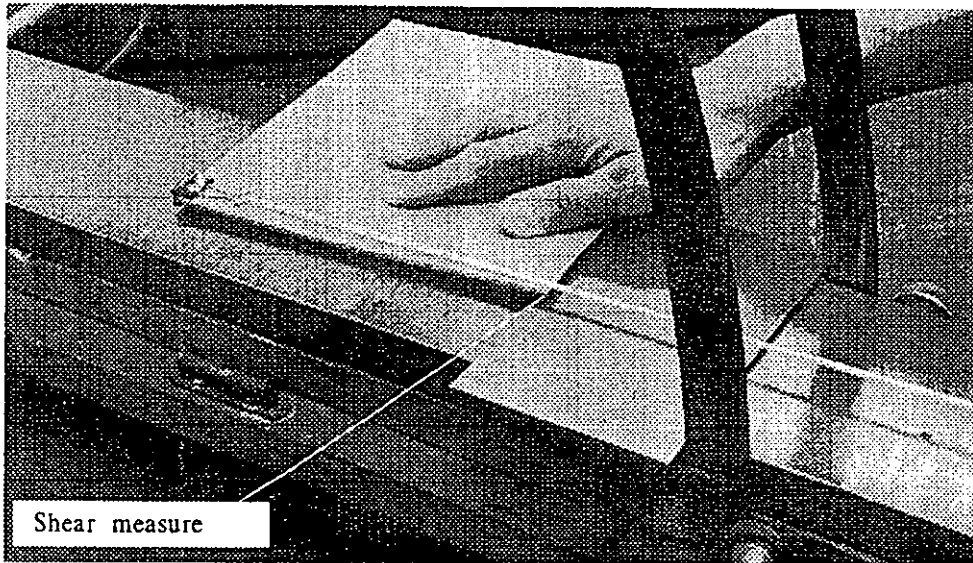


Fig. 9c.1 Shear test measure on Fletcher's Trolley.

Essentially, the folded board sample is placed onto the platform of the Fletcher's trolley, with the edge of the base panel acting against the steel. By attaching a spring clip onto the corner of the overlapping panel, and loading it with a pulley mechanism, the shear effect can thus be simulated under experimental condition. The fishtailing measure will be determined by the displacement between the edges of the panels.

Calibration

A calibration test was conducted on the HH 300(B) board samples with a size of 100 mm x 400 mm. Following creasing at a compression ratio of 90 % and folding by means of the folding test rig, the fishtail result was measured before loading the sample onto the Fletcher's trolley. The shear measure was then recorded at each mass increment until the board could no longer withstand any more shear loading. The shear radian could hence be derived by dividing the difference in shear before and after loading by the edge length of the overlapping panel. In order to differentiate between the direction in which shear could take place, a positive shear was designated for the one with the panel displacing in the direction of the applied load, and a negative shear for the contrary.

The results, including the first peak of the folding resistance, were as tabulated below:

No.	Shear before	Shear after	Edge length	Shear radian	First peak	Comments
1	1.5	3.5	198.5	0.01	0.407	**
2	-1.0	0.5	199.5	0.007	0.416	**
3	5.0	6.0	199.0	0.005	0.367	**
4	-2.0	0.5	198.5	0.012	0.442	**
5	-1.5	0	199	0.007	0.447	**
6	-8.0	-7.0	201.0	0.004	0.469	**
7	-4.0	-3.0	198.5	0.005	----	Tearing on creasing
8	0.5	1.5	199.5	0.005	----	**
9	-8.0	-6.0	201.0	0.009	0.433	**
10	-2.0	0	200.5	0.009	0.424	**

** Buckling of liner immediately next to the crease.

Table below showing the shear deformation (after) at different load increments:

Load/g	199.9	299.1	397.2	495.6	595.5	694.1	792.2
1	3.5	6	18	23	25	---	---
2	0.5	2	4	32	---	---	---
3	6.0	9	28.5	37	49	---	---
4	0.5	3.5	10	18.5	25	---	---
5	0	0.5	3	17.5	---	---	---
6	-7.0	-6	-4.5	-2.0	---	---	---
7	-3.0	-1	0	9.5	19	24.5	---
8	1.5	4	17	25	35	---	---
9	-6.0	---	---	---	---	---	---
10	0	3	5.5	31	---	---	---

in terms of shear radians:

Load/g	199.9	299.1	397.2	495.6	595.5	694.1
1	0.01	0.022	0.083	0.108	0.118	---
2	0.007	0.015	0.025	0.165	---	---
3	0.005	0.02	0.118	0.160	0.226	---
4	0.012	0.027	0.06	0.103	0.136	---
5	0.007	0.01	0.022	0.095	---	---
6	0.004	0.009	0.017	0.029	---	---
7	0.005	0.015	0.02	0.068	0.115	0.143
8	0.005	0.017	0.082	0.122	0.172	---
9	0.009	---	---	---	---	---
10	0.009	0.024	0.037	0.164	---	---

A plot of the shear radians against load for the first five load sets is as shown in Figure 9c.2.

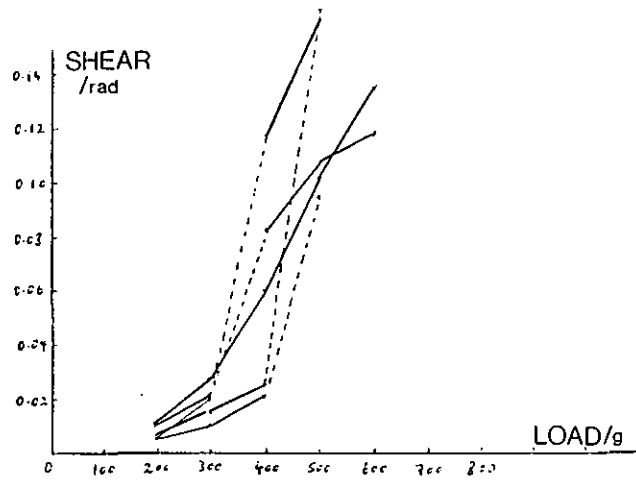


Fig. 9c.2 Calibration plot of shear vs. load.

Recommendation

From the calibration test, it was found that a mass of around 0.7 kg would be suitable for loading the single-wall boards whose sample size is 200 mm x 400 mm. A mass of 1.4 kg would be recommended for loading the double-wall boards. The masses must be kept constant throughout the experiment as evidence from the shear radian plot suggested that sudden shear jumps might occur as a result of increasing the load. This sudden transition in shear deformation could be explained by the buckling of the flute structure.

Appendix 9d

First Experiment Results

The folding resistance first peak data for all the experiments have been stored in the following computer file directories:

Experiment no.	File directory
1, 2, 3, 10, 11, 12	JUN29
4, 5, 6, 13, 14, 15	JUN30
7, 8, 9, 16, 17, 18	JUL01

The sample number has been labelled in terms of the experimental number, the batch material number and the number within the test batch. For example, 'ONE111' corresponds to the first sample in the eleventh material batch type of experiment ONE.

The comment column is designated with the following abbreviations:

CL - cracked liner

SFB - secondary flute buckling

MC - misaligned crease

SC - skewed crease

MD - missing data

N.B Only CL and SFB have been considered as failures in the experiment.

Expt. 1: Lab. RH = 45%,

No.	1st peak	Shear before	Shear after	Edge length	Shear radian	Comment
ONE11	0.703	-1	17.5	195.5	0.094	MC
ONE12	0.734	1	15	194.5	0.071	
ONE13	0.73	1	17.5	196	0.084	
ONE14	0.818	-1	16.5	196.5	0.089	
ONE15	0.752	-1	17.5	197.5	0.093	SFB
ONE41	1.279	-1.5	3.0	193.5	0.023	
ONE42	1.504	-0.5	4.0	195.5	0.023	
ONE43	1.473	-1.5	1.5	198.5	0.015	
ONE44	1.279	-1.5	5.5	197	0.035	SFB
ONE45	1.283	-1.5	-1.0	197	0.002	
ONE71	2.19	-2.5	-2.0	198.5	0.002	
ONE72	2.41	-0.5	0.5	197	0.005	
ONE73	2.39	-2.0	-1.0	198.5	0.005	MC
ONE74	2.28	0.5	1.5	196.5	0.005	MC
ONE75	2.62	-0.5	0.5	197.5	0.005	
ONE101	2.61	-2.0	-1.0	197	0.005	
ONE102	2.53	1.0	2.0	196	0.005	
ONE103	2.77	-6.5	16.0	195.5	0.115	SFB
ONE104	2.62	0.5	2.5	196.5	0.01	
ONE105	2.67	0	2.5	196	0.012	
ONE111	---	---	---	---	---	CL
ONE112	---	---	---	---	---	CL
ONE113	---	---	---	---	---	CL
ONE114	2.36	2.5	7.5	190	0.026	
ONE115	3.14	0.5	1.5	193	0.005	

Expt. 2: Lab. RH = 45%,

No.	1st peak	Shear before	Shear after	Edge length	Shear radian	Comment
TWO11	0.854	0	6	190	0.031	SFB
TWO12	0.712	2	10	195.5	0.040	SFB
TWO13	0.792	0.5	6.5	193	0.031	SFB
TWO14	0.938	0.5	11.5	194.5	0.056	SFB
TWO15	0.947	0.5	7.5	189.5	0.036	SFB
TWO41	1.51	0.5	2.5	193.5	0.01	
TWO42	---	0	1.0	191.5	0.005	
TWO43	1.76	2	6	191	0.02	
TWO44	0.76	3	5	196.5	0.01	SC
TWO45	1.75	2.5	3	190.5	0.002	
TWO71	2.46	5	5	194	0	
TWO72	2.80	3.5	3.5	192.5	0	
TWO73	3.04	2	2.5	194.5	0.002	
TWO74	2.84	0.5	1.5	193.5	0.005	
TWO75	2.60	1.0	1.5	190.5	0.002	
TWO101	3.2	-11.5	-11	200	0.002	
TWO102	3.19	2	1	196.5	0.005	
TWO103	3.35	-9	-8.5	199.5	0.002	
TWO104	3.33	-9.35	-9	200.5	0.002	
TWO105	3.33	-7.5	-6	199	0.007	
TWO111	3.18	3.0	7.5	187.5	0.024	
TWO112	----	----	----	----	----	CL
TWO113	1.85	----	----	----	----	SFB
TWO114	2.58	3.5	6	188	0.013	
TWO115	3.02	----	----	----	----	

Expt. 3: Lab. RH = 45%,

No.	1st peak	Shear before	Shear after	Edge length	Shear radian	Comment
THR11	0.77	0.5	10.5	195.5	0.051	SFB
THR12	0.73	7.5	6.5	195.5	0.005	MS
THR13	0.64	----	----	----	----	SFB
THR14	0.93	6.5	10.5	195.5	0.018	
THR15	0.83	----	----	----	----	SFB
THR41	1.49	----	----	----	----	SFB
THR42	1.78	----	----	----	----	SFB
THR43	1.6	----	----	----	----	SFB
THR44	1.63	15	15	197.5	0	
THR45	1.83	9.5	10.5	188.5	0.005	
THR71	2.63	13.5	13.5	188.5	0	
THR72	----	16.5	16.5	186.5	0	
THR73	----	----	----	----	----	MD
THR74	2.68	14	14.5	186.5	0.002	
THR75	2.53	18	18	187	0	
THR101	2.46	15.5	16	183.5	0.002	
THR102	----	----	----	----	----	CL
THR103	----	----	----	----	----	CL
THR104	----	----	----	----	----	CL
THR105	2.68	8	9	190	0.005	
THR111	----	----	----	----	----	CL
THR112	----	----	----	----	----	CL
THR113	----	----	----	----	----	CL
THR114	----	----	----	----	----	CL
THR115	----	----	----	----	----	CL

Expt. 4: Lab. RH = 45%,

No.	1st peak	Shear before	Shear after	Edge length	Shear radian	Comment
FOU11	----	----	----	----	----	SFB
FOU12	1.0	0	7	195	0.035	
FOU13	----	----	----	----	----	SFB
FOU14	----	----	----	----	----	SFB
FOU15	----	----	----	----	----	SFB
FOU41	2.32	----	----	----	----	SFB
FOU42	----	----	----	----	----	SFB
FOU43	----	----	----	----	----	SFB
FOU44	----	----	----	----	----	SFB
FOU45	2.16	-2.5	-2.0	197.5	0.002	
FOU71	3.59	-2	-1.5	198	0.002	
FOU72	3.26	-2	-1.5	196	0.002	
FOU73	3.57	-3	-2.5	195.5	0.002	
FOU74	3.74	0	0.5	195.5	0.002	
FOU75	3.22	0.5	1.0	195	0.002	
FOU101	4.17	-2	0	195	0.01	
FOU102	3.87	-1.5	1	194.5	0.002	
FOU103	3.73	2.5	3	191.5	0.002	
FOU104	3.54	1.5	1	192.5	0.002	
FOU105	4.7	-1.5	0	193.5	0.007	
FOU111	2.97	1	2	191	0.005	
FOU112	2.46	3.5	5	189.5	0.007	
FOU113	3.31	0	7	188	0.037	
FOU114	3.4	0.5	2.5	190.5	0.01	
FOU115	2.9	-1	3	191	0.01	

Expt. 5: Lab. RH = 45%,

No.	1st peak	Shear before	Shear after	Edge length	Shear radian	Comment
FIV11	0.57	2.5	6	193	0.018	
FIV12	0.55	-2.5	1	195.5	0.007	
FIV13	0.65	6.5	15	195	0.004	
FIV14	0.65	10.5	13	195	0.015	
FIV15	0.63	2.5	7	193.5	0.022	
FIV41	1.15	0.5	0.5	194	0	
FIV42	1.06	-1	-0.5	194.5	0.002	
FIV43	1.06	-2.5	-2	198	0.002	
FIV44	1.13	5	6	195	0.005	
FIV45	1.11	8	9.5	191.5	0.007	
FIV71	1.6	-0.5	0	195	0.002	
FIV72	1.65	-2	-1.5	195.5	0.002	
FIV73	1.94	4.5	5	192.5	0.002	
FIV74	1.91	10.5	10.5	198	0	
FIV75	1.53	-1	-1	199	0	
FIV101	2.48	4.5	6	197	0.007	
FIV102	2.09	5	6	195	0.005	
FIV103	2.35	3	4	195.5	0.005	
FIV104	2.04	6.5	7.5	195	0.005	
FIV105	2.21	2.75	3.5	198	0.003	
FIV111	----	----	----	----	----	CL
FIV112	----	----	----	----	----	CL
FIV113	----	----	----	----	----	CL
FIV114	----	----	----	----	----	CL
FIV115	----	0	1.5	191	0.007	

Expt. 6: Lab. RH = 45%,

No.	1st peak	Shear before	Shear after	Edge length	Shear radian	Comment
SIX11	----	----	----	----	----	SFB
SIX12	----	----	----	----	----	SFB
SIX13	1.04	0	1.5	187	0.008	
SIX14	0.8	-2.5	5	193.5	0.038	
SIX15	----	----	----	----	----	SFB
SIX41	1.86	3	3.5	193.5	0.002	
SIX42	2.08	-0.5	0	193.5	0.002	
SIX43	1.75	3	3.5	192.5	0.002	
SIX44	1.85	0.5	0	191.5	0.002	
SIX45	1.81	-0.5	0.5	192.5	0	
SIX71	2.89	11.5	11.5	198	0	
SIX72	2.85	-2	-1.5	196	0.002	
SIX73	2.83	2	2	193.5	0	
SIX74	2.54	-1.5	-1	198	0.002	
SIX75	5.84	0	0.5	198	0.002	
SIX101	3.47	-6.5	-6	198	0.002	
SIX102	3.06	-2.5	-2	195.5	0.002	
SIX103	3.1	2	2.5	197.5	0.002	
SIX104	3.16	-5	-4.5	196	0.002	
SIX105	----	----	----	----	----	CL
SIX111	----	----	----	----	----	CL
SIX112	----	----	----	----	----	CL
SIX113	----	----	----	----	----	CL
SIX114	----	----	----	----	----	CL
SIX115	----	----	----	----	----	CL

Expt. 7: Lab. RH = 47%,

No.	1st peak	Shear before	Shear after	Edge length	Shear radian	Comment
SEV11	0.96	----	----	----	----	SFB
SEV12	0.77	----	----	----	----	SFB
SEV13	0.87	----	----	----	----	SFB
SEV14	0.79	-1.5	5	195	0.033	
SEV15	0.96	----	----	----	----	SFB
SEV41	2.03	-3.5	-3	199	0.002	
SEV42	2.04	-3.5	-1	194.5	0.012	
SEV43	1.82	-1	1	199.5	0.01	
SEV44	1.93	-1	2	198.5	0.005	
SEV45	1.93	-0.5	1.5	198.5	0.01	
SEV71	3.13	1.5	1.5	196	0	
SEV72	2.77	-2	-1.5	197	0.002	
SEV73	2.7	-3	-2	195.5	0.005	
SEV74	3.15	-4.5	-1.5	194	0.015	
SEV75	3.54	7	7.5	192.5	0.002	
SEV101	3.41	-0.5	2	190	0.007	
SEV102	3.48	-2.5	-1	191.5	0.007	
SEV103	3.72	-4.5	-3	194.5	0.007	
SEV104	3.31	-1	0.5	189	0.007	
SEV105	3.22	0.5	1.5	191	0.005	
SEV111	2.81	0.5	1.5	187	0.001	
SEV112	3.02	1.5	4.5	188	0.015	
SEV113	----	----	----	----	----	CL
SEV114	3.24	1	3	189.5	0.01	
SEV115	3.08	1	----	190.5	----	MD

Expt. 8: Lab. RH = 45%,

No.	1st peak	Shear before	Shear after	Edge length	Shear radian	Comment
EIG11	----	----	----	----	----	SFB
EIG12	1.08	----	----	----	----	SFB
EIG13	1	----	----	----	----	SFB
EIG14	0.8	----	----	----	----	SFB
EIG15	1.16	----	----	----	----	SFB
EIG41	2	----	----	----	----	SFB
EIG42	1.82	----	----	----	----	SFB
EIG43	1.9	-0.5	0	196.5	0.002	
EIG44	2.02	-1	0	195	0.005	
EIG45	1.96	-0.5	0	194	0.002	
EIG71	3.37	4.5	4.5	198.5	0	
EIG72	2.84	-6	-5.5	200	0.007	
EIG73	2.99	2	2	198	0	
EIG74	2.92	-5	-4.5	198	0.002	
EIG75	2.94	3	3.5	196.5	0.002	
EIG101	2.84	-2.5	-2	197.5	0.002	
EIG102	2.64	-1.5	-1	198	0.002	
EIG103	3.09	-2	-1	196.5	0.005	
EIG104	2.62	-1.5	-1	197	0.002	
EIG105	3.28	-1.5	-0.5	198	0.005	
EIG111	2.07	1.5	2.5	191	0.005	
EIG112	----	----	----	----	----	CL
EIG113	----	----	----	----	----	CL
EIG114	----	----	----	----	----	CL
EIG115	----	----	----	----	----	CL

Expt. 9: Lab. RH = 45%,

No.	1st peak	Shear before	Shear after	Edge length	Shear radian	Comment
NIN11	0.51	1	11	193	0.051	SFB
NIN12	0.56	----	----	----	----	SFB
NIN13	0.55	----	----	----	----	SFB
NIN14	0.57	4	14.5	196	0.053	
NIN15	0.56	-1	7	194.5	0.041	
NIN41	1.05	4	6	196.5	0.01	
NIN42	----	----	----	----	----	MD
NIN43	1.19	3.5	5	191	0.007	
NIN44	1.47	-1	0	192.5	0.005	
NIN45	1.58	1.5	0.5	189.5	0.005	
NIN71	1.21	3	3	190	0	
NIN72	2.16	0	0.5	189	0.002	
NIN73	1.95	6	6.5	190	0.002	
NIN74	1.95	3	3.5	191	0.002	
NIN75	2.33	0	0	192	0	
NIN101	----	----	----	----	----	CL
NIN102	----	----	----	----	----	CL
NIN103	----	----	----	----	----	CL
NIN104	2.35	3	5.5	192.5	0.012	
NIN105	----	----	----	----	----	CL
NIN111	----	----	----	----	----	CL
NIN112	----	----	----	----	----	CL
NIN113	----	----	----	----	----	CL
NIN114	----	----	----	----	----	CL
NIN115	----	----	----	----	----	CL

Expt. 10: Lab. RH = 45%,

No.	1st peak	Shear before	Shear after	Edge length	Shear radian	Comment
TEN11	----	----	----	----	----	SFB
TEN12	0.376	4	8.5	187	0.024	
TEN13	0.358	----	----	----	----	SFB
TEN14	0.81	-1	15	192.5	0.083	
TEN15	1.07	----	----	----	----	SFB
TEN41	2.11	----	----	----	----	SFB
TEN42	1.82	-1	3	193.5	0.02	
TEN43	1.85	2	5.5	190.5	0.018	
TEN44	0.81	----	----	----	----	SFB
TEN45	1.94	----	----	----	----	SFB
TEN71	3.06	2	2.5	189.5	0.002	
TEN72	3.43	-1.5	-1.5	190	0	
TEN73	3.13	5	5.5	190.5	0.002	
TEN74	3.11	2.5	3	191	0.002	
TEN75	3.28	1.5	2	191.5	0.002	
TEN101	3.79	14.5	15.5	186	0.005	
TEN102	4.12	17	19	189	0.01	
TEN103	3.74	10	11.5	186	0.008	
TEN104	3.66	17.5	19	187.5	0.008	
TEN105	3.79	13	14	189	0.005	
TEN111	2.41	6	8.5	182	0.013	
TEN112	2.13	0.5	6	190	0.005	
TEN113	1.82	4	6.5	190	0.013	
TEN114	2.65	3	8	184	0.027	
TEN115	----	----	----	----	----	CL

Expt. 11: Lab. RH = 45%,

No.	1st peak	Shear before	Shear after	Edge length	Shear radian	Comment
ELE11	0.76	----	----	----	----	SFB
ELE12	0.77	----	----	----	----	SFB
ELE13	0.80	2	7	193.5	0.025	
ELE14	1.13	1	6	193.5	0.025	MS
ELE15	1.15	0	5.5	194.5	0.028	
ELE41	2.5	----	----	----	----	SFB
ELE42	2.59	----	----	----	----	SFB
ELE43	2.55	-2	-1	195.5	0.005	
ELE44	----	-5	-4.5	200	0.002	
ELE45	2.48	----	----	----	----	SFB
ELE71	3.48	-1	-1	198	0	
ELE72	3.52	-2	-1.5	198	0.002	
ELE73	3.73	4	5	192	0.005	
ELE74	3.64	-2.5	-2	191	0.002	
ELE75	3.74	----	----	----	----	SFB
ELE101	4.42	-1	1	196	0	
ELE102	4.37	-4.5	-3.5	196	0.005	
ELE103	3.73	-8	-6	193.5	0.01	
ELE104	4.26	-7.5	-5.5	193.5	0.01	
ELE105	3.43	0.5	1.5	196	0.005	
ELE111	----	----	----	----	----	CL
ELE112	----	----	----	----	----	CL
ELE113	----	----	----	----	----	CL
ELE114	2.79	0.5	1.5	193.5	0.005	
ELE115	2.69	----	----	----	----	SFB

Expt. 12: Lab. RH = 45%,

No.	1st peak	Shear before	Shear after	Edge length	Shear radian	Comment
TWE11	----	----	----	----	----	CL
TWE12	0.624	----	----	----	----	SFB
TWE13	----	----	----	----	----	CL
TWE14	----	----	----	----	----	CL
TWE15	0.522	----	----	----	----	SFB
TWE41	1.14	1	1	198.5	0	
TWE42	1.07	1	1.5	194.5	0.002	
TWE43	----	----	----	----	----	CL
TWE44	1.35	-2	-2	195	0	
TWE45	1.15	2.5	2.5	192	0	
TWE71	1.73	2.5	2.5	190	0	SC
TWE72	1.93	0.5	0.5	193	0	
TWE73	1.5	-2.5	-2.5	193	0	
TWE74	1.36	-0.5	-0.5	192.5	0	
TWE75	1.52	0	0.5	192.5	0.002	
TWE101	----	----	----	----	----	CL
TWE102	----	----	----	----	----	CL
TWE103	----	----	----	----	----	CL
TWE104	----	----	----	----	----	CL
TWE105	----	----	----	----	----	CL
TWE111	----	----	----	----	----	CL
TWE112	----	----	----	----	----	CL
TWE113	----	----	----	----	----	CL
TWE114	----	----	----	----	----	CL
TWE115	----	----	----	----	----	

Expt. 13: Lab. RH = 45%,

No.	1st peak	Shear before	Shear after	Edge length	Shear radian	Comment
THI11	0.93	1.5	3.5	192.5	0.005	
THI12	----	----	----	----	----	SFB
THI13	----	----	----	----	----	SFB
THI14	----	----	----	----	----	SFB
THI15	----	----	----	----	----	SFB
THI41	----	----	----	----	----	SFB
THI42	----	----	----	----	----	SFB
THI43	----	----	----	----	----	SFB
THI44	----	----	----	----	----	SFB
THI45	----	----	----	----	----	SFB
THI71	3.35	1	1.5	192.5	0.002	
THI72	3.84	4.5	5	188	0.002	
THI73	4.07	8	8.5	194.5	0.002	
THI74	3.74	0.5	1	196	0.002	
THI75	4.14	5.5	6	193.5	0.002	
THI101	4.47	2	3	193.5	0.005	
THI102	----	----	----	----	----	MD
THI103	4.43	1.25	2.5	190	0.006	
THI104	4.16	1.5	2.5	191	0.005	
THI105	4.19	5	6	189.5	0.005	
THI111	----	----	----	----	----	CL
THI112	----	----	----	----	----	CL
THI113	3.24	0.5	1.5	185	0.005	
THI114	3.45	1.5	2	185	0.002	
THI115	3.15	0	1	186	0.005	

Expt. 14: Lab. RH = 45%,

No.	1st peak	Shear before	Shear after	Edge length	Shear radian	Comment
FOR11	0.6	-2	-	197.5	0.005	
FOR12	0.63	----	----	----	----	SFB
FOR13	0.5	-5	-4	197	0.005	
FOR14	0.58	9	10.5	192	0.007	
FOR15	0.64	5	6.5	195	0.007	SC
FOR41	1.26	-0.5	1	196	0.007	
FOR42	1.22	9	10	191	0.005	
FOR43	1.09	-4	-3.5	198	0.002	
FOR44	0.89	0	1	195.5	0.005	
FOR45	1.05	-2.5	-1.5	196	0.0005	
FOR71	1.69	-2.5	-2	200	0.002	
FOR72	1.66	-3.5	-3	198	0.002	
FOR73	1.66	-5	-4.5	198	0.002	
FOR74	1.91	-2.5	-2	197	0.002	
FOR75	1.62	-2.5	-2	199.5	0.002	
FOR101	1.86	6	7	197	0.005	SC
FOR102	2.17	-2	-1.5	197.5	0.002	
FOR103	1.89	0.5	1.5	193.5	0.005	
FOR104	1.96	4	4.5	192	0.002	
FOR105	1.94	2.5	3	196.5	0.002	
FOR111	----	----	----	----	----	CL
FOR112	----	----	----	----	----	CL
FOR113	2.27	2.5	4	194	0.007	
FOR114	----	----	----	----	----	SFB
FOR115	----	----	----	----	----	CL

Expt. 15: Lab. RH = 45%,

No.	1st peak	Shear before	Shear after	Edge length	Shear radian	Comment
FIF11	0.84	-1.5	6	198	0.037	
FIF12	----	----	----	----	----	SFB
FIF13	----	----	----	----	----	SFB
FIF14	----	----	----	----	----	SFB
FIF15	0.97	6.5	9	194.5	0.012	SC
FIF41	1.72	-2.5	-2	197.5	0.002	
FIF42	1.56	-2.5	-2.5	196	0	
FIF43	1.19	-3	-2.5	196.5	0.002	
FIF44	1.37	-1	-0.5	196.5	0.002	
FIF45	1.26	-4	-3.5	196.5	0.002	
FIF71	2.04	1.5	1.5	195	0	
FIF72	2.21	0.5	0.5	195	0	
FIF73	2.32	2	2	196.5	0	
FIF74	2.16	-0.5	0	198.5	0.002	SC
FIF75	2.4	4	4	198	0	
FIF101	1.91	0	0	192	0	
FIF102	2.04	0.5	1	190	0.002	
FIF103	2.02	0.5	1	193	0.002	
FIF104	1.9	0	0	193	0	
FIF105	----	----	----	----	----	CL
FIF111	----	----	----	----	----	CL
FIF112	----	----	----	----	----	CL
FIF113	----	----	----	----	----	CL
FIF114	----	----	----	----	----	CL
FIF115	----	----	----	----	----	CL

Expt. 16: Lab. RH = 45%,

No.	1st peak	Shear before	Shear after	Edge length	Shear radian	Comment
SXT11	0.67	----	----	----	----	SFB
SXT12	0.75	----	----	----	----	SFB
SXT13	0.64	----	----	----	----	SFB
SXT14	0.84	----	----	----	----	SFB
SXT15	0.66	----	----	----	----	SFB
SXT41	1.45	----	----	----	----	SFB
SXT42	1.47	----	----	----	----	SFB
SXT43	1.33	----	----	----	----	SFB
SXT44	1.35	----	----	----	----	SFB
SXT45	1.42	----	----	----	----	SFB
SXT71	2.25	0.5	1.5	196.5	0.005	
SXT72	2.39	-2.5	2	199.5	0.002	
SXT73	----	-8.5	7.5	198	0.005	MC
SXT74	----	1.5	2	196.5	0.002	
SXT75	----	----	----	----	----	MD
SXT101	2.31	----	----	----	----	SFB
SXT102	2.64	-4.5	3	193.5	0.007	
SXT103	2.33	2	4	190	0.01	
SXT104	2.55	0	3	194	0.015	
SXT105	2.63	2	3.5	197	0.007	
SXT111	----	----	----	----	----	CL
SXT112	2.58	-1	3	193	0.02	
SXT113	3	5	11.5	188	0.034	
SXT114	----	----	----	----	----	CL
SXT115	2.71	0.5	2	190.5	0.007	

Expt. 17: Lab. RH = 45%,

No.	1st peak	Shear before	Shear after	Edge length	Shear radian	Comment
SVT11	0.89	----	----	----	----	SFB
SVT12	0.73	----	----	----	----	SFB
SVT13	0.74	----	----	----	----	SFB
SVT14	0.87	----	----	----	----	SFB
SVT15	0.79	----	----	----	----	SFB
SVT41	1.5	0	0.5	196.5	0.002	
SVT42	1.5	----	----	----	----	SFB
SVT43	1.49	0	0.5	195	0.002	
SVT44	1.67	-1	0	192.5	0.002	
SVT45	1.59	----	----	----	----	SFB
SVT71	2.85	11.5	12	192	0.002	
SVT72	2.34	5	5	200	0	
SVT73	2.31	12.5	13	195	0.002	
SVT74	----	1	1	196	----	MD
SVT75	2.48	-0.5	0	195	0.002	
SVT101	2.08	-2	-1.5	198.5	0.002	
SVT102	3.09	8.5	11.5	191.5	0.015	
SVT103	2.43	-0.5	0	192.5	0.002	
SVT104	2.45	4.5	5.5	191.5	0.005	
SVT105	2.33	0.5	1.5	193	0.002	
SVT111	1.78	----	----	----	----	SFB
SVT112	----	----	----	----	----	CL
SVT113	----	----	----	----	----	CL
SVT114	----	----	----	----	----	CL
SVT115	----	----	----	----	----	CL

Expt. 18: Lab. RH = 45%,

No.	1st peak	Shear before	Shear after	Edge length	Shear radian	Comment
EGT11	0.38	----	----	----	----	SFB
EGT12	----	----	----	----	----	MD
EGT13	0.87	----	----	----	----	SFB
EGT14	0.87	----	----	----	----	SFB
EGT15	0.89	----	----	----	----	SFB
EGT41	1.97	-1.5	1	191.5	0.002	
EGT42	1.92	-2.5	2	194	0.002	
EGT43	0.87	2.5	2.5	192	0	
EGT44	1.95	----	----	----	----	SFB
EGT45	1.78	----	----	----	----	SFB
EGT71	3.12	2.5	2.5	196.5	0	
EGT72	3.31	1.5	1.5	195.5	0	
EGT73	3.14	-2	-2	197	0	
EGT74	2.98	-2	-1.5	197.5	0.002	
EGT75	3.05	-2	-2	199.5	0	
EGT101	2.21	-0.5	0.5	195	0	
EGT102	2.42	-1	-1	195	0	
EGT103	2.27	-1.5	-0.5	192.5	0.002	
EGT104	2.27	-0.5	0.5	194	0	
EGT105	2.06	1	2.5	195.5	0.007	
EGT111	----	----	----	----	----	CL
EGT112	----	----	----	----	----	CL
EGT113	----	----	----	----	----	CL
EGT114	----	----	----	----	----	CL
EGT115	----	----	----	----	----	CL

Appendix 9e

Defective Sample Results

	Board Type				
	230 CC	250 TH	400 KT	400 KK	250 TCH
A1	0.62	0.23	0	0.2	0.68
A2	0.73	0.49	0	0.16	0.73
B1	0.63	0.37	0	0.3	0.7
B2	0.5	0.3	0	0.07	0.67
B3	0.9	0.41	0	0.17	0.76
C1	0.7	0.6	0	0.07	0.31
C2	0.6	0.23	0	0	0.8
C3	0.72	0.24	0	0.47	1.0
D1	0.6	0.34	0	0.2	0.73
D2	0.76	0.3	0	0.17	0.69
D3	0.67	0.43	0	0.17	0.7
E1	0.52	0.23	0	0.07	0.76
E2	0.9	0.4	0	0.23	0.63
E3	0.6	0.45	0	0.24	0.73
F1	0.77	0.37	0	0.24	0.8
F2	0.69	0.34	0	0.13	0.6
F3	0.57	0.37	0	0.17	0.72
G1	0.5	0.24	0	0.37	0.77
G2	0.77	0.17	0	0.07	0.69
G3	0.76	0.67	0	0.1	0.67
H1	0.55	0.3	0	0.07	0.73
H2	0.73	0.45	0	0.21	0.7
H3	0.73	0.33	0	0.27	0.69

Appendix 9f
S/N Ratio ANOVA Tables

Folding resistance

N.B 'F' ratios marked with *** indicate those control factors which have been pooled:

230 CC
Overall mean = 2.128

Factor	Sum of Sq	DoF	Ave. Sq	F	Rank
A	0.156	1	0.156	***	
B	0.457	2	0.229	***	
C	1.281	2	0.64	2.815	4
D	0.552	2	0.276	***	
E	2.097	2	1.049	4.61	2
F	1.376	2	0.688	3.024	3
G	13.7	2	8.352	36.72	1
H	0.427	2	0.214	***	
Total	23.05	15			
Error	1.592	7	0.227		

250 TCH

Overall mean = -4.04

Factor	Sum of Sq	DoF	Ave. Sq	F	Rank
A	0.273	1	0.273	***	
B	1.326	2	0.663	***	
C	1.777	2	0.889	1.993	4
D	2.046	2	1.023	2.295	3
E	2.621	2	1.311	2.94	2
F	0.206	2	0.103	***	
G	26.29	2	13.15	29.48	1
H	1.316	2	0.658	***	
Total	35.86	15			
Error	3.121	7	0.446		

400 KT

Overall mean = -8.26

Factor	Sum of Sq	DoF	Ave. Sq	F	Rank
A	0.007	1	0.007	***	
B	0.378	2	0.189	***	
C	7.629	2	3.814	36.41	2
D	0.148	2	0.074	***	
E	0.786	2	0.393	3.751	4
F	0.2	2	0.1	***	
G	31.18	2	15.59	148.8	1
H	2.929	2	1.465	13.98	3
Total	43.26	15			
Error	0.733	7	0.105		

400 KK

Overall mean = -9.09

Factor	Sum of Sq	DoF	Ave. Sq	F	Rank
A	0.146	1	0.146	***	
B	4.933	2	2.467	6.472	4
C	12.58	2	6.291	16.51	2
D	0.856	2	0.428	***	
E	0.015	2	0.008	***	
F	1.65	2	0.825	***	
G	13.58	2	6.788	17.81	1
H	5.481	2	2.74	7.19	3
Total	39.24	15			
Error	2.668	7	0.381		

250 TCH

Overall mean = -7.82

Factor	Sum of Sq	DoF	Ave. Sq	F	Rank
A	2.282	1	2.282	***	
B	11.81	2	5.907	1.472	3
C	7.975	2	3.987	***	
D	11.9	2	5.951	1.483	2
E	12.79	2	6.393	1.593	1
F	10.3	2	5.148	1.283	4
G	8.573	2	4.287	***	
H	9.261	2	4.631	***	
Total	74.89	15			
Error	28.09	7	4.013		

Lateral shear

230 CC

Overall mean = 31.5

Factor	Sum of Sq	DoF	Ave. Sq	F	Rank
A	44.4	1	44.44	***	
B	170	2	84.8	4.82	1
C	55.8	2	27.9	1.59	3
D	79.5	2	39.77	2.26	2
E	16.7	2	8.368	***	
F	9.34	2	4.67	***	
G	44.2	2	22.08	***	
H	43.5	2	21.75	***	
Total	463	15			
Error	158	9	17.58		

250 TH

Overall mean = 47.8

Factor	Sum of Sq	DoF	Ave. Sq	F	Rank
A	22.9	1	22.87	***	
B	88.2	2	44.11	2.84	2
C	233	2	116.4	7.51	1
D	6.01	2	3.006	***	
E	59.6	2	29.8	1.92	3
F	37.5	2	18.76	***	
G	53.5	2	26.77	1.73	4
H	42.1	2	21.06	***	
Total	543	15			
Error	109	7	15.5		

400 KT

Overall mean = 54.1

Factor	Sum of Sq	DoF	Ave. Sq	F	Rank
A	8.83	1	8.828	***	
B	20.6	2	10.31	3.58	3
C	129	2	64.63	22.4	1
D	0.65	2	0.327	***	
E	25.9	2	12.95	4.5	2
F	7.1	2	3.549	***	
G	2.67	2	1.336	***	
H	6.68	2	3.338	***	
Total	202	15			
Error	25.9	9	2.881		

400 KK

Overall mean = 45.1

Factor	Sum of Sq	DoF	Ave. Sq	F	Rank
A	4.14	1	4.139	***	
B	99.2	2	49.59	7.68	3
C	130	2	64.98	10.1	1
D	47.2	2	23.61	3.66	4
E	26.7	2	13.35	***	
F	12.6	2	6.316	***	
G	119	2	59.33	9.19	2
H	1.72	2	0.858	***	
Total	440	15			
Error	45.2	7	6.456		

250 TCH

Overall mean = 40.5

Factor	Sum of Sq	DoF	Ave. Sq	F	Rank
A	0.89	1	0.89	***	
B	39.9	2	19.96	2.42	4
C	14	2	63.994	***	
D	36.1	2	18.03	***	
E	60.3	2	30.16	3.66	2
F	61.6	2	30.8	3.74	1
G	48	2	23.98	2.91	3
H	6.77	2	3.385	***	
Total	268	15			
Error	57.7	7	8.245		

Appendix 9g

Optimum Settings

Optimum set for 230 CC (B).

230 CC	1	2	3	4	Comment
P(defect)	C2	D2	F3	G1	Not ranked
Folding resistance	G1	-	F2	C3	
Shear	-	D2	C2	-	
Optimum	G1	D2	C2	F2	

Optimum set for 250 TH (B).

250 TH	1	2	3	4	Comment
P(defect)	C2	D2	F2	G2	Not ranked
Folding resistance	G1	-	D2	C3	
Shear	C3	-	-	G3	
Optimum	G2	C3	D2	F2	

Optimum set for 400 KT (B).

400 KT	1	2	3	4	Comment
P(defect)	-	-	-	-	Not ranked
Folding resistance	G1	C3	-	-	
Shear	C3	-	-	-	
Optimum settings	G1	C3			

Optimum set for 400 KK (Gemini).

400 KK	1	2	3	4	Comment
P(defect)	C2	D2/3	F2	G2	Not ranked
Folding resistance	G1	C3	-	-	
Shear	C3	G2	-	D3	
Optimum settings	C2	G2	D3	F2	

Optimum set for 250 TCH (B/C).

250 TCH	1	2	3	4	Comment
P(defect)	C1	D2	F2	G3	Not ranked
Folding resistance	-	D1	-	F1	
Shear	F2	-	G1	-	
Optimum settings	F2	G3	C1	D1	

Appendix 9h

Confirmation Run Results

N.B Letter next to the 1st peak folding resistance indicates the position of crease along the flute.

No.	1st peak	Shear before	Shear after	Edge length	Shear radian	Comment
CR41	1.53C	-2.5	-2	198	0.002	
CR42	1.46A	1.5	1.5	198	0	
CR43	2.08B	9	9.5	195	0.002	SC
CR44	1.53C	-4.5	-4	196.5	0.002	
CR71	1.89C	-1	-0.5	1999	0.002	
CR72	1.73A	-1.5	-1	197.5	0.002	
CR73	2.19B	1.5	1.5	196	0	
CR74	1.91C	3.5	3	199.5	0.002	
CR101	2.19C	1	1.5	193	0.002	
CR102	2.55A	-2	-1.5	195.5	0.002	
CR103	3.1B	-3	-2.5	197.5	0.002	
CR104	3.42C	0	1	197	0.005	
CR111	3.04C	0	2	191	0.01	
CR112	3.61A	0	1.5	186.5	0.008	
CR113	4.11B	-3.5	-2	196.5	0.007	
CR114	2.87C	1	3	189	0.01	

Appendix 9i
Profile Design for 2nd Experiment

The generation of the twin roll creaser profile was based on the geometrical analysis of a double-flute structure. To replace the pre-crusher would mean the incorporation of the crushing function into the creaser itself. Consequently, the profile must be wide enough to reduce the section thickness of the corrugation to a reasonable level, but not too wide to encourage shear deformation.

The depth of penetration for the creaser could be estimated from the thickness of the buckled medium over which the creaser would define a score line. For example, there would be at least five layers of buckled material in a creased double-wall board. The width of the creaser could also be estimated from the pitch of the C-flute board, since, being the top layer of the double-wall board, the C-flute would be subject to the creasing and crushing forces on initial contact with the creaser.

The twin roll creaser design consists of a pair of identical creaser rolls with shoulder radius ' R ' and tip radius ' r ', as shown in Figure 9i.1.

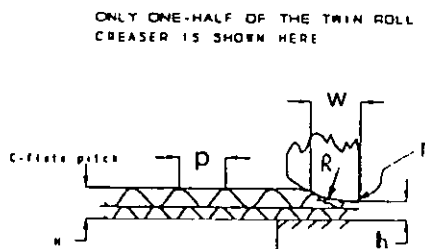


Fig. 9i.1 Twin roll creaser design for 2nd experiment.

where $p = f \times \text{C-flute pitch}$.

f = fraction of the flute pitch

k = compression ratio as defined by Vogelpohl [51]

w = effective width over which creaser has contact with the board

H = total board caliper

h = creaser roll gap

The following expressions can be derived geometrically:

$$R = \frac{(kH)^2 + p^2}{2kH}$$

$$w = \sqrt{2RH - 2Rh + 2Hh - H^2 - h^2}$$

Choosing the values 1.5, 1.75 and 2 for 'f', and a C-flute flute pitch of 7.547 mm under an 80 % compression (i.e $k=0.8$), the following values were calculated and were subsequently used in the experiment:

Creaser no.	R	h	w
1	15.57	1.5	11.9
2	20.31	2	13.4
3	25.78	2.5	14.6
4	15.57	2.5	11
5	20.31	1.5	14
6	25.78	2	15.3
7	15.57	2	11.5
8	20.31	2.5	12.8
9	25.78	1.5	16

Appendix 9j

Second Experiment Results

Expt	No.	1st peak	Shear before	Shear after	Edge length	Shear radian	Comment
I	B1	0.761	-0.5	4	194	0.023	SFB
	B2	0.889	0	5	197	0.025	
	B3	---	0	4.5	194	0.023	
	B4	0.672	-1	1	198.5	0.01	
	B5	0.69	0	4	196	0.02	SFB
II	B1	0.925	-1.5	4.5	193.5	0.031	SFB
	B2	0.991	0	6	196.5	0.03	
	B3	0.863	-2	4	197	0.03	
	B4	0.801	-2.5	2.5	196.5	0.025	
	B5	1	-1.5	4	196	0.028	
III	B1	1.261	-1.5	5	194	0.033	SFB
	B2	1.279	0	5.5	196	0.028	SFB
	B3	1.279	0	4.5	195	0.023	SFB
	B4	1.434	-2	2.5	190	0.023	SFB
	B5	1.451	0	3	198	0.015	
IV	B1	1.354	-1	3	193.5	0.02	
	B2	1.27	2	5.5	189	0.018	SFB
	B3	1.305	0	5	192.5	0.025	
	B4	1.35	-1	3	190	0.021	SFB
	B5	1.261	-1	5	192.5	0.031	SFB
V	B1	0.818	0	4.5	193	0.023	
	B2	0.54	2.5	6.5	192.5	0.02	CL
	B3	0.823	0	4.5	194	0.023	
	B4	0.734	0	5	193.5	0.025	

	B5	0.796	-1	5	193	0.031	
VI	B1	1.022	0	3.5	196	0.017	SFB
	B2	1.208	5	6.5	193	0.007	
	B3	0.942	-1	3	196.5	0.02	SFB
	B4	1.084	0	5	193.5	0.025	SFB
	B5	0.92	1	3	197	0.01	
VII	B1	1.168	2.5	10	189	0.039	SFB
	B2	1.124	-1.5	8	190	0.05	SFB
	B3	1.155	-0.5	9	191	0.049	SFB
	B4	1.199	-3.5	7	192	0.054	SFB
	B5	0.911	-0.5	5	193	0.028	SFB
VIII	B1	1.27	-1	1.5	193.5	0.012	
	B2	1.376	-1.5	4	194	0.028	
	B3	1.487	0	4.5	191	0.023	SFB
	B4	1.327	0	2.5	193.5	0.012	
	B5	1.327	0	4	193	0.02	
IX	B1	0.792	0	5.5	195	0.028	
	B2	0.867	0	5.5	194	0.028	
	B3	0.978	-2.5	5	196	0.038	SFB
	B4	0.902	8.5	11.5	190	0.015	
	B5	0.712	0	3.5	193	0.018	SFB

Percentage of defects and signal-to-noise ratios for both the first peak folding resistance and the shear deformation are tabulated as follows:

Factors	% Defects	Folding resistance	Shear deformation
r1	46.6	0.19	33.73
r2	46.6	-0.22	35.32
r3	53.3	-0.75	33.33
R1	66.6	-0.29	33.34
R2	20	0.02	32.36
R3	60	-0.51	36.65
g1	40	-0.2	36.46
g2	40	-0.08	32.02
g3	66.6	-0.5	34.13
h1	33.3	1.91	32.6
h2	60	-0.18	36.11
h3	53.3	-2.51	34.57

ANOVA tables for the folding resistance and the shear deformation are as follows:

Folding resistance

Factor	Sum of Sq.	DoF	Mean Sq.	F
Radius, r	1.33	2	0.66	3.7
Radius, R	0.42	2	0.21	---
Gap, g	0.28	2	0.14	---
Roll gap, h	9.77	2	4.88	27.8
Total	11.8	8		
(Error)	0.7	4	0.175	

Shear deformation

Factor	Sum of Sq.	DoF	Mean Sq.	F
Radius, r	6.71	2	3.35	---
Radius, R	30.39	2	15.19	4.5
Gap, g	29.59	2	14.79	4.4
Roll gap, h	18.99	2	9.49	2.8
Total	85.68	8		
(Error)	6.71	2	3.35	

Appendix 9k

Third Experiment Results

No.	Peak 'A'	Peak 'B'	Grad 'D'	Shear before	Shear after	Edge length	Shear radian	Note*
I	2.54	2.63	0.073	1.5	4	195	0.012	
	1.75	2.28	----	-4	7	194.5	0.056	NPA
	1.75	3.91	----	2	5.5	189	0.018	NPA
	1.82	2.79	0.116	2	13	195	0.056	
	1.82	2.57	0.009	10	13	190	0.015	
	1.95	2.32	----	11.5	22	188	0.055	NPA
II	2.75	3.59	0.109	-2	0	187	0.01	
	2.74	3.8	0.12	-5.5	-2.5	193	0.015	
	2.82	3.48	0.06	-1	4	188	0.026	
	2.65	2.46	0.055	-3.5	6	189	0.05	
	1.7	3.01	----	0	3	191	0.015	NPA
	2.6	2.7	0.067	-9	-4.5	200	0.022	
III	2.66	2.48	0.003	-1	8	192.5	0.046	
	3.15	3.6	0.127	1.5	6.5	189	0.026	
	3.23	3.97	0.113	0.5	3.5	187	0.016	
	4.15	3.3	0.121	0.5	13	191	0.065	
	2.49	2.73	0.02	-2.5	2	197	0.022	
	2.24	3.48	0.091	-3.5	-0.5	190	0.015	
	2.84	2.73	0.125	2	9.5	190	0.039	
	2.78	2.63	0.143	-1.5	3	182	0.024	
IV	2.46	2.93	0.056	-4	-2	197.5	0.01	
	2.67	3.33	0.079	-2	3	191.5	0.026	
	3.08	2.85	0.147	1.5	5	189	0.018	
V	2.82	2.61	0.225	-3	4	193	0.036	
	3.39	3.43	0.152	-2.5	8	190	0.055	

	2.51	3.4	0.131	0	2.5	194.5	0.012	
	2.25	2.76	0.04	3	14	189	0.058	
	2.81	2.37	0.091	-4.5	4	192.5	0.044	
	2.58	3.49	0.033	1.5	11.5	191.5	0.052	
	2.47	2.86	0.081	4	10	188.5	0.031	
	2.05	2.82	----	0	10	190	0.052	NPA
	2.88	2.37	0.124	1.5	10	189	0.044	
VI	1.45	3.28	----	-0.5	5	193.5	0.028	NPA
	2.51	2.3	0.04	-9	8	192.5	0.088	
	2.4	2.75	0.012	0	14	196	0.074	
	2.19	2.95	0.023	3.5	11.5	191.5	0.041	
	1.91	2.88	0.013	0	5	190.5	0.026	
VII	3.51	4.72	0.197	0	3.5	188.5	0.018	
	3.18	3.3	0.183	-1	1	193	0.01	
	3.2	3.3	0.076	-11	-7.5	199.5	0.017	
VIII	2.66	3.64	0.18	6.5	11	193	0.023	
	2.59	3.62	0.098	-2.5	2	193	0.023	
	1.82	2.4	0.013	-5.5	9	188	0.077	
	1.8	2.86	0.06	-1.5	10	192	0.059	
IX	3.32	2.42	0.104	-2	7.5	194	0.048	
	3.54	2.85	0.098	2.5	15	195	0.064	
	3.24	3.3	0.171	0	9	194.5	0.046	
	3.08	3.12	0.114	-2	13.5	195	0.079	
	2.46	2.35	0.073	5.5	9	190	0.018	
	3.43	2.7	0.16	-5	8	193.5	0.067	
	2.94	2.32	0.104	0.5	6.5	191	0.031	
	2.68	3.05	0.07	-1.5	1	188.5	0.013	

* NPA - No clearly defined peak 'A', hence 1st peak gradient could not be recognized by software.

Test No.	No. and type of defects ⁺
I	4 PCC
II	3 PCC, 1 WC
III	2 PCC
IV	1 PCC, 6 CC
V	1 PCC
VI	2 PCC, 3 CC
VII	1 PCC, 6 CC
VIII	6 CC
IX	1 PCC, 1 CC

+ Key to the type of defects:

PCC - cracked liner due to pre-crushing

CC - cracked liner due to creaser

WC - wandering crease

S/N ratios for the fraction of defective samples (with the two types of failure being separated, i.e. those due to pre-crushing and creasing), the folding resistance peaks 'A' and 'B' and gradient 'D', and the shear deformation are as shown below:

Exp No.	Orth. Array	PCC Defect Rate			CC Defect Rate		
		p	1-p	η_{def}	p	1-p	η_{def}
1	1111	4/10	6/10	1.76	0	1	----
2	1222	3/9	6/9	3.01	0	1	----
3	1333	2/10	8/10	6.02	0	1	----
4	2123	1/10	9/10	9.54	6/9	3/9	-3.01
5	2231	1/10	9/10	9.54	0	1	----
6	2312	2/10	8/10	6.02	3/8	5/8	2.21
7	3132	1/10	9/10	9.54	6/9	3/9	-3.01
8	3213	0	10	----	6/10	4/10	-1.76
9	3321	1/10	9/10	9.54	1/9	8/9	9.03

Exp no.	Orth. Array	Shear		Folding resistance				
		η_{shear}	No.	η_A	η_B	No.	η_D	No
1	1111	27.78	6	-5.83	-8.95	6	-36.23	3
2	1222	31.53	6	-8.2	-10.13	6	-22.94	5
3	1333	28.99	8	-9.52	-9.98	8	-41.54	8
4	2123	34.35	3	-8.78	-9.66	3	-22.43	3
5	2231	26.97	9	-8.51	-9.33	9	-23.98	8
6	2312	24.96	5	-6.55	-9.09	5	-35.84	4
7	3132	36.24	3	-10.37	-11.66	3	-18.82	3
8	3213	25.82	4	-7.06	-10.03	4	-31.99	4
9	3321	25.87	8	-9.84	-8.9	8	-20.16	8

In terms of contributions due to each factor level:

Fac	η_{PCC}	η_{CC}	η_A	η_B	η_D	η_{shear}
A1	3.59	---	-7.85	-9.69	-33.57	29.43
A2	8.36	-0.4	-7.95	-9.36	-27.42	28.76
A3	9.54	1.42	-9.09	-10.2	-23.66	29.31
B1	**	-3.01	-8.33	-10.09	-25.83	32.79
B2	**	-1.76	-7.92	-9.83	-26.3	28.11
B3	**	5.62	-8.64	-9.32	-32.51	26.61
C1	**	0.22	-6.48	-9.36	-34.69	26.19
C2	**	3.01	-8.94	-9.56	-21.84	30.58
C3	**	-3.01	-9.47	-10.32	-28.11	30.73
D1	**	9.03	-8.06	-9.06	-26.79	26.87
D2	**	-0.4	-8.37	-10.29	-25.87	30.91
D3	**	-2.38	-8.45	-9.89	-31.99	29.72

** η_{PCC} deliberately left out because no pre-crushing failures could possibly be due to these factors.

ANOVA Tables:

I) Fraction defective, $M = 0.75$

Factor	Sum of sq.	DoF	Ave. Sq.	F	Rank
A	3.54	1	3.54	----	
B	132.46	2	66.23	18.7	2
C	58.57	2	29.28	8.27	3
D	239.03	2	119.51	33.76	1
Total	433.6	7			
Error	3.54	1	3.54		

II) Folding resistance η_A , $M = -8.30$

Factor	Sum of sq.	DoF	Ave. Sq.	F	Rank
A	2.85	2	1.43	5.56	2
B	0.77	2	0.38	----	
C	15.25	2	7.62	29.7	1
D	0.26	2	0.13	----	
Total	19.13	8			
Error	1.03	4	0.26		

III) Folding resistance η_B , $M = -9.75$

Factor	Sum of sq.	DoF	Ave. Sq.	F	Rank
A	1.07	2	0.53	----	
B	0.91	2	0.46	----	
C	1.55	2	0.78	1.57	2
D	2.37	2	1.19	2.40	1
Total	5.91	8			
Error	1.98	4	0.49		

IV) Folding resistance η_D , M = -28.21

Factor	Sum of sq.	DoF	Ave. Sq.	F	Rank
A	150.28	2	75.14	2.02	2
B	83.5	2	41.75	----	
C	247.47	2	123.74	3.33	1
D	65.31	2	32.66	----	
Total	546.56	8			
Error	148.82	4	37.2		

V) Shear deformation η_{Shear} , M = 29.17

Factor	Sum of sq.	DoF	Ave. Sq.	F	Rank
A	0.77	2	0.39	----	
B	62.42	2	31.21	80.95	1
C	40.03	2	20.01	51.91	2
D	25.81	2	12.91	33.48	3
Total	129.03	8			
Error	0.77	2	0.39		

Confirmation run results:

The settings for the confirmation run are ranked as follows:

Response\Rank	1	2	3
Defects %	D1	B3	C2
Shear	B1/2	C3/2	D2/3
Folding resistance 'D'	C2	A3/2	
Folding resistance 'A'	C1	A1/2	
Folding resistance 'B'	D1/3	C1/2	

The optimized settings chosen were D1, B2, C2 and A2, and the experiment was conducted at 53 % rel. humidity and room temperature of 24 °C. Two samples were torn during the experiment: one during pre-crushing and one during creasing. The results were as follows:

Expt.	Peak 'A'	Peak 'B'	Grad 'D'	Shear before	Shear after	Edge length	Shear / radian
1	3.04	2.79	0.1	2.5	6	196.5	0.017
2	2.76	3.36	0.09	1	3.5	186	0.013
3	2.96	2.72	0.092	-2	21.5	190	0.123
4	3.1	2.8	0.134	0	8.5	185.5	0.045
5	2.49	3.13	0.075	-1.5	4	197	0.027
6	3.36	2.58	0.09	3	14	187.5	0.058
7	3.02	2.78	0.075	1.5	8	188.5	0.034
8	2.12	2.62	0.109	0	10	189.5	0.052

REFERENCES

- [1] Ball, R.S., "The theory of screws", Cambridge University Press, 1900.
- [2] Benson, R.E., "Effects of relative humidity and temperature on tensile stress-strain properties of kraft linerboard", TAPPI 54(5), p699-703, 1971.
- [3] Buchanan, J.S., "The effect of crease form on the compressive strength of corrugated cases", Packaging, vol. 34, 1963.
- [4] Chakraborty, J. & Dhande, S.G., "Kinematics and Geometry of Planar and Spatial Cam Mechanisms", Wiley Eastern Ltd., 1977.
- [5] Chen, F.Y., "Mechanics and Design of Cam Mechanisms", Pergamon Press, 1982.
- [6] Corte, H. in "Paper and Board - A Survey in Composite Materials", ed. by L. Holliday, Elsevier Publishing Co., Amsterdam, 1965.
- [7] Edholm, B. & Eriksson, E.L., "Swedish study tells how flap folding affects cartoning", Packaging, vol.28, 1983.
- [8] Goodman, J.W., "Laser Speckle and Related Phenomenon", Chap2, ed. J.C. Dainty, Springer-Verlag, Berlin, 1975.
- [9] Grebe, V.W. & Nebel, F., "Über das Rillen von Wellpappe", Papier & Kunststoff Verarbeiter, Teil 2: 8/80 und Teil 3: 2/81.
- [10] Hain, K, "Applied Kinematics", McGraw-Hill, 1967.
- [11] Hain, K, "Konstruktion des Gegenprogiles in dreigliedrigen Wälzkurvengetrieben", T. Zprakt. Metallbearb. (64), p331-334, 1970.
- [12] Hanlon, J.F., "Handbook of Package Engineering", p.5-8, McGraw-Hill, 1971.

- [13] Hohmann, H.J., "Biegesteifigkeit von Pappe und Karton", Verpackungs-Rundschau, nr.5, 1971.
- [14] Hrones, J.A., "Analysis of dynamic force in a cam-driven system", Trans. ASME, 70:473-482, 1948.
- [15] Hunt, K.H., "Kinematic Geometry and Mechanisms", OUP, 1970.
- [16] Ishikawa, K., "What is Total Quality Control? The Japanese Way", Prentice-Hall, 1985.
- [17] ISO 3037, "Corrugated fibreboard - Determination of edgewise crush resistance", 2nd ed., 1982.
- [18] Jackson, C.A., Koning, J.W. and Gatz, W.A., "Edgewise compressive test of paperboard by a new method", Pulp Paper Mag. Can., vol.77, part 10, p43-46, Oct.1976.
- [19] Johnson, et al., "Failure Phenomenon", in "Handbook of Physical and Mechanical Testing of Paper and Paperboard", ed. by Mark, R.E. and Murahami, K., Marcel Dekkar Inc., N.Y. 1983.
- [20] Jones, R., Wykes, C., "Holographic and speckle interferometry", Cambridge University Press, 1989.
- [21] Kawabata, S., "Non-linear Mechanics of Woven and Knitted Materials", in "Textile Structural Composite", ed. by T.W. Chou and F. Ko, Elsevier, 1989.
- [22] Kellicutt, K.Q., "How Paperboard Properties Affect Corrugated Container Performance", TAPPI Journal, vol.44, no.3, March 1961.

- [23] Kennedy, A.B.W., "The Mechanics of Machinery", Macmillan, London, 1886.
- [24] Lau, A.M. & Davies, T.H., "Case-making Process Optimization", TAPPI Conf. Journal, Oct. 1992.
- [25] Leung, F.B., "Dynamic of a spatial cam", BSc Project Report, Mech. Eng., Loughborough University of Technology, 1993.
- [26] McKee, R.C. & Altmann, F.J., "Comparative Evaluation of panel or body creasing wheel contours", TAPPI vol. 39, part 7, 1956.
- [27] McKee, R.C., Gander, J.W. and Wachuta, J.R., "Flexural Stiffness of Corrugated Board", Paperboard Packaging, Dec. 1962.
- [28] McKee, R.C., Gander, J.W. and Wachuta, J.R., "Compression strength formula for corrugated boxes", Paperboard Packaging, 48(8), p.149-159, 1963.
- [29] Mechanica v.4: "Applied Structure", licensed under Rasna Corporation, 2590 North First St., #200, San Jose, California 95131, U.S.A.
- [30] Nordman, L., Kolhonen, E. and Toroi, M., "Investigation of the compression of corrugated board", FEFCO, 15th Congress, Estoril, Portugal.
- [31] Olmstead, E.H., "Poppet valve dynamics", J. E.S. Taylor Aeronautical Sci., p.370-375, 6 Jul., 1939.
- [32] Paul, R., "Robot Manipulators: Mathematics, Programming and Control", MIT Press, Cambridge, MA, 1982.
- [33] Phadke, M.S., "Quality Engineering using Robust Design", Prentice-Hall International Inc., 1989.

- [34] Phillips, E.A, "Quick calculations for corrugation stiffness", published in "Engineering Data for Product Design", edited by D C Greenwood, McGraw-Hill, 1961.
- [35] Phillips, J.R. & Hunt, K.H., "On the theorem of three axes in the spatial motion of three bodies", Aust. J. Applied Science, vol.15, 1964.
- [36] Phillips, J., "Freedom in Machinery", vol. 1 & 2, Cambridge University Press, 1984 & 1989.
- [37] Plucker, J., "On a new geometry of space", Phil. Trans., vol.155, 1865.
- [38] Rothbart, H.A., "Cams: Design, Dynamics and Accuracy", Wiley, NY, 1956.
- [39] Rother, V., "Faltung im Luftstrom", Papier & Kunststoff Verarbeiter, Nr. 3, 1988.
- [40] Rushforth, E., PhD thesis (in preparation), Loughborough University of Technology.
- [41] Ruvo, A., Fellers, C. and Engman, C., "The influence of raw material and design on the mechanical performance of boxboard", Svensk Papperstidning, nr.18, 1978.
- [42] Seymour, W.B. & Terle, M., "Perfect Square Box Folding with the Multi-T Belt Concept", TAPPI Journal, Jan. 1985.
- [43] Shulman, J.J., "Introduction to flexo-folder gluers", Jelmar Publishing Co., Inc., N.Y., 1986.

- [44] Smith, G.E., "Elastic buckling in shear of infinitely long corrugated plates with clamped edges", thesis submitted for the MAeroEng, Cornell Univ., USA, 1957.
- [45] Sprague, C.H. & Whitsitt, W.J., "Medium fracture and strength losses in fluting", TAPPI Journal, Oct. 1982.
- [46] Sze, W.S. & Yu, K.M., "Rapid prototyping - a review", Hong Kong Engineer, Dec. 1993.
- [47] Taguchi, G., Elsayed, A. & Hsiang, T.C., "Quality Engineering in Production Systems", McGraw-Hill Book Company, 1989.
- [48] Taguchi, G., "System of Experimental Design", ed. by D. Clausing, NY: UNIPUB/Kraus International Publications, vol. 1 and 2, 1987.
- [49] Taguchi, G., "Introduction to Quality Engineering", Asian Productivity Organization, 1986.
- [50] Thomas, C.E., "Single-facer process study - preconditioning alternatives", TAPPI Proceedings, 1979.
- [51] Vogelpohl, V.H. & Hohmann, H.J., "Versuche zur Optimierung des Rillens von Wellpappen", Verpackung-Rundschau, Nr.8, 1987.
- [52] Vollmer, W., "Klima- und Feuchtigkeitseinfluß auf Wellpappe", Verpackungs-Rundschau, 15 nr.6, Techn.-wiss. Beilage, S.41-46, 1964.
- [53] Vyse, B., Frankling, P., "Testing of Adhesives" in "Industrial Packaging Adhesives", ed. K. Booth, Blackie & Sons Ltd., 1990.

- [54] Werner, A.W., "The Manufacture of Fibre Shipping Containers", Fibre containers, part 12, p42, Dec. 1940.
- [55] Whitsitt, W.J., "Relationships between runnability and medium properties", TAPPI Proc. Corrugated Containers Conf., 1987.
- [56] Whitsitt, W.J., "Papermaking Factors affecting Box Properties", TAPPI Proc., Corr. Containers Conf., 1988.
- [57] Wykes, C., "Use of electronic speckle pattern interferometry in the measurement of static and dynamic surface displacements", Opt. Eng., 21(3), 400-406, May/June, 1982.

